SOLAR RADIATION INTERACTIONS WITH SEASONAL SEA ICE

by

Jens Kristian Ehn

A Thesis submitted to the Faculty of Graduate Studies of
The University of Manitoba
in partial fulfillment of the requirements of the degree of

DOCTOR OF PHILOSOPHY

Centre for Earth Observation Science
Department of Environment and Geography
University of Manitoba
Winnipeg

THE UNIVERSITY OF MANITOBA

FACULTY OF GRADUATE STUDIES

*****

COPYRIGHT PERMISSION

Solar Radiation Interactions with Seasonal Sea Ice

BY

Jens Kristian Ehn

A Thesis/Practicum submitted to the Faculty of Graduate Studies of The University of Manitoba in partial fulfillment of the requirement of the degree

DOCTOR OF PHILOSOPHY

Abstract

Presently, the Arctic Ocean is undergoing an escalating reduction in sea ice and a transition towards a seasonal sea ice environment. This warrants detailed investigations into improving our understanding of the seasonal evolution of sea ice and snow covers, and their representation in climate models. The interaction of solar radiation with sea ice is an important process influencing the energy balance and biological activity in polar seas, and consequently plays a key role in the earth's climate system. This thesis focuses on characterization of the optical properties—and the underlying physical properties that determine them—of seasonal sea ice during the fall freeze-up and the spring melt periods. Both periods display high spatial heterogeneity and rapid temporal changes in sea ice properties, and are therefore poorly understood. Field data were collected in Amundsen Gulf/Franklin Bay (FB), southern-eastern Beaufort Sea, in Oct.-Nov. 2003 and Apr. 2004 and in Button Bay (BB), western Hudson Bay, in Mar.-May 2005 to address 1) the temporal and spatial evolution of surface albedo and transmittance, 2) how radiative transfer in sea ice is controlled by its physical nature, and 3) the characteristics of the bottom ice algae community and its effect on the optical properties.

The fall study showed the importance of surface features such as dry or slushy bare ice, frost flowers and snow cover in determining the surface albedo. Ice thickness was also important, however, mostly because surface features were associated with thickness. For example, nilas (<10 cm thick) was typically not covered by a snow layer as snow grains were dissolved or merged with the salty and warm brine skim layer on the surface, while surface conditions on thicker ice types were cold and dry enough to support a snow cover. In general, the surface albedo increased exponentially with an ice thickness increase, however, variability within ice thickness types were very large. It is apparent that a more complete treatment of brine movement towards the surface ice of the ice cover and the formation of surface features—such as frost flowers or slush layers—is required to understand the albedo of newly formed sea ice.

The sea ice had reached its maximum thickness by late April in both FB and BB (~1.8 m vs. 1.5-1.7 m). However, surface conditions differed notably as surface melting had not been initiated in FB, while melting had progressed to an advanced stage in BB, illustrating the difference in climate between the two regions (Arctic vs. sub-Arctic). The shortwave partitioning between the atmosphere, sea ice and the ocean—as well as within the sea ice—was strongly

affected by diurnal freeze-thaw processes and synoptic weather events that controlled the optical characteristics of the surface.

In spring, *in situ* measurements with a high vertical resolution were conducted within the bottom sea ice layers. The optical properties were strongly affected by ice algae present in the bottom few centimeters. Particulate absorption decreased quickly within the ice above the living algae layer, and showed characteristics of detrital matter. The optical properties for the bottom layers of the sea ice were found to significantly differ from interior ice. This is expected as the bottom ice is very porous and has a lamellar platelet structure, in addition to containing high concentrations of biological matter.

These findings emphasize the importance of processes occurring near the surface and bottom boundaries in determining radiative transfer in sea ice covers. Ultimately, a focus on linking numerous aspects of sea ice physics and biology is required in order to predict the seasonal evolution of the sea ice cover in a changing climate.

Acknowledgements

A sincere thank you to my supervisor David Barber for providing the opportunity for me to conduct fulltime research. It has been an interesting period of my life and I have learned lots here in Canada. I would also like to thank the committee members Tim Papakyriakou, Jay Doering and Thomas Grenfell, as well as the anonymous reviewers of the various journal papers, for their significant contributions in improving the quality of this thesis. Many colleagues at CEOS have also made valuable contributions in this work and in the process become good friends. I would especially like to acknowledge Debbie Armstrong, Ryan Galley, Mats Granskog, Leah Hartwig, Bob Hodgson, Philip Hwang, Alex Langlois, C. J. Mundy and Owen Owens. The rest of the staff at CEOS also deserve acknowledgement for creating a pleasant and inspiring work environment. I am very grateful to my family back home in Finland for their understanding and support of my move to Canada. This distance relationship has not always been easy. I am especially indebted to Tracy Taylor for all her support and patience while I have been working away on this thesis. This work has been funded through grants by the Natural Sciences and Engineering Research Counsil (NSERC) for the CASES and ArcticNet networks.

Table of contents

List of Tables

List of Figures

CHAPTER 1: Introduction

1.1 Scientific rationale

Recent evidence of heightened reduction in areal extent (*Parkinson et al.*, 1999; *Comiso*, 2003, 2008; *Nghiem et al.*, 2007) and perennial ice thickness (*Yu et al.*, 2004) of the northern hemisphere sea ice have focused attention on the fact that impacts of global climate change can already be seen in the high latitudes of our planet (*ACIA*, 2005; *IPCC*, 2007). Trends based on observations point towards a transition to a seasonally ice-free Arctic Ocean within the first half of this century (e.g., *Maslanik et al.*, 2007). This development is corroborated by general circulations models (GCMs) that collectively project a continuing decrease in ice extent and thickness (e.g., *ACIA*, 2005). However, the simplified treatment in GCMs of many highly coupled processes operating within the ocean-sea ice-atmosphere (OSA) system result in considerable uncertainties in these predictions (*Serreze et al.*, 2000; *ACIA*, 2005), and the scientific community is actively developing and improving parameterizations to better reflect the observed trends.

The current development is concerning because sea ice in the polar waters is an important component in the global climate system. At any one time it covers 3-6% of the total surface area of the earth (*Comiso*, 2003). By acting as a thermal insulator and a mechanical cover, sea ice strongly influences the air-sea exchange of energy, water and momentum (e.g., *Maykut*, 1986), and thereby significantly affects weather and meteorological conditions. Its growth expels salt and can lead to vertical convection in the ocean and deep-water formation (e.g., *Winsor and Björk*, 2000). Thus, sea ice formation is a significant contributor to the global thermohaline "conveyor belt" circulation—a major mechanism that transports oceanic heat poleward and sequesters atmospheric CO_2 into the deep ocean (e.g., *Anderson et al.*, 2004). Its low salinity melt water, however, inputs freshwater and thus stratifies the upper layer of the ocean aiding phytoplankton to remain within the euphotic zone and forms a barrier against entrainment of warm Atlantic water (e.g., *Aagaard and Carmack*, 1989). Sea ice drift may cause melting to occur at significant distances from the place of formation, and thus constitute an important freshwater and latent heat flux (e.g., *Vinje*, 2001). However, since the sea ice cover is relatively thin, small changes in the energy balance lead to rapid changes in its thickness and extent. Thus, the presence or absence of sea ice serves as a sensitive indicator and amplifier of climate change.

Sea ice is also a vital component in the polar marine ecosystem as it forms an important habitat for a range of organisms from viruses to polar bears and humans. Sea ice provides a stable substrate on which ice algae growth may occur. Highest ice algae concentrations (up to 200 mg chlorophyll-*a* m^{-2}) are typically found near the ice-ocean interface where the access to nutrient as well as radiation is optimized (*Arrigo*, 2003). Ice algae and also other micro organisms (bacteria, viruses) are, however, present in small concentrations throughout the ice matrix and thought to originate from cells that were trapped within brine inclusions as the sea ice formed (*Garrison et al.*, 1989; *Junge et al.*, 2004). Recent evidence point towards a possibility that atmospheric CO_2 may serve as a carbon source for the interior micro organisms (*Semiletov et al.*, 2004; *Rysgaard et al.*, 2007). As irradiance levels increase concurrently with the ice melt progression during spring, conditions are reached when ice algae are released to the water column due to melt water flushing (*Lavoie et al.*, 2005) and a loss of substrate in response to increased absorption of radiation by the algae themselves (*Zeebe et al.*, 1996). Melt water stabilization of the water column together with increasing irradiance levels, and a possible seeding effect of released ice algae, are thought to be important factors in initiating the spring phytoplankton bloom (*Michel et al.*, 1993).

One of the key issues in energy balance studies is the treatment of solar radiation interaction with the ever-changing sea ice cover. This interaction may be embodied by the surface albedo feedback (SAF) mechanism (e.g., *Curry et al.*, 1995). Its importance is stressed by *Hall* (2004), who concluded from a model investigation that SAF accounted for about half of the response to a doubling of atmospheric CO_2 in high latitudes, and that it had a warming impact on regions as far away as the tropics. However, a common feature in model studies (see, e.g., *ACIA*, 2005) is the oversimplified treatment of those properties and processes that determine sea ice albedo (e.g., *Hwang et al.*, 2006). Note that the SAF mechanism is a natural part of the seasonal cycle: During winter, the typically snow covered sea ice surface has a high albedo (>0.8). With spring, increased radiation levels result in sufficient absorption within the sea ice/snow volume to trigger melting and a consequent decrease in albedo, which then leads to more absorption and further albedo decrease (a positive feedback loop). On a larger scale, the reduction in sea ice extent and concentration causes a regional decrease in albedo and warming of the upper water layers. The excess heat input to the water column is balanced by lateral and bottom melt of the sea ice, resulting in further reduction in the regional albedo. Qualitatively, the SAF mechanism is thus well understood. However, the prediction of future climates and ice states in response to increases in greenhouse gas emissions requires a quantitative understanding of the processes involved in the interaction of radiation within the OSA.

The sea ice cover is more complex than simply a homogenous slab of ice placed between the atmosphere and the ocean. Sea ice and its snow cover are layered media composed of ice, brine, solid salts, air and impurities. Snow is more porous than sea ice with spaces between the ice crystals/grains/clusters that are mainly filled with air (and water vapor). Brine is also present as a film on the snow grain surfaces. In sea ice, brine and air are collected into inclusions that are trapped in interstices of the ice crystal lattice. One of the main objectives in optical studies within the OSA is to determine how radiation is partitioned between reflection, absorption and transmission as the system undergoes changes in its geophysical and thermodynamic state. How the snow and sea ice structure is formed and evolves, and how the inclusions are shaped and distributed within, determine how radiation interacts with it. Structural-optical relationships (Grenfell, 1983) may be used to go from physical properties—such as temperature, salinity and density—to inherent optical properties (IOPs)—such as absorption and scattering—that can be used to solve for apparent optical properties (AOPs)—including, e.g., albedo and transmittance. AOPs, in turn, are the necessary properties needed to obtain a radiation budget (*Jin et al.*, 1994). This approach, however, requires information on inclusion sizes, number densities and their distribution, something that is not easily obtained.

Inclusion size distributions are now known to some extent for the interior portion of first-year ice when temperatures are low (see *Light et al.*, 2003; 2004, and references therein). When sea ice temperatures are low (below about -5°C), brine inclusions are separate and reasonably well represented by individual spherical inclusions (*Light et al.*, 2003). It is thus straightforward to calculate the relevant optical properties from measured temperature, salinity and density fields. In addition, radiative transfer in dry snow is well explained by the sizes of individual snow grains and impurities (e.g., *Warren*, 1982). These structural-optical relationships are only valid for winter and early spring conditions when temperatures are cold.

With the onset of melt in late spring, metamorphic processes result in the enlargement and clustering of snow grains and eventually drainage of melt water and superimposed ice formation. Temperatures increase to values above -5°C throughout the sea ice cover. Note, however, that temperatures near the ice-ocean interface, and generally in thin newly formed ice, are strongly affected by the presence of underlying seawater and therefore remain close to the freezing point at all times. A rise in sea ice temperatures to values above -5°C is significant, as this typically corresponds to a brine volume increase above 5%. Above -5°C, brine inclusions begin to merge and the connectivity of the brine networks increase dramatically (*Golden et al.*, 1998; *Light et al.*, 2003). As temperatures rise further, brine volume fractions become increasingly sensitive to temperature changes. High temperatures not only impact the structure and thereby the optical properties of sea ice, but also its porosity and permeability which enables dynamic processes to significantly alter the ice properties with time. How these processes are interrelated is only beginning to become understood (*Eicken et al.*, 2004; *Vancoppenolle et al.*, 2007), and more of both field observations and modeling efforts are warranted.

1.2 The present work

In view of the importance of shortwave radiation both for physical and biological processes, and the current lack of information on warm sea ice, this thesis focuses around *in-situ* observations of solar shortwave radiation in the seasonal sea ice environment. Here, 'warm sea ice' implies sea ice with a temperature above about -5°C. Processes connected to seasonal sea ice are thought to gain in importance as the Arctic Ocean is pushed towards a seasonally ice-free state (*IPCC*, 2007). A focus on warm sea ice is further motivated by the proposition that variability observed in sea ice optical properties can be related to processes that occur(red) at temperatures above -5°C. The variability is mainly related to brine dynamics, which include, e.g., the initial trapping of salts and impurities as the ice is formed, thermal equilibrium phase changes, and resultant internal pressures causing brine expulsion and drainage, and the summer-time flushing mechanism (*Cox and Weeks*, 1988; *Maus*, 2007; *Vancoppenolle et al.*, 2007). Particular attention in this study is directed towards the effects of organic matter that mainly alter the optical properties through absorption. A striking feature is bottom ice algae community whose settlement is facilitated by the high porosities near the ice-ocean interface, and may in fact themselves alter the sea ice structure (see, e.g., *Krembs et al.*, 2002) and in the process change the optical properties.

The penultimate scientific objective of this thesis is to determine the optical properties of seasonal sea ice during fall freeze-up and the spring melt periods. Both periods are characterized by high spatial heterogeneity and rapid temporal changes that result in difficulties in interpreting remotely sensed data (e.g., *Zhou and Li*, 2003; *Hanesiak et al.*, 2001) or assessing responses to climate variability and change (e.g., *Drobot and Maslanik*, 2003; *Barber and Hanesiak*, 2004; *Belchansky et al.*, 2004; *IPCC*, 2007). In general, electromagnetic radiation signatures from sea ice are linked through the physical properties that determine them. Thus our observations were supplemented by detailed observations of the relevant physical characteristics of the snow-sea ice-ocean system. These include snow/sea ice temperature, salinity, density and structure. Optically active impurities, such as particulates at the bottom ice algae layer, need to be included in the case of visible radiation. An emphasis is set on the characterization of the most relevant components affecting shortwave radiative transfer and partitioning, and in turn relating them to the physical state of the ice and its immediate surroundings. Such measurements are rare and a necessary step towards the improvement and verification of climate models, as well as the development of more detailed integrated models that account for the evolution of physical, optical and biological properties of the sea ice. More specifically, the thesis objectives can be segmented into the following interrelated questions:

I. What is the spatial and temporal variability of the climatologically important apparent optical properties (AOPs) of seasonal sea ice during the fall freeze-up period?
II. What are the principal environmental variables affecting AOPs and IOPs during the fall freeze-up period?
III. What is the spatial and temporal variability of the climatologically important AOPs of seasonal sea ice during the spring melt period?
IV. What are the principal environmental variables affecting AOPs and IOPs during the spring melt period?
V. Can AOPs be used to predict IOPs for 'warm' sea ice conditions during the fall of spring periods examined in 1-4 above?

The thesis is structured into seven chapters, which provide new information addressing the five questions posed above. Chapter 2 first provides a review of the physical propeties and processes on which radiation interactions within the ocean-sea ice-atmosphere (OSA) depend. This includes a description of recent developments in Arctic sea ice extent and thickness, the seasonal evolution of the surface energy balance and its components, typical values used for spectral reflection and transmission in the OSA. In addition, basic concepts of radiation and radiative transfer modeling are reviewed.

Chapters 3 to 6 are presented in the standard form of a scientific publication, i.e., with introduction, methods, results, discussion and conclusions sections. The data presented in

Chapters 3 and 4 are from investigations conducted as a part of the Canadian Arctic Shelf Exchange Study (or CASES; see http://www.cases.quebec-ocean.ulaval.ca) in the Amundsen Gulf and Franklin Bay (south-eastern Beaufort Sea, Arctic Ocean) during 2003-2004. Chapter 3 focuses on a characterization of the physical, structural and optical properties of newly formed ice during the fall freeze-up period. The emphasis is on (1) the identification of typical features in the sea ice that control interactions with shortwave radiation, and (2) to examine variability within World Meteorological Organization (1985) ice categories. This chapter directly addresses research questions I and II (above) and identifies steps needed to answer question V. This chapter has been published as

> Ehn, J. K., B.-J. Hwang, R. Galley, and D. G. Barber (2007), Investigations of newly formed sea ice in the Cape Bathurst polynya: 1. Structural, physical, and optical properties, *J. Geophys. Res.*, 112, C05002, doi:10.1029/2006JC003702.

Other related publications that combine the above results with microwave emission signatures from the fall period include:

> Hwang, B. J., J. K. Ehn, D. G. Barber, R. Galley, and T. C. Grenfell (2007), Investigations of newly formed sea ice in the Cape Bathurst polynya: 2. Microwave emission, *J. Geophys. Res.*, 112, C05003, doi:10.1029/2006JC003703.

> Hwang, B. J., J. K. Ehn, D. G. Barber (2006), Relationships between albedo and microwave emissions over thin newly formed sea ice during fall freeze-up, *Geophys. Res. Lett.*, 33, L17503, doi:10.1029/2006GL027300.

Hwang, B. J., J. K. Ehn, and D. G. Barber (2008), Impact of ice temperature on microwave emissivity of thin newly formed sea ice, *J. Geophys. Res.*, 113, C02021, doi:10.1029/2006JC003930.

This work adresses the need to improve the interpretation of remotely sensed data for application to Arctic-wide assessments of e.g. mass- and energy balance and biological productivity. Particularly, new ice types are poorly identified by the passive microwave algorithms currently in use.

Chapter 4 describes a spring experiment, which used the aid of divers to measure transmitted spectral irradiance within the warm and porous bottom layers of landfast sea ice in the Arctic. The main goals of the experiment were (1) to obtain information on apparent and inherent optical properties (i.e., AOPs and IOPs) to facilitate the development and verification of structural-bio-optical models, and (2) to asses the importance of absorbing impurities, predominantly ice algae and their derivatives, and the sea ice structure itself on the spectral distribution of radiation near the ice-water interface. This chapter directly addresses research questions III, IV and V (above). Chapter 4 has been published as

Ehn, J. K., C. J. Mundy, and D. G. Barber (2008), Bio-optical and structural properties inferred from irradiance measurements within the bottommost layers in an Arctic sea ice cover, *J. Geophys. Res.*, 113, C03S03, doi:10.1029/2007JC004194.

The next two chapters deal with field observations of landfast sea ice in Button Bay (south-western Hudson Bay) during spring 2005, which were conducted under the umbrella of the ArcticNet project (see http://www.arcticnet-ulaval.ca). Button Bay may be considered a sub-

Arctic region in terms of its southern latitude (58°N) and spring and summertime insolation levels, however, sea ice conditions in Button Bay are comparable to landfast ice regions in the Arctic in terms of ice thickness at the end of winter (e.g., ice thickness 1.5-1.7 m in Button Bay in 2005 compared to about 1.8 m in Franklin Bay the year before) and thermophysical properties.

In Chapter 5 the seasonal evolution and diurnal variability in the surface energy balance and surface properties is studied using time series data obtained from a micrometeorological station installed at a fixed location on the ice and from a program that observed spectral albedo and transmittance of sea ice in the area with various surface types. An emphasis is put on (1) the characterization of diurnal variations in broadband albedo, and on (2) identifiying spatial and temporal variability in the spectral albedo (thereby addressing questions III and IV). This variability in surface properties—such as the partitioning of surface into bare ice areas (blue ice) and snow covered mounds (white ice)—controls the partitioning of shortwave radiation in the OSA system, and also the seasonal evolution of a melting sea ice cover. A limited version of Chapter 5—focusing solely on surface exchange processes—has been published as

> Ehn, J. K., M. A. Granskog, T. Papakyriakou, R. Galley and D. G. Barber (2006), Surface albedo observations of Hudson Bay landfast sea ice during the spring melt, *Ann. Glaciol.*, 44, 23-29.

Within Chapter 5, however, additional time series data on spectral transmittance is presented (subsection 5.3.4) elaborating on radiation partitioning into reflected, transmitted and internally absorbed components in the sea ice system during parts of the experiment.

In Chapter 6, a more detailed look at the partitioning of shortwave radiation within a melting sea ice cover is taken. This chapter addresses reseach questions IV and V by examing the connections between IOPs and AOPs within the spring sea ice cover. The manuscript prepared of this chapter has been accepted for publication as

> Ehn, J. K., T. N. Papakyriakou, D. G. Barber (2007), Inference of optical properties from radiation profiles within melting sea ice, accepted for publication in Journal of Geophysical Research—Oceans. Copyright 2008 American Geophysical Union.

Particular emphasis is put on the characterization of (accounting for) the radiation field in the ice as it significantly affects the interpretetion of optical properties near the surface and bottom boundaries.

In Chapter 7, the main elements of the thesis are summarized and a conceptual summary of the nature of fall and spring period AOPs and IOPs is provided; how the linkages between AOPs and IOPs may be used to provide improved information about this critical period of 'warm' sea ice is discussed; and the importance of various environmental variables to the specification of observed AOPs and IOPs is described. Chapter 7 is concluded with a statement of limitations of this work and recommendations for continued investigation of processes and properties of 'warm' sea ice.

CHAPTER 2: Background and Theory

2.1 Preface

This chapter reviews the physical properties and processes on which radiation interactions within the ocean-sea ice-atmosphere (OSA) depend. The characteristics of Arctic sea ice are described in section 2.1. In section 2.2, the energy balance of the sea ice environment is reviewed in terms of its seasonal evolution. The basic concepts of radiation and what is required for its modeling is discussed in section 2.3. The above sections stress the interrelated nature of the processes in particular. For example, radiation input to the sea ice lead to structural changes that further promote increases in radiation levels – a positive feedback. However, it may also promote ice algae growth which result in less radiation passing through the ice into the water column. Finally, magnitudes and shapes of (spectral) reflection and transmission in the OSA are illustrated in section 2.4, with an emphasis on observations, and explained in terms of gained knowledge of inherent physical properties of the system.

2.2 Physical characteristics of Arctic sea ice

2.2.1 Thickness and extent

In the northern hemisphere, the sea ice extent typically fluctuates reaching a maximum in February/March and a minimum in September. The average maximum (light grey in Figure 2.1) and minimum (dark grey) extent since 1979 has been 15.7 and 6.9 million km^2, respectively (*Richter-Menge et al.*, 2006). The fluctuating part is essentially made up of seasonal sea ice that forms every year and then melts. However, passive microwave data observed using satellites show a general decrease in the northern hemisphere sea ice extent by about -34300 km^2 per year (-2.8% per decade) from 1978 to 1996 (*Parkinson et al.*, 1999). In recent years this decreasing trend has been accentuated (*ACIA*, 2005; *Stroeve et al.*, 2005) reaching a record monthly minimum for each month in 2005 except May (*Richter-Menge et al.*, 2006). Within 2005, the maximum (red line) and minimum (blue line) values were 14.8 and 5.6 million km^2, respectively. Recent data (see http://nsidc.org/) shows that sea ice reached a new absolute minimum record extent of 4.1 million km^2 in mid September 2007 (Figure 2.1), and although ice growth commenced, the previous record minimum in September 2005 was not reached until mid October. The abrupt decrease in sea ice extent experienced in 2007 has led to concerns that a 'tipping point' may have been reached transforming the system towards an era of diminished ice cover [e.g., *Holland et al.*, 2006].

Also the thickness of the sea ice cover has been observed to decrease. By analysing data collected using submarines, *Rothrock et al.* (1999) concluded that the thickness of the perennial ice cover in the central Arctic basin decreased from an average of 3.1 m in 1956-1978 to an average of 1.8 m in 1993-1997, even as the portion of first-year ice increased from 24% to 33% (*Yu et al.,* 2004). This amounted to a sea ice volume loss of 32%. If the trend with decreasing ice extent and thickness continues, we may experience a seasonally ice free Arctic within the first half of this century (*ACIA*, 2005). On the other hand, no statistically significant change has been observed for ice thickness in the *seasonal sea ice zone* (SSIZ) (*Melling et al.*, 2005). The landfast sea ice cover represents an important portion of the SSIZ that follows the coasts surrounding the Arctic Ocean. Presently, landfast sea ice accounts for approximately 15% of the Arctic sea ice area during winter (*Yu and Stern*, 2005). Maximum thickness of undeformed, thermodynamically grown landfast sea ice in the Canadian Arctic typically ranges between 1.5 and 2.4 m, largely depending on the overlying snow cover thickness (*Flato and Brown,* 1996).

Figure 2.1. Maximum and minimum ice extents. The filled areas are the average extents from 1979 to present, while the contours show the record minimum extents observed during 2005 and 2007.

Other ice zones of interest include the *shear zone* and the *marginal ice zone* (MIZ). At the shear zone, pack ice meets landmass causing it to converge and form ridges. The shear zone forms a distinct boundary between the landfast ice and the pack ice with significantly thicker ice, which may restrict water exchange between the estuary and the basin. The MIZ is the part of the ice that is affected by the presence of the open ocean. Its width is about 100-200 km, the outer part of which is characterised by broken-up floes that rapidly decrease in size due to wave action when approaching the edge (*Wadhams*, 1981). The MIZ displays highly variable properties (eddies, upwelling, high light levels and ice melting) that support high biological activity and is therefore of considerable inter-disciplinarily interest. Remote sensing of the MIZ is difficult due to its fractioned character with flow sizes smaller than available instrument resolution (*Zhou and Li*, 2003).

2.2.2 Sea ice formation, structure and types

In the Arctic, the formation of new sea ice typically starts in October-November (*Maykut*, 1986) once the sea surface has cooled down to the seawater freezing point (T_f) by heat loss to the atmosphere. Normally this requires that the entire upper water layer (mixed layer) is at T_f because a temperature reduction of seawater with a salinity (S_{sw}) above 24.7‰ results in an increase in density and thermo-haline convection (*Winsor and Björk*, 2000). T_f is a function of S_{sw} and the pressure; e.g., seawater with S_{sw} = 34‰ has a $T_f \approx$ -1.89°C (*Fofonoff and Millard*, 1983).

Once the sea surface reaches the freezing point, additional heat loss produces slight supercooling of the water and ice formation (*Weeks and Ackley*, 1982; *Weeks*, 1998; *Eicken*, 2003). At first small platelets and needles, called *frazil ice*, are formed in the surface layer and accumulates at the surface. When freezing continues, the formation of a thicker, soupy mixture of frazil ice, called *grease ice*, follows. This layer quickly consolidates forming a continuous ice cover of roughly 1-10 cm thickness (*Smedsrud and Skogseth*, 2006). With significant wave action, the frazil collects to form rounded discs collectively called *pancake ice*. Pancake sizes range from a few tens of centimeters to a few meters (*Wadhams et al.*, 1987). The pancakes continually collide and separate resulting in characteristic elevated rims. With ongoing freezing the pancakes adhere into a continuous ice sheet. Because of the turbulent nature (wind and waves) of early ice formation, the upper 1-10 cm of the ice cover typically consists of a granular texture with small, randomly oriented crystals. This ice type is usually termed *granular* or *frazil* ice.

Once a solid surface layer has formed, further ice growth typically commences through congelation at the ice-water interface. The growth rate becomes dependent on how fast heat can be conducted from the ice-water interface towards the air/ice surface, i.e. the thermal conductivity and temperature gradient in the ice (*Saloranta*, 1998). Congelation ice crystals with a more horizontal c-axis orientation have a slight growth advantage (*Weeks*, 1998). Further ice growth therefore results in geometric selection towards ice crystals with their c-axis in the horizontal plane (Figure 2.2) and an increase of their size with depth (*Weeks and Ackley*, 1982). This transition occurs within a few centimetres thick transition zone that forms a structure of termed *intermediate ice* or the *transition zone* (*Eicken*, 2003). Once horizontal directions in the c-axis dominate, the ice type formed is called *columnar ice* and is the most commonly encountered ice type in undeformed ice.

At the growth (ice/water) interface a so-called *skeletal layer* builds up of ocean-facing lamellar platelets protruding into the water column (Figure 2.2) (*Eicken*, 2003; *Mundy et al.*, 2007b). The skeletal layer is interesting as the platelet and crystal structure of the resulting columnar ice is largely determined as it forms at this interface. In addition, brine inclusions are incorporated into the sea ice as it forms and concentrated between the ice grains. Thus as the ice grows thicker, a record of the physical conditions that prevailed at the time of formation is retained in the ice structure. Within a crystal the platelets are typically parallel with widths ranging from about 0.4 to 1.0 mm with the width thought to be inversely related to growth rate (*Weeks and Hamilton*, 1962; *Lofgren and Weeks*, 1969; *Nakawo and Sinha*, 1984). The skeletal layer is also of interest because this porous layer is where the bulk part of the sea ice algae community resides (*Arrigo*, 2003).

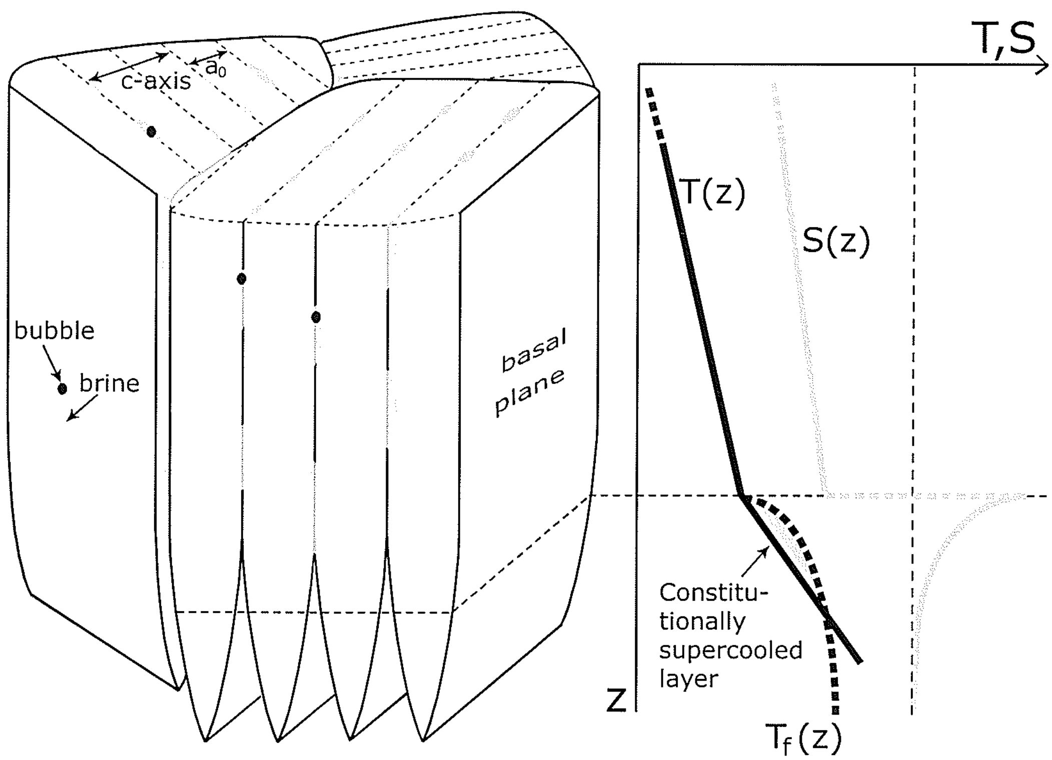

Figure 2.2. The sea ice structure in the skeletal layer at the ice-water interface with corresponding temperature and salinity profiles. T_f is the freezing point temperature profile as determined by salinity (S). Heat is transported (upwards) faster than salt (downwards), and thus the temperature (T) of a thin layer ahead of the interface is heated from below more rapidly than it receives salt from above as new ice forms. Because of this mismatch, the grey-shaded layer is constitutionally supercooled.

WMO ice thickness types—Sea ice is commonly classified based on its thickness according to *World Meteorological Organization* (1985) (*WMO*) nomenclature. A short description follows: New ice is a weakly or non-consolidated collection of ice crystals which usually include frazil ice and grease ice. Once consolidated, nilas (0-0.10 m thick) is formed, which is further classified into dark nilas (0-0.05 m) and light nilas (0.05-0.10 m). When the ice sheet becomes thicker than 0.10 m the ice is classified as young ice. Young ice includes grey ice (0.10-0.15 m thick) and grey-white ice (0.15-0.30 m thick). Based solely on thickness, pancake ice may be classified to belong to either the nilas or the young ice types. Recently formed sea ice thicker than 0.30 m is termed first-year sea ice and typically does not reach a 2-m-thickness within a season. It is typically covered by snow. Ice thicker than 2 m is typically deformed or has survived at least one summer melt cycle. Sea ice surviving one melt cycle is termed second-year ice. If it survives two or more summers, it is called multi-year ice. Multi-year ice is thicker, denser and less salty than first- and second-year ice. The surface of multi-year ice is characterised by smooth hummocks and, during summer, large melt ponds.

2.2.3 Surface features

Snow cover—Once the newly formed ice sheet has reached a sufficient thickness (about 5-10 cm), it may begin to sustain a snow cover. The thickness of the snow cover can be spatially highly variable due to wind that redistributes the snow effectively (*Mundy et al.*, 2005). The presence of snow is significant as already a thin snow cover will significantly increase backscattering of solar radiation. Additionally, snow strongly affects the growth rate of the sea ice by effectively isolating the ice from the cold atmosphere (*Papakyriakou*, 1999). As a rule of thumb, 10 cm of snow has the same insulating effect as roughly 1 m of sea ice. The snow density can vary from about 0.05 g cm^{-3} for newly fallen snow to about 0.4 g cm^{-3} for wind packed snow, which imply and air volume fraction of at least 50%.

Snow is a granular material composed of a large collection of ice crystals with various shapes and sizes. After initial deposition, snow crystals undergo metamorphic changes with time affecting crystal sizes, shapes and the overall density of the snowpack. In short, snow can be subdivided into dry or wet snow depending on if its temperature is below or at the melting point (*Colbeck*, 1982). The metamorphism at the two temperature regimes is different. Dry snow metamorphism results from water vapor movement within the snow structure, which is controlled by the temperature gradient (e.g., *Langlois et al.*, 2006). In the absence of a significant temperature gradient, e.g., shortly after deposition or during wind events, destructive metamorphism occurs with an overall effect of reducing size and rounding crystals (Figure 1 in *Colbeck*, 1982). With a temperature gradient, on the other hand, crystal enlargement occurs with large growing ones on the expense off small. The result is more angular and faceted crystals (Figure 2 in *Colbeck*, 1982). Wet snow metamorphism occurs when melt water or brine is present. In the pendular regime, i.e., unsaturated snow with liquid water content below about 7% of the volume, grain clusters tend to form (Figure 3 in *Colbeck*, 1982). However, once saturated (funicular regime), liquid water begins to drain leaving behind well-rounded crystals (Figure 4 in *Colbeck*, 1982). As melt water percolates through the snow pack it may encounter below freezing temperatures, and thus refreeze forming ice layers and lenses. This is typical during spring when diurnal variability in insolation levels and temperature causes melting during the day and refreezing during night.

Snow ice and superimposed ice—Often the load of snow cover on the ice can be sufficient to induce flooding of seawater onto the ice surface, thus forming a layer of snow soaked with seawater, a so-called slush layer. The slush layer can freeze very fast during cold air temperatures, beginning from the top, and form snow ice (e.g., *Kawamura et al.*, 2001). Thus in certain regions (e.g., Baltic Sea, Antarctica), snow ice formation can contribute a significant portion to the overall ice thickness. Snow may also melt, in response to warm weather events, rainfall or absorption by shortwave radiation, and then refreeze at the snow/ice interface to form superimposed ice (*Eicken et al.*, 1994; *Nicholaus et al.*, 2003). This superimposed ice layer will continue to grow as long as melt water supply is sustained and temperatures remain below the freezing point. The different ice formation mechanisms in snow can be traced by looking at crystal structure and at oxygen isotope ratios (*Eicken et al.*, 1994; *Kawamura et al.*, 2001). Basal superimposed ice layers may be important during spring and summer for the development of mounds and melt ponds. Being nearly impermeable, they restrict vertical movements and thereby force melt water to move laterally towards more depressed areas of the ice surface, which eventually form melt ponds (*Eicken et al.*, 2004). Similarly, superimposed ice may affect the timing and extent of melt water flushing events (see section 2.1.4.2) (*Vancoppenolle et al.*, 2007).

Brine skim and frost flowers—In new forming sea ice, an about 1-mm-thick brine skim layer is often observed on the ice surface (*Perovich and Richter-Menge*, 1994). This brine skim may have a salinity in excess of 100‰. The liquid brine is thought to be the source of vapor needed in the formation of frost flowers (*Martin et al.*, 1996), which form under cold and calm conditions. They can take the shape of clumps, dendrites or needles on the scale of milli- to centimeters (see *Martin et al.*, 1996). Frost flowers are important as they have a significant impact on the thermal and electromagnetic properties of the sea ice.

2.2.4 Bulk composition

Excellent reviews on the sea ice composition are included in *Weeks and Ackley* (1982) and more recently in *Weeks* (1998) and *Eicken* (2003). As a part of the ice growth process, forming ice crystals expel impurities and thus consist of pure water. Brine solute is partly rejected from the ice and partly trapped along the boundaries and in interstices of ice crystals and the platelet substructure (*Lake and Lewis*, 1970). The brine within the sea ice is concentrated into brine pockets, tubes and channels of various sizes, shapes and numbers (see section 2.2.5) (*Light et al.*, 2003). Properties such as temperature, salinity, brine and air volume show large variations in the vertical, changing significantly from the surface of the ice to the water interface. A change in e.g. the ice temperature results in changes in the ice/brine volume ratio and thus affects the way in which light interacts with the ice (*Light et al.*, 2003; 2004).

Equations for brine, solid salts and gas volume—The size of the brine inclusions (both in snow and sea ice) is temperature dependent through phase change; a decrease (or increase) in the temperature will result in additional freezing (or melting) on the walls of the inclusions (*Assur*, 1958; *Richardson*, 1976). The brine volume fraction (v_b) in sea ice can thus be determined, based on the requirement of phase equilibrium between brine and ice, using parameterizations by *Cox and Weeks* (1983):

$$v_b = \rho_{si} S_{si} / F_1 , \tag{2.1}$$

where ρ_{si} and S_{si} are the sea ice density (g cm^{-3}) and salinity (‰), respectively. The air volume fraction (v_a) is obtain with knowledge of the density of pure ice (ρ_{pi}):

$$v_a = 1 - \rho_{si}/\rho_{pi} + v_b F_2, \quad (2.2)$$

where $\rho_{pi} = 0.917 - 1.403 \times 10^{-4} T_{si}$ and T_{si} the sea ice temperature (°C). F_1 and F_2 are 4th order polynomials as functions of temperature based on the phase relationships with coefficients found in *Cox and Weeks* (1983) and *Leppäranta and Manninen* (1988).

Brine dynamics in sea ice—Variations in S_{si} are controlled by entrapment of salt during growth and by brine migration occurring after formation. The salt entrapment is largely dependent on the salinity of the seawater and the ice growth rate (*Cox and Weeks*, 1974; *Nakawo and Sinha*, 1981). The initial salinity S_{ini} of a newly grown layer is modeled as $S_{ini} = k_{eff}S_{sw}$ where k_{eff} is a segregation coefficient obtained empirically as a function of growth rate (*Weeks and Ackley*, 1986).

Brine migration processes are responsible for removing salt from the ice (*Untersteiner*, 1968), and relatively quickly after formation result in a S_{si} profile with a C-like shape with high values at the top and bottom layers and low values around 4-6‰ in the interior parts (Figure 2.3a) (*Nakawo and Sinha*, 1981). The balance between entrapment and migration result in a general decrease in the average S_{si} as sea ice thickens (Figure 2.3b). After the initial salt entrapment, the following mechanisms are taking place that move the brine in the ice (*Weeks and Ackley*, 1986):

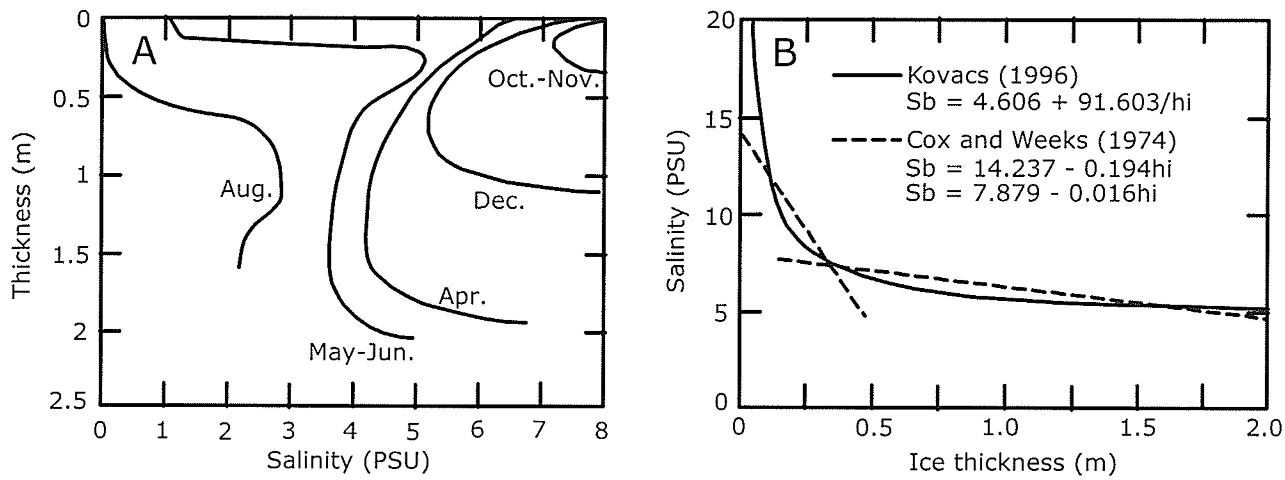

Figure 2.3. (a) Schematic of the evolution of the salinity profile (modified from *Eicken*, 1993), and (b) bulk salinity as a function of ice thickness (Cox and Weeks, 1974; *Kovacs*, 1996).

1. *Brine pocket migration.* There is a temperature gradient in the ice sheet between the cold surface and the warm bottom, and similarly there must be a vertical temperature gradient in the brine inclusions. Freezing occurs at the cold end and melting of ice at the boundary of the warm end, which results in a slow migration of the brine inclusion towards the warm side of the ice.

2. *Brine expulsion.* With a T_{si} decrease, some brine freezes in the brine inclusions, and consequently there is a positive change in volume. This produces microscopic cracks in the surrounding ice, making it possible for brine to escape either down or up towards the surface (*Eicken*, 2003). Especially for thin, newly formed ice upward movement of brine is facilitated by the large temperature gradient and high porosities near the surface. The result is the formation of a brine skim and frost flowers (*Perovich and Richter-Menge*, 1994; *Martin et al.*, 1996).

3. *Gravity drainage.* As the ice grows thicker, the surface rises higher above the sea level (freeboard increase) while the brine in interconnected tubes/channels will want to remain at sea level. The created pressure will drive brine downward and some out into the water

column. A second process acting in this mechanism is convective overturning within the brine networks caused by an unstable brine density profile in response to increasing T_{si} with depth. These processes are thought to be effective mechanisms to remove salt from the sea ice provided that there are interconnected tubes in hydrostatic balance with the underlying seawater. Sufficient connectivity is thought to occur once v_b reaches 5-7%, typically after T_{si} > -5°C (*Golden et al.*, 1998). In larger features such as *brine drainage channels* (*Cole and Shapiro*, 1998), i.e., a river system of relatively large channels extending all the way down to the ice/water interface (*Lake and Lewis*, 1970), a flow moving up- and downwards in an oscillatory fashion is observed (*Eide and Martin*, 1975). The brine moving out is replaced by less salty seawater and the result is a desalination of the ice column.

4. *Meltwater flushing* occurs during the summer season as snow melts or rain falls to the ice surface (e.g., *Vancoppenolle et al.*, 2007). Surface water then penetrates the ice and flushes out the brine. This is believed to be a very efficient mechanism to remove salt from the sea ice and responsible for the low salinity of deteriorated first-year ice which ends up forming multi-year ice.

2.2.5 Inclusions in sea ice

Knowledge of volume fraction of ice, brine and gas within sea ice, calculated according to *Cox and Weeks* (1983), may be sufficient when calculating thermal properties of sea ice. However, in order to understand radiative transfer in sea ice, it is necessary to have detailed information regarding the size, number density and the spatial distribution of its inclusions. It is the brine and gas inclusions that largely determine the electromagnetic, thermal, mechanical and permeable properties of sea ice (*Golden et al.*, 1998; *Perovich and Gow*, 1996; *Hwang et al.*, 2006). What is known about these inclusions is reviewed in this section. Other substances present in sea ice that are important for its optical properties, but not directly related to equilibrium phase changes, are discussed in section 2.4.3.

Brine inclusions—Observations of brine inclusions are most commonly made from so-called thin sections prepared from ice cores that were either artificially grown or transported from the field (e.g., *Perovich and Gow*, 1996; *Cole and Shapiro*, 1998; *Eicken et al.*, 2000; *Light et al.*, 2003). This method has its problems since ice samples need to be prepared in a cold room at -20 to -15°C, which may result in an alteration in the sample temperature and thus also the size of the brine inclusions (*Eicken et al.*, 2000). Nevertheless, interior ice samples from first-year ice collected and kept at temperatures near the required cold room temperatures may not undergo considerable structural changes.

Analyzing horizontal sections of first-year sea ice, *Perovich and Gow* (1996) obtained a brine inclusion mean cross-sectional area of 0.056 mm^2 with a number density (N) of 1.0 mm^{-3} for granular ice near the surface, while the columnar ice had areas of 0.019-0.023 mm^2 with N = 1.6-4.5 mm^{-3} (see their Table 1). A detailed study on vertically oriented brine inclusions were conducted by *Light et al.* (2003). They found larger elongated brine tubes with numerous smaller brine pockets in between (similar to Figure 2.4). The number density for brine inclusions as a function of their length (l) were found to be well represented by

$$N(l) = 0.28 l^{-1.96} \tag{2.3}$$

for l between 0.01 and 8 mm (r^2=0.92). This corresponds to an overall N of 24 mm^{-3}. Similarly,

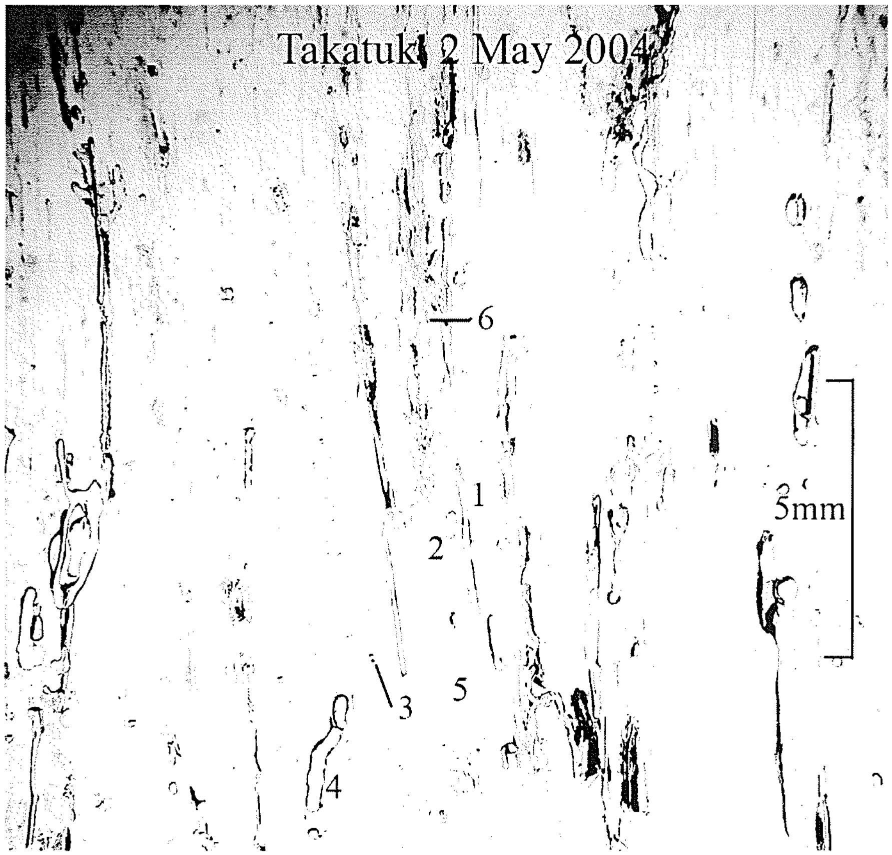

Figure 2.4. Vertical thin section of first-year sea ice at -15°C. The sample was taken on 2 May, 2004, at the CASES over-wintering sampling site. Numbers indicate (1) brine tube, (2) brine pocket, (3) bubble, (4) drained inclusion, (5) transparent area, and (6) poorly defined inclusions (clusters).

the aspect ratio (γ) between 1 and 70, was correlated as

$$\gamma(l) = 10.3l^{0.67} \tag{2.4}$$

for $l \geq 0.03$ mm (r^2=0.77). Using a non-destructive magnetic resonance technique, the evolution of brine inclusions in first-year ice samples during a warming sequence from -21 to -6°C was studied by *Eicken et al.* (2000). They observed an increase in N from 0.36 to 0.71 mm^{-3} with a corresponding increase in the mean l from 0.45 to 0.78 mm and γ from 3.3 to 8.3. Importantly, a subsequent decrease in temperature may not bring about a reversible change in the inclusion structures (*Light et al.*, 2003). However, little observational data exists on ice inclusions at $T_{si} > -5°C$ where v_b change drastically in response to T_{si} changes (*Light et al.*, 2004).

Solid salts—When the temperature decreases, the salinity of the brine will increase and dissolved salts will be saturated and begin to precipitate. The different dissolved salts will become saturated at different temperatures; $CaCO_3 \bullet 6H_2O$ (Ikaite) will form at -2.2°C, $Na_2SO_4 \bullet 10H_2O$ (Mirabilite) at -8.2°C and $NaCl \bullet 2H_2O$ (Hydrohalite) at -22.9°C. Colder temperatures are seldom reached and thus KCl, $MgCl_2$ and $CaCl_2$ precipitations are rare, as they only start to form at temperatures below -36.8°C (*Weeks*, 1998). The precipitated salts settle to the bottom of the brine pockets/tubes (see Figure 12 of *Light et al.*, 2003). A portion also appears to remain suspended in the brine. A possibility is also that they form a salt-ice layer on the brine pocket walls. In general, solid salts are optically unimportant—because of their low concentration—at temperatures above -8.2° by *Light et al.* (2003). However, they may have biogeochemical implications because the precipitation of $CaCO_3$ causes a release of CO_2 (*Rysgaard et al.*, 2007).

Gas bubbles—Air can get entrapped between the ice crystals forming bubbles when brine drains out from the ice. This happens especially when the ice is lifted above the sea level. Gas bubbles also form within brine inclusions as a result of melting and enlargement of the brine inclusions due to the density difference between ice and water (Figure 2.4). These are small, spherical bubbles, which often merge as the brine inclusions become larger, form clusters and connect. Analysis of bubbles within brine in Figure 2.4 yielded a good power law fit:

$$N(r) = N_0 r^{-1.5} \tag{2.5}$$

for sphere radii (r) between 0.004 and 0.07 mm and the constant $N_0 = 0.06$ at -15°C resulting in an overall N=1.3 mm^{-3} (*Light et al.*, 2003). Sometimes gas bubbles rising from the sea floor (e.g. methane gas) can be incorporated into the ice. At some locations, due to the bottom conditions, these gas bubbles can be very abundant. *Grenfell* (1983) found a similar relationship for larger bubbles with r = 0.1–2 mm with N_0 = 0.012 obtained from the relation v_a = 10.3 N_0 and an exponent in Eq. 2.5 of -1.24.

2.3 The energy balance of sea ice

2.3.1 Surface energy balance

The energy balance at the snow, ice or water surface is illustrated in Figure 2.5. It is a balance between exchanges with the atmosphere, both through radiative (Q^*) and convective exchanges of sensible (Q_H) and latent heat of evaporation (Q_E), and conduction (Q_C) from the underlying media (*Oke*, 1987):

$$Q^* + Q_H + Q_E + Q_C = 0. \tag{2.6}$$

Q^* is the net radiation to the surface and often separated into a net shortwave (SW^*) and net longwave (LW^*) component:

$$Q^* = SW^* + LW^* = SW_\downarrow - SW_\uparrow + LW_\downarrow - LW_\uparrow, \tag{2.7}$$

where the arrows are denotations for down- and upwelling short- or longwave radiation, respectively. The convention here is that positive terms represent an energy gain to the system, while negative terms represent losses. Units are in watts per square meter (or W m^{-2}).

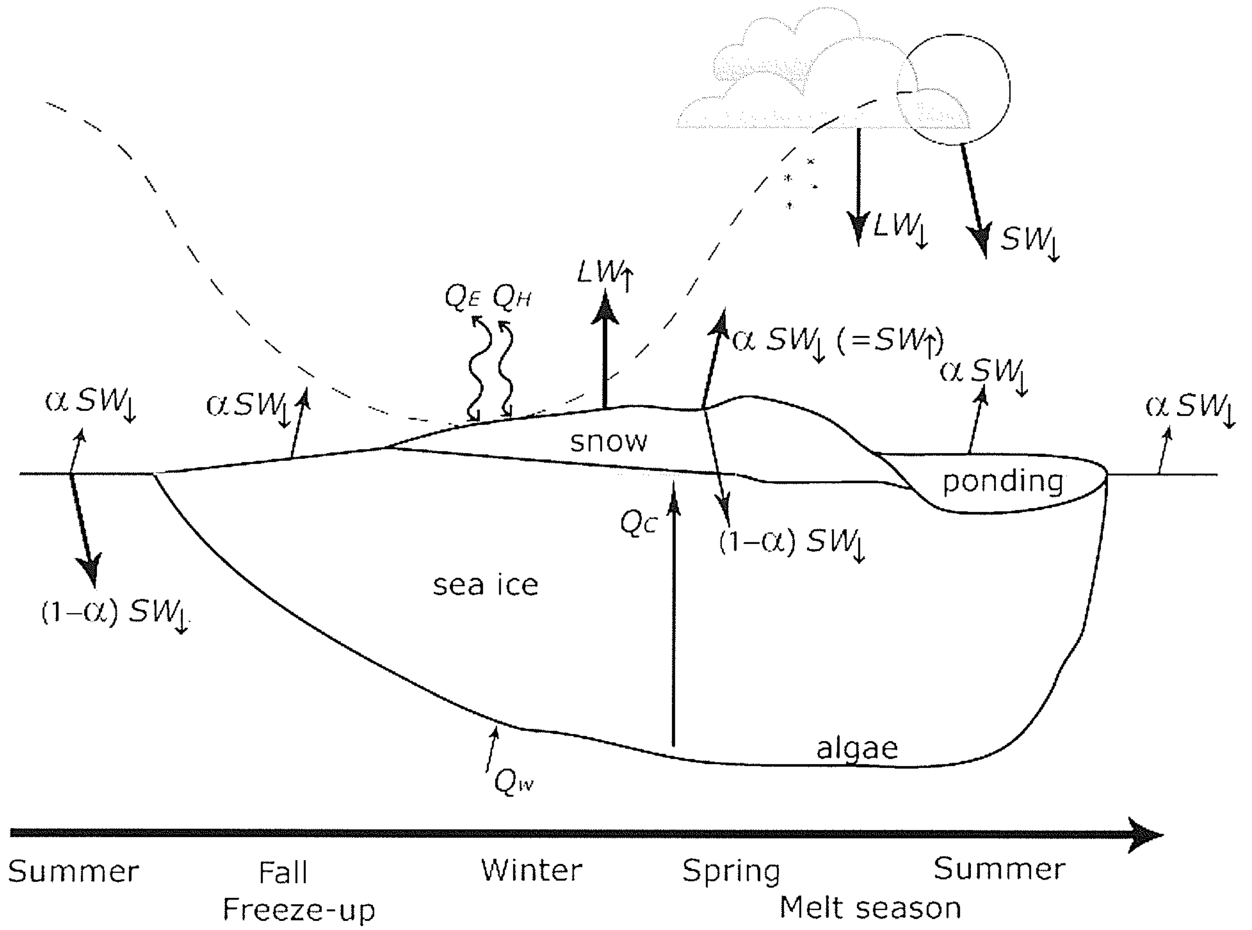

Figure 2.5. Schematic representation of the temporal evolution in the vertical dimension of a seasonal sea ice cover and the components of the energy balance.

A surface is a massless plane by definition (*Oke*, 1987). Thus, the energy input to the surface must be equal to the energy output. However, the above is not always true for a snow/ice system where a significant portion of $SW_\downarrow$ penetrates through the surface and where the internal energy of the system is strongly affected by temperature and phase changes. Thus, it is more appropriate to consider a volume in which energy absorption and release are accounted for:

$$Q^* + Q_H + Q_E + Q_C + \Delta Q_S + \Delta Q_M = 0, \tag{2.8}$$

where ΔQ_S account for sensible heat changes (i.e., temperature changes) in the volume, and ΔQ_M accounts for phase changes within the volume (i.e., melting, freezing, sublimation, evaporation and condensation).

Temporal evolution—In high latitude regions, Q^* largely control the surface energy balance with values often an order of magnitude larger than Q_H and Q_E (*Maykut*, 1986). However, *Steffen and DeMaria* (1996) found that the latter two are important for growing landfast ice, especially through Q_H (see their Fig. 6) during initial formation (young ice). During winter months, the above are typically negative (energy flow away from the surface), with Q^* dominated by LW^* (*Steffen and DeMaria*, 1996; *Papakyriakou*, 1999). The surface losses are balanced to a large degree by conductive heat flux (Q_C) to snow base, which is defined as

$$Q_C = -k_{si} \frac{\partial T_{si}}{\partial z}, \tag{2.9}$$

where k_{si} is the thermal conductivity of sea ice and $\partial T_{si}/\partial z$ the temperature gradient with depth.

$SW\downarrow$ is essentially zero during the Arctic winter. With the return of solar insolation in late winter and spring, Q^* gradually evolves from an energy sink to a source, and becomes controlled by SW^*. The monthly average $SW\downarrow$ rises to about 300 W m^{-2} during June (*Maykut*, 1986). Additionally, frequent incursions of warm air masses increase $LW\downarrow$ significantly (Papakyriakou, 1999). Later during the melt season, large diurnal variability is seen in $SW\downarrow$, while $LW\uparrow$ is limited by melting at the surface (0°C $\rightarrow$ ~320 W m^{-2}). This leads to daytime melting and overnight refreezing of the snow pack and consequent changes in its structure. Later the sea ice is fractioned into a number of surface types, such as white ice, blue ice and melts ponds. A key parameter during the melt period is the shortwave albedo (α), defined as the fraction of $SW\downarrow$ reflected from the surface, or

$$\alpha = \frac{SW_{\uparrow}}{SW_{\downarrow}}. \tag{2.10}$$

The albedo is a major controlling variable in the Arctic climate system through the ice-albedo feedback mechanism and will be discussed further in section 2.5.

2.3.2 Growth and melt of sea ice

Congelation ice growth requires that the latent heat produced by the ice formed from seawater and any additional heat flux from the underlying ocean (Q_W) is conducted away from the interface, generally through the sea ice towards the colder surface. The energy balance at the ice/ocean interface can be expressed by

$$\rho_{si} L_{si} \left(\partial h_{si} / \partial t \right) + Q_W = Q_C , \tag{2.11}$$

where ρ_{si} is the density of the formed sea ice, L_{si} the latent heat of fusion and ∂h_{si} the thickness of the layer that formed within the time ∂t. Thus, the ice growth rate depends on how rapidly heat can be transferred through the ice. Firstly, Q_C becomes smaller with ice thickness increase as $\partial T_{si}/\partial z$ becomes smaller. Secondly, Q_C depends on the brine volume present in the sea ice as it affects k_{si}. *Oertling and Watts* (1998) expresses k_{si} as

$$k_{si} = (1 - \nu_b) k_{pi} + \nu_b k_b , \tag{2.12}$$

where the thermal conductivities for pure ice (k_{pi}) and brine (k_b) are functions of temperature (see, e.g., *Eicken*, 2003). k_b is about four times smaller than k_{pi} ($\approx$2.0 W m^{-1} K^{-1} at 0°C) resulting in an overall reduction of k_{si} when salt is present.

While early sea ice thermodynamic models assumed a constant Q_W of around 2.0 W m^{-2} to the ice bottom (*Maykut,* 1986), resent studies have found that solar radiation, absorbed in the upper layers of water column through leads or after transmission through the ice pack, control the seasonal cycle of Q_W (*Perovich and Maykut*, 1990; *Ebert and Curry*, 1993; *Maykut and McPhee*, 1995). Melting of sea ice is more complicated than a mere reversal in ice growth when Q_W-Q_C becomes positive in Eq. 2.11. Melting occurs most strongly at the surface due to a positive Q^* and warm air temperatures. Melting within the ice interior results in an overall porosity increase, which will increase brine drainage to the ocean. Furthermore, ablation at the ice/ocean interface is in fact a dissolution process rather than melting as seawater temperatures typically remain below the melting point of the fresher sea ice. As ice melts, a layer that is both less salty and warmer (at its freezing point) than the seawater below is formed at the interface, causing the water column to become stably stratified. Because salt diffusion is much slower than heat diffusion, the bottom ablation rate is limited by the salt flux towards the interface (*McPhee et al.*, 1987).

Effects of a snow cover on heat transfer—The presence of a snow cover can reduce Q_C by as much as 50% and consequently significantly affect growth rates (*Eicken*, 2003). This is because snow is an effective thermal insulator. The thermal conductivity (k_{sn}) of dry snow is on the order of 0.1-0.4 Wm^{-1}K^{-1} but can vary by one order of magnitude with changing snow properties (density, grain size, wetness, etc.) (*Sturm et al.*, 2002). On sea ice, brine commonly gets drawn up into the snow pack. Salinities in excess of 20‰ have been observed near basal layer by, e.g., *Barber and Thomas* (1999) and *Langlois et al.* (2006). *Crocker et al.* (1984) reported v_b going beyond 30%. This has significant impacts on the insulting properties of the snow pack on sea ice, as brine-wetted snow has a 3-5 time larger k_{sn} compared to dry snow (*Crocker*, 1984; *Steffen and DeMaria*, 1996). A snow cover during the melt season, on the other hand, acts in the opposite way, insulating the ice from the warm T_{air} and slows down ice melt. Additionally, snow has a high albedo, which further contributes to a delay in sea ice melt (*Curry et al.*, 1995). Further discussion of snow will be in terms of its optical properties (section 4).

2.3.3 Electromagnetic radiation

As seen above, radiation is one of the most important components in the energy balance of sea ice. Here the basics behind the radiative processes are delineated with the perspective of the surface radiation balance. In the next sections a closer look is taken on the processes pertinent to shortwave radiation interaction with the OSA system.

All objects whose temperature is above the absolute zero, i.e. 0 K, emit radiation. The spectral radiance, $L(\lambda)$, is described by Planck's law (e.g., *Apel*, 1987; *Thomas and Stamnes*, 1999)

$$L(\lambda,T) = \varepsilon \cdot \frac{2hc^2}{\lambda^5} \frac{1}{e^{hc/\lambda k_B T} - 1}, \qquad [\mathrm{J\ s^{-1}\ m^{-2}\ sr^{-1}\ nm^{-1}}] \qquad (2.13)$$

where h is Planck's constant, c the speed of light, λ the wavelength, k_B is Boltzmann's constant, and T the temperature (K). The emissivity (ε) compensates for the fact that objects in nature rarely emit radiation perfectly, i.e., they are not *blackbodies* ($\varepsilon = 1$) but so called *greybodies* ($\varepsilon \leq 1$).

Consequently, as the sun has a high surface temperature (~5777 K) a major portion of the radiation is emitted at shorter wavelengths, compared to relatively more of longer wavelength radiation emitted by the earth's surface or its atmosphere. In energy balance studies, radiation is therefore commonly subdivided into shortwave radiation (with solar origin) and longwave radiation (with terrestrial origin). The cutoff between these two is somewhat arbitrarily placed at about 3.0 μm (*Oke*, 1987).

Shortwave radiation—The shortwave solar radiation incident on a plane perpendicular to the rays at the top of the atmosphere is characterised by the *total solar irradiance* (or *solar constant*) (I_0). It has an average value of roughly 1366 Wm^{-2} (*Fröhlich and Lean*, 1998) of which about 38% lies in the PAR (Photosynthetically Active Radiation) region (*Thomas and Stamnes, 1999*) (see also www.grida.no/climate/ipcc_tar/wg1/244.htm).

Even during a clear sky, the solar radiation is significantly attenuated as it passes through the atmosphere. During its passage the solar radiation is (1) absorbed mainly by ozone, water vapour, carbon dioxide and oxygen, and (2) scattered by small particles and molecules, and by larger dust particles (aerosols) (*Thomas and Stamnes*, 1999). The reduction is about 14% for a dry and clean atmosphere with the sun vertically overhead, and about 40% for a moist and dusty atmosphere (*Kirk*, 1994). The fraction of PAR to $SW\downarrow$ reaching the Earth's surface is between 45-50%. This fraction is higher than above the atmosphere because a larger proportion of the infrared wavelengths are absorbed compared to PAR wavelengths. As the solar elevation decreases, the portion of solar radiation reaching the surface also decreases due to the longer path taken by the photon through the atmosphere. The path length is approximately inversely proportional to the sine of the solar elevation. For example, the path length is twice as long with a solar elevation of 30° compared to the sun in zenith.

In the absence of a cloud cover, the $SW\downarrow$ at the Earth's surface varies along the day in much the same way as the solar elevation, i.e., smoothly and sinusoidally. When the sun drops below the horizon, only diffuse radiation scattered by the atmosphere remains. A cloud cover modifies the incoming surface irradiance strongly, both in spectral shape and magnitude. The presence of a few isolated clouds in an otherwise clear sky can, due to reflection from the sides of the clouds, increase $SW\downarrow$ values by 5-10%, as long as they are not directly obscuring the sun (*Kirk*, 1994). On the other hand, a continuous cloud sheet always reduces the irradiance reaching the surface. A thin sheet of cirrus clouds may reduce $SW\downarrow$ to around 70% of clear sky values, while a thick layer of stratus clouds might reduce it down to 10% (*Kirk*, 1994).

Longwave radiation—The longwave radiation emission by a surface or a volume can be obtained by integrating Eg. 3.8 to obtain the Stefan-Boltzmann's law:

$$LW = \varepsilon \sigma T^4, \qquad [\mathrm{W\ m^{-2}}] \qquad (2.14)$$

where ε is the emissivity (≤ 1), σ Stefan-Boltzmann's constant ($= 5.67 \times 10^{-8}$ Wm^{-2}K^{-4}) and T the temperature (K). For a snow or ice surface, $LW\uparrow$ can be obtained simply by using the surface temperature T_0 and ε of about 0.98-0.99 (e.g., *Grenfell et al.*, 1998). $LW\downarrow$ is more complicated and depends on the temperature, water vapour and carbon dioxide profiles in the atmosphere (*Oke*, 1987). In contrast to $SW\downarrow$, it displays little diurnal variability, however, significant differences are seen between a clear and a cloud-covered atmosphere (*Papakyriakou*, 1999).

Maximum cloud coverage in the Arctic occurs during summer (90%), and minimum during winter (40-50%) (*Curry and Ebert*, 1992).

2.4 Light interaction in the sea ice environment

2.4.1 Basic concepts of the light field

Electromagnetic radiation is composed of a large number of photons traveling with the speed of light. Even though every photon has a particulate nature, their energies are related to their wavelength through hc/λ (see Eq. 2.13). Thus the longer the wavelength of a photon, the lower its energy is. For instance, a wavelength increase from 400 nm (blue) to 700 nm (red) decreases the energy of a photon to 57%.

The measure of radiation is spectral radiance, $L(\theta,\phi,\lambda)$, which is the power in a ray of light at wavelength λ and moving in a particular direction defined here by the zenith angle θ and the azimuth angle ϕ (Figure 2.6). The spectral radiance is defined as the radiant energy Q, per unit of time t (or the radiant flux), per unit wavelength per unit area A, per unit solid angle Ω, in a particular direction:

$$L(\theta,\phi,\lambda) = \frac{d^4Q}{\cos\theta dt dA d\Omega d\lambda} \quad [\mathrm{W\ m^{-2}\ nm^{-1}\ sr^{-1}}], \tag{2.15}$$

where *sr* is steradians.

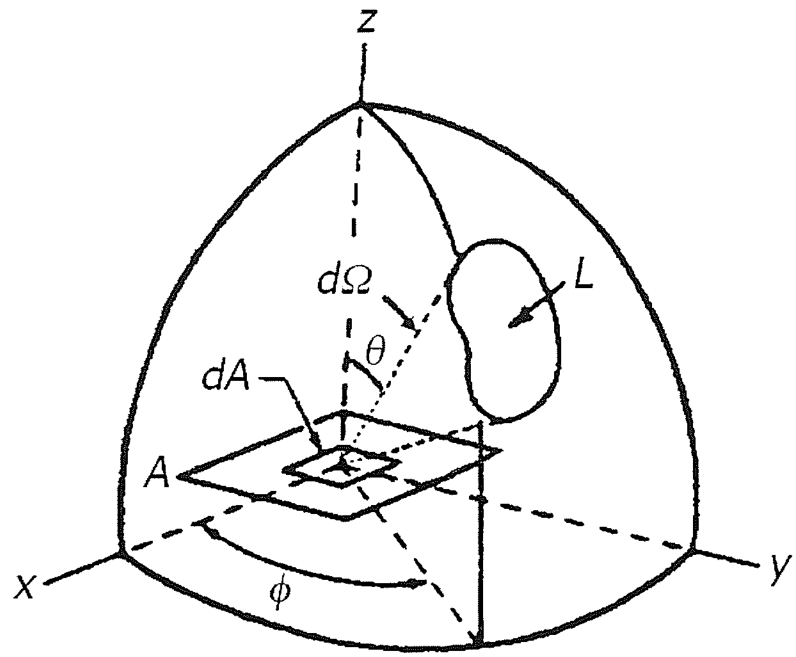

Figure 2.6. Definition of radiance incident upon the area element dA.

The other main quantity is spectral irradiance, $F(\lambda)$, which is the radiance projected on to a plane surface and integrated over a hemisphere. It has the unit of W m^{-2} nm^{-1}. The down- and upwelling irradiances, $F\downarrow(\lambda)$ and $F\uparrow(\lambda)$, are the integrated $L(\theta,\phi,\lambda)$ over all upward and downward direction, respectively. Often it is practical, especially in biology, to consider the number of photons instead of the energy and express the units as E s^{-1} m^{-2} nm^{-1} where E is the unit Einstein, which is equal to 6.022×10^{23} photons (=quanta) or 1 mole photons. For monocromatic irradiance it is easy to convert the units from W to E s^{-1} by multiplying with N_0hc/λ, where N_0 is Avogadro's number.

2.4.2 Radiative transfer theory

A photon in any medium can be (1) absorbed or (2) scattered in some direction or (3) undergo reflection/refraction. These fundamental processes are illustrated in Figure 2.7 for the OSA system. The latter arises in a medium where the index of refraction varies, such as over the air/ice interface or internally in the ice between ice and inclusions. Internal reflection/refraction in anisotropic sea ice is of unknown importance and has to date received little attention in the literature. The former two are fully characterized for any wavelength by the spectral absorption coefficient, $a(\lambda)$, scattering coefficient, $b(\lambda)$, and volume scattering function, $\beta(\lambda,\Theta)$, where Θ is the scattering angle. These three depend only on the substances comprising the medium and not on the geometric structure of the light field and are thus referred to as *inherent optical properties* (IOPs) (*Apel*, 1987). Often the phase function, $p(\lambda,\Theta)$, is used rather than $\beta(\lambda,\Theta)$ where $p(\lambda,\Theta) = \beta(\lambda,\Theta) / b(\lambda)$ so that $\int p(\lambda,\Theta)d\Theta = 1$. The scattering angle Θ expresses the change in direction from (μ', ϕ') into direction of the solution (μ, ϕ) where $\mu = \cos(\theta)$.

The radiative transfer equation expresses the propagation of radiation in any medium such as ice. Three processes alter the propagation: (1) absorption, (2) scattering out of, and (3) scattering in to the beam. When considering a plane-parallel medium, i.e., a horizontally homogeneous but with varying absorption and scattering properties in the vertical dimension (*Perovich*, 1996), the equation becomes:

$$\mu \frac{dL(\tau,\mu,\phi,\lambda)}{d\tau} = -L(\tau,\mu,\phi,\lambda) + S(\tau,\mu,\phi,\lambda) \qquad (2.16)$$

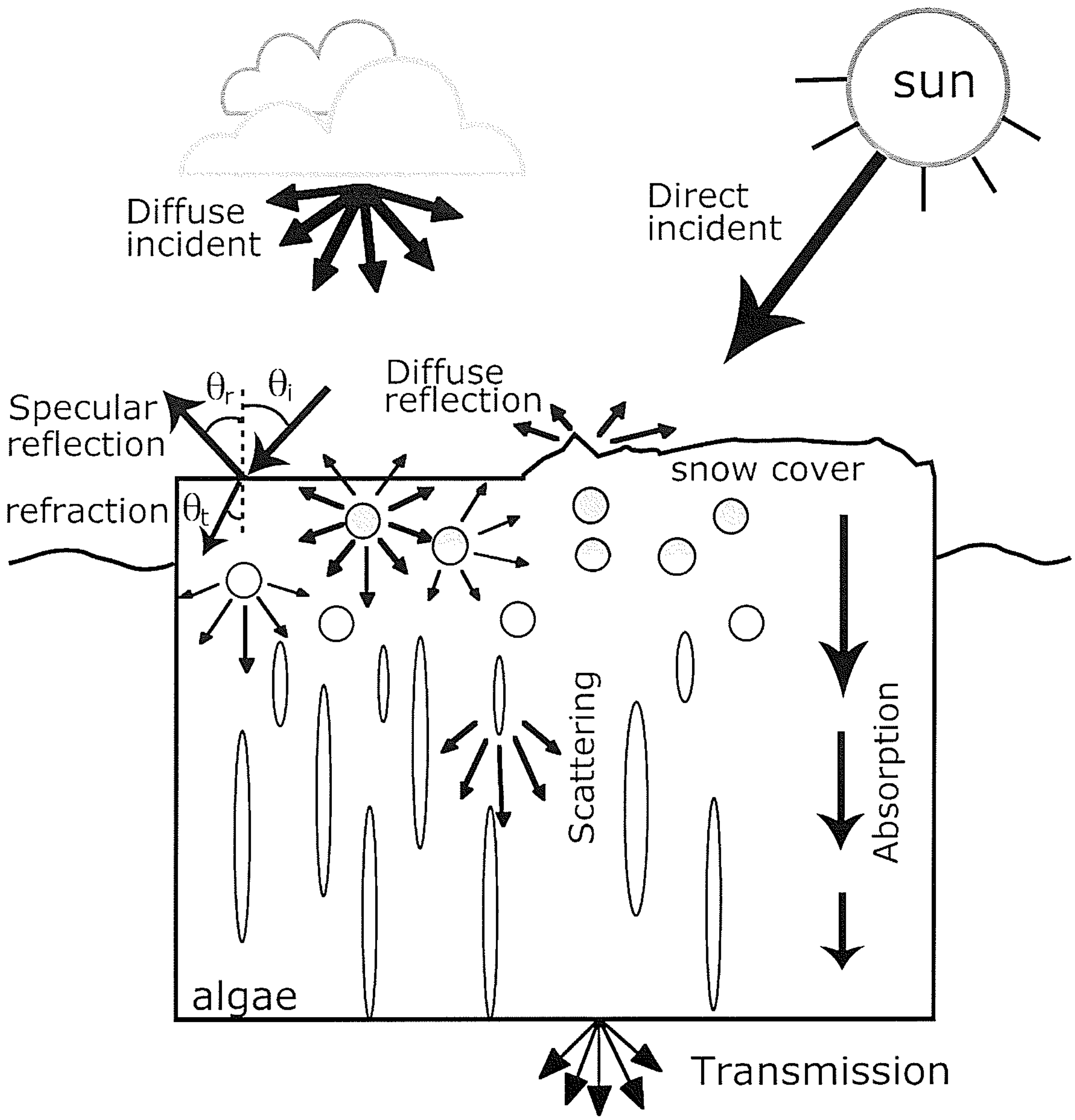

Figure 2.7. Radiative transfer in the atmosphere-sea ice-ocean system (modified from *Eicken*, 2003).

where S is the source function, $\mu = \cos(\theta)$ and $d\tau = (a+b)dz$ is the optical depth for the distance dz where z is the physical depth. The source function accounts for the scattering in to the beam and is expressed as (omitting the parenthesis in Eq. 2.16):

$$S = \frac{\varpi}{4\pi} \int_0^{2\pi} \int_{-1}^{1} p(\mu,\phi;\mu',\phi') L d\mu' d\phi' + \frac{L_0}{4} p(\mu,\phi;\mu',\phi') e^{-\tau/\mu_0}, \qquad (2.17)$$

where $\varpi = b / (a+b)$ is the single scattering albedo. The first term gives the contribution from the diffuse radiation that is scattered from any direction toward (μ, ϕ), and the second gives the contribution of scattered light from the attenuated direct beam L_0. In a non-scattering medium (i.e., b=0) the source function can be neglected and Eq. 2.16 reduces to

$$\mu \frac{dL}{dz} = -aL, \tag{2.18}$$

which when solved with μ=1 becomes Beer's law (*Perovich*, 1996):

$$L(z_2, \lambda) = L(z_1, \lambda) e^{-a(z_2 - z_1)}. \tag{2.19}$$

The radiation thus decreases exponentially with distance due to absorption when propagating from z_1 to z_2 where $z_2 > z_1$. Therefore, Beer's law is commonly known as the law of exponential decay.

2.4.3 Optical modeling of the OSA

Optical modeling involves solving Eq. 2.16 or its approximations, which requires determining the IOPs for the medium. The simplest and most used approximation has the form of Eq. 2.19 with modification to account for finite wavelength bands (see, e.g., *Grenfell and Maykut*, 1977). Other more advanced solutions include the discrete ordinates method (e.g., *Jin et al.*, 1994) and the Monte Carlo method (e.g., *Haines et al.*, 1997; *Light et al.*, 2004) that both can be used to solve the angular distribution of radiance. A common approach in modeling the ocean-sea ice-atmosphere (OSA) is to divide the system into a number of vertically varying but horizontally homogeneous layers with distinct IOPs. In addition, the boundary conditions between layers with different indices of refraction need to be considered, e.g., reflection and refraction at the interface between ice and the atmosphere (Figure 2.7).

The absorption coefficient, $a(\lambda)$, scattering coefficient, $b(\lambda)$, and phase function, $p(\lambda, \Theta)$, within a layer can be obtained as a sum of k components (e.g., *Hamre et al.*, 2004):

$$a(\lambda) = \sum_{j=1}^{k} a_j(\lambda), \tag{2.20}$$

$$b(\lambda) = \sum_{j=1}^{k} b_j(\lambda), \tag{2.21}$$

$$p(\lambda, \Theta) = \sum_{j=1}^{k} \frac{b_j(\lambda) p_j(\lambda, \Theta)}{b(\lambda)}, \tag{2.22}$$

where j denotes the different components. These components and their magnitudes are discussed below for the OSA system.

Absorption—As shortwave radiation propagates in the atmosphere, it is subject to absorption by molecules and aerosols to a degree depending respective concentrations and on wavelength (for a detailed account on radiative transfer in the atmosphere the reader is referred to e.g. *Thomas and Stamnes*, 1999). Shortly, in the visible or PAR region, i.e., about 400-700 nm, absorption is weak and radiative transfer is dominated by scattering. However, within the ultraviolet (UV) band (λ < 400nm) absorption is controlled by ozone (O_3). Most UV radiation with λ < 280 nm is absorbed in the atmosphere before reaching the surface. Between 280 nm ≤ λ ≤ 400 nm some radiation reaches the surface depending on the O_3 optical depth. In the near infrared, i.e., about 700 nm ≤ λ ≤ 3.0 μm, radiation is absorbed in discrete wavelength bands by oxygen, water vapor and carbon dioxide (*Thomas and Stamnes*, 1999). Shortwave radiation that after scattering reaches the surface is termed *diffuse*, while the un-scattered part is called *direct* (Figure 2.7). This distinction has impacts on how radiation is reflected from the surface (*Warren*, 1982).

In snow, sea ice and seawater, $a(\lambda)$ is due to contributions by seawater (SW) and ice (I) itself, and by other optically active substances (OAS). The OAS are commonly separated into three groups; (1) phytoplankton (algae) with absorbing pigments (CHL), (2) non-algal particulates of biological or terrestrial origin (NAP), and (3) coloured dissolved organic matter (CDOM) or yellow substance. For each layer in snow/sea ice/seawater, the absorption coefficient can be expressed as:

$$a(\lambda) = v_i a_i(\lambda) + v_b a_{sw}(\lambda) + a_{chl}(\lambda) + a_{nap}(\lambda) + a_{dom}(\lambda), \tag{2.23}$$

where subscripts denote the above absorbing components. In snow and sea ice, $a_i(\lambda)$ and $a_b(\lambda)$ are are multiplied by their respective volume fractions (section 2.2.4), while in seawater $v_i = 0$ and $v_b = 1$. Absorption spectra for pure ice and seawater have been measured by, e.g., *Grenfell and Perovich* (1981) and *Smith and Baker* (1981), respectively. The spectral shape and magnitude of OAS absorption is commonly modeled using

$$a_{chl}(\lambda) = m_{chl} A_{chl}(\lambda)[\mathrm{CHL}], \tag{2.24}$$

$$a_{nap}(\lambda) = m_{nap} e^{S_{nap}(440-\lambda)}[\mathrm{NAP}], \tag{2.25}$$

$$a_{dom}(\lambda) = e^{S_{dom}\cdot(440-\lambda)} a_{dom}(440), \tag{2.26}$$

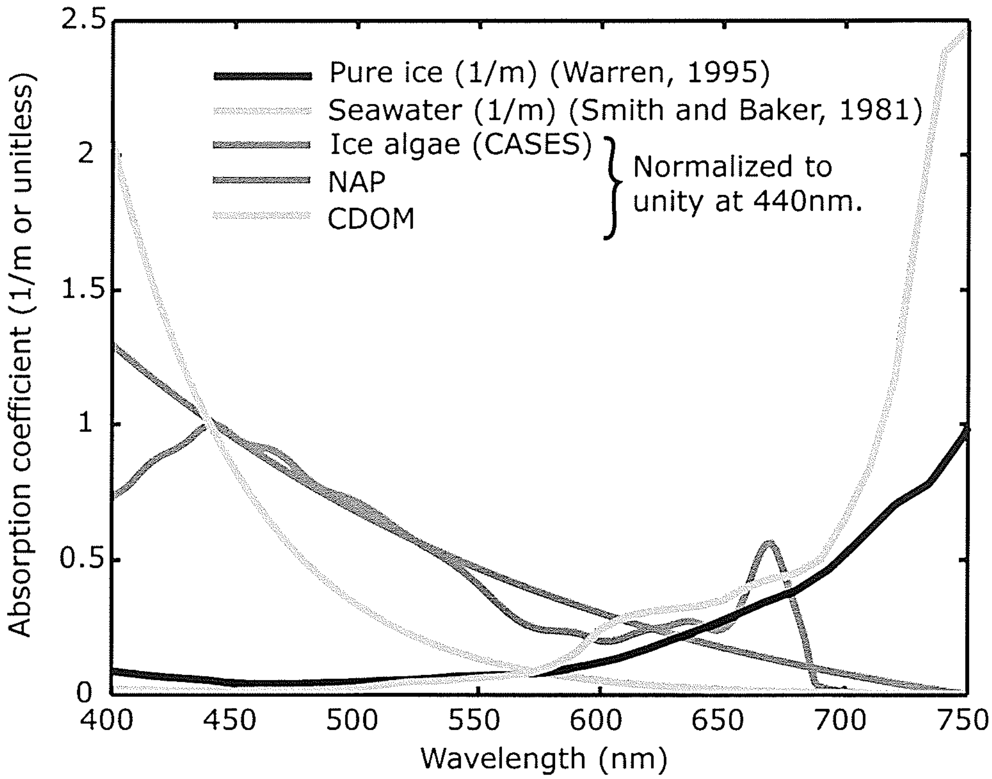

Figure 2.8. The optically active components in sea ice and the water column. The spectra for phytoplankton (green), non-algal particulate matter (blue) and coloured dissolved organic matter (yellow-brown) are normalized.

where m_{chl} (~0.06) and m_{nap} (~0.05) are constants controlling the magnitude, A_{chl} the normalized absorption coefficient for the algae, S_{nap} (~0.005) and S_{dom} (~0.018) are slope factors, [CHL] and [NAP] concentrations, and $a_{dom}(440)$ the absorption coefficient for CDOM at 440 nm (*Roesler and Perry*, 1995). Figure 2.8 illustrates the shape of these components.

Phytoplankton or algae are unicellular plants found everywhere in the euphotic layer of the marine environment as well as in sea ice and snow. Due to the absorbing properties of the water molecule, they have adjusted into absorbing light in the PAR region (about 400-700 nm). Chlorophyll-*a* (CHL) is the main light-absorbing pigment and present in all photosynthetic algae. It is relatively easy to measure and is therefore often used as a measure of biomass. CHL has two major absorption peaks – one near 440 nm and the other near 670 nm (*Apel*, 1987). Depending on species, a number of so-called accessory pigments are present, which are specialized in capturing photons at distinct spectral regions (and thereby also identified) and mainly pass the absorbed energy on to the CHL. Through the process of photosynthesis the captured solar energy is then turned into and stored as organic carbohydrates.

CDOM is mostly derived from remains and metabolic products of marine plants and animals that have dissolved in the water. However, especially in coastal regions, a large part of CDOM originates from terrestrial sources. The general characteristic of CDOM is an absorption that increases exponentially with decreasing wavelength (see Eq. 2.26). This gives it reddish-yellowish colour and it is therefore often termed *yellow substance*. The exponential slope may vary significantly from one place to another (*Roesler and Perry*, 1995).

The disperse group of NAP or so-called suspended particles include all organic and inorganic matter, with the exception of phytoplankton, that have particle sizes large enough to be collected on filters (*Roesler and Perry*, 1995). It has a similar absorption curve as CDOM but with smaller exponential slope. Substantial amounts of NAP are deposited at the surface from the atmosphere in the form of soot or dust, and are know to affect the albedo (*Warren*, 1982). However, most are of lithogenic origin transported by rivers and currents. These inorganic sediments and their derivatives are incorporated into the ice during its formation and during flooding events. NAP also include biogenic matter, such as rest products of dead algae and zooplankton (detritus).

The distinction between the three OAS is made complicated by biogenic matter such as viruses and bacteria, which are too small to be collected on filters, and although particles become classified as CDOM. In addition, aggregates with mixed properties may form out of algae, detritus, bacteria and CDOM.

Scattering—In weakly absorbing media, such as the atmosphere and the ocean within visible wavelengths, molecular scattering is important. Molecular scattering can be explained using Rayleigh scattering theory where $b_{molecule}(\lambda)$ shows λ^{-4} wavelength-dependence (e.g., p. 72 in *Thomas and Stamnes*, 1999). The Rayleigh scattering phase function is

$$p_{molecule}(\Theta) = \frac{1}{4\pi}\frac{3}{3+r_{pol}}\left(1+\cos^2(\Theta)\right), \tag{2.27}$$

where r_{pol} is the polarization ratio equal to 1 in the atmosphere and 0.84 in seawater (*Morel and Gentili*, 1991). For seawater, Morel (1974) found

$$b_{sw}(\lambda) = (129/\lambda)^{4.32} \tag{2.28}$$

However, in sea ice and snow, where scattering is dominated by inclusions and grains that are >> λ, $b(\lambda)$ can be taken as wavelength-independent. In general, b_j in sea ice and snow can be obtained using Mie scattering theory assuming that the components j can be described as discrete spheres with the radius r distributed uniformly within the layer. This often involves representing the inclusions with equivalent volume and area spheres (*Light et al.*, 2003). b_j becomes

$$b_j = \int_{r_{\min}}^{r_{\max}} \pi r^2 Q_j(r) N_j(r) dr, \tag{2.29}$$

where Q_j is the scattering efficiency, and N_j the number density (see section 2.2.5) as a function of r. Q_j approaches 2 when r>>λ. Often there is not sufficient information on $N_j(r)$ which is consequently approximated using and effective radius (r_{eff}) obtained by matching modeled irradiance values against measurements. r_{eff} defined as

$$r_{eff} = \int N_j(r) r^3 dr \Big/ \int N_j(r) r^2 dr, \tag{2.30}$$

and $b_j = 2\pi r_{eff,j}^2 N_j$ where N_j is the number of inclusions j per volume. Then, because v_j for spherical inclusions is $v_j = 4\pi r_{eff,j}^3 N_j$, it is convenient to express b_j for brine and air as

$$b_j = \frac{3v_j}{2r_{eff}}. \tag{2.31}$$

The phase function for spherical inclusions can be can be calculated using Mie theory or approximated using the Henyey-Greenstein phase function (*Henyey and Greenstein*, 1941),

$$p_j(\Theta) = \frac{1}{4\pi} \frac{1 - g_j^2}{(1 + g_j^2 - 2g_j \cos(\Theta))^{3/2}}, \tag{2.32}$$

where g_j is the average cosine or the asymmetry parameter obtained using Mie theory. For brine inclusions (including brine pockets and tubes), solid salts, air bubbles and particulates in sea ice, g_j is found to be about 0.982-0.997, 0.97-0.99, 0.85-0.86 and 0.93, respectively (*Hamre et al.*, 2004; *Light et al.*, 2004). Furthermore, *Light et al.* (2004) reported a decrease in g_{brine} from 0.995 to 0.982 when T_{si} decreased from -4 to -28°C. The higher the g_j, the more the radiation is forward scattered (i.e., Θ is small).

Effects of the surface—When the light crosses the interface between two optically different media (e.g., from air to water, ice or snow) it will be reflected and refracted. Specular reflection predominates from surfaces that are smooth in length scales relative to the wavelength, while diffuse reflection (or scattering) predominates from rough surfaces. For both, the incident angle of the incoming radiation is important, whether it is diffuse or mostly direct radiation. These different media have different indices of refraction, n, which are specific for the material. For air n is close to 1.0, while it is 1.33-1.34 for water, depending on temperature and salinity, and about 1.31 for ice. The angle of refraction, θ_t, measured normal to the surface of the rays of this light penetrating below the surface is given by Snell's law:

$$n_t \sin(\theta_t) = n_i \sin(\theta_i)\,, \tag{2.33}$$

while the angle of reflection θ_r is equal to θ_i (see Figure 2.7). An important effect of the surface is that the cone of rays entering water or ice becomes narrower. Radiation from any direction in the upper hemisphere will enter through a smooth water surface within a cone with an apex of about 2 (*Dera*, 1992). In the same way light emerges through the surface back into the atmosphere only through such a cone. Upwelling radiation in the water column with $\theta_t > 48.5°$ will be internally reflected at the air-water interface.

The energy ratios of reflected and refracted to incident radiance is obtained with Fresnel's equations (e.g., *Apel*, 1987). For fully diffuse incident radiation, 6.6% of the incident radiation is reflected with 93.4% being transmitted into the water column. The reflected portion is about 2% for a radiation beam with an incidence angle between 0 and 40° and then increases exponentially to about 6% at 60°, 13% at 70°, 35% at 80° and 100% at 90°.

2.5 Observations of apparent optical properties

In contrast to IOPs, the apparent optical properties (AOPs) are measured using the natural light field, and thus depend not only on the optical properties of the medium, but also on light and boundary conditions. Consequently, it is more difficult to relate them to the physical properties of the medium. But it is with AOPs that the energy partitioning within the OSA system can be directly determined. The AOPs include, e.g., the albedo, transmittance and the diffuse attenuation coefficient, which are defined and demonstrated in this section.

2.5.1 The albedo

The spectral albedo, $\alpha(\lambda)$, is defined as the ratio of upwelling irradiance, $F_{\uparrow}(0^{+},\lambda)$, to the downwelling irradiance, $F_{\downarrow}(0^{+},\lambda)$, immediately above a surface (*Perovich*, 1996):

$$\alpha(\lambda) = \frac{F_{\uparrow}(0^{+},\lambda)}{F_{\downarrow}(0^{+},\lambda)}. \tag{2.34}$$

The total shortwave albedo, α, already defined in Eq. 2.10, is related to $\alpha(\lambda)$ through integration over the shortwave solar spectrum, i.e.,

$$\alpha = \frac{\int_{\Delta\lambda} \alpha(\lambda) F_{\downarrow}(0^{+},\lambda) d\lambda}{\int_{\Delta\lambda} F_{\downarrow}(0^{+},\lambda) d\lambda}, \tag{2.35}$$

where $250\text{nm} \le \Delta\lambda \le 3.0\mu\text{m}$. It is a measure of the amount of solar energy absorbed below the snow/ice surface. The albedo is most strongly related to surface conditions, however, it is clear from Eq. 2.35 that the albedo also depends on the spectral shape of the incident radiation. Thus the sky condition, i.e., clear or cloud covered, has an effect on the overall value. A cloud-covered sky may increase the albedo by up to 10% by absorbing radiation more strongly in the near infrared (>700 nm). *Allison et al.* (1993) found variations in the albedo ranging 0.01-0.08 due to varying cloud coverage. However, within visible radiation, where the albedo is the highest, spectral changes (in shape) are small. In addition, most spectroradiometers used in field investigations are capable of measuring radiation up to 1000-1100 nm. Changes in shortwave radiation above 1000 nm due to sky conditions are at most ±0.009 (*Allison et al.*, 1993).

The total albedo can vary significantly both temporally and spatially. Perovich (1996) summarized the range of observed values spanning about 0.06 for open water to 0.87 for new snow on the ice surface (Table 2.1). Due to its range, the albedo is the most important factor in determining the partitioning of solar energy within the OSA system (*Jin et al.*, 1994). New and young ice types (section 2.2.2), which are not included in Table 2.1, span from open water values to roughly 0.20 (*Allison et al.*, 1993; *Brandt et al.*, 2005). The presence of a snow cover, even on relatively thin ice, increases the albedo to values above 0.7 largely independent of the underlying ice thickness.

Table 2.1. Observed range of values of the total shortwave albedo in the Arctic (adapted from *Perovich*, 1996).

Open water	Old melt pond	Ponded FYI	Mature pond	Melting blue ice	Refrozen melt pond	Bare FYI	Melting white ice	Frozen white ice	Melting snow	Wind-packed snow	New snow
0.06	0.15	0.21	0.29	0.32-0.34*	0.40	0.52	0.56-0.68	0.70	0.77	0.81	0.87

*estimate from Figure 3 in *Perovich* (1996).

Seasonal progression—In section 2.2, the seasonal evolution of sea ice was discussed. Here it is extended with a discussion of spectral albedo. Figure 2.9 shows spectral albedos measured over a range of ice types. The albedo for seawater is predominantly due to specular reflection at the surface. Because of the low backscattering in (clear) seawater, most radiation penetrating below the surface is absorbed. For dark nilas (<0.05m) the albedo is comparable to open water values because the ice is relatively warm and porous with almost no air inclusions. As the ice thickness increases, it becomes colder and inclusions are trapped. This increases the scattering in the ice, and thus the albedo, but also the overall absorption due to the increased distance traveled by photons within the sea ice (*Jin et al.*, 1994). *Perovich* (1990b) found that the albedo of newly formed sea ice in a lead in the Arctic increased from 0.1 (open water) to 0.9 (snow covered ice) within a few days. Similar results were found by *Allison et al.* (1993) and *Brandt et al.* (2005) for Antarctic sea ice (Figure 2.9).

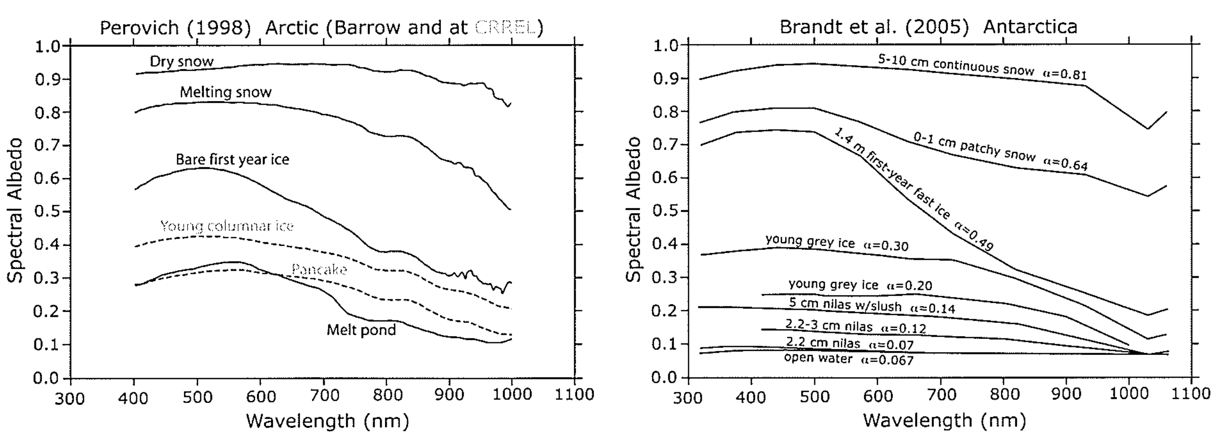

Figure 2.9. Examples of spectral albedo measured in the Arctic and the Antarctic (drawn from data presented in *Perovich* (1998) and *Brandt et al.* (2005)).

The surface conditions of a sea ice cover play a central role in determining the albedo. A snow cover of a few centimeters effectively hides the underlying ice so that the albedo is that of the snow cover. Other significant surface features include frost flowers and simply the surface layer of the ice (particularly the portion above the freeboard) that often is composed of granular ice with numerous air inclusions. A high scattering surface layer results in more backscattering to the atmosphere, but also in a decrease in transmission to deeper layers in the ice and ocean. Frost flower covered sea ice remains highly under-studied mainly due to logistical difficulties to access and work with new sea ice formed under natural conditions. However, laboratory studies indicate that the presence of frost flowers may increase the surface albedo to an extent similar to snow (*Grenfell et al.*, 1998). *Grenfell et al.* (1998) observed an increase in albedo by 0.1-0.2.

During winter and early spring, sea ice is generally covered with snow. Consequently the albedo remains relatively constant with values > 0.9 within PAR (Figure 2.9). The albedo of the snow pack is due to scattering, the magnitude of which is determined by the snow grain sizes, and the presence of impurities that increase absorption above pure snow levels. Additionally, the solar zenith angle and the fraction of diffuse to direct radiation affect the albedo (*Warren*, 1982). During late spring and summer, melting causes the surface to fraction into a number of surface types, e.g., melting snow, white ice, blue ice and melt ponds. Melt pond coverage on level ice reaches a maximum of 25-50% by mid-July with a corresponding decrease in albedo from 0.75-0.80 to 0.25-0.45 (*Morassutti and LeDrew*, 1995). *Barber and Yackel* (1999) observed melt pond coverage up to 80% during SIMMS'95 in the Canadian Archipelago. As the melt season progesses, porous ice, cracks and seal holes result in the draining of the surface, thereby reducing pond coverage (*Barber and Yackel*, 1999). Furthermore, diurnal processes are important. For example, overnight freezing often results in the formation of a thin ice layer on the melt pond that disappears during the day. An increase in albedo of 0.03-0.07 was observed for refrozen melt ponds by *Hanesiak et al.* (2001). Towards freeze-up in fall, melt ponds remain frozen throughout the day and eventually freeze throughout. This is especially common for multi-year ice with melt ponds that not always drain during summer (*Morassutti and LeDrew*, 1995).

Regional albedo—The albedo shows large spatial and temporal variability that is most pronounced during the fall freeze-up and spring/summer melt periods (Table 2.1 and Figure 2.9). What is thus important for climate-scale studies and modeling is to obtain a regional albedo estimate. Regional (spectral or broadband) albedos are a weighted average of statistically determined surface types. In summer, the surface is typically divided into areas of open water, deformed ice (ridges), level blue and white ice, and melt ponds. During freeze-up, a multitude of new and young ice types are present with highly variable surface reflective properties. White ice surfaces are interesting, as they tend to sustain a fairly constant albedo even as the ice thickness decreases. This is because white ice is characterized by a snow-like, high scattering surface layer above the freeboard, which is maintained by drainage through the permeable ice (*Eicken*, 2003). However, to what extent a stable white ice albedo is maintained as summer melt progresses and the timing of its breakdown is currently not well known.

Satellite sensors operating in visible and near infrared wavelengths can and have been used for direct measurements of regional albedo in a climatologically significant scale (e.g., *Robinson et al.*, 1986; *De Abreu et al.*, 1994; *Hanesiak et al.*, 2001; *Zhou and Li*, 2003). However, the interpretation of satellite data is significantly hampered by the masking effect of the atmosphere (e.g., *Vermote et al.*, 1997), anisotropic surface reflection (e.g., *Perovich*, 1996), and limited sensor resolution leading to heterogeneity of many surface types within a pixel (e.g., *Zhou and Li*, 2002). Furthermore, observations in visible wavelengths are largely unusable during large parts of the year low insolation levels during dark winter months and a prevailing cloud cover during summer. Note however that the albedo in itself is of limited importance during dark period of the year even though surface heterogeneity is still a major issue for the energy balance through spatially variable sensible and latent heat conduction and longwave radiation emission to the atmosphere.

Radiation in microwave frequencies are largely unaffected by atmospheric conditions and can be used throughout the year. Therefore satellite sensors operating in microwave frequencies are typically utilized in remote sensing of sea ice in high latitudes. As discussed in section 2.2.1, microwave data is regularly used for Arctic-wide estimates of ice concentration and extent (e.g. *Parkinson et al.*, 1999). More specific algorithms, using combinations of various frequencies and polarizations, have been developed for the detection of various ice types (e.g. *Hwang et al.*, 2007, and references therein). These algorithms need to consider heterogeneous ice types and variations in ice concentration within pixels. For regional energy balance estimates in ice covered seas, arguably the most important variables needed are sea ice thickness and surface temperature for the ice types encompassed within a pixel. Furthermore, during summer months the shortwave albedo is of critical importance. The above variables can be deduced, through empirical relationships or more detailed modeling, from satellite microwave data (see, e.g., *Hwang et al.*, 2006; 2007; 2008, and references therein).

2.5.2 Transmission

Transmission measurements are more rare compared to albedo measurements mainly because of the difficulty in placing sensors below the ice. Knowledge on radiation transmission is important, as biological activity in and under the ice is to a large part controlled by the availability of PAR. The spectral transmittance, $T(\lambda)$, is the fraction of $E_d(0^+,\lambda)$ to what is transmitted, $E_d(z,\lambda)$, to a certain depth z:

$$T(\lambda) = \frac{E_d(z,\lambda)}{E_d(0^+,\lambda)}. \tag{2.36}$$

The composition and thickness of the layer essentially determine the magnitude and spectral distribution of $T(\lambda)$. Overall transmission through the ice pack is largely controlled by high scattering near the surface and the highly absorbing algae near the bottom (Figure 2.10). *Perovich* (1996) showed that less radiation is transmitted through the sea ice due to an increase

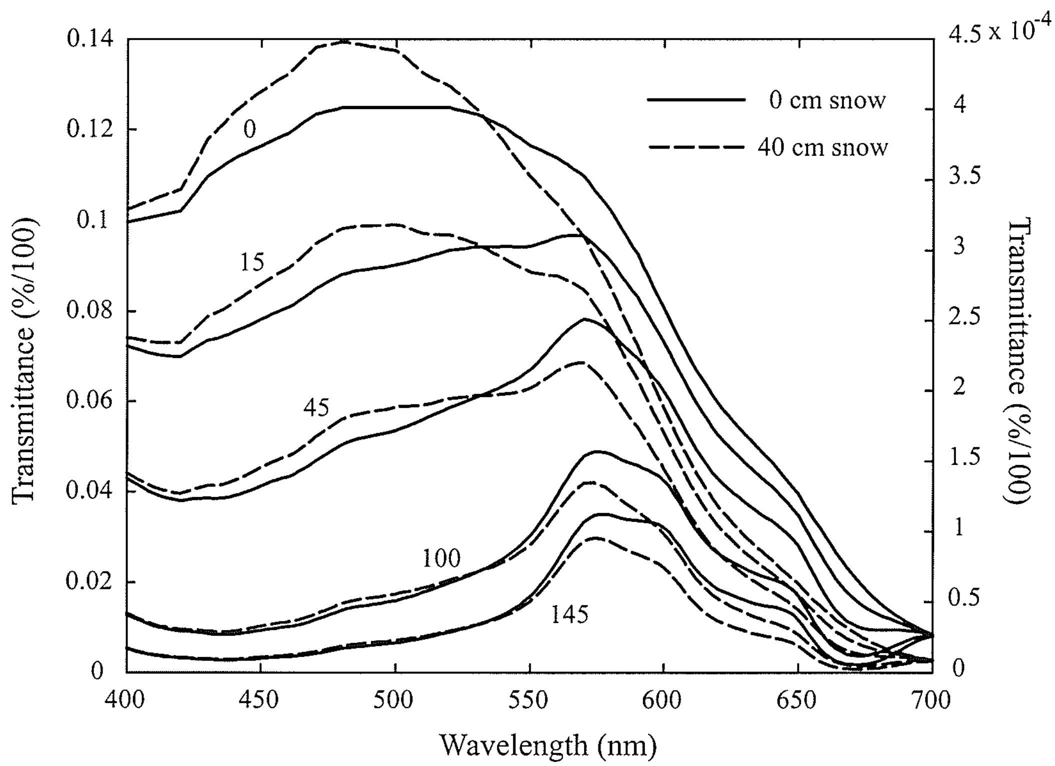

Figure 2.10. Effect of snow and the bottom algae layer on the transmission of radiation through 1.45 m thick first-year ice as predicted by a two-stream radiative transfer model presented in *Mundy et al.* (2007). Model validation data obtained from Resolute Passage (NU) in 2003 (courtesy C.J. Mundy).

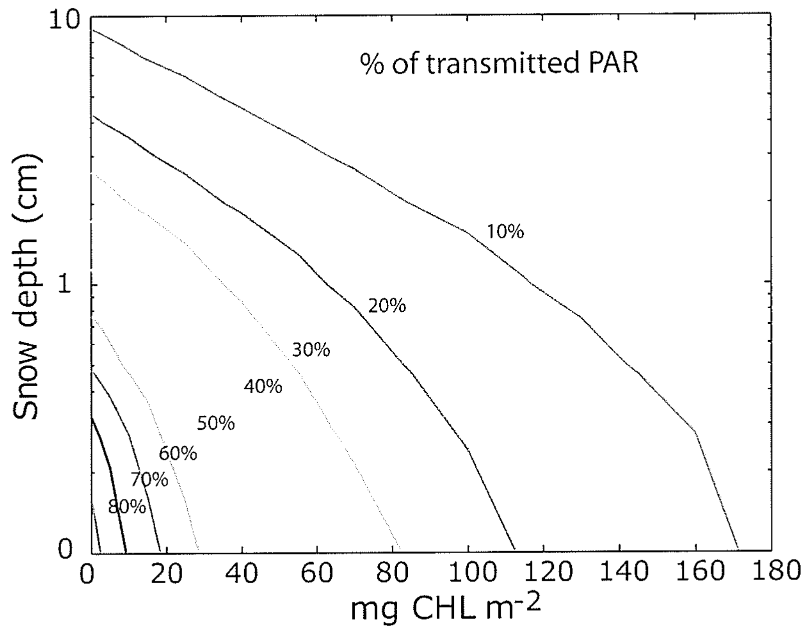

Figure 2.11. Effect of snow cover versus algae layer biomass (CHL) as predicted by a two-stream radiative transfer model presented in *Mundy et al.* (2007).

in algae concentration (from 119 to 157 mg CHL m^{-2}) even though the snow thickness reduced by 14 cm (from 19 to 5 cm). A recent study in Resolute Passage (Nunavut, Canada) resulted in data that allowed a modeling comparison of the influence of snow and CHL on transmitted radiation through landfast ice (*Mundy et al.*, 2007) (Figures 2.10 and 2.11). Results indicate that a snow thickness of 10 cm has a similar effect on *T*(PAR) as a CHL of about 170 mg m^{-2} (Figure 2.11). Similarly, about 40 mg CHL m^{-2} compares to a snow thickness of 1 cm.

However, $T(\lambda)$ also decreases as it passes through the interior portion of sea ice. As a general rule, $T(\lambda)$ drops off in an exponential manner with increasing depth. As a result, the *diffuse attenuation coefficient*, $K_d(\lambda)$, is regularly used to express this attenuation:

$$K_d(\lambda) = -\frac{d\ln(E_d)}{dz}. \tag{2.37}$$

Figure 2.12 shows commonly adopted values used for $K_d(\lambda)$ in snow, sea ice and seawater. The range spans 1-2 orders of magnitude between the different types depending on their scattering and absorption characteristics (section 2.4.3). The general feature is minimum values near 450-500 nm and a strong increase towards infrared wavelengths where absorption by the ice and water dominates. Recent observations by *Pegau and Zaneveld* (2000), *Grenfell et al.* (2006) and *Light et al.* (2008) have questions the magnitude of some of these spectra, especially for longer wavelengths.

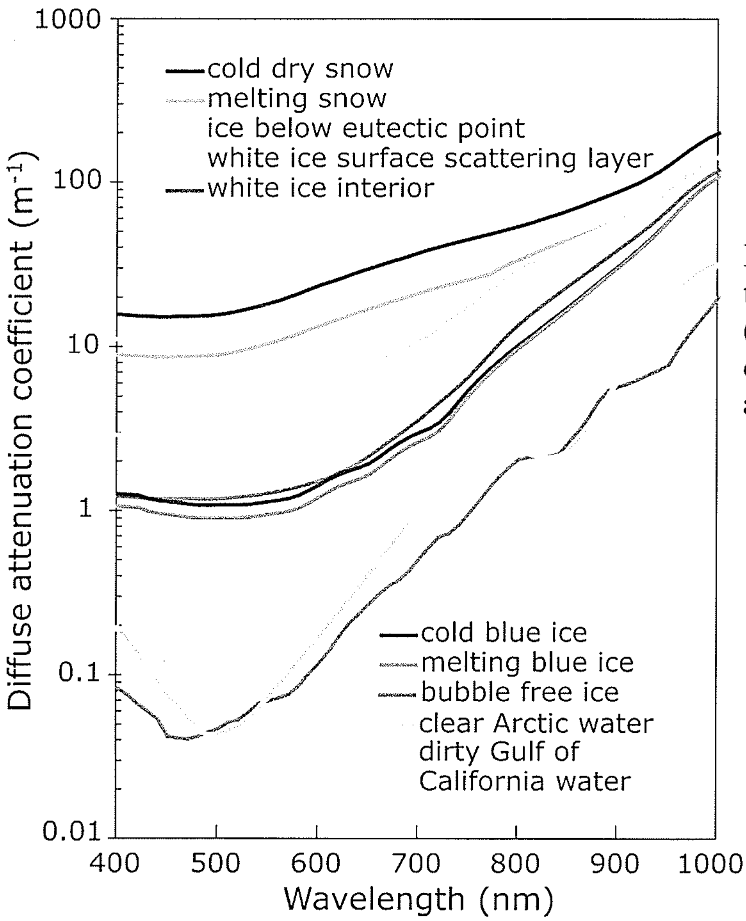

Figure 2.12. Spectral diffuse attenuation coefficients for ice and water types (drawn from two-stream model input data courtesy of D.K. Perovich; see also *Perovich*, 1990).

CHAPTER 3: Investigations of newly formed sea ice in the Cape Bathurst polynya: Structural, physical and optical properties

3.1 Preface

The material in this chapter has been published in Ehn, J. K., B. J. Hwang, R. Galley, and D. G. Barber (2007), Investigations of newly formed sea ice in the Cape Bathurst polynya: 1. Structural, physical, and optical properties, *J. Geophys. Res.*, 112, C05002, doi:10.1029/2006JC003702 (Reproduced by permission of American Geophysical Union). I was responsible for the major part of the work in this paper, inluding field sampling and analysis, data analysis and writing. The contents of the chapter address research questions I and II of my thesis.

3.2 Introduction

Recent evidence of changes in the areal extent (*Parkinson et al.*, 1999; *Serreze et al.*, 2003; *Barber and Massom*, 2006) and thickness (*Wadhams and Davis*, 2000; *Yu et al.*, 2004) of northern hemisphere sea ice have focused scientific attention on the fact that we may already be seeing the first and strongest impacts of global climate change in the high latitudes of our planet (*ACIA*, 2005). The reduction in perennial sea ice and the later formation of annual ice underscores the need to better understand the geophysics and radiative transfer of newly forming sea ice as this form of ice may likely become increasingly common, both spatially and temporally, in the northern hemisphere.

Polynyas are particularly prone to change, being areas of thinner ice and reduced ice cover (*Morales Maqueda et al.*, 2004; *Barber and Massom*, 2006). Nonetheless, as winds and currents continuously move forming ice and new ice-free areas appear, polynyas are also areas of extensive ice production. As a result, both spatial and temporal variability in ice properties are large with a multitude of newly formed sea ice types and conditions occurring within small areas. Thin sea ice plays an important role in the Arctic climate system. It significantly lowers the surface albedo and approximately doubles the atmosphere-ocean heat exchange compared to thicker ice (*Maykut*, 1978). Its rapid growth increases the salt flux to the surface layers of the ocean which drives thermohaline convection (*Winsor and Björk*, 2000) and there is growing evidence that brine kinetics plays a role in the flux of carbon dioxide across the ocean-sea ice-atmosphere interface (*Miller et al.*, 2005).

Sea ice formation requires a supercooled surface layer in the ocean. Suspended ice crystals form in this layer that rise and accumulate to the surface collecting into a uniform layer of frazil ice crystals called grease ice (*Weeks and Ackley*, 1982; *Smedsrud and Skogseth*, 2006). During calm conditions this layer quickly consolidates into a solid ice cover of randomly oriented ice crystals. With significant wave action, the frazil collects to form rounded discs collectively called pancake ice. Pancake sizes range from a few tens of centimeters to a few meters. The pancakes continually collide and separate resulting in characteristic elevated rims. With ongoing freezing the pancakes adhere into a continuous ice sheet. Once a solid surface layer has formed, further ice growth typically commences through congelation at the ice-water interface. Ice crystals with a more horizontal c-axis orientation have a slight growth advantage. Therefore, further ice growth results in geometric selection towards columnar ice crystals with their c-axes in the horizontal plane and an increase of their size with depth (*Weeks and Ackley*, 1982). This transition occurs within a few centimeter-thick transition zone that forms so-called intermediate granular/columnar ice (*Eicken and Lange*, 1989).

As a part of the ice formation and growth process, salt is partly rejected from the ice and partly trapped along the boundaries and in interstices of ice crystals and the platelet substructure (e.g., *Weeks and Ackley*, 1982). The initial entrapment of salt is largely dependent on the salinity of the seawater and the ice growth rate (*Weeks*, 1998). The brine within the sea ice is concentrated into brine pockets, tubes and channels of various sizes, shapes and numbers (*Light et al.*, 2003). These brine inclusions determine, to a large extent, the electromagnetic, thermal, mechanical and permeability properties of sea ice (*Barber et al.*, 2000; *Golden et al.*, 1998; *Perovich and Gow*, 1996). The size of the brine inclusions is temperature dependent; a decrease (increase) in the temperature will result in additional freezing (melting) on the walls of the inclusions. The brine volume fraction in sea ice can thus be determined, based on the requirement of phase equilibrium between brine and ice, using parameterizations by *Cox and Weeks* (1983). As ice temperatures decrease, pressure build-up in brine cells force brine to migrate upward and downward through a process called brine expulsion (*Weeks and Ackley*, 1982). Upward movement is facilitated by high porosities within a few centimetres of the surface layer (*Perovich and Richter-Menge*, 1994). A result is also the formation of a high salinity layer on the ice surface, which under cold and calm conditions may lead to frost flower formation (*Perovich and Richter-Menge*, 1994; *Martin et al.*, 1996).

Satellites operating in visible and microwave frequencies have severe difficulties detecting areas of thin ice (*Comiso et al.*, 2003; *Zhou and Li*, 2003). The key improvements of this problem rely on a better understanding of the interaction between electromagnetic radiation and brine within sea ice. Brine inclusions within sea ice affect radiation propagation primarily through scattering (e.g., *Perovich*, 1990b). In addition, through formation of the surface brine layer and frost flowers, brine in the ice significantly affects the interaction of electromagnetic radiation with the ice surface. Laboratory studies indicate that the presence of frost flowers increases the surface albedo to an extent similar to snow (*Grenfell et al.*, 1998). *Perovich* (1990b) found that the albedo of newly formed sea ice in a lead in the Arctic increased from 0.1 (open water) to 0.9 (snow covered ice) within a few days. Similar results were found by *Allison et al.* (1993) for Antarctic sea ice. Despite its importance, few field observations have been conducted over newly formed ice in the Arctic (e.g., *Perovich and Richter-Menge*, 1994; *Smedsrud and Skogseth*, 2006) mainly due to logistical difficulties to access and work with new sea ice formed under natural conditions.

The second leg of the Canadian Arctic Shelf Exchange Study (CASES), onboard the research icebreaker *CCGS Amundsen* in October-November 2003, provided a unique opportunity to study thin, newly formed sea ice in the Cape Bathurst polynya (southeastern Beaufort Sea). The fall freeze-up program was designed to improve our understanding of the geophysics and electromagnetic properties of very young ice. Due to sampling challenges this type of ice is rather underrepresented in the literature, yet, this period plays a very important role in exchange of mass and energy across the ocean-sea ice-atmosphere interface and thus is of considerable interest from the perspective of climate change. In this study detailed sea ice geophysical and thermodynamic state variables were sampled coincident with observations of reflectance spectra in visible and near infrared wavelengths, and passive and active microwave signatures of the sea ice. This paper focuses on the characterization of structural, physical and optical properties of the new ice types, while the accompanying paper by *Hwang et al.* (2007) deals with the microwave emission characteristics and its interaction with the prevailing structural and physical ice properties. The long-term goal of this work is to develop a theory linking the physical-structural properties of sea ice with its optical and microwave properties. Here, the approach is to identify the typical features that dominated the ice properties during the experiment, and examine variability within commonly used *World Meteorological Organization* (1985) ice categories.

3.3 Methods

3.3.1 Site description

The Cape Bathurst polynya is an enlargement of the circumpolar flaw lead system (*Barber and Massom*, 2006). The flaw lead forms at the interface between landfast first-year sea ice and the offshore mobile pack ice which circulates throughout the year in the southern Beaufort Sea (*Barber and Hanesiak*, 2004), in the area southeast of Banks Island (Figure 3.1). It is generated and maintained by forcing related to the anti-cyclonic motion of the Beaufort gyre (*Fett et al.*, 1994) and in particular the hemispheric motion of the mobile ice away/towards the landfast edge in Amundsen Gulf. The seawater properties are affected by runoff from the Mackenzie River about 150 km to the west (*Carmack et al.*, 1989). The riverine influence results in lower salinity surface plumes with a terrestrial signal (*Carmack et al.*, 1989; *Guéguen et al.*, 2005). However, the river water is largely constrained to the coastal zone once the landfast sea ice is formed with the stamukhi zone at its boundary. The stamukhi is a line of thick compression ridges parallel to the coast formed through the interaction between the landfast ice and the mobile pack ice (*Barber and Hanesiak*, 2004). Ice formation is initiated during October -early November and the polynya is fully ice covered by December (*Arrigo and van Dijken*, 2004).

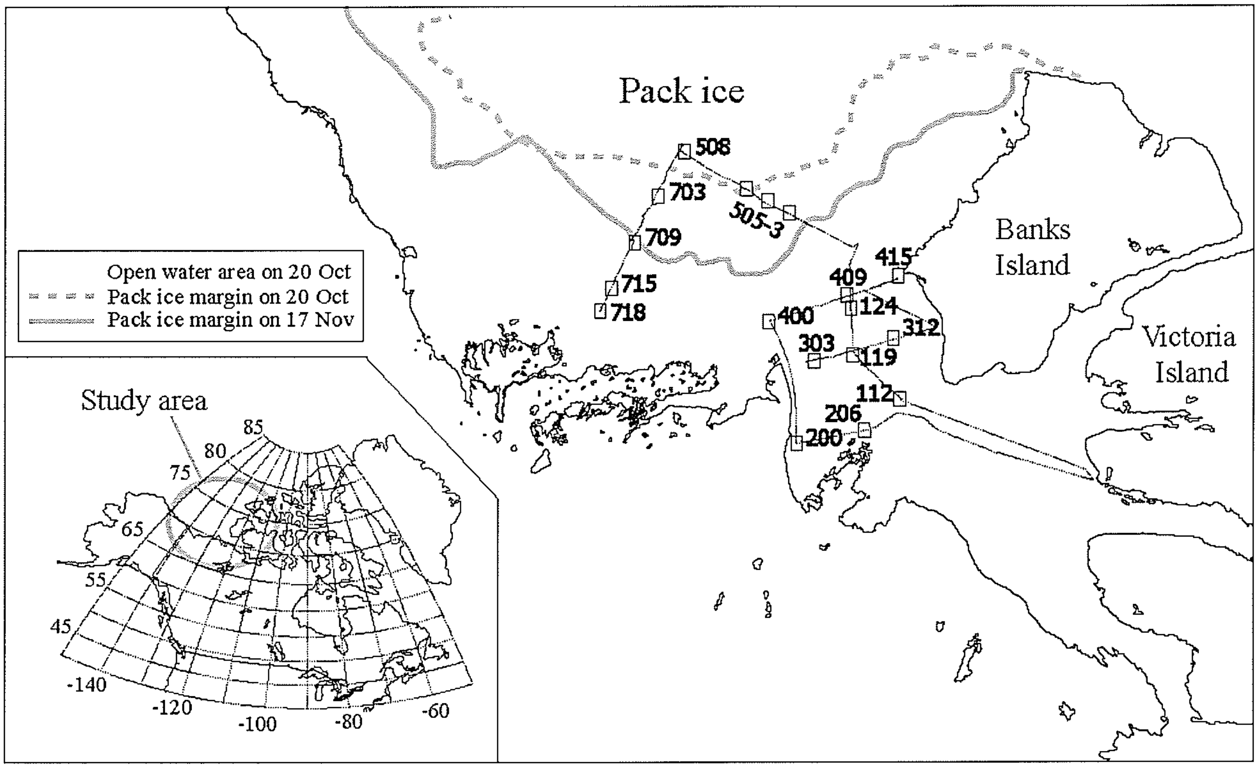

Figure 3.1. Map of the study area with sampling sites. The ice information is summarized from ice charts provided by Canadian Ice Service.

3.3.2 Data collection and analysis

The meteorological conditions were monitored throughout the experiment onboard the icebreaker. An automated station was located at the bow of the ship with sensors mounted 10 m above the foredeck, about 17 m above the sea level. Air pressure, temperature, wind speed and direction were recorded as 1-minute averages. Wind speed and direction were additionally monitored by the ship navigation system from sensors located above the wheelhouse roughly 30 m above sea level.

A total of 41 ice stations were visited as part of the field program. The sampling sites were chosen to be representative of the dominant ice types encountered in the area. The variability inherent to the sampling sites is illustrated in Figure 3.2b, which shows broken-up light nilas and grey ice floes during sampling at station 718 (19 October) with rafting evident where floes touched and dark nilas where they moved apart. However, sampling of deformed ice, such as rafted or ridged ice, was avoided. To access the very thin ice types, either a small air-ice boat (Figure 3.2a) or an "ice cage" lowered from the icebreaker was used. The air-ice boat enabled frequent sampling during a single launch of unaltered thin ice types at a sufficient distance away from the ships influence. During air-ice boat based sampling or immediately before or after ice cage operations, temperature-salinity-density casts were carried out onboard the icebreaker, providing near coincident observations of surface water salinity, S_w, and temperature, T_w.

At the ice stations, ice and water surface temperatures were obtained using a handheld temperature probe (Hart Scientific Model 1522). The manufacturer calibrated the instrument to a temperature accuracy of ±0.005 °C. For ice surface temperature, the probe was placed directly on the surface and shaded when necessary from direct solar radiation either by the air-ice boat or the observer. For snow covered ice, the surface temperature refers to the snow/ice interface temperature. For thicker ice, temperature profiles were measured immediately in the field from ice cores taken using a MARK II coring system (9 cm internal diameter, Kovacs Enterprise). This was done by drilling holes at specific depths towards the ice core center and inserting the temperature probe.

Figure 3.2. (a) The air-ice boat at station 508 on 23 October 2003. (b) Aerial photograph (by B.J. Hwang) of station 718 with *CCGS Amundsen* (length about 98 m). Ice floes were of light nilas or grey ice type while dark nilas and rafted ice are seen at the floe edges.

To determine ice salinities, 5 cm or shorter ice core sections were placed in airtight Ziploc plastic bags and melted overnight onboard the icebreaker. The conductivity of the melt water was measured using a handheld conductivity meter (Hoskin Scientific Cond 330i) and converted into salinity units using UNESCO 1983 algorithms (*Fofonoff and Millard*, 1983). Some brine drainage will have occurred during the process of cutting and bagging the samples, even though efforts were made for quick handling of ice samples. The reported salinities may thus to some extent underestimate the actual salinity and consequently the brine volume of the ice sheet under observation. To compare salinity profiles of sea ice with variable thickness and type, the midpoint layer depths of the ice slabs were segmented into top, middle and bottom one thirds of the total ice thickness. The exception to this normalization procedure was dark nilas, whose small thickness (< 5 cm) did not permit any subsampling. For surface salinity, a thin layer of the surface was scraped into a bag and determined as described above. When snow was present on the sea ice, snow samples were collected for salinity determination following the same approach as for sea ice. Layers in the snow were described categorically (if more than one was present, e.g., slush layer, new snow layer, intermediate layer). From the temperature and salinity profiles it was possible to estimate the brine volume fraction and the density of the sea ice using equations given in *Cox and Weeks* (1983) and *Leppäranta and Manninen* (1988). For these calculations the mid-layer temperature was used, as temperature profiles were nearly linearly increasing with depth. Furthermore, as densities were not measured directly, it was assumed that air volume fractions in the ice were negligible. This assumption is reasonable since thin newly formed ice has a high brine volume fraction and a small freeboard. However, using the above referenced equations, it can be found that a 1% increase in air volume fraction similarly results in a decrease of sea ice density by 1%.

Additional ice cores where taken from 31 of the sites. Two of the sites were of a consolidated pancake ice type and 2 cores per site were subsequently obtained. The cores were placed in plastic sleeves and brought back to the icebreaker for immediate storage at –20 °C until processed in the cold laboratory onboard the ship to determine sea ice microstructure. First, each core was divided into approximately 10 cm sections which were further cut vertically. The resultant slabs were attached onto glass plates for stability and planed down to 5 mm thickness, so-called thick sections, using a hand plane. Pictures of the general distribution of brine and air bubbles were taken from these vertical thick sections with a digital camera (Canon Powershot G2 4.2 mega-pixels). Higher resolution images of the inclusions were taken using a stereomicroscope (Leica MZ 7.5) with an adapter to the digital camera. The resolution of most images was roughly 320 pixels per mm. Once finished, the thick sections were further planed down to thin sections of about 1 mm thickness. Pictures of crystal structure were taken from the thin sections using a light table and cross- and parallel-polarized sheets with a macro setting on the camera. Additionally, horizontal thick and thin sections were selectively prepared similarly to the above description in order to further characterize the ice crystal structure. Size and shape statistics for crystals, grains and inclusions were calculated using image analysis software (ImageJ®). Detailed information of sea ice microstructure is important to understand its effects on radiative transfer within sea ice in optical (mainly through scattering processes) and microwave frequencies (dielectric properties) (e.g., *Light et al.,* 2003; *Grenfell et al.*, 1998). The circularity was defined as $4\pi A/P^2$, where A is the crystal/grain area and P the perimeter. A circularity of less than 1 indicates a deviation from a perfect circle. For grains and brine inclusions with a more regular elliptical shape, as is also the case for platelets, the aspect ratio, i.e., the ratio between the major and minor axis of the best fitting ellipse, is a good indicator of shape.

Using the air temperature record from the location of the icebreaker, the age of the ice at the time of sampling could be roughly determined. The time since formation, t, was estimated by subtracting the change of ice thickness, h_i,

$$\Delta h_i = \frac{k_i}{h_i \rho_b L}(T_w - T_a)\Delta t \tag{3.1}$$

for each time step Δt (1-minute averages) until $h_i = 0$ (*Leppäranta*, 1993), where ρ_b is the sea ice bulk density, v_b the brine volume fraction, and T_w and T_a the seawater and air temperatures, respectively, and k_i the thermal conductivity of the ice. The thermal conductivity was calculated using the exponential regression suggested by *Yen* (1981). ρ_b was estimated as a function of h_i using the regressions for v_b shown in section 3.4. The latent heat of fusion, L, was kept at 333.9 kJ kg^{-1}. The above equation is a simplification as it assumes congelation ice growth, a constant T_w during the ice growth, that T_a observed onboard the ship was representative for a larger area, no oceanic heat flux and no snow cover. Nevertheless, estimates that serve for a qualitative comparison with salinity data were obtained. Furthermore, a linear temperature profile through the ice is assumed, however, regressions through available points in temperature profiles verified that the assumption of linearity explained more than 95% of the variation for $h_i < 0.2$ m.

Surface-leaving spectral reflectance was measured at the ice stations using a dual-headed spectroradiometer (FieldSpec, Analytical Spectral Devices Inc., Boulder, Colorado). The instrument measures radiation in the wavelength region 350-1050 nm simultaneously with two separate fiber optic probes. Instrument calibration was performed by the manufacturer prior to the investigation using a NIST traceable light source that is guaranteed to be accurate to 1-2% in total irradiance. The random error in the calibration was estimated to be within 0.5% over the spectral range in use. Upwelling spectral radiance ($L_{\uparrow\lambda}$) was measured from nadir using a 25-degree field-of-view fore optic and compared against a white reference plate (Labsphere Spectralon) with known reflectance properties. Coincident cosine corrected downwelling irradiance measured using the second fiber optic probe was used to correct for changes in the incoming spectral irradiance ($F_{\downarrow\lambda}$). The surface-leaving spectral reflectance (ρ_λ) was thus calculated as

$$\rho_\lambda = \frac{L_{\uparrow\lambda} \cdot F_{\downarrow\lambda}^{wr}}{L_{\uparrow\lambda}^{wr} \cdot F_{\downarrow\lambda}}, \tag{3.2}$$

where the superscript *wr* denote spectra obtained from measurements of the reference plate. If the surface was lambertian, i.e., $L_{\uparrow\lambda}$ independent of viewing angle, then ρ_λ would be identical to the surface albedo. This is a reasonable approximation for snow covered ice and/or under overcast sky conditions when $F_{\downarrow\lambda}$ is largely diffuse (*Perovich*, 1996). The wavelength-integrated reflectance (ρ) was calculated from ρ_λ as

$$\rho = \frac{\int \rho_\lambda F_{\downarrow\lambda} d\lambda}{\int F_{\downarrow\lambda} d\lambda}, \tag{3.3}$$

where the integration limits are 350 and 1050 nm. The percentage of incident shortwave irradiance above 1050 nm is around 10% during overcast conditions and is not accounted for in the present calculation of ρ (*Allison et al.*, 1993).

3.4 Results and Discussion

3.4.1 Environmental conditions and ice observations

Various types of sea ice with thicknesses ranging from 0.01 to 0.45 m were sampled during the investigation. These are categorized based on the commonly used *World Meteorological Organization* (1985) nomenclature. New ice is a weakly or non-consolidated collection of ice crystals which usually include frazil ice and grease ice. Once consolidated, nilas (0-0.10 m thick) is formed, which is further classified into dark nilas (0-0.05 m) and light nilas (0.05-0.10 m). When the ice sheet becomes thicker than 0.10 m the ice is classified as young ice. Young ice includes grey ice (0.10-0.15 m thick) and grey-white ice (0.15-0.30 m thick). Recently formed sea ice thicker than 0.30 m is termed first-year sea ice. The special case here is pancake ice which is formed as a result of wave action. Based solely on thickness, pancake ice may be classified to belong to either the nilas or the young ice types.

During the first two weeks of observations in late October (YD 292 to 306) a total of 31 ice sampling sites were visited (Table 3.1, stations 718A to 206B). The Canadian Ice Service (CIS) ice charts for YD 293 and 300, also show a mixture of new ice, nilas, grey ice and grey-white ice in the area. Air temperature remained around –2 to –4 °C during the first week with wind speed of about 5 m/s (Figure 3.3). However, colder temperatures had prevailed during the previous week (see Figure 3.3). Light snowfall was observed on YD 293, 294, 295 and 298, however, the amount of snow accumulated on the ice was small and quickly merged with the brine-wetted surface forming a soft surface slush layer.

Table 3.1. Bulk physical properties at the ice stations.

Station	718A	718B	718C	718D	715A	715B	709A	709C	703B	703C	703E	703F	508A	508B	508C	508D	505	504_p	504_c	503_p	503_c	124A
YD	292	292	292	292	293	293	294	294	295	295	296	296	296	296	296	296	297	297	297	298	298	299
UTC	1840	1915	1930	2001	1847	1919	1824	1908	2327	2335	0029	0051	1940	2020	2045	2130	1840	2218	2218	0147	0147	2009
T_s	-1.7	-1.6	-2.4	-2.4	-2.1	-2.1	-2.2	-2.1	-2.3	-3.8*	-3.2	-2.8	-3.7*	-2.5*	-3.4*	-4.2*	-3.9	-4.8	-4.8	-5.2	-5.2	-3.3
T_w	-1.1	-1.1	-1.1	-1.1	-1.1	-1.2	-1.3	-1.4	-1.4	-1.4	-1.5	-1.6	-1.4	-1.4	-1.4	-1.4	-1.5	-1.5	-1.5	-1.5	-1.5	-1.5
S_w	20.9	20.9	20.9	20.9	21.4	21.4	25.6	25.6	25.9	25.9	25.9	25.9	26.7	26.7	26.7	26.7	27.0	27.6	27.6	27.9	27.9	25.3
S_s	19.9	16.9	20.0	20.4	13.7	18.3	21.9	7.4		16.5	19.5	19.9	26.7				23.4	10.6				17.6
S_b	5.8	5.5	6.4	4.2	5.8	5.3	6.0	5.1	16.3		6.8	6.8	7.5	9.0	6.3	6.3	3.5	4.8	4.4	5.1	4.2	6.2
ν_b	.204	.200	.181	.119	.187	.162	.171	.144	.459		.140	.124	.131	.231	.127	.108	.064	.074	.068	.073	.060	.129

Station	124B	124C	124D	124E	124F	119	112A_p	112B_p	112C_p	112C_c	206A	206B	200A	200B	200C	200D	200E	400	409_p	409_c	415	312	303
YD	299	299	299	299	299	300	301	301	301	301	305	305	308	308	308	308	308	309	310	310	311	315	317
UTC	2029	2046	2100	2140	2200	1807	1600	1610	1620	1620	1530	2035	1840	1900	1930	2015	2045	1730	1900	1900	1715	1815	2000
T_s	-3.6	-3.2	-3.3	-3.3	-2.1	-4.2	-4.1*	-2.2*	-4.4	-4.4	-2.4	-2.9	-5.2	-4.6	-2.5	-5.0	-7.2	-4.0	-3.4	-3.4	-2.9	-10.3	-7.2
T_w	-1.5	-1.5	-1.5	-1.5	-1.5	-1.4	-1.3	-1.3	-1.3	-1.3	-1.5	-1.5	-1.5	-1.5	-1.5	-1.5	-1.6	-1.3	-1.4	-1.4	-1.4	-1.5	-1.4
S_w	25.3	25.3	25.3	25.3	25.3	25.7	27.4	27.4	27.4	27.4	28.3	27.6	27.3	27.3	27.3	27.3	27.3	27.6	27.0	27.0	27.1	27.5	27.5
S_s	16.0	19.3	19.9	12.1	17.7	23.6	13.9		28.7		7.8	26.2	39.0	28.0	16.8	40.0	31.9		18.0			37.6	25.6
S_b	6.5	5.9	7.5	6.5	14.7	7.2	2.8	5.1	5.2	4.9	3.2	5.5	11.1	10.5	5.1	12.0	10.2	3.3	4.1	5.1	3.7	4.6	4.8
ν_b	.126	.126	.155	.134	.433	.126	.050	.148	.089	.083	.084	.118	.165	.169	.125	.185	.115	.061	.085	.108	.084	.039	.054

Symbols (and units) are as follows: YD, year day; UTC, universal time (hours minutes); T_s and T_w, surface and seawater temperatures (° C), respectively; S_w, S_s and S_b, surface seawater, ice surface and bulk ice salinities (PSU), respectively; and ν_b, brine volume fraction. T_s values marked with '*' denote estimates using Eq. 3.4.

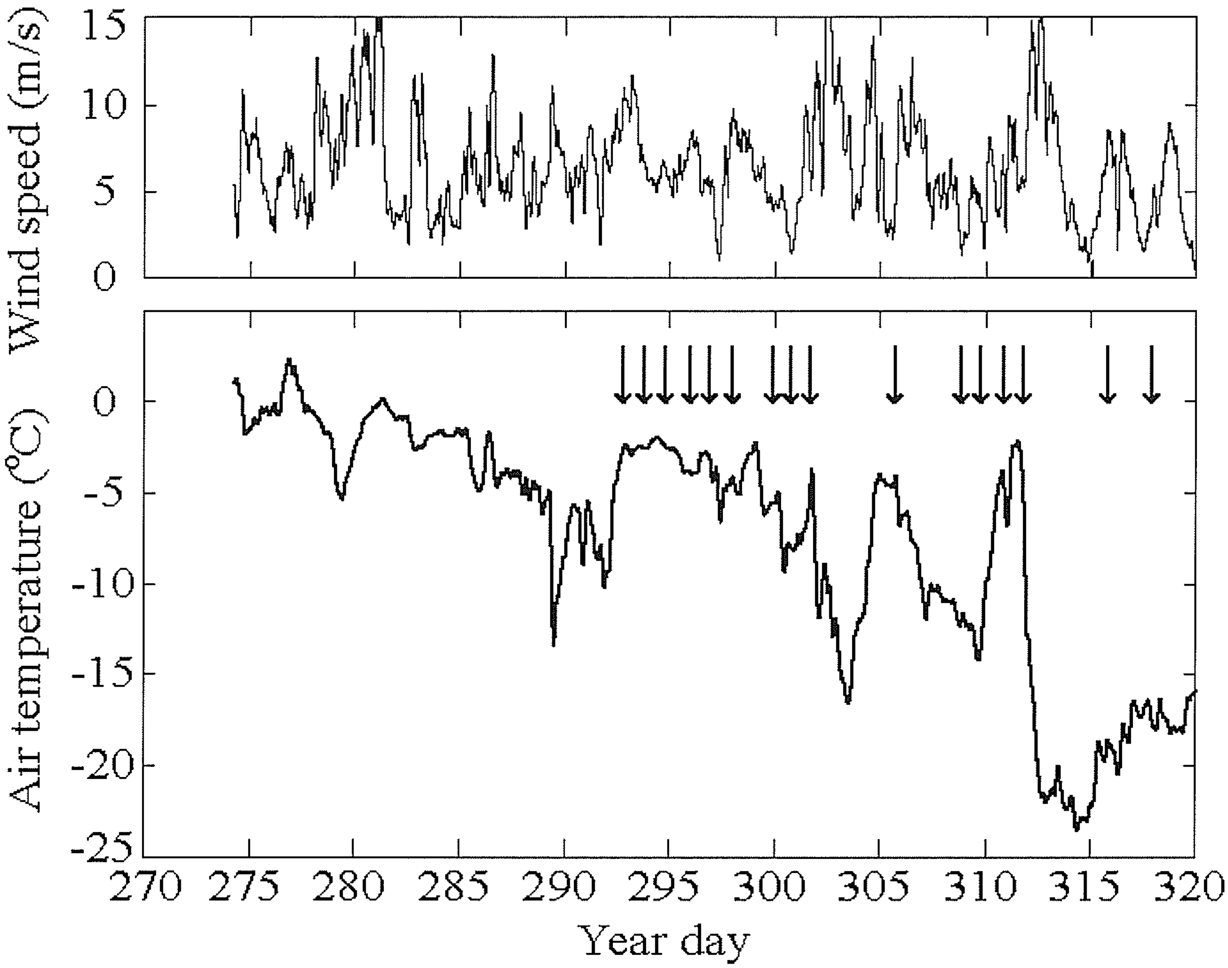

Figure 3.3. Temporal trends of wind speed and air temperature observed onboard the ship. A 3-hour moving average was applied on the data. The wind speed was additionally corrected for ship motion. The arrows indicate the times when ice samples were collected.

Sudden changes in air temperatures and wind speeds occurred during the second week. Temperatures decreased to –16 °C on YD 303 (Figure 3.3) and later again increased briefly to as high as –1 °C on YD 305. Frequent snowfall events were observed throughout the week and the snow cover accumulated to significant thickness on the predominantly grey and grey-white ice types (Figure 3.4, stations 206A and B). On nilas ice a slush layer quickly formed when snow merged with the surface brine.

During the third week of the observation (YD 307 ~ 313), 8 sites (stations 200A to 415) were visited. Grey and grey-white ice were dominant on the CIS ice chart for YD 310. The air temperature decreased to –14 °C on YD 309 and again rose to –2 °C on YD 311 (Figure 3.3). Snowfall was frequent during the week.

From then on, air temperatures decreased below –15 °C. These cold air temperatures quickly thickened the ice cover. The CIS ice chart for YD 314 shows that the dominant ice types were grey-white and thin first-year ice. This ice was predominantly snow covered. Low light levels and temperatures limited the sampling opportunities and as a result only two sites (stations 312 and 303) were visited during the late stage of the experiment.

A high salinity surface layer was commonly observed during the investigation (Table 3.1). According to *Perovich and Richter-Menge* (1994) the presence of a surface brine layer is essential for the formation of frost flowers. The surface brine layer can have a salinity in excess of 100‰. The brine is a source of water vapour that nucleates into frost flowers above small roughness protrusions on the ice surface.

Frost flowers were first observed on YD 296 at station 508, which was the station closest to the multi-year ice pack. This was surprising as air temperatures remained close to –4 °C. Substantially lower temperatures have prevailed during previous investigations (*Martin et al.*, 1995; *Perovich and Richter-Menge*, 1994). Most likely these frost flowers had formed sometime around YD 287-291 when colder air temperatures prevailed. Temperatures down to –14 °C were observed at the icebreaker's location (Figure 3.3). Particularly the 2 m air temperatures obtained from National Centers for Environmental Prediction/National Center for Atmospheric Research (NCEP/NCAR) reanalysis data nearest to station 508 showed temperatures as low as –17 °C on

YD 291 (data not shown here). For the same time, NCEP data shows an 80 Wm^{-2} net loss of longwave radiation from the surface, relative to 50 Wm^{-2} on YD 296, due to thin and high clouds. The prevalence of a thin cloud cover could also be confirmed by visually inspecting MODIS RGB images. The surface of the thicker grey-white ice, i.e. 508A and D (Figure 3.4), had an about 10-mm-thick slush layer beneath the frost flowers. The frost flowers appeared as clumps that had partly merged together resulting in an areal coverage of about 50-60%. Station 508C (h_i = 0.14 m) did not have a distinct slush layer present and the areal coverage of frost flowers was about 10-15%. These frost flowers had formed into about 100 mm^2 clumps with needle-like protrusions (order of 10 mm long). The 0.05-m-thick ice sampled at station 508B did not have frost flowers present, however, the uneven, slushy surface suggested that an earlier presence of frost flowers was possible.

During the second and third week frost flowers were often sited from the ship, however, the next sampling opportunity occurred at station 200 in Franklin Bay on YD 308. At this time, lower air temperatures prevailed (-12 °C). The areal coverage of frost flowers on the bare light nilas (stations 200A and D) surfaces were around 50-70% and for the dark nilas (200B and E) which had a coverage between 1-5%. The appearance of the ice surface for dark nilas was not unlike that of station 508C. Frost flowers formed distinct clumps, 10-100 mm^2 in size, with small needle-like protrusions extending roughly 10 mm above the surface. On the light nilas, frost flower clumps had merged into clusters of 1-10 cm^2 sizes. The thicker ice was mostly snow covered (Figure 3.4).

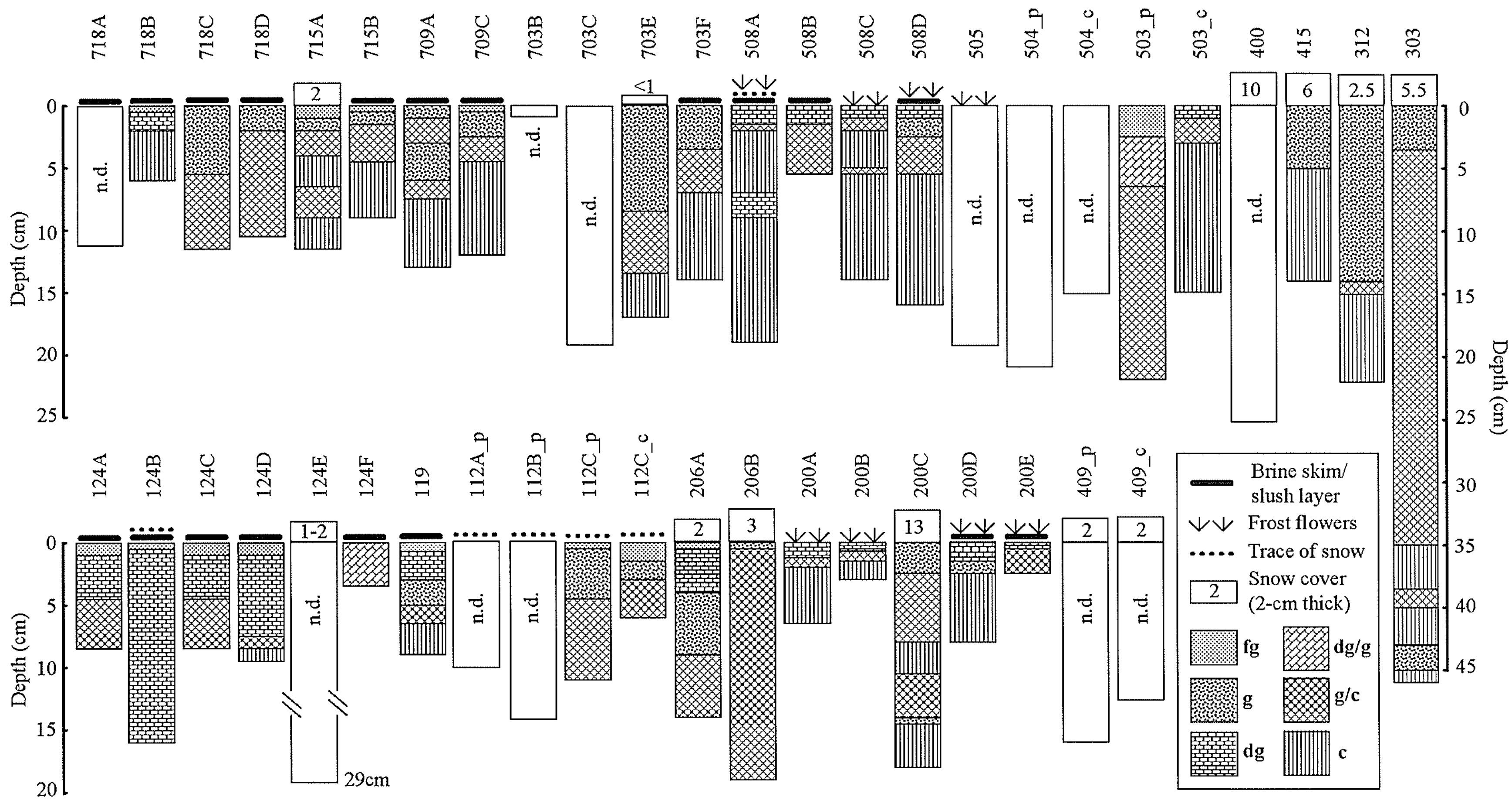

Figure 3.4. Summary of ice thicknesses, surface conditions and ice core stratigraphies. Textural features include: fine-grained granular ice (**fg**); disc-like granular ice (**dg**); mixture of disc-like and orbicular granular ice (**dg/g**); orbicular granular ice (**g**); intermediate granular/columnar ice (**g/c**); and columnar ice (**c**). Station 508A had a complex surface with slush, nearly melted frost flowers and small traces of new snow; station 200C had 0.09 m of new snow above 0.04 m of slush; station 415 had a 0.04 m new snow layer above 0.02 m of slush; and station 303 had 0.035 m of new snow above 0.02 m of old snow.

3.4.2 Textural characteristics of the sea ice

The undeformed ice typically consisted of orbicular granular ice (**g**) at the top portion of the ice cover, and a gradual shift into columnar ice (**c**) with increasing depth. The zone of transition between these two ice types, showing properties of both, is termed intermediate granular-columnar ice (**g/c**). Often the uppermost part of the ice column was characterized by a distinct layer of a more fine-grained variant of granular ice (hereafter termed **fg**). The above classification follows that by *Eicken and Lange* (1989) (see their Table 3.1) with the addition of the more specific granular ice types **fg** and **dg** (disc-like granular ice; described below). These textural features are summarized in Figure 3.4 for all ice samples collected. The large variability in thickness and texture of the ice samples highlights the highly variable growth conditions and formation mechanisms of the sea ice in the area. Apart from the pancake ice samples and station 508A (were rafting appeared to have occurred when the ice was approximately 0.07 m thick) all sampled sea ice were undeformed. The portion of granular ice (i.e., **fg**, **dg**, **dg/g** and **g**) for all the ice structure samples ranged between 2.6% to 100%, with an all-sample (a total of 4.22 m of core was examined for texture) combined mean of nearly 33%. The portions of **g/c** and **c** were about 37% and 30%, respectively.

The ice core sampled at station 124A on YD 299 illustrates a nilas structural classification (Figure 3.5). The **fg** surface layer is likely formed partly out of snow (i.e. snow-ice), however, oxygen isotope analysis was not conducted to confirm these observations. The **fg** grain size ranged from undetectable to roughly 1.6 mm^2, causing the texture to appear opaque and white. Occasional grain inclusions of up to 4 mm^2 were found. The sizes and shapes for the ice textural types for all analysed cores are compiled in Figure 3.6 where crystal properties are weighted by the total measured area in order not to skew observations towards the smaller, more numerous crystals. Detectable **fg** grains were rounded with diameters and circularities averaging 0.72 mm^2 and 0.71 (unitless), respectively.

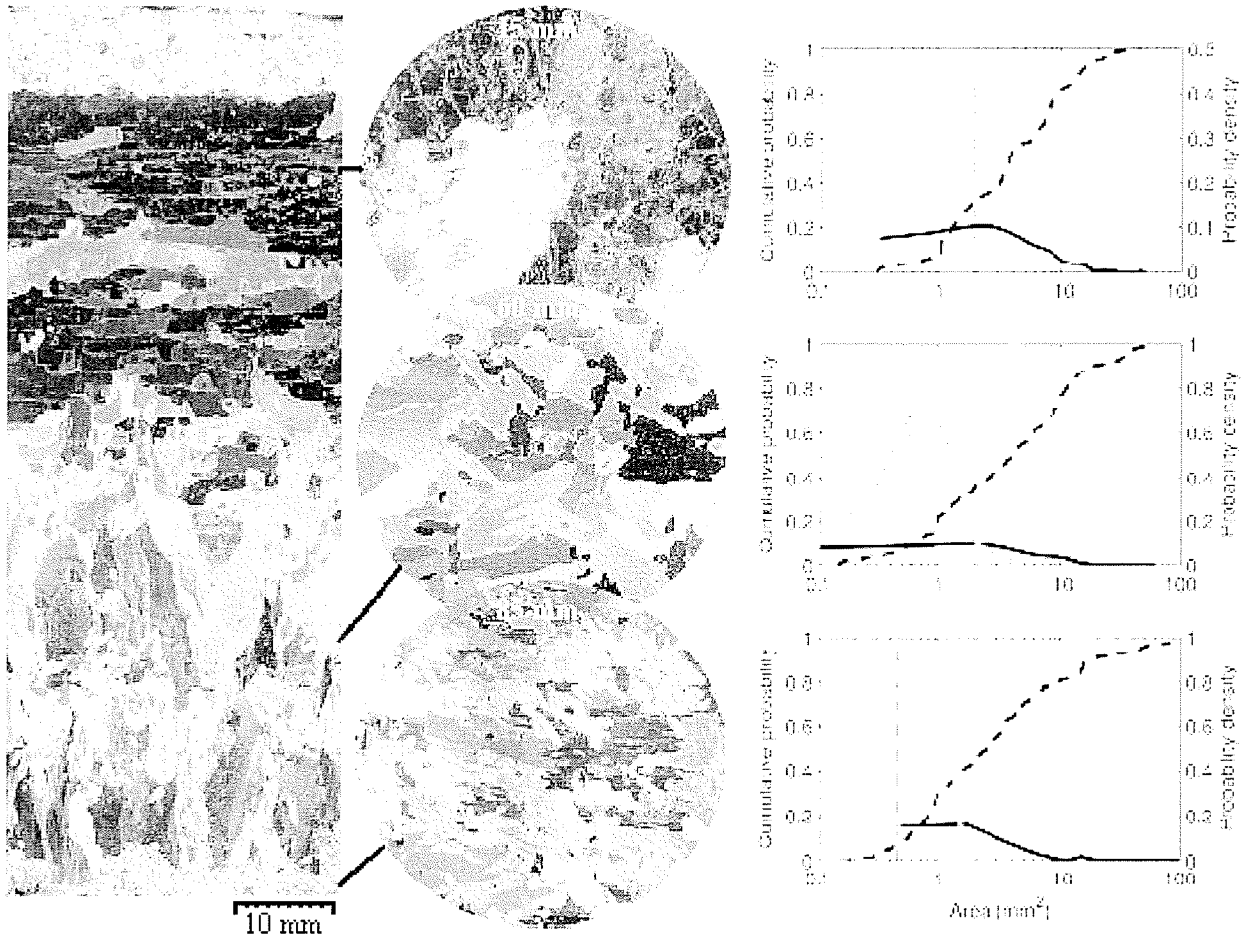

Figure 3.5. Example of vertical (left) and horizontal (middle) thin sections of nilas ice taken at station 124A on 26 October (YD 299), with associated graphs of crystal (black) and platelet (gray) size distributions (dashed lines are cumulative probability, while solid lines are the probability density) at 15, 60 and 85 mm depths, respectively. The vertical dashed lines are the brine layer spacing with millimeter as a unit.

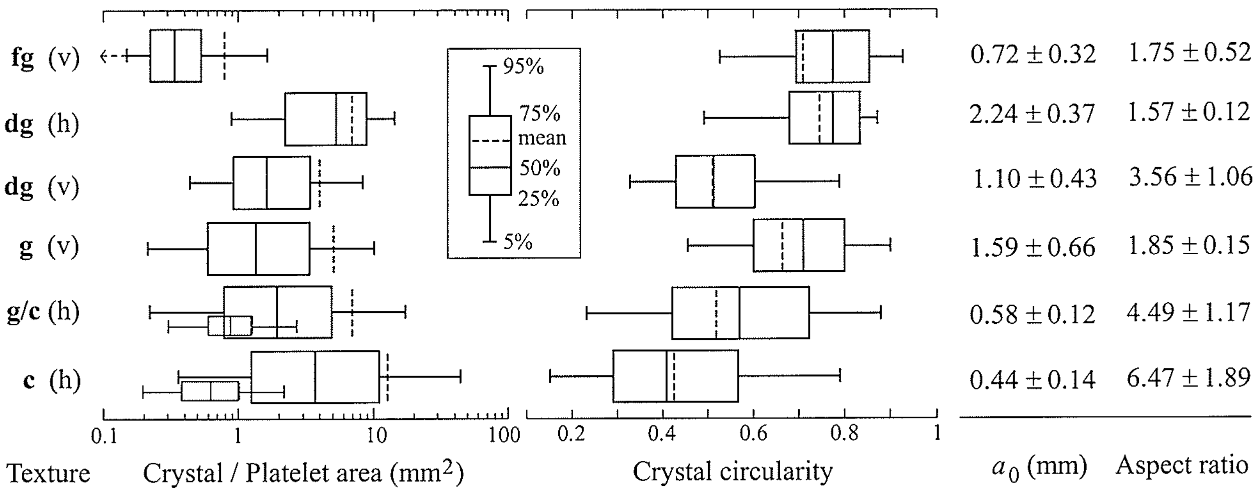

Figure 3.6. Crystal and platelet size and shape for textural types based on thin section analysis. The smaller size box plots are for platelets in c and g/c ice types. The parenthesis shows the thin section orientation; v for vertical, h for horizontal. The tabulated values (mean ± standard deviation) for the brine layer spacing, a0, and the aspect ratio are calculated from the major and minor axis of a best fitting ellipsoid to platelets and crystals (in case of granular ice). Analysis of **fg** was conducted for grains between 0.1-4.0 mm2; the arrow towards left indicates that smaller grain sizes were not detected and the sample looked opaque between cross-polarized sheets. Stations starting from 124A (YD 299) had **fg** areas < 1.2 mm2.

The granular ice observed at depths between about 1 and 4 cm in Figure 3.5 show disc-like crystals, i.e., horizontally elongated crystals that appear rounded in shape when viewed from above. Henceforth, this ice will be called disc-like granular ice (**dg**). Disc-like granular ice was commonly observed in many of the ice samples (Figure 3.4). The graphs on the right-hand side in Figure 3.5 show the grain size distribution for three depths from station 124A. For this sample the median **dg** grain size at 15 mm depth was about 2.5 mm^2. For all samples, **dg** grain widths ranged roughly 1-6 mm and areas 0.4-10.5 mm^2 with circularities averaging 0.74 (Figure 3.6). The largest observed grain was 12 mm wide. Vertical layer thicknesses, which in Figure 3.6 are identical to the brine layer spacing for **dg** (h), ranged between 0.2 and 3.9 mm averaging 1.1 mm.

It is noteworthy that **dg** was present at the ice surface for all ice samples with frost flowers, while a surface with a slush layer (e.g., station 124A) or a snow cover related to **fg** and **g** structure (Table 3.1 and Figure 3.4). This further supports that **fg** indeed was snow-ice. The correspondence with frost flowers suggests that **dg** may to some extent result from upward brine expulsion and consequent freezing of brine on the surface. This may be supported by observations of an increase in brine skim and frost flower salinities and that more brine came to the ice surface with decreasing temperatures (*Martin et al.*, 1996). Furthermore, *Martin et al.* (1995) found that once clusters of frost flowers formed on the ice surface, the slushy layer beneath them slowly grows in thickness. On other instances, **dg** seems more reasonably related to frazil ice consolidation at the surface, e.g. stations 124A-D (Figure 3.4).

On the bottom half of the ice sample, congelation ice growth dominated resulting in **g/c** and **c** ice types. The bottom 40 mm in the vertical thin section from station 124A (Figure 3.5) gives an example of the **g/c** ice type and possibly **c** for the bottommost 10 mm. In general for the ice samples, **g/c** and **c** crystal sizes averaged 7.0 mm^2 and 12.8 mm^2, respectively, with type-specific size distributions shown in Figure 3.6. The platelet substructure was clearly seen in these crystals. Towards the bottom, both ice crystals and platelets became more aligned in the horizontal direction. This process of horizontal alignment is suggested to be related to under-ice currents (*Weeks and Ackley*, 1982). Furthermore, platelet widths decreased with depth as is typical (*Weeks and Ackley*, 1982). In the 124A sample the platelets widths decreased from 1.98 mm to 0.59 mm and to 0.45 mm at the 1.5, 6 and 8.5 cm depths, respectively (Figure 3.5).

The sampled consolidated pancake ice had pancakes that were 5-8 cm thicker than the surrounding ice and characterized by their elevated rims. In addition, the pancake ice structure was much different from the surrounding ice, indicating different growth conditions during formation. This is illustrated most distinctly by the vertical thin sections of pancake ice from station 503 on YD 298 and the ice grown just outside of the pancake (labelled by '_p' and '_c', respectively, after station number in Figure 3.4). Within the pancake ice growth had been very dynamic resulting in granular or very irregular crystals. However, outside of the pancake, growth occurred during calm conditions with predominantly columnar ice as a result.

3.4.3 Inclusion microstructure

An attempt to characterize the brine and air inclusions from thick sections was done from high-resolution images. The main limitation in the method is that ice samples need to be processed in a freezer room at temperatures close to –15 °C. The temperature of the thin ice is, however, near the freezing point of seawater. Because there are strong temperature-dependent changes on brine volume (*Light et al.*, 2003), the decrease in ambient temperature from near the freezing point will significantly reduce the brine volume within the ice. The reduction in brine volume results not only in the shrinking of inclusions, but also inclusions with high aspect ratios, such as brine tubes, fractions into many smaller pockets, thus changing inclusion number densities (*Light et al.*, 2003). It also facilitates the formation of a high-salinity layer on the ice sample surface, indicating that interior brine is removed through brine expulsion during storage and processing. Thus for the newly formed, thin ice samples under study, a detailed description of brine inclusions was found unrepresentative of the natural state of the newly formed sea ice.

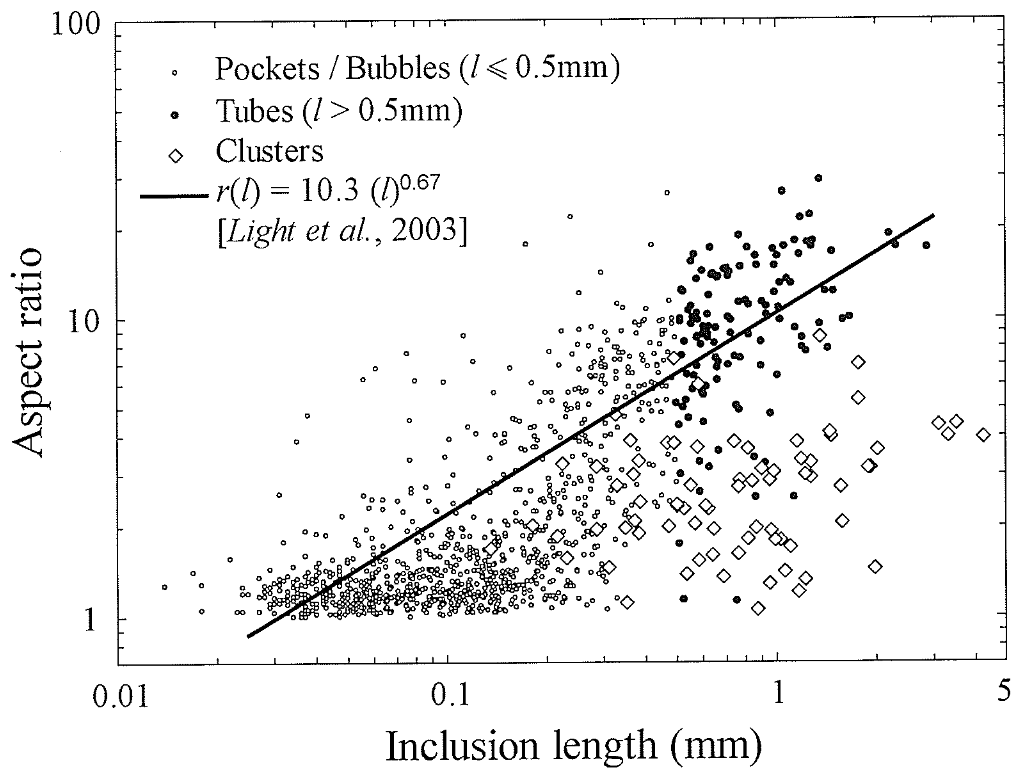

Figure 3.7. Aspect ratio (major to minor axis of best fitting ellipse) versus inclusion length (major axis) measured for inclusions seen in three complete ice cores (stations 718, 124A and 415) at approximately –15 °C. Collections of indistinguishable brine tubes, channels and pockets are referred to as clusters.

Nonetheless, since data on inclusions in newly formed sea ice are limited in the literature, results obtained from analysis of vertical thick sections of three ice cores (stations 718, 124A and 415) at temperatures close to –15 °C are presented in this section. These samples may provide insight into changes that can occur in structure with further ice growth and colder winter temperatures. Prior to freezer room processing, the cores were stored at –20 °C. A total of 1088 inclusions were identified. It was extremely difficult to distinguish between air bubbles, brine pocket and tubes. Some of the brine inclusion may additionally have drained after sample retrieval forming air inclusions. Therefore, the analysis followed *Light et al.* (2003) and did not separate between brine and air inclusions, and classified everything with a major axis longer than

0.5 mm to be brine tubes. In general, brine pockets/air bubbles were mostly contained within what appeared to be frozen brine tubes; i.e., high aspect ratio tubes appeared to have been broken into strings of lower aspect ratio inclusions. The diameters of these inclusions were representative of brine tube diameters which were found to range from 0.014 to 0.2 mm (corresponding to an area of 0.07-1 mm^2). However, brine pockets with diameters down to the detection limit of about 0.004 mm were observed. Brine tube lengths (major axis) were found to be shorter than 3 mm (Figure 3.7).

The aspect ratio (r) of the inclusions increases with the major axis length (l) of the best fitting ellipse roughly following the power law $r = 7.95\ l^{0.65}$. This regression is in close agreement with the power law reported by *Light et al.* (2003) for the interior part of first year ice (Figure 3.7) indicating that inclusion sizes in sea ice are mostly determined by brine phase changes related to temperature. That is, the decrease in ice temperature introduced by sample storage resulted in inclusions with sizes and shapes similar to colder first year ice. The large number of very small air bubbles/brine pockets, whose aspect ratios tend towards unity in this analysis due to image resolution, may explain the difference in the regression. Additionally, the regression line underestimates r when $l > 0.3$ mm, and when considering $l > 0.1$ mm a steeper linear expression $r = 11.6\ l$ ($r^2 = 0.62$) appears to better explain $r(l)$. Because we were not able to precisely measure the thickness and to focus the microscope at all "depths" of the thick section, we were not confident in reporting on inclusion number densities. Basically, for number density estimation the thick sections were optically too thick. Furthermore, a large part of the brine was concentrated in clusters consisting of a complex and interconnected structure of tubes, pockets and bubbles. These clusters and brine pockets may appear very different when observed at temperatures near the seawater freezing point. The microstructure of the newly formed ice, at their *in situ* temperatures, may thus be better represented by a collection of interconnected tubes merging into cluster-sized large pockets.

Instead, temperature related changes in brine volume may be calculated from measurements of temperature and salinity (*Cox and Weeks*, 1983). These give an estimate of the overall porosity of an ice sample with the brine concentrated at boundaries between ice crystals and grains. Furthermore, some of the microstructure parameters important for interpreting, e.g., remote sensing data over sea ice, such as brine layer spacing (platelet width in columnar ice) and crystal size and shape, are less sensitive to a temperature change of the sample associated with freezer room processing. Significant retexturing may, however, occur if the temperature of the sample is again increased after storage (*Perovich and Gow*, 1996).

3.4.4 Relationships with ice thickness and salinity

Large variability in salinity was observed among the ice samples (Figure 3.8). The number of samples for each ice type, their bulk salinities and thickness, can be deduced from Figure 3.4 and Table 3.1. Surface and bottom salinities were higher than at the middle of the ice cover, and a general C-shape is evident in the profile. The salinity data show a gradual decrease in salinity as the ice becomes thicker. When the ice is 1 cm thick, a salinity of up to 16.3‰ was obtained (see Figure 3.9b). The average for four dark nilas samples with thicknesses between 1 and 3 cm was 12.9‰. Light nilas salinity is also somewhat higher at all depths compared to thicker ice types. The measured salinities for dark nilas are comparable to observations by *Smedsrud and Skogseth* (2006) of about 12-15‰, however, their light nilas salinities are somewhat higher (about 9-14‰) likely due to their higher water salinities and lower air temperatures.

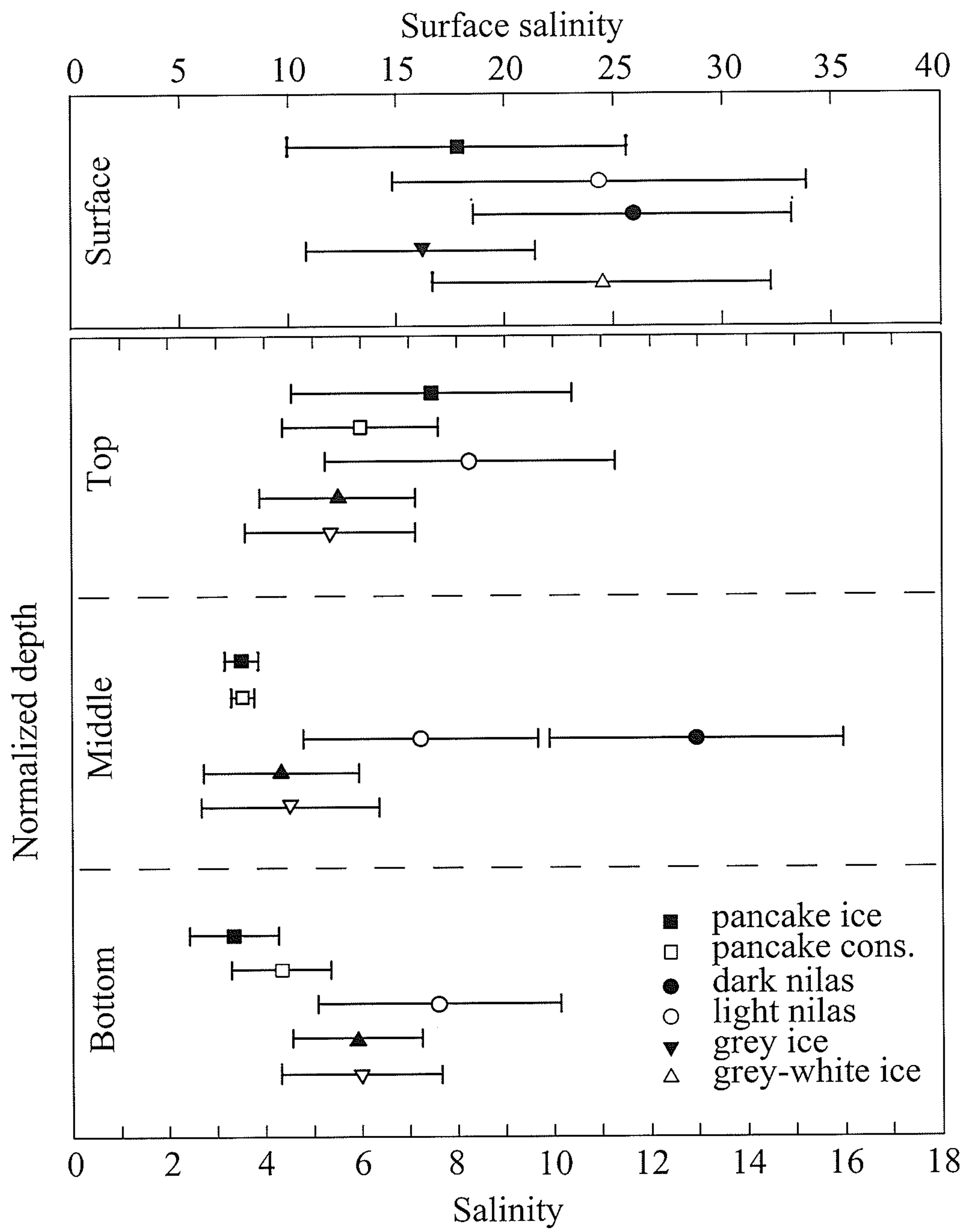

Figure 3.8. Surface salinities and normalized salinity profiles for the encountered ice types. Horizontal error bars show the standard deviation.

For thicker ice, interior salinities as low as 1.6‰ were observed. This low salinity sample was taken at station 505 that is located close to the pack ice margin (Figure 3.1). Previously melted pack ice may thus have contributed to the low values, although salinity profiles obtained at the icebreaker location did not indicate fresher surface waters. The pancakes and their consolidated surrounding tended to have lower bottom salinities, but with comparable or higher salinities at the surface. However, the obtained data does not fully explain the observed variability from age, ice thickness and formation processes. Ice samples were collected within a large area over 25 days, and ice formation was subject to variable hydrographical and meteorological conditions.

Observed surface ice salinities (S_s) ranged between 7.4 and 40‰, with an all-sample average of 21‰ (Table 3.1 and Figure 3.8). For nilas ice, a significant relationship between ice thickness (h_i) and S_s was found: S_s = 14.74 -1.03h_i (r^2 = 0.68, p-value < 0.05), where h_i is in centimetres, showing a decreasing trend with ice thickness. However, for all samples the correlation was weak and no significant differences were observed between ice types (Figure 3.8). The large variation in S_s is partly due to differences in surface properties of the ice, e.g., snow-covered versus bare ice. As snow falls on the surface, it melts into and dilutes the surface brine layer and a saline slush layer forms. On the other hand, a significant, although weak, relationship was found with air temperature: $S_s = 13.74 - 1.12T_a$ (r^2 = 0.39, p-value < 0.05), showing higher surface salinities at lower air temperatures. This relationship can be explained by enhanced brine expulsion to the surface as ice temperatures decrease, while increasing temperatures cause the surface to melt and thus lower salinities.

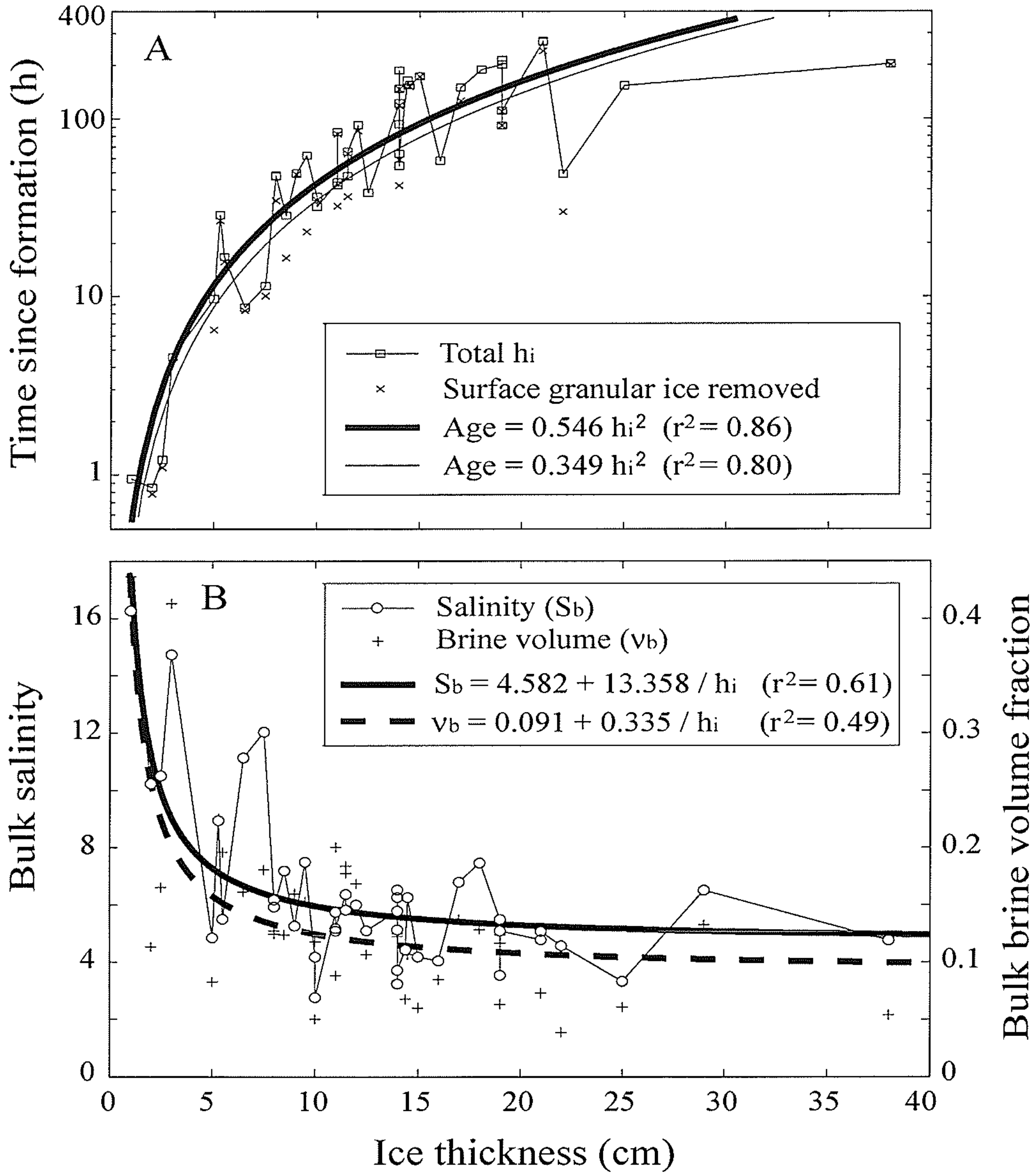

Figure 3.9. Relationships of (a) estimated age with (thick line) and without (thin line) surface granular ice, and (b) bulk salinity and bulk brine volume versus ice thickness. Equations for statistically significant (p-value < 0.001) regression curves are given in the legends.

In general, as the ice becomes thicker, the bulk salinity decreases (Table 3.1 and Figure 3.9b). Here, the term 'bulk' refers to the average value for the entire ice core. The best correlation was found by the inverse regression S_b = 4.582 + 13.358/h_i (r^2 = 0.605, p-value < 0.001), which is similar in its form to the one used by *Kovacs* (1996). *Shih* (1998) observed a linear desalination rate of $S_b = 16.0 - 0.53h_i$ for ice less than 10 cm thick. The bulk salinity for the ice in this study is lower, and the desalination is faster: $S_b = 14.3 - 0.95h_i$ ($r^2 = 0.53$).

The associated bulk brine volume fractions (v_b) and sea ice bulk densities (ρ_b) calculated using equations by *Cox and Weeks* (1983) and *Leppäranta and Manninen* (1988) resulted in the following regression: $v_b = 0.090 + 0.333/h_i$ ($r^2 = 0.507$, p-value < 0.001). The obtained v_b ranged from 4% to 46% and is linked to the ice temperature and hence closely related to ice thickness and air temperature (Table 3.1). As the thin ice was very porous, the contribution of air inclusions to the overall porosity of the ice was assumed negligible. The sea ice bulk density could be empirically linked to the brine volume fraction simply as $\rho_b = 0.918 + 0.104v_b$ ($r^2 = 0.98$).

With the prevailing T_a at the icebreaker location, calculations using Eq. 3.1 suggest that the ice initially grew with a rate of about 1-3 cm h^{-1} and as the ice grew thicker the rates dropped below 0.5 cm h^{-1} (Figure 3.9a). A 0.2 m ice thickness was reached after about 2 days. Granular ice may however form rapidly when grease ice consolidates. Calculating the age by only considering congelation growth of **c** and **g/c** did not significantly alter the estimates (Figure 3.9a) suggesting that the more slow congelation growth dominated the age and that granular ice formation occurred relatively quickly. However, when considering the difference between T_a and T_s by means of a transfer coefficient, K_a, in a flux balance relation (*Leppäranta*, 1993)

$$K_a(T_a - T_s) = k_i/h_i\,(T_s - T_w)\,, \tag{3.4}$$

estimated ages approximately doubled, resulting in the T_a record not being sufficiently long for some samples. K_a for an ice thickness range $0.01 \le h_i \le 0.4$ m was obtained from fitting field data as $K_a = -3.53 + 1.65/h_i$ ($r^2 = 0.70$). These expressions assume that K_a mostly depend on h_i and T_a, however, atmospheric conditions also have an effect which is neglected here. Overcast sky conditions generally dominated in the sampling region during the fall period. Furthermore, temperature-salinity-density casts from the icebreaker revealed that there was substantial heat (J/m2) stored within a still-intact mixed layer at almost all the stations (unpublished data). The effect of oceanic heat flux was not considered, however, it would generally cause the age of the samples to be underestimated.

Ice temperatures were not obtained for the few stations denoted by asterisks in Table 3.1. T_s for these stations were therefore calculated using Eq. 3.4. Note that these stations were not considered in the correlation analysis above, but only to obtain reasonable values for the purpose of discussion and estimation of brine volume. K_a was estimated from other ice stations with the most similar ice thickness and air temperature (112C_p for 112A_p, 206A for 112B_p, 718B for 508B, 709A for 508C, 504_c for 508D, and 505 for 508A and 703C; see Table 3.1). This step is critical, because the larger the differences in h_i and T_a between stations, the larger the change in K_a becomes and thus the error in the T_s estimate. T_w is less important as it is more constant between stations. Also the atmospheric conditions affect K_a. However, the days that were compared had similar atmospheric conditions. In fact, stations used for T_s estimation using Eq. 3.4 all had northeasterly wind with comparable wind speeds. All measurements were performed under overcast conditions (8/8) except for 504_c/508D which were measured under mainly cloudy skies (pers. comm. A. Tat, CASES meteorological observations). To estimate the error, T_s was also recreated for stations with already measured surface temperatures but with larger differences in T_a and h_i (e.g., using 112C_p to obtain T_s for 715B and 124D resulted in errors of 0.35 and 0.005 °C, respectively, and using 505 for 504 and 503 gave errors of 0.21 and 0.36 °C, respectively). The error in the T_s from flux balance calculations is thus estimated conservatively to be smaller than ±0.35 °C.

Generally high growth rates result in more brine being trapped within the ice structure while gravity drainage reduces salinities as the ice ages (*Weeks*, 1998). Brine expulsion further complicates the prediction of S_b. Low temperatures, generally causing rapid ice growth, also decreases brine porosities in the ice and increases brine expulsion, and thus tends to lower S_b. High temperatures may, on the other hand, leave the ice porous enough to make possible intrusions of warm, salty seawater. Natural oscillations in air temperatures thus result in complex brine dynamics within the thin sea ice volume. Furthermore, dynamic growth through consolidation of grease ice is observed to retain higher salinities than congelation ice growth (*Smedsrud and Skogseth*, 2006). However, a statistically significant relationship between ice textural features and salinity was not found in the analysis of the ice data.

3.4.5 Spectral reflectance of the thin ice types

A key objective of the study was to find relationships between ice physical properties and radiative transfer at optical (this paper) and microwave wavelengths (*Hwang et al.*, 2007). Figure 3.10 shows the range of surface-leaving spectral reflectance (ρ_λ) observed in the Cape Bathurst polynya region during the field experiment. For calm open water conditions the maximum ρ_λ is nearly 0.03, which is below the albedo of about 0.05 due to Fresnel reflection on a water surface under diffuse light conditions (*Perovich*, 1996). The low values may be explained by the relatively low solar angles during the open water measurement (e.g., 8.6° above the horizon) at station 715C when the sky was fully overcast but with good visibility and the solar disc weakly visible and the fact that ρ_λ is measured from nadir surface-leaving radiance. Direct specular reflection from the surface would thus have a lesser contribution to nadir angles than for hemispherical upwelling irradiance. Once the ice becomes thicker, and later the presence of frost flowers and snow, the surface becomes more lambertian and the estimate of ρ_λ more representative of full-angle measurements, especially under overcast sky conditions.

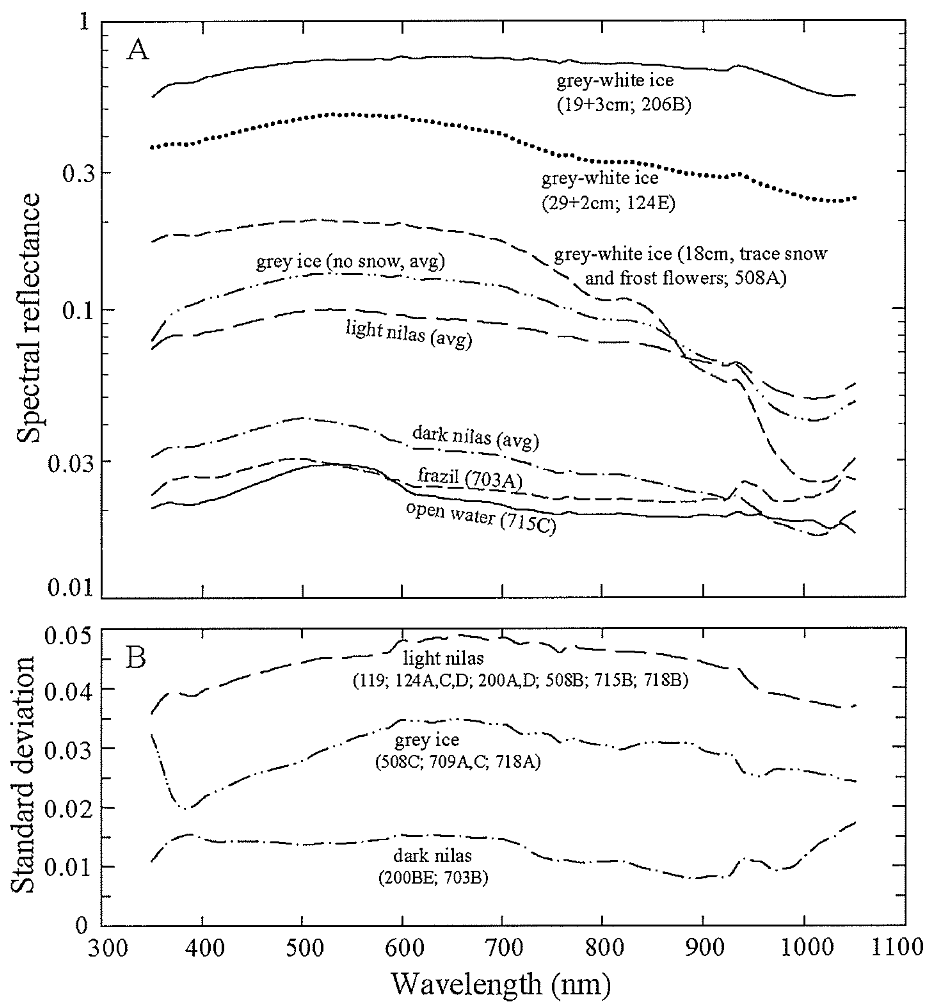

Figure 3.10. Range of spectral reflectance observed for ice types when pointing the sensor head directly downward. Ice and snow thickness is shown in the parenthesis with the ice station name. The 'avg' in the parenthesis refer to an average reflectance of all observed spectra of the specific ice type, while (b) shows the standard deviation with the station names in parenthesis.

It is evident from the spectral shape of ρ_λ for open water (Figure 3.10) that neither absorption nor scattering in the seawater were negligible in the study area. Negligible scattering in the water column is assumed in many model studies (e.g., *Perovich*, 1990b). A peak in ρ_λ for station 715C was observed in the 500-570 nm range, related to wavelengths of minimum absorption and weak wavelength-dependence of scattering in the water column. Station 715 was one of the stations closest to the Mackenzie River (Figure 3.1) that has an annual runoff of 330 km^3 containing large amounts of suspended particles (124 Tg) and dissolved organic matter (1.3 Tg) (*Macdonald et al.*, 1998).

Due to the high transparency of the dark nilas ice (appears dark), the reflectance peak from the seawater could clearly be seen through the ice (Figure 3.10), although the peak was somewhat shifted to shorter wavelengths. This wavelength shift is most likely related to a decrease in the amount of dissolved and particulate matter, as this station is further away from the estuary. However, a 2-3 fold increase in ρ_λ occurred when going from dark to light nilas. For light nilas and thicker ice the contribution of upwelling radiance from the water column became small and surface properties relatively more important (e.g. frost flowers were not present in dark nilas).

The grey-white ice ρ_λ showed large variability related mostly to surface conditions. The observations ranged from 0.20 to 0.72 at 500 nm, and from 0.025 to 0.57 at 1000 nm (stations 508A and 206B, respectively). The presence of snow increased the ρ_λ, but reduced the spectral dependence in the visible. The large range seen in longer wavelengths is related to the high absorption by brine at the top layers and surface of the ice. The lowest ρ_λ for grey-white ice was measured for station 508A under relatively high air temperatures (-4 °C) and a slushy surface of partly melted frost flowers (Figure 3.4).

The response of ρ to ice thickness, and thus also to seasonal evolution, is summarized in Figure 3.11. As the season progressed, ice became thicker and colder, and could therefore support the weight of a snow cover. Later in the season (station 206 onwards), it appears that roughly a thickness of grey-white ice (0.15 m) was required to sustain a snow cover (Figure 3.4). For thinner ice any snow accumulation quickly resulted in the formation of slush. ρ for the ice thickness classes ranged around 0.032 ± 0.012 for dark nilas, 0.085 ± 0.044 for light nilas, 0.138 ± 0.088 for grey ice, and 0.398 ± 0.200 for grey-white ice, where the numbers denote the mean followed by the standard deviation.

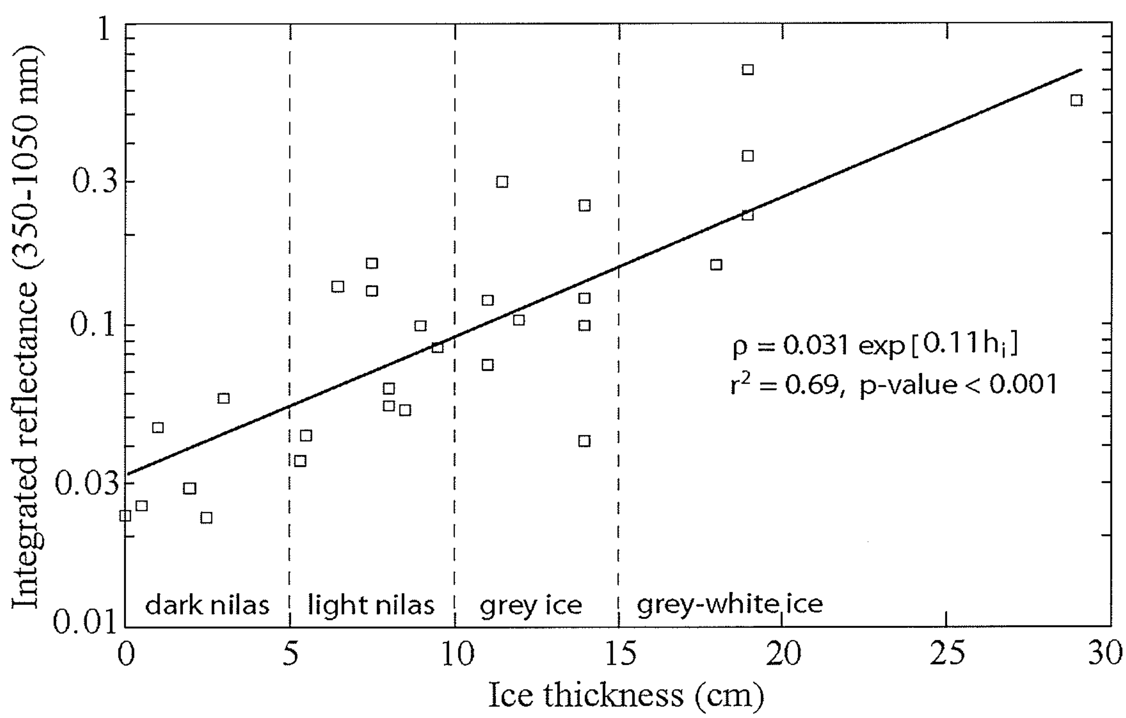

Figure 3.11. Integrated reflectance for the wavelength region between 350 and 1050 nm versus ice thickness.

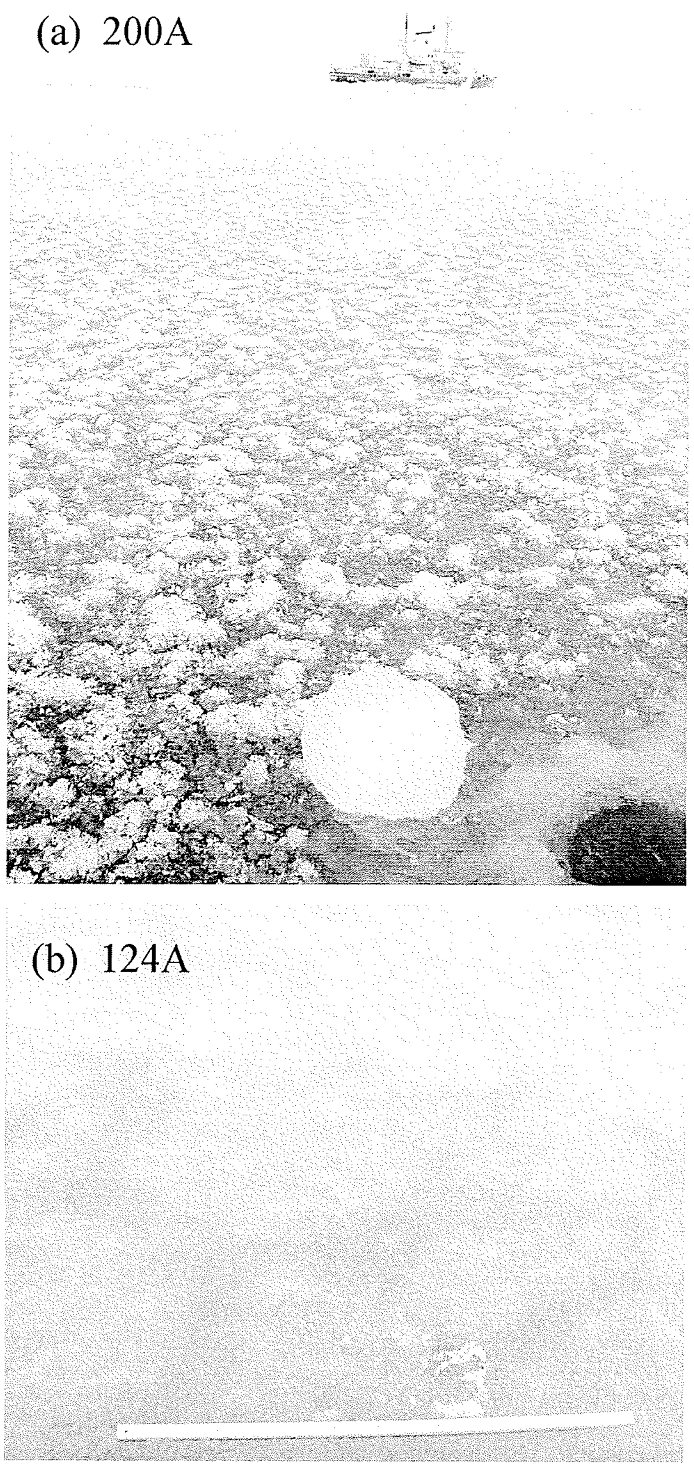

Figure 3.12. Example of light nilas surface types encountered. (a) Station 200A, visited on 4 November, had an ice thickness of 6.5 cm and a distinct cover of frost flowers. The ice core in the front has a diameter of 9 cm. *CCGS Amundsen* is seen in the background. (b) The ice thickness of station 124A (26 October 2003) was 8.5 cm and a thin, slushy layer covered the surface. The scale in the foreground is 1 m.

The observed ρ for the thin ice types were most strongly related to the surface condition. No significant relationships were found with either air or surface temperature, while the correlation with ice thickness (Figure 3.11) seems largely related to surface features. Any addition of snow significantly increased ρ to a degree where ice thickness variation had little effect (Figure 3.10, grey-white ice). However, for most nilas and grey ice samples, a snow cover was not present in observable amounts. For these bare ice cases the presence of frost flowers had a marked effect. This is demonstrated in Figure 3.12, which shows two light nilas stations, one with a wet, slush covered surface (124A) and one covered with frost flowers (200A). In this case, the presence of frost flowers approximately doubled ρ_λ between 500-600 nm from 0.07 to 0.14, and tripled ρ (350-1050 nm) from 0.04 to 0.12. Between stations 124A and 200A the air temperature changed by –5.4 °C (from –5 to –11.4 °C) and consequently the surface temperature changed by about –2 °C (Table 3.1). This temperature difference provided the forcing for brine movement and the formation of the characteristic surface types of these two stations. These surface types were also found to relate to observed surface salinities; the frost flower covered station 200A had a high S_s of 39.0‰, while the slush covered station 124A had a S_s of 17.6‰ (Table 3.1). Thus in summary, it is apparent that understanding ρ_λ of thin ice formed under highly varying conditions requires a more complete treatment of brine movement towards the surface of the ice sheet and the formation of surface features such as frost flowers or slush layers. This may necessitate the use of some sort of complex relationship with ice salinity, temperature and thickness. We consider this an important evolution for future coupled radiative transfer and 1-D thermodynamic sea ice models.

The data did not support correlation between ρ and the textural characteristics observed for the ice (see Figure 3.4). This may be a subject that is better approached through structural-optical modeling efforts where surface characteristics and ice thickness can be accounted for. More importantly, however, is the appropriate modeling to obtain proper surface characteristics of the thin ice types. For example more work is required to understand how grain structure, brine channel morphology and temperature affect the formation and distribution of surface skim and frost flowers in newly forming sea ice. Dedicated laboratory experiments are therefore warranted to improve the treatment of brine kinetics in sea ice models.

3.5 Conclusions

Fieldwork was conducted in the Cape Bathurst polynya during the fall freeze-up period in October-November 2003 using an air-ice boat to gain access to thin and undisturbed sea ice away from the influence of the icebreaker. Samples were collected for textural and physical characteristics of the sea ice coincidently with surface-leaving reflectance measurements. A main point to emphasize is the large variability in all observed properties of the sea ice. A single sample cannot be considered representative for the area. The processes, which give rise to this large spatial and temporal variability, can, within the context of this study (41 stations over 25 days), be summarized as follows:

1. Growth and desalination processes resulted in C-shaped salinity profiles with higher salinities at the surface and bottom (Figure 3.8). With increasing thickness, salinities in the sea ice decreased in a logarithmic manner (Figure 3.9). Dark nilas had bulk salinities of 10-16‰, whereas for grey ice the salinities had decreased to about 5‰. Bulk salinities (S_b) were found to

decrease with h_i (cm) according to $S_b = 4.582 + 13.358/h_i$ for all collected samples. Correspondingly, the brine volume fraction followed a similar relationship: $v_b = 0.090 + 0.333/h_i$.

2. Frost flowers were observed on the sea ice surface at relatively high air temperatures (around –4 °C on YD 297). However, they may be remnants of frost flowers formed during an earlier period with lower air temperatures (Figure 3.3). Frost flowers on the ice surface corresponded to a surface layer of disc-like granular ice (**dg**). The data suggests that **dg** could partially result from freezing of the brine skim at the base of the flowers. However, frost flowers were not seen when snow had merged on the ice surface forming a slush layer or snow ice (**fg**). Snowfall on nilas and grey ice resulted in melting and the formation of a slushy surface layer. Only after station 206A (14 cm thickness) on YD 305 was a snow cover commonly observed (Figure 3.4). Snow precipitation and the subsequent formation of the slush layer probably led to the formation of **fg** surface layer.

3. The ice texture consisted of nearly equal parts of granular, intermediate granular-columnar and columnar ice types, i.e., 33%, 37% and 30%, respectively, testifying to changing ice growth conditions in the polynya. Crystallographic analysis of 33 ice cores confirmed that the sampled ice floes were undeformed with one exception; rafting was observed at station 508A (Figure 3.4). Congelation ice growth (**c** and **g/c**) was found for relatively thin samples (Figure 3.4) formed during relatively quiescent conditions. Thin section analysis revealed increasing crystal sizes and horizontal c-axis alignments with depth with a well-developed platelet substructure (Figures 3.4 and 3.5). The sizes and shapes for the brine inclusions observed at a temperature close to –15 °C agreed well with observations by *Light et al.* (2003) (Figure 3.7) at a

similar temperature but for the interior part of first-year landfast ice, suggesting that brine inclusion changes may mostly be controlled by temperature.

4. Coincident information on spectral reflectance and physical properties is crucial in the interpretation of optical radiative transfer studies. Dark nilas had a high transparency and the optical properties of the seawater column affected the spectral shape of reflectance (ρ_λ) resulting in a peak at 500-570 nm. The surface characteristics became more important for the thicker ice types. In general, the integrated reflectance (ρ) increased exponentially with ice thickness (Figure 3.11). Still, the variability of ρ is so large within one ice thickness type that it can be mistaken for any of the other types. Future studies are needed to examine in more detail how the surface characteristics (brine skim, frost flowers and slush) are formed and affect the reflectance of thin ice at low sun angles typical of the Arctic fall period.

CHAPTER 4: Bio-optical and structural properties inferred from irradiance measurements within the bottommost layers in an Arctic landfast sea ice cover

4.1 Preface

This chapter directly addresses research questions III, IV and V. Chapter 4 has been accepted for publication as Ehn, J. K., C. J. Mundy, and D. G. Barber (2008), Bio-optical and structural properties inferred from irradiance measurements within the bottommost layers in an Arctic sea ice cover, *J. Geophys. Res.*, 113, C03S03, doi:10.1029/2007JC004194 (Reproduced by permission of American Geophysical Union). I was in charge of collecting the data (with the aid of the divers J. Stuart and W. Smith and other members of the science team), programming of the computer model, data analysis. In addition, I took a lead role in writing the manuscript.

4.2 Introduction

Sea ice plays a key role in the earth's climate system partly because of its high albedo that causes a large portion of the incident solar radiation to be backscattered back from the surface (*ACIA*, 2005). The surface albedo of sea ice has been studied extensively and found to be controlled to a large extent by the near surface properties, e.g., snow-covered, bare ice or melt ponds (e.g., *Grenfell and Maykut*, 1977). However, much less is known about how radiation is transmitted to the bottom layers or through the sea ice, and how this affects the partitioning of radiation between reflection, absorption and transmission. The bottommost layers of sea ice are of considerable physical and ecological interest as its porous structure creates a habitat for a thriving algal community composed mainly of diatoms (*Horner et al.*, 1992) which use chloroplastic pigments to effectively absorb radiation at visible wavelengths. Algal chlorophyll *a* (chl *a*) concentrations >300 mg m^{-2} have been observed in the bottom few centimeters of landfast first-year sea ice (e.g., *Welch and Bergmann*, 1989). Small amounts of algae may also be present throughout the ice column (e.g., *Perovich et al.*, 1998).

Subsequent to its initial formation, sea ice growth is typically determined by the energy balance at the ice-ocean interface (e.g., *Bitz and Lipscomb*, 1999). At the growth interface, a so-called skeletal layer builds up from ocean-facing lamellar platelets protruding into the water column (e.g., *Weeks and Ackley*, 1982; *Eicken*, 2003). The platelet and crystal structure of the resulting ice is largely determined as it forms at this interface (*Weeks*, 1998). Thus, as the ice grows thicker, a record of the physical conditions that prevailed at the time of formation is retained in the ice structure. In addition, brine and air are incorporated between ice grains into the sea ice as it forms. These inclusions are effective scatterers and thus largely determine how radiation interacts with the sea ice (e.g., *Grenfell*, 1983; *Buckly and Trodahl*, 1987). Pure sea ice, without ice algae or other absorbing impurities, absorbs radiation within visible wavelengths comparable to clear oceanic water (*Smith and Baker*, 1981; *Warren*, 1984). However, impurities within sea ice significantly alter the spectral distribution of radiation through absorption. Other contributing impurities apart from microalgae are from colored dissolved organic matter (CDOM) and non-algal particles (NAP), i.e., mineral particles and organic detritus (*Belzile et al.*, 2000; *Light et al.*, 1998; *Roesler and Iturriaga*, 1994).

The traditional approach for studying light attenuation by ice algae has been to collect and melt ice samples to determine spectral absorption properties of ice algae on glass fiber filters (e.g., *Roesler and Iturriaga*, 1994). This neglects any potential effect of ice structure and geometry of the algae population (*Perovich et al.*, 1993). Furthermore, chloroplastic pigment degradation may occur during the process of melting and filtering (*Stramski*, 1990). These measurements are therefore difficult to use directly in estimating spectral transmission through sea ice. A few studies have measured radiation transmitted through the ice cover before and after removal of the bottom ice algae layer (*Welch and Bergmann*, 1989; *Perovich et al.*, 1993; *Perovich et al.*, 1998). However, these measurements have been confined to the 0.02-0.03 m thickness of the bottom skeletal layer.

In this chapter, the vertical extent of *in situ* observations in the bottom ice is increased using data collected as a part of the Canadian Arctic Shelf Exchange Study (CASES). The observations included transmitted irradiance spectra measured at vertical increments within the bottom layers of landfast first-year sea ice acquired with the assistance of divers. The goal here is to assess the importance of absorbing impurities, predominantly ice algae and their derivatives, and the sea ice structure itself on the spectral distribution of radiation near the ice-water interface. Direct observations of structural properties are methodologically difficult as the near-melting and porous sea ice is subject to brine drainage and freezing as the sample is removed. However, the obtained data allowed for an iterative approach to estimate the inherent optical properties (IOPs), i.e., the absorption and scattering coefficient, of the sea ice using the discrete ordinates radiative transfer (DISORT) model by *Stamnes et al.* (1988). It is noted that knowledge of the IOPs is a critical step in designing a structural-optical model that can accurately simulate temporal evolution of radiative transfer in sea ice.

4.3 Methods

The icebreaker *C.C.G.S. Amundsen* over-wintered in Franklin Bay and provided laboratory facilities and logistical support for the fieldwork conducted on landfast sea ice (Figure 4.1). The under ice diving program was held during three weeks in April-May 2004 with the divers performing alternating measurements of ice-water interface chemistry, biology and physics. The focus of this paper is on the irradiance data collected during under ice dives conducted on 22, 24, 28 April and 9 and 18 May around local noon. Each dive lasted approximately 45 minutes. All sampling was conducted within a 5-by-20 m area located about 50 m south of the ship. Approximately 5 m north of the area, a hole was cut through the sea ice and covered with a heated tent to allow the divers access to the seawater.

The snow cover did not have a uniform thickness over the sampling area. It was expected that the variable snow thickness might affect the ice structure and the bottom ice algae community (*Mundy et al.*, 2005; *Riedel et al.*, 2006). Thus, sampling locations were divided into thick (> 0.1 m) and thin (< 0.1 m) snow areas. Spectral irradiance measurements and samples for sea ice physical and biological properties were all taken from thin snow sites, whereas only bottom ice algal samples were collected from thick snow areas. In general, the snow cover was dry and the snow/ice interface was smooth and distinct. Ice thickness at the thin snow area increased from 1.74 m on 10 April to 1.82 m on 28 April and 1.87 m on 5 and 9 May. Sky conditions were clear on 22 and 24 April, completely overcast (solar disc not visible) on 28 April and 5 May, and partly cloudy on 9 May.

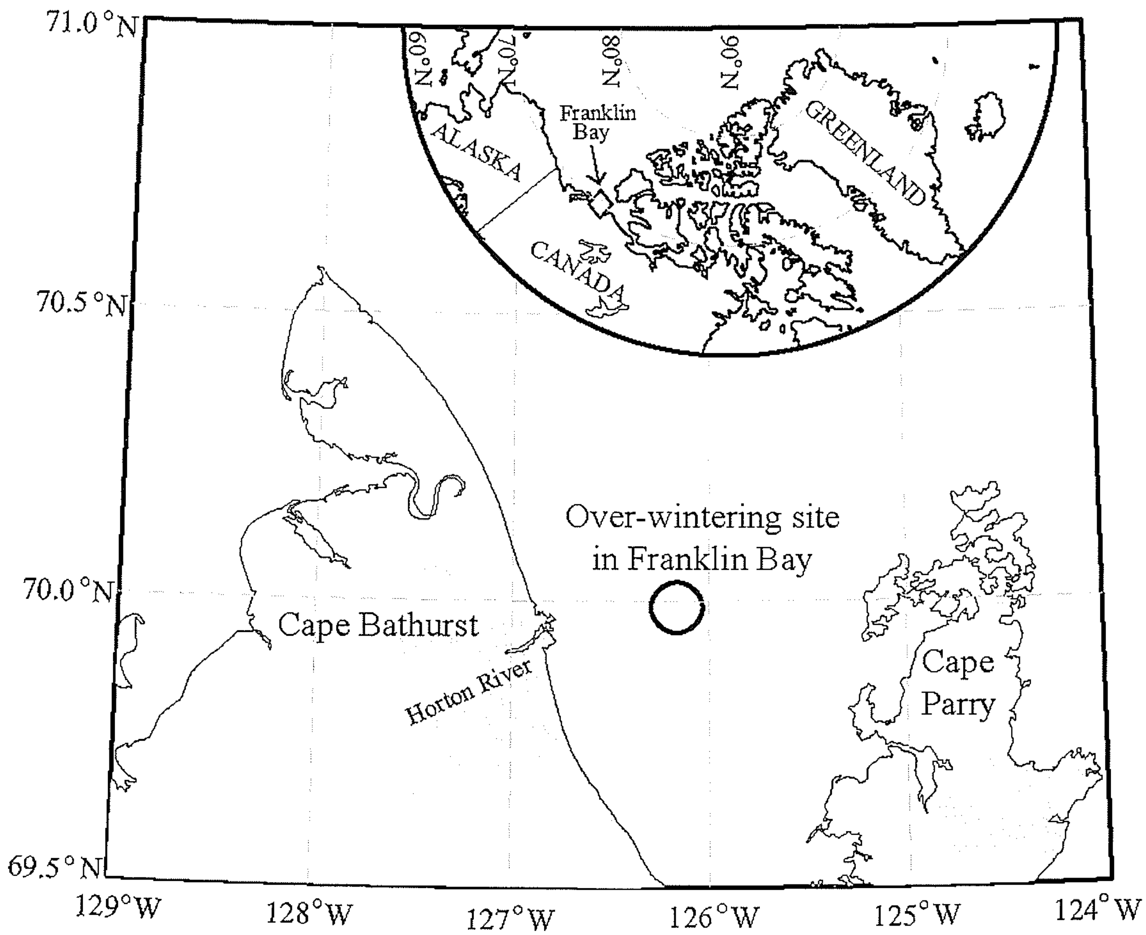

Figure 4.1. The location of the Franklin Bay sampling site in the southern Beaufort Sea.

4.3.1 Spectral irradiance measurements

Downwelling spectral irradiance measurements for the bottom part of the sea ice were conducted using an underwater cosine collector attached to a dual-headed spectroradiometer (Analytical Spectral Devices, Inc.) through a waterproof fiber-optical cable. The instrument has two channels that both measures 512 wavelength bands ranging from 350 to 1050 nm. The cosine collector was not calibrated with the spectroradiometer, and therefore only relative irradiance measurements of transmittance were made. Incident spectral irradiance was measured simultaneously with the in and under ice irradiance to account for any changes in the incident light field. For this a reference cosine collector was placed on a tripod about 1.5 m above ground, levelled and connected with a fiber-optical cable to the second channel of the spectroradiometer.

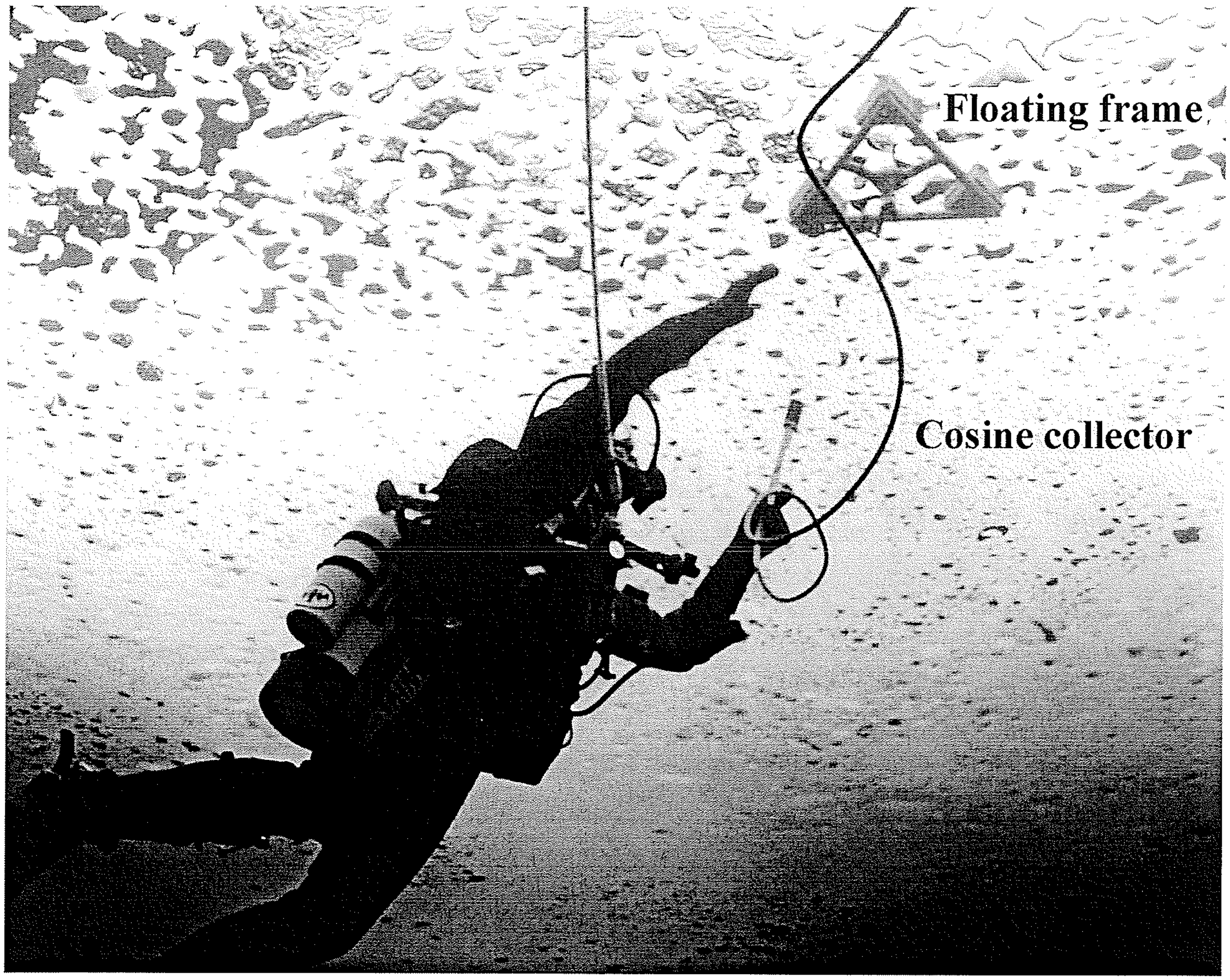

Figure 4.2. Diver in process of attaching the spectroradiometer cosine collector to the floating triangle.

In order to conduct bottom ice spectral measurements, a hole was drilled through the ice about 2-3 m north of the planned measurement location through which the sensing head, with the optical cable, was lowered for the diver to position at the selected location. A metal tube was placed around the optical cable immediately below the cosine collector to keep the cable from bending (Figure 4.2). The tube fit tightly into a holder the center of a triangular floating frame that pressed against the bottom of the sea ice (Figure 4.2). By attaching the tube to the floating frame, it was ensured that the cosine collector was levelled and at a fixed position close to the sea ice bottom. The spectroradiometer unit was operated from the surface. To make a successful series of measurements within the available diving time, integration times were reduced by increasing light levels reaching the ice bottom. This was accomplished by removing the snow from a 2-by-2 m area on the ice surface prior to the dives. It was assumed that this would have little impact on the radiation field near the bottom of the ice after propagation through about 1.6 m of sea ice with 0.05-0.10 m granular ice surface layer. This assumption is feasible as multiple scattering and possibly the anisotropic structure of the sea ice reduces horizontal transmission of light more than vertical transmission (*Pegau and Zaneveld*, 2000; *Buckley and Trodahl*, 1987). Furthermore, the light field has been found to reach the asymptotic state within the first meter of the ice cover (e.g., *Pegau and Zaneveld*, 2000). Near the ice bottom, however, the light field is affected by underlying seawater from which little radiation is backscattered. After a completed measurement under the ice, the diver drilled a 0.05 m diameter auger hole 0.05 m upwards into the ice and pushed the cosine collector to the top of the hole where measurements were made. The cosine collector was fixed to the top of the hole by using a clip that attached around the tube and hindered any downward movement past the holder in the floating frame (Figure 4.2). This process was continued until an irradiance profile with 0.05 m interval was obtained from the bottom portion of the sea ice. Depending on the effective time available the number of depth intervals into the ice bottom varied. Unfortunately, snow precipitation and drift affected the spectra obtained in May. The highest quality profile was thus measured on 28 April up to a distance of 0.20 m from the ice-water interface.

4.3.2 Physical properties

Ice samples taken from the site both before and after the dive program and after each irradiance measurement were analysed for salinity, temperature, microstructure (10 April, 5 and 9 May) and density (28 April and 5 May). Bottom ice samples for spectral absorption by particulate matter were obtained after each dive. Ice cores were obtained using a MARK II coring system (0.09 m diameter, Kovacs Enterprise).

A full-length ice core was used to measure temperatures immediately after extraction using a handheld drill and a temperature probe (Hart Scientific 1522). Ice temperatures at depths between the surface and 1 m and the water temperature below the ice at 2 m were additionally recorded with 10 minute intervals from a nearby thermocouple string. Ice cores for salinity determination were cut into 0.1 m sections and immediately placed into plastic jars or airtight plastic bags before transfer onboard the ship where they were then melted. Other extracted cores were placed in plastic sleeves and stored at –20°C until processing on board the ship. Conductivity was measured from the melted ice samples using a handheld conductivity meter (Hoskin Scientific Cond 330i; accuracy ±0.5% of reading). The conductivity was converted into salinity units using UNESCO algorithms (*Fofonoff and Millard*, 1983).

Sea ice density was determined in the cold room by cutting ice core pieces into the shape of cuboids with a mass of about 150-300 g and using a digital calliper and balance (Denver Instrument P-403) for volume and weight measurements, respectively. Weights of the cuboid samples were measured to a precision of ±0.1 mg, while the lengths of the sides were measured to ±0.01 mm. However, the accuracy of the measurements was affected by small variations from plane faces and small chips broken loose from edges and corners. The overall effect is to underestimate the density of the sample. Furthermore, brine expulsion and drainage, that may occur after the ice sample is taken, result in a decrease in density. *Kawamura et al.* (2001) estimated the accuracy of this method to be ±10 kg m^{-3}, however, analysis of 85 columnar ice samples taken from depths between 0.65 and 1.65 m in 9 ice cores sampled during CASES (data not shown) resulted in a mean (± standard deviation) density of 917.3 ± 4.3 kg m^{-3}.

To obtain detailed information on sea ice microstructure, ice cores were processed into so-called thick sections and thin sections. Vertical and horizontal segments were selectively cut from the ice cores using a band saw. The segments were attached to glass plates and planed down to approximately 5 mm (thick section) and then 1 mm (thin section) thickness. The ice sections were placed on a light table between cross-polarized sheets and photographs of crystal and platelet structure were taken using a digital camera (Canon Powershot G2, 4.2 mega-pixel).

4.3.3 Bottom ice algae sampling

The bulk of algae within first-year landfast sea ice are typically confined to the bottommost centimetres (e.g., *Smith et al.* 1990). Therefore, chl *a* concentrations and spectral particulate absorption coefficients, $a_{p(f)}(\lambda)$, were only determined for the bottom 0-0.09 m of the sea ice. Ice core sections obtained by coring from the surface were immediately cut and placed in plastic containers. A known volume of seawater filtered through glass fiber filters (Whatman GF/F, nominal pore size 0.7 μm) was added in order to avoid lysis of the algae cells caused by the rapid salinity change while melting the ice samples (*Horner et al.* 1992). All samples were melted in dark at 4 °C. Subsamples of the melt were filtered onto GF/F filters and chl *a* was determined fluorometrically after extraction in 90% acetone for a minimum of 24 hours (*Parsons et al.*, 1989).

Optical density spectra of the particulate material were measured from the remainder of the ice melt. First, the particulate material in the samples was filtered onto GF/F filters. The spectroradiometer with a one-degree fore-optic attached to the optical fibre end was used immediately before and after filtering to measure the background transmittance, $T_{bgrd}(\lambda)$, and sample spectral transmittance, $T_{sample}(\lambda)$, through the filter pad. The background transmittance was measured on a GF/F filter made wet with milli-Q water. The light source (Schott iQLED backlight) was based on white-light emitting diodes that produced a measurable signal between λ = 400-900 nm. The optical density was then calculated with

$$OD(\lambda) = \log_{10}\left(\frac{T_{sample}(\lambda)}{T_{bgrd}(\lambda)} - \frac{T_{sample}(750\,\text{nm})}{T_{bgrd}(750\,\text{nm})}\right), \tag{4.1}$$

where $OD(\lambda)$ is the spectral optical density with the baseline signal at 750 nm subtracted. The spectral particulate absorption spectra was then calculated from

$$a_{p(f)}(\lambda) = \frac{2.303\,OD(\lambda)}{\beta\,\gamma\,(V/A)}, \tag{4.2}$$

where A is the effective area of the filter, V the volume of the sample filtered, γ the dilution factor to account for the addition of filtered seawater, and β the path length amplification factor to correct for the scattering by the filter itself (*Roesler*, 1998). For sufficiently high concentrations of particles on the filters, β approaches 2 (*Roesler*, 1998), which was also assumed in this study. $a_{p(f)}(\lambda)$ was finally divided by the chl *a* concentration to obtain the chl *a*-specific particulate absorption coefficient, $a^*_{p(f)}(\lambda)$.

4.3.4 Radiative transfer model

To link physical properties and inherent optical properties (IOPs) of the ice-water system with observed apparent optical properties (AOPs), the discrete-ordinate radiative transfer (DISORT) code (*Stamnes et al.*, 1988) was utilized. In this study, the use of DISORT was limited to sea ice and seawater, and changes in the refractive index at layer boundaries were not considered (*Jin et al.*, 1994). Based on *in situ* measurements on 28 April, the bottom 0.1 m of the ice was divided into two horizontally homogeneous 0.05 m layers in addition to one layer from 0.1-0.2 m from the ice-water interface. For each of these layers, DISORT requires information on the IOPs, i.e., spectral absorption coefficient, $a_{tot}(\lambda)$, scattering coefficient, $b_{tot}(\lambda)$, and phase function, $p(\lambda, \theta)$, to solve the equation of radiative transfer (e.g., *Thomas and Stamnes*, 1999). 16 streams were used to characterize the radiation field at the border interfaces. To obtain the IOPs, DISORT runs were iterated until the model calculated spectral diffuse attenuation coefficient, $K_d(\lambda)$, matched observed values to within ± 0.0001 m^{-1} for all layers simultaneously. $K_d(\lambda)$ for each layer was calculated from the downwelling spectral irradiance, $F{\downarrow}(\lambda)$, according to

$$K_d(\lambda) = \ln\left[\frac{F_\downarrow(\lambda, z_1)}{F_\downarrow(\lambda, z_2)}\right] \Big/ (z_1 - z_2), \qquad (4.3)$$

where z_1 and z_2 denote the depth of the layer interfaces. This approach requires some assumption regarding the optical properties of the sea ice, which are described below.

1. Any wavelength dependence in $K_d(\lambda)$ is assumed to be caused by absorption (e.g., *Grenfell*, 1983). For each sea ice layer, $a_{tot}(\lambda)$ was calculated as the sum of absorbing components:

$$a_{tot}(\lambda) = v_{pi} a_{pi}(\lambda) + v_b a_{sw}(\lambda) + a_{imp}(\lambda), \qquad (4.4)$$

where $a_{pi}(\lambda)$ and $a_{sw}(\lambda)$ are the absorption coefficients for pure ice and brine (assumed identical to pure seawater), which are multiplied by their respective volume fractions, v_{pi} and v_b. Values for pure ice and brine absorption were taken from *Warren* (1984) and *Smith and Baker* (1981), respectively. $a_{imp}(\lambda)$ is the absorption coefficient for impurities including algal and non-algal particulate matter, as well as colored dissolved organic matter (CDOM). Essentially it is the residual absorption required to explain $a_{tot}(\lambda)$ and thus one of the unknowns being iterated for.

2. Scattering is assumed to be dominated by brine and air inclusions that are significantly larger than wavelengths within the visible light regime, i.e., $b_{tot}(\lambda)$ becomes independent of wavelength (hereafter b_{tot}). Particulate impurities are assumed to have a negligible contribution to the overall scattering. This may not be the case, however, no published account exists in the sea ice literature to suggest the contrary. If the optical properties of the inclusions furthermore are assumed to be well represented by spheres with an effective radius r_{eff}, (e.g., *Hamre et al.*, 2004; *Light et al.*, 2004), b_j for inclusion j (denoting either brine or air) can be expressed as

$$b_{tot} = \frac{3}{2}\sum_j \frac{v_j}{[r_{eff}]_j},\tag{4.5}$$

where v_j is the volume fraction (*Hamre et al.*, 2004). Because absorption at 750 nm is predominantly by water and ice and thus known, it is possible to first solve for the wavelength-independent scattering coefficient.

3. The phase function, $p_j(\theta)$, for all scattering inclusions denoted by subscript j (i.e., spherical brine or air inclusions) was approximated using the Henyey-Greenstein phase function (*Henyey and Greenstein*, 1941),

$$p_j(\theta) = \frac{1}{4\pi}\frac{1-g_j^2}{(1+g_j^2-2g_j\cos(\theta))^{3/2}},\tag{4.6}$$

where g is the average cosine or the asymmetry parameter and θ the scattering angle. For brine and air inclusions, the asymmetry parameters were chosen to be suitable for ice temperatures near the melting point, i.e., set to $g_b = 0.997$ and $g_a = 0.855$, respectively (*Hamre et al.*, 2004; *Light et al.*, 2004). This results in a strongly forward scattering phase function which is typical for the sea ice and seawater environment (*Mobley et al.*, 1998). $p_j(\theta)$ for the components were then combined to a total phase function using (*Grenfell*, 1983)

$$p(\theta) = \sum_j \frac{b_j\, p_j(\theta)}{b_{tot}}.\tag{4.7}$$

4. Within the interior parts of the sea ice cover the radiation field has been found to reach an asymptotic state and does not significantly change with depth (e.g., *Pegau and Zaneveld*, 2000). However, in the ice near the ice/water interface the radiation field becomes increasingly affected

by the presence of the water column with little backscattering. For DISORT to correctly simulate the radiation field in the proximity of the ice/water interface, a 0.05-m-thick snow layer above a 1.5-m-thick homogeneous layer of (interior) ice were added on top of the layers of interest. These two layers were assumed to be free of impurities, i.e., absorption was solely from ice and water. For the interior ice layer, r_{eff} for brine inclusions was calculated from salinity profile according to *Jin et al.* (1994) and found to be 0.76 mm. For air inclusions r_{eff} was set to 0.96 mm following to *Hamre et al.* (2004). The scattering coefficient, b_{tot}, was then calculated using Eq. 4.5. The density of the snow pack was set to 300 kg m^{-3} and composed of snow grains with constant radii set to an arbitrary value of 0.2 mm. These values were chosen as they resulted in representative irradiance magnitudes at the bottom ice layers.

In addition, a 50 m thick homogeneous seawater layer was included below the ice. This layer was modeled following the formulations in *Hamre et al.* (2004) (see references therein) with the only impurity being a low concentration of phytoplankton, 0.2 mg chl *a* m^{-3}, with the same absorption properties as in the bottommost layer of the sea ice. It is noted that irradiance levels in the ice were not sensitive to this concentration.

The incident irradiance to the ice surface was assumed diffuse and its values tuned to match the 0.2 m level spectral transmittance. Trial runs with direct incident irradiance showed that changes in the incidence angle did not significantly affect the bottom layer $K_d(\lambda)$ calculated by the model. Figure 4.3 shows the directional distribution of radiance as it propagates through the bottommost layers of the sea ice according to the model. Note that the model reproduces the predominately downward directed radiation field (peak at 180°) with little backscatter from the water column, i.e., modest intensity values at angles < 90° at the ice-water interface. Radiation that is transmitted through sea ice has been found to be largely downward directed (*Buckley and Trodahl*, 1987). Because brine inclusions in warm columnar ice near the bottom are generally vertically aligned, it can be expected that a_{tot} and b_{tot} depend on the orientation of the structure in relation to the radiation field (*Pegau and Zaneveld*, 2000; *Light et al.*, 2004). Thus, a_{tot} and b_{tot} values reported here are related to the radiation field shown in Figure 4.3 with magnitudes tuned to fit measured irradiances.

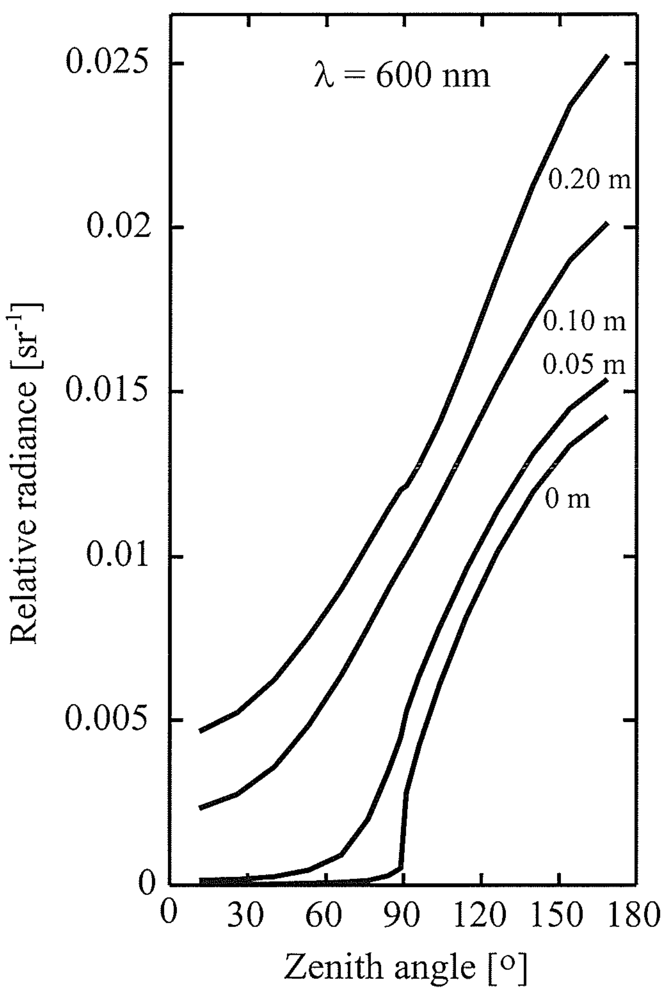

Figure 4.3. Modeled radiant intensity distribution (azimuthally averaged) at 600 nm relative to the surface incident irradiance (units: W m-2 sr-1 per W m-2). The adjacent numbers denote the distance of the border from the ice/water interface.

4.4 Results and Discussion

4.4.1 Physical properties

The sea ice, sampled in this study, can be considered typical for landfast first-year sea ice in the Arctic. Below the snow cover, the uppermost 0.05-0.10 m of the sea ice was composed of granular ice, while the rest consisted of columnar ice with the bottommost 0.01-0.02 m having a porous skeletal structure. Visible coloration was apparent towards the bottom of the skeletal layer due to the presence of ice algae. During the period 28 April and 5 May, the ice thickness grew by about 0.05 m, i.e., from 1.82 m to 1.87 m. A part of this increase may also be due to local ice thickness variability.

Analysis of ice core sections taken on 5 May revealed that the sea ice near the ice-water interface was composed of jagged crystals with a distinct platelet substructure (Figure 4.4). The combination of crystal size and circularity, platelet width and brine volume give an indication of border surface area between interstitial brine and ice and therefore can be potentially used to quantify scattering properties of sea ice. The mean crystal size decreased with distance from the ice-water interface, with the exception of the bottommost 0.05 m layer. Within this newly formed layer, smaller grains developed with a lesser degree of horizontal c-axis alignment. The formation of small grains during late winter/early spring, when ice growth rates are slow, was also noted by *Weeks* (1998) but has not been explained. The mean (and maximum) horizontal single crystal cross sectional areas observed from the ice-water interface upwards to 0.39 m in Figure 4.4 were 18 mm^2 (155 mm^2), 60 mm^2 (480 mm^2), 32 mm^2 (350 mm^2), 24 mm^2 (670 mm^2) and, 20 mm^2 (490 mm^2), respectively. Note that crystal areas may be underestimated as potentially large crystals were not fully contained within the ice core area and thus excluded from the analysis. Circularity of the ice crystals, defined as $4\pi AP^{-2}$, where A is the crystal area and P the perimeter, were 0.23, 0.17, 0.16, 0.15, and 0.28, respectively. These low values indicate a strong deviation from a perfect circle which would have a circularity value of 1. The above crystal areas and circularities are in general agreement with figures in literature (e.g., *Weeks and Ackley*, 1982; *Weeks*, 1998).

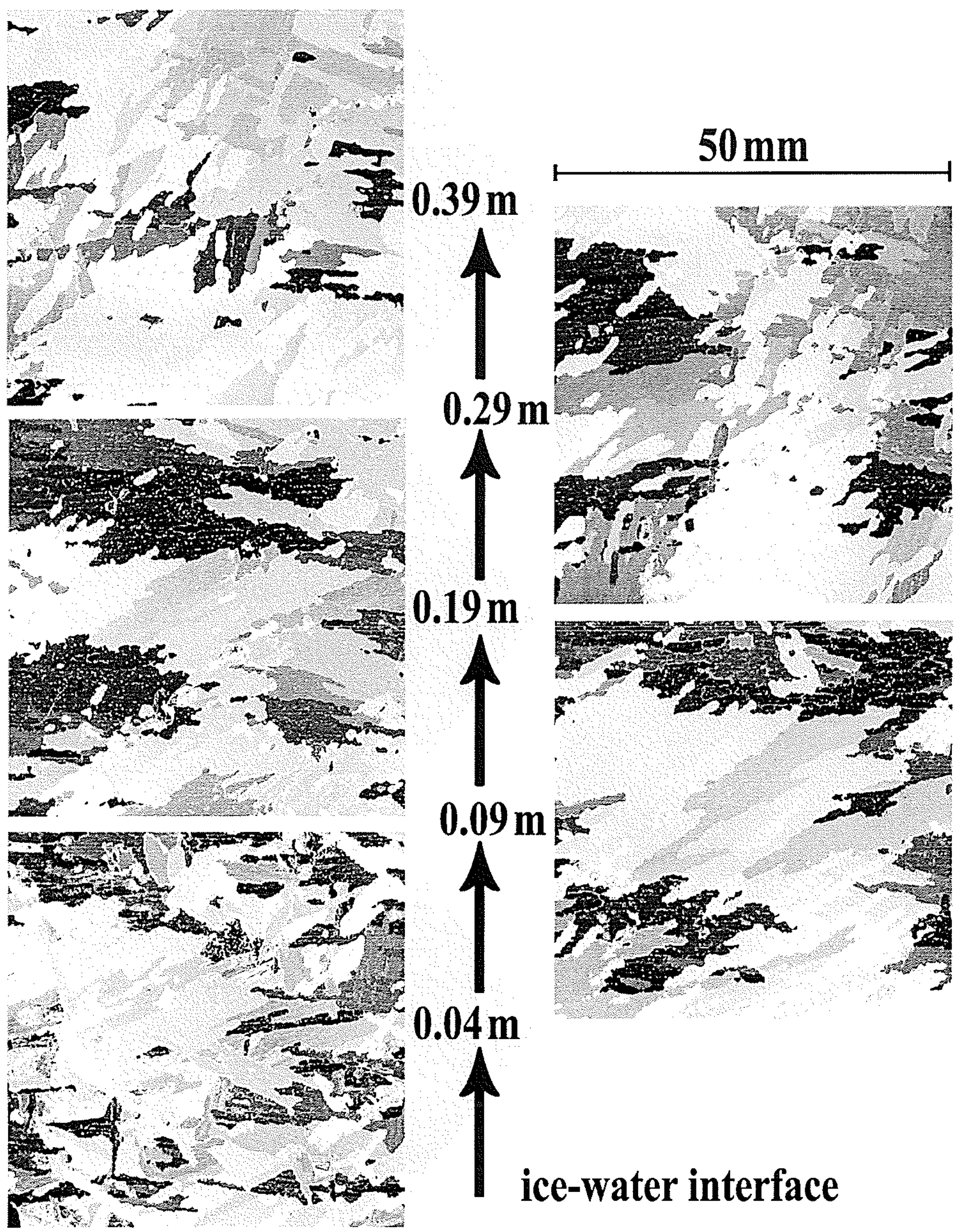

Figure 4.4. 1-mm-thick thin sections showing the columnar ice structure immediately above the ice-water interface observed on 5 May when the ice thickness was 1.87 m.

Brine inclusions were concentrated at the interface or plane between adjacent platelets. At –20 °C (temperature of cold room) these inclusions generally appeared as pockets, however, at *in situ* temperatures the brine may be mostly contained within interconnected tubes and channels (*Light et al.*, 2003). The brine layer spacing, i.e., the distance in the direction of the c-axis between adjacent planes containing brine inclusions, may therefore be less affected by temperature (*Eicken*, 2003). Going towards the bottom in the five thin sections shown in Figure 4.4, the brine layer spacing was 1.04 ± 0.21 mm, 1.14 ± 0.39 mm, 0.87 ± 0.21 mm, 0.85 ± 0.17 mm and 0.91 ± 0.17 mm, respectively. These values are in general agreement with previous observations of the structure near the bottom of thick first-year sea ice (*Mundy et al.*, 2007b; *Nakawo and Sinha*, 1984; *Weeks and Ackley*, 1982).

Ice temperatures increased with depth into the sea ice (Figure 4.5a). Over the three-week period, ice surface temperatures increased from about –12 °C to –6.4 °C, however, little change in temperature was observed in the bottom ice which is the subject of the present study. In the bottom layers, temperatures were close to the under ice seawater temperature which increased from –1.3 °C to –1.1 °C during the sampling program. At the 1.40 m depth, which corresponds to 0.40 m above the ice-water interface, the temperatures thus increased from –4.2 °C to –3.0 °C over the sampling period.

Salinity profiles had typical C-shapes with high values at the top and at the bottom (Figure 4.5b). Surface values (upper 0.05 m) ranged between 5.1‰ and 9.6‰ with no apparent trend over the sampling period. Interior ice salinities remained nearly constant between 0.2-1.0 m averaging 4.1‰. Below 1.0 m, salinities decreased with depth until a minimum value of around 3‰ was reached. This occurred, depending on ice thickness, at depths between 1.5 and 1.6 m. At the ice bottom a salinity increase up to 7.3‰ was observed, however, these values should be interpreted with caution due to the likely occurrence of brine drainage during ice core extraction.

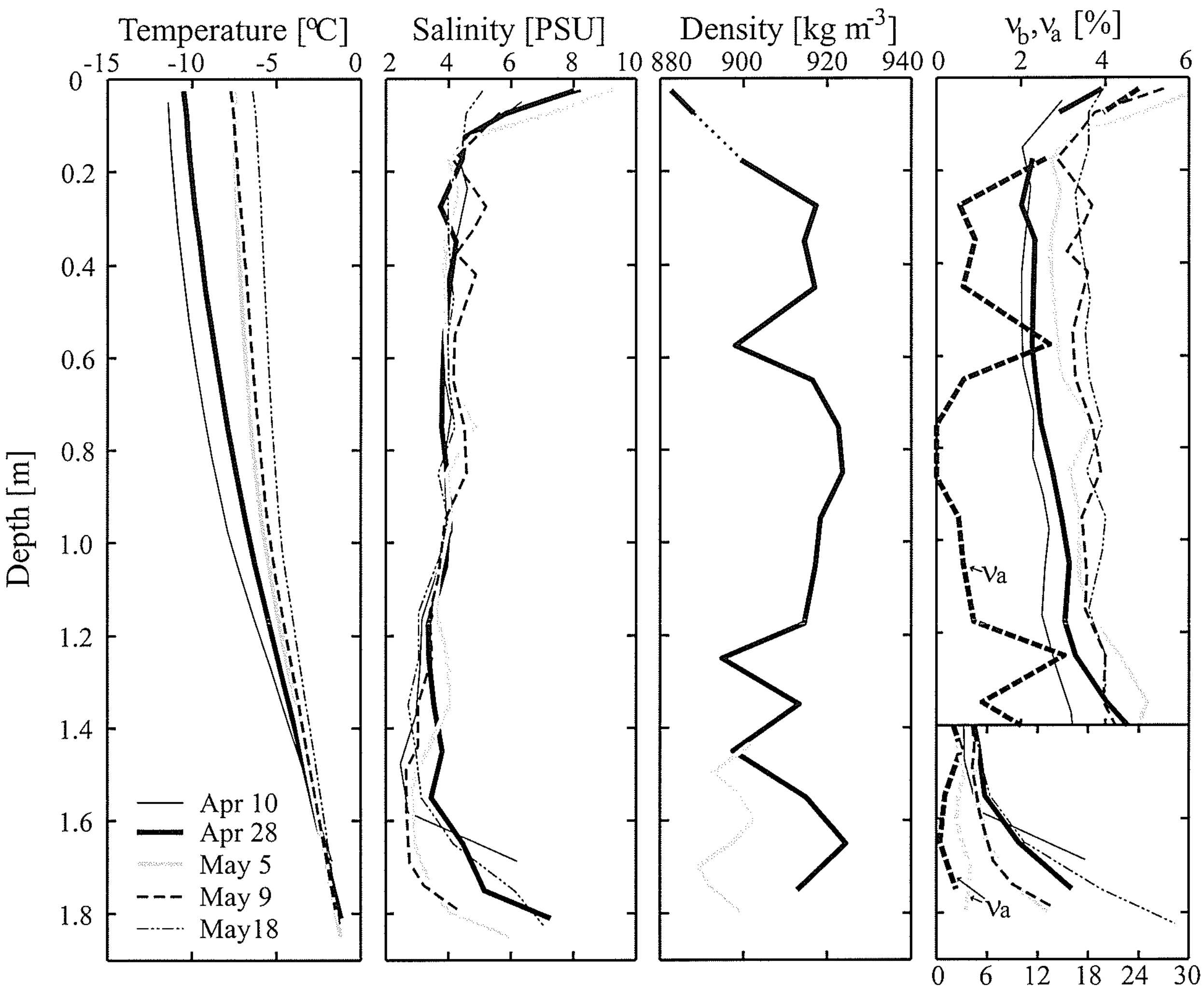

Figure 4.5. Typical temperature and salinity profiles measured before (10 April), during and after (18 May) the experiment. Brine volume fractions were calculated for these dates; however, the associated air volume fraction is shown for 28 April and 5 May when the density profiles were obtained. Ice thickness increased from 1.74 m on 10 April to 1.82 m on 28 April to 1.87 m on 5 and 9 May.

Noted in the Materials and Methods section, the measured density values presented in Figure 4.5c are likely underestimates. However, the densities shown for 28 April at depths of about 0.6 m, 1.25 and 1.45 m are highly questionable due to deviation from adjacent measurements above and below the respective depths. Near the surface, the ice was partly composed of granular ice, and lower densities were expected. Here values from about 880 to 900 kg m^{-3} were observed in the ice core taken on 28 April. Ignoring clearly lower values, interior ice densities ranged between 913 and 924 kg m^{-3}. In general, densities approached a value of 920 kg m^{-3}, which was used in the model study. Compared to 28 April, lower bottom densities were found on 5 May with values ranging from 889 to 902 kg m^{-3}. This may be explained by brine drainage from the somewhat warmer and more porous ice.

Brine and air volume fractions in sea ice can be estimated using equations provided by *Cox and Weeks* (1983), and *Leppäranta and Manninen* (1988). Air volume estimates within the ice are very sensitive to density and thus prone to overestimation, however, brine volume estimates are less sensitive to density. That is, brine volumes are more governed by bulk temperatures and salinities (Figures 5a, b). The calculated brine volume profile remained fairly constant between 10 April and 5 May. At the surface, the brine volume was about 4% and decreased to a minimum of about 2.2% at 0.14 m depth (Figure 4.5d). From there downwards the brine volume in the interior ice increased with depth to about 4.1-4.5% at 1.4 m. An increase in interior ice brine volume of about 2.2%-units was observed for 9 and 18 May. For the bottom 0.10 m (including the skeletal layer) the brine volume increased significantly to 7.5-28% due to high salinities and temperature. Air volume in the ice was found to be about 0.5-1%. However, keeping in mind the uncertainties in density estimates, within the bottom 0.4 m on 5 May, air occupied about 2.3-4.0% of the ice volume.

4.4.2 Observed optical properties

Spectral transmittance, $T(\lambda)$, profiles are illustrated by the measurements on 28 April shown in Figure 4.6. These spectra are normalized to the incident irradiance at the surface. On 28 April the sky was fully overcast with the solar disc not visible to the eye. Note that the snow cover was partially removed shortly before the irradiance measurements and that these $T(\lambda)$ are not representative of levels under an undisturbed snow cover. The original snow thickness at the site was about 0.04 m. However, the bare ice surface was optically rough with snow remnants after the snow removal and the upper ice layers composed of granular ice, with an overall diffusing effect on the radiation. Above the bottommost layer, maximum $T(\lambda)$ occurred close to 485 nm. This indicates that there were very low levels of absorbing impurities present in the sea ice above the bottom level. However, the shape of $T(\lambda)$ reaching the bottom of the ice cover was significantly altered mostly due to absorption by ice algae. Within a distance of 0.05 m the maximum peak shifted to 530 nm and local minima were observed between 415-440 nm and near 675 nm (Figure 4.6).

The major uncertainty in $K_d(\lambda)$ calculations result from inaccuracies in the distance drilled by the diver, which could be measured to ±5 mm. Values measured above 0.10 m from the ice-water interface (dashed curves in Figure 4.7) have magnitudes representative for $K_d(\lambda)$ in the interior parts of landfast sea ice (*Grenfell and Maykut*, 1977), however, shapes differ significantly between the two curves. The reason for this is a somewhat deviating spectral shape of the transmission curve measured at the 0.15 m level from the ice-water interface, which is not easily seen in Figure 4.6. We are not able to explain the cause of this deviation and therefore, in the model comparison, the two layers were merged. A sharp increase occurred in $K_d(\lambda)$ for the

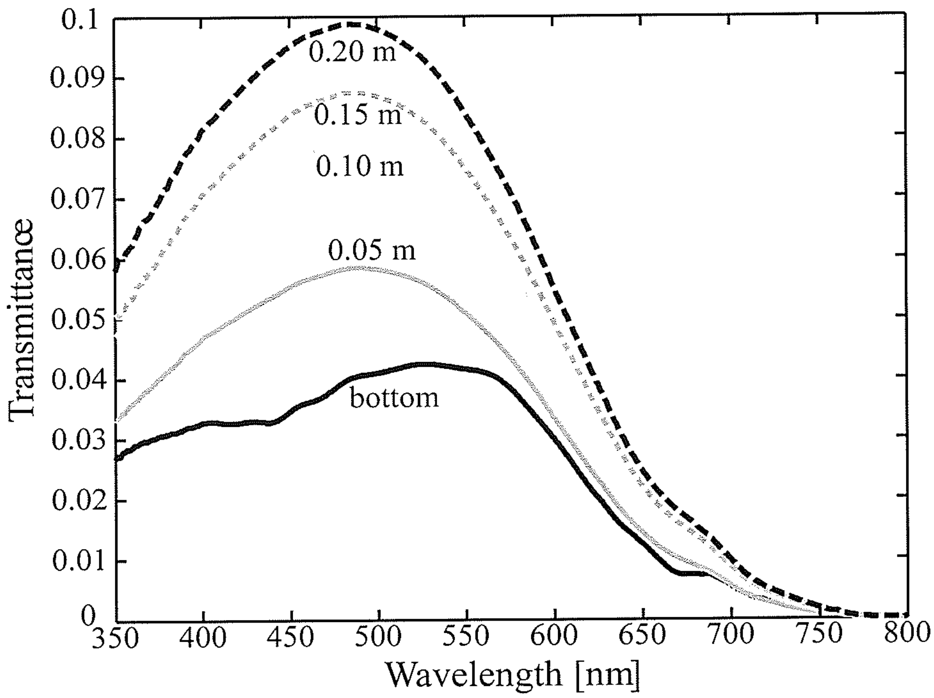

Figure 4.6. Spectral transmittance to the bottom 0-0.20 m of the sea ice cover measured on 28 April. The legend entries indicate distance from sea ice bottom. Magnitudes are relative because of the partial removal of snow from the surface.

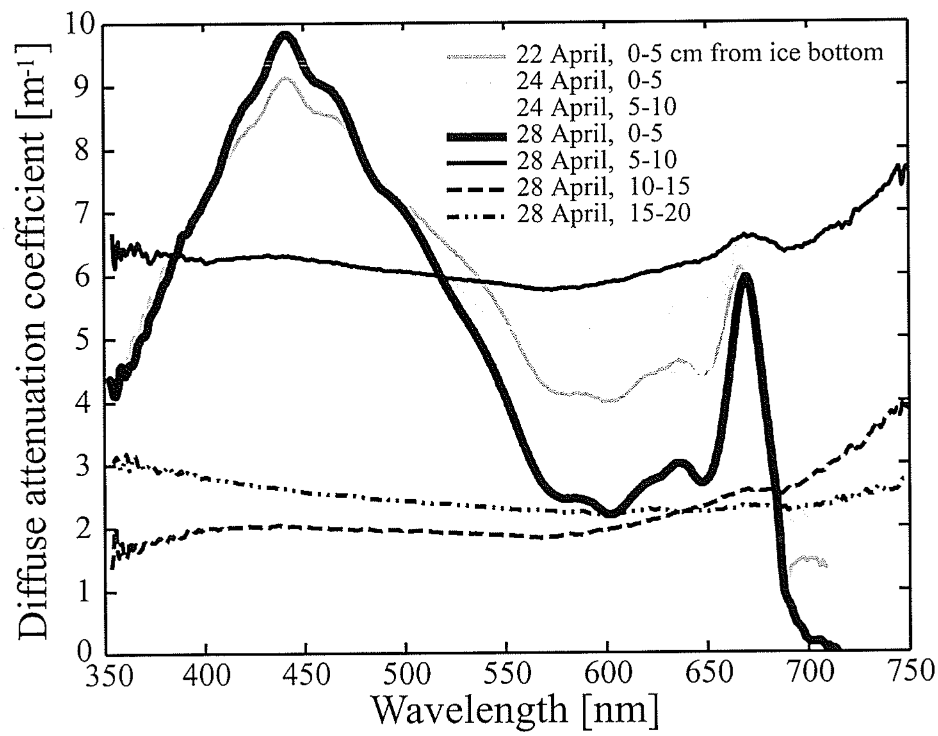

Figure 4.7. Spectral diffuse attenuation coefficients calculated from the irradiance profile measured on 28 April (black curves) with additional examples from other days.

bottom 0.10 m (Figure 4.7). Both the spectra between 0.05-0.10 m and 0-0.05 m show strong evidence of an ice algal influence, e.g., indicated by the chl *a*-related peaks around 440 and 675 nm. The presence of accessory pigments was also evident (e.g., absorption by chl *c* at 460 and 640 nm and by fucoxanthin at 450-550 nm). However, between 0.05-0.10 m substantially less wavelength-dependence was observed, but with all values in the spectra above 5.8 m^{-1}. This indicates less algal absorption compared to the underlying layer and increased scattering due to air and/or brine inclusions, with possible contributions from small particulates such as bacteria or viruses (*Stramski and Mobley*, 1997). For the bottommost layer, on the other hand, the low $K_d(\lambda)$ minima at wavelengths around 600 nm indicate low scattering. This is reasonable, as the high porosity of the bottom skeletal layer would result in relatively few large vertically oriented brine inclusions that would not efficiently scatter the dominantly downward directed radiation. Air bubbles may have also collected up into the ice where brine tubes and channels narrow, possibly as far as the 0.05-0.10 m layer causing an increase in scattering within this overlying layer.

The small $K_d(\lambda)$ above about 680 nm that was measured for the bottommost layer (Figure 4.7) are unrealistic and likely related to the detection limit of the spectroradiometer for the low radiation levels. A longer integration time would have been required to sufficiently increase the resolution of the irradiance spectra measured above 680 nm. Note also that *Roesler and Perry* (1995) used natural fluorescence to explain deviations between estimated and *in situ* reflectance measurements between wavelengths of 660 to 730 nm for a study over open ocean. Similarly, solar stimulated chl *a* fluorescence may have contributed to the low $K_d(\lambda)$ values above 680 nm in this study, particularly for the bottom layers with ice algae.

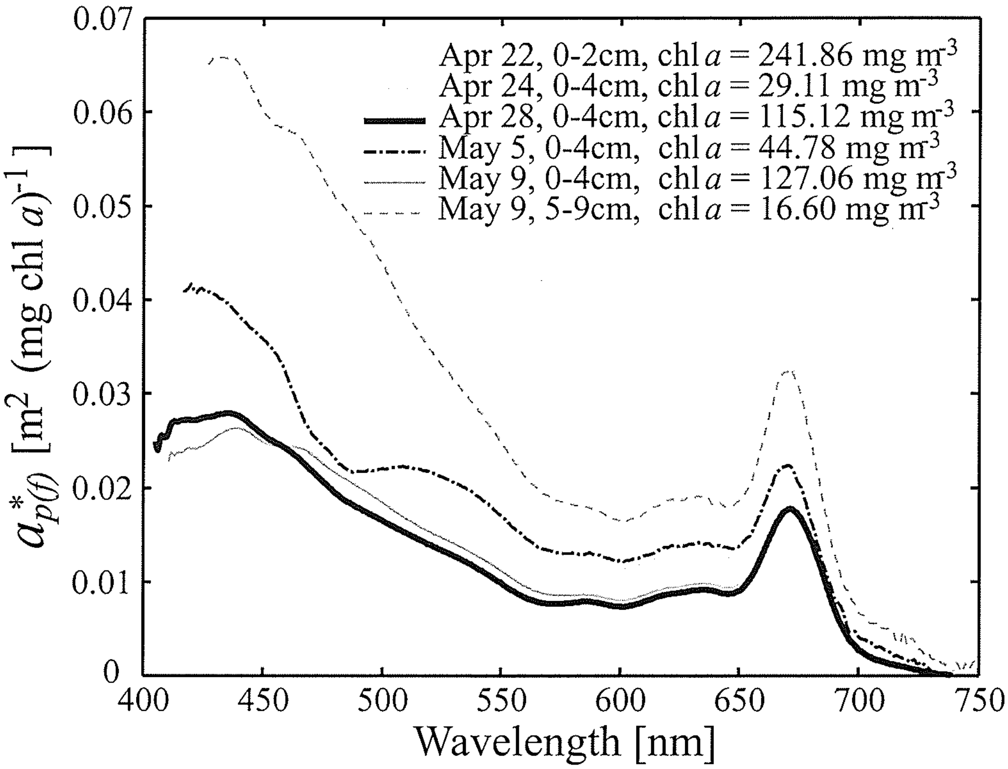

Figure 4.8. Chl *a*-specific particulate absorption spectra measured from particles collected onto GF/F filters. The associated chl *a* concentration is shown in the legend for layers measured from the ice/water interface.

As the *in situ* $K_d(\lambda)$, the particulate spectral absorption coefficient obtained from melted ice samples using the filter technique, $a_{p(f)}(\lambda)$, also show the presence of pigments (Figure 4.8). The magnitude of the chl *a*-specific particulate absorption coefficient, i.e., $a^*_{p(f)}(\lambda) = a_{p(f)}(\lambda)\left[\text{Chl } a\right]^{-1}$, shows an inverse relationship with chl *a* concentration as explained by pigment packaging effects and contribution of accessory pigments (e.g., *Bricaud et al.*, 1995; *Roesler*, 1998). Chl *a* concentrations that were measured from on a parallel filter ranged from 16.60 to 241.86 mg m^{-3} with concentrations increasing towards the ice bottom (Figure 4.8). In addition, the chl *a* related peak at 440 nm was not as pronounced and in some cases had shifted towards shorter wavelengths. These shifts may be indicative of pigment degradation that can occur during the melting and filtering of ice samples (*Stramski*, 1990). Additionally, the strong signal from accessory pigments seen in Figure 4.7 is less marked in the $a_{p(f)}(\lambda)$ spectra. While running the model, it was found that $a_{p(f)}(\lambda)$ could not be used to match model AOPs to those measured because of differences in spectral shape particularly for wavelengths shorter than about 600 nm. Tuning of input IOPs was required as described in the next section.

4.4.3 Model tuning

In this section input parameters required by the DISORT code are inferred by matching the modeled irradiances to the measured. The absorption and scattering coefficient, i.e., $a_{tot}(\lambda)$ and b_{tot}, were obtained by running iterations of the DISORT code until modeled and measured $K_d(\lambda)$ values matched. Spectral absorption by optically active substances shows that water and ice dominates $a_{tot}(\lambda)$ at wavelengths above 700 nm. Because absorption by pure seawater, $a_{sw}(\lambda)$, increases more sharply from 700 nm to 750 nm than that of pure ice, $a_{pi}(\lambda)$ (Figure 4.9b), the model estimated a_{tot} (λ) gave the interesting opportunity to determine the partitioning between absorption by brine and ice (*Warren*, 1984; *Smith and Baker*, 1981). That is, the brine volume fraction, v_b, in Eq. 4.4 was adjusted during the iterative process to obtain a correct increase with wavelength above 700 nm. However, due to unrealistically low values of the measured $K_d(\lambda)$ at wavelengths above ~680 nm in the bottommost layer (Figure 4.7), an alternative approach was needed to estimate the partitioning between absorption by brine and ice. Firstly, the spectral shape above 600 nm of $a_{imp}(\lambda)$ in Eq. 4.4 was assumed to be the same as $a_{p(f)}(\lambda)$ for the 0-0.04 m layer measured on 28 April (Figure 4.8). The magnitude of $a_{imp}(\lambda)$ was then adjusted (using chl *a* concentration as a multiplier) together with b_{tot} during the iterations of the model until the model estimated $K_d(\lambda)$ matched the measured $K_d(\lambda)$ at 600 nm and 675 nm. These wavelengths were chosen to represent the maximum and minimum absorption by chloroplastic pigments in the algae, as observed in the dataset (see Figures 7 and 8). Thus, the introduction of $a_{p(f)}(\lambda)$ as another independent variable allowed for the determination of b_{tot} at 600 nm.. Secondly, as scattering in the bottommost layer was assumed to be solely by brine inclusion and the density chosen to be constant at 920 kg m^{-3}, it was possible to obtain estimates of v_b and v_a, and thus $a_{tot}(\lambda)$ at wavelengths above 680 nm from Eqs. 4.4 and 4.5.

Since temperature is more reliably measured, v_b was tuned by changing the input salinity. A good fit between estimated and measured $K_d(\lambda)$ was obtained when the salinity in layers 0-0.05 m and 0.05-0.10 m were adjusted from a measured ~6.6‰ to 9.5‰ and ~5.1‰ to 7.5‰ (Figure 4.5), respectively. This may account for brine drainage that occurred during sampling. No adjustment was needed for the 0.10-0.20 m layer which had a measured salinity of about 4.5‰. The associated v_b, calculated using equations by *Cox and Weeks* (1983) and *Leppäranta and Manninen* (1988), are summarized in Table 4.1 for the three layers. The air volume fractions, v_a, also shown in Table 4.1, were estimated by keeping the density fixed at 920 kg m^{-3}. Thus the estimated total porosities of the three layers from the ice-water interface upwards were about 40%, 25% and 11%, respectively. Such high porosities are not reflected in the thin sections seen in Figure 4.4, which illustrate some of the structural changes occurring within the ice sample as its temperature is decreased during storage and analysis.

With the above described adjustments to the bulk composition and $a_{tot}(\lambda)$ of the sea ice, b_{tot} was obtained for each layer (Table 4.1). The results are in general agreement with a b_{tot} of

341-448 m^{-1} suggested by *Light et al.* (2004) for the high temperature regime (T > –8 °C), except for the uppermost layer with a b_{tot} of about half the magnitude. Note, however, that the temperature and salinity values of this uppermost layer were the most comparable to the ice sample studied by *Light et al.* (2004). *Hamre et al.* (2004) reported b_{tot} > 1000 m^{-1} near the ice bottom, which exceeds values found here. This variability in reported scattering values show that additional detailed observations comparing microstructure to optical properties are needed to understand the nature of radiative transfer in sea ice.

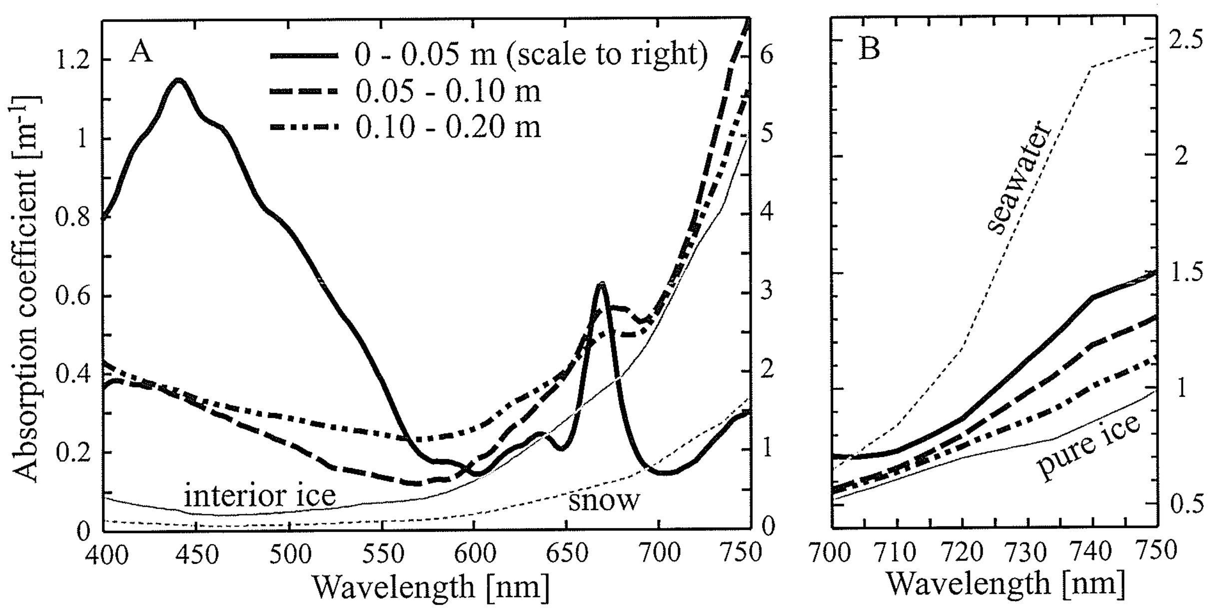

Figure 4.9. (a) The total spectral absorption coefficients obtained for three bottom sea ice layers through iterations of the radiative transfer model (note the change of scale for the bottommost layer). The dashed lines show the absorption coefficients used in the above ice and snow cover. (b) Close-up of the absorption within 700-750 nm, with the thin dashed and solid lines showing the absorption coefficients for the clearest natural waters (*Smith and Baker*, 1981) and pure sea ice (*Warren*, 1984), respectively, and the thicker lines being the same as in (a).

Table 4.1. Values obtained through radiative transfer model iterations for layers denoted by their distance from the ice/water interface. The density was kept constant at 920 kg m^{-3}.

Layer	0-0.05 m	0.05-0.10 m	0.10-0.20 m	[Unit]
v_b	36.9	23.0	10.4	[%]
v_a	3.8	2.4	1.0	[%]
$[r_{eff}]_{brine}$	1.000	0.606	0.717	[mm]
$[r_{eff}]_{air}$	∞	0.460	0.505	[mm]
g_{tot}	0.997	0.980	0.980	
b_{tot}	369.8	430.9	165.3	[m^{-1}]

The next step was to compare b_{tot} to the refined v_b and v_a estimates using Eq. 4.5. Detailed information on size distribution and number density was not possible to obtain for the observed ice samples at their *in situ* temperatures. Therefore, the approach by *Jin et al.* (1994) to estimate the brine inclusion number density, $N_{brine} = 0.6 \times S$, where S is sample salinity, was adopted to fix the effective radius, r_{eff}, for brine and air inclusions (*Hamre et al.*, 2004). However, it was found that this approach overestimated the scattering within the bottommost layer because the high v_b led to very high scattering. Therefore, r_{eff} in this layer was set manually. With the assumed v_b and v_a values reported above for a constant density of 920 kg m^{-3}, the required r_{eff} are summarized in Table 4.1. In the bottommost layer, the air bubble r_{eff} was set to approach infinity, which causes scattering from air inclusions to disappear (see Eq. 4.5). This result can also be achieved by raising the density of the sample until $v_a = 0$. These r_{eff} are realistic and comparable to observations by *Light et al.* (2003) within this temperature regime.

Furthermore, it may be reasonable to assume $v_a = 0$ as the very porous and interconnected brine inclusions would cause air inclusions to move upward in the sea ice. However, a number of combinations of brine and air inclusion r_{eff} values may be used to obtain b_{tot} and related using the similarity parameter (e.g., *van de Hulst*, 1980; *Light et al.*, 2004). Furthermore, it is not currently known to what extent particulate impurities, such as algae, bacteria and viruses, contribute to scattering. For particulates in the water column, e.g., *Stramski and Mobley* (1997) reported highly varying spectral scattering coefficients. Again, information on structural causes for the scattering is limited by inadequate data sets. Innovative ways to observe structural properties of sea ice at warm temperatures and/or *in situ*, e.g., *Mundy et al.* (2007), are warranted.

The absorption spectra (Figure 4.9a) show the effect of ice algae absorption, however, radiative transfer within these layers was still strongly influenced by scattering. For example, $K_d(\lambda)$ values (Figure 4.7) were approximately an order of magnitude larger than $a_{tot}(\lambda)$ (Figure 4.9) for layers above 0.05 m and nearly double for the bottommost layer. Furthermore, note that the absorption coefficient for impurities, $a_{imp}(\lambda)$ (Eq. 4.4), can be obtained by removing the contribution by seawater and ice, i.e.,

$$a_{imp}(\lambda) = a_{tot}(\lambda) - v_b a_{sw}(\lambda) - (1 - v_b - v_a) a_{pi}(\lambda). \tag{4.8}$$

$a_{imp}(\lambda)$ can be further partitioned into particulate and dissolved components:

$$a_{imp}(\lambda) = a_p(\lambda) + a_{CDOM}(\lambda), \tag{4.9}$$

where $a_p(\lambda) = a_{CHL}(\lambda) + a_{NAP}(\lambda)$ is the particulate absorption coefficient composed of contributions from chl *a* containing algae (CHL) and non-algal particulates (NAP), and $a_{CDOM}(\lambda)$

the absorption by CDOM. However, $K_d(\lambda)$ and $a_{p(f)}(\lambda)$ (Figures 6 and 8) show little evidence for any presence of CDOM, whose absorption typically increases exponentially with decreasing wavelength with an exponential slope factor, S_{CDOM}, of around 0.018 nm^{-1} (*Guéguen et al.*, 2005). The model calculated $a_p(\lambda)$ for the three layers, assuming negligible contribution by CDOM, show large variations in magnitude mostly due to the abundance of algae causing an up to 17-fold increase in absorption in the bottommost layer compared to layers higher up in the sea ice (Figure 4.10).

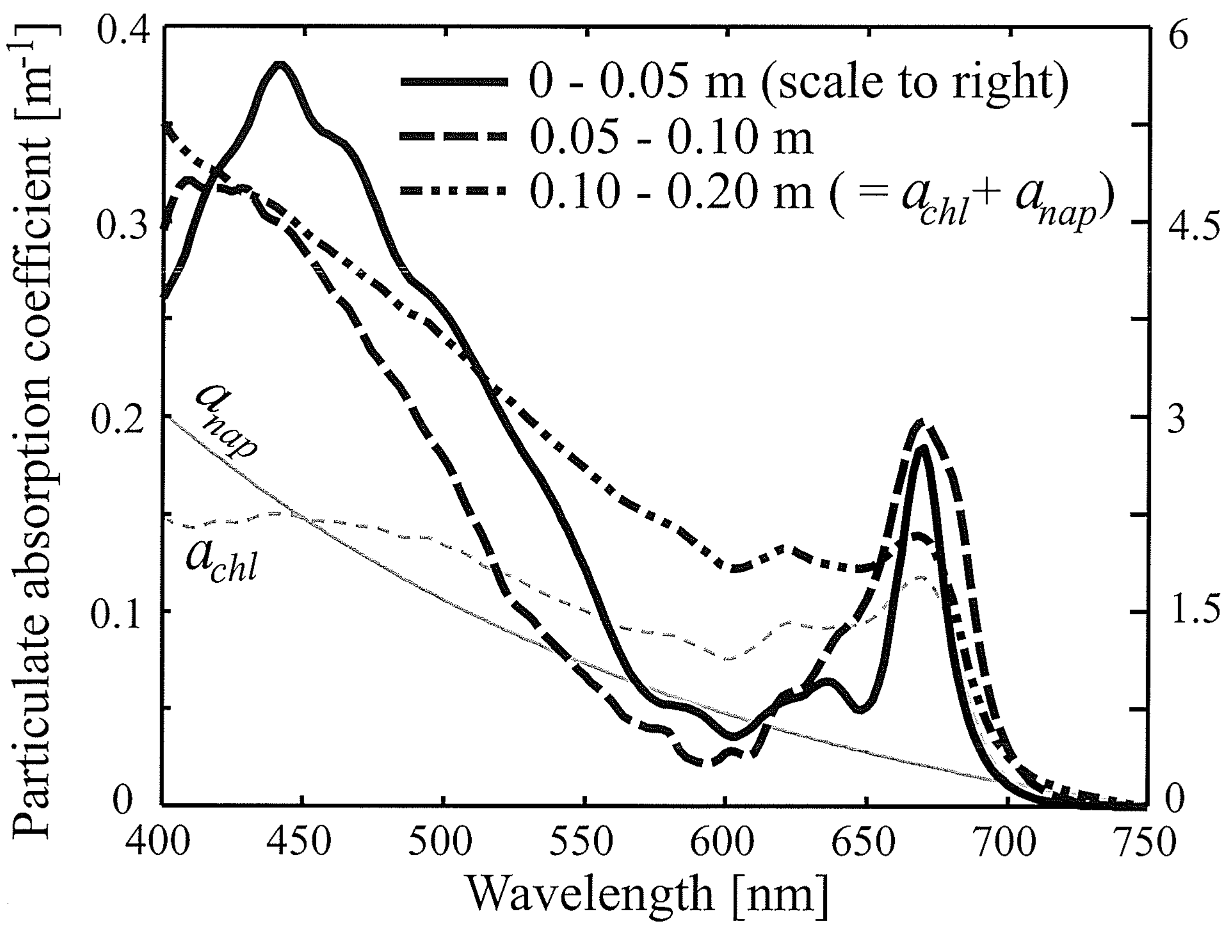

Figure 4.10. Particulate absorption coefficients for the three bottom layers required to match field results.

The spectral shape of $a_p(\lambda)$ indicate that the optical properties of the 0-0.05 m and 0.05-0.10 m layers were strongly influenced by ice algae absorption. Furthermore, the algae community within the bottommost layer (0-0.05 m) appears healthy as indicated by absorption peaks centered at 440 and 675 nm (e.g., *Bricaud et al.*, 1995; *Roesler and Perry*, 1995). However, within the overlying layers the absorption peaks near 440 nm appear to have shifted towards shorter wavelengths within the 0.05-0.10 m layer and were not present in the 0.10-0.20 m layer. Ice thickness increased approximately 0.05 m over the study period and, therefore, it may be suggested that the spectral shape of $a_p(\lambda)$ within the 0.05-0.10 m layer was due to remnants of a previously active and healthy bottom ice algae community that became trapped within the ice as it grew. This suggestion is corroborated by observations that ice core sections collected more than 0.03 m from the ice bottom usually have a higher proportion of empty algal cells compared to the bottommost skeletal layer (M. Gosselin, pers. comm.). In the 0.10-0.20 m layer, no absorption peak can be seen in the wavelength region between 400-450 nm. This may indicate that algal cells present within this layer have to some extent died and turned into detritus (or NAP) and that their chloroplastic pigments have degraded either physically or through activity of grazers and decomposers (e.g., *Lizotte*, 2003). Some pigments are, however, still present within the layer as indicated by the chl *a* peak at 675 nm in the $a_p(\lambda)$ curve. NAP absorbs radiation in a similar fashion to CDOM, i.e., a_{NAP} increases exponentially with decreasing wavelength (e.g., *Roesler and Iturriaga*, 1994). As this appears to be the case for $a_p(\lambda)$ in the 0.10-0.20 m layer, it may be a valid assumption to partition $a_p(\lambda)$ into contributions by CHL and NAP (Figure 4.10). The absorption curve for NAP in Figure 4.10 is described by $a_{NAP}(\lambda)$ =

0.1576 exp[S_{NAP} (440 - λ)], where the slope S_{NAP} = 0.005 and the multiplier result in a wavelength dependence that correspond relatively well with $a_p(\lambda)$ at $\lambda < 550$ nm. This also results in $a_{CHL}(\lambda)$ with a peak at 438-442 nm. These results confirm that sea ice absorption is dominated by the healthy ice algae community immediately above the ice-water interface as concluded by, e.g., *Perovich et al.* (1993). However, the results also point towards the secondary importance of a decomposed biological community further up within the ice. A more detailed vertically resolved bio-optical model may need to consider the influence of algae related absorption further within the sea ice.

4.5 Conclusions

Irradiance spectra measured at vertical increments within the bottom layers of landfast sea ice in Franklin Bay during early spring (22 April to 9 May 2004) allowed an estimation of sea ice IOPs (absorption and scattering coefficients) using the DISORT radiative transfer code. To the authors' best knowledge, the inference of IOPs using an iterative modeling approach is adopted here for the first time in a sea ice environment. In the model, the scattering coefficient, *b*, was assumed to be wavelength independent within visible wavelengths, while any wavelength dependence was accounted for by the absorption coefficient $a_{tot}(\lambda)$. The obtained IOPs were discussed in terms of observed physical (temperature, salinity and density) and biological (algal spectral absorption) properties of the 1.8 m thick first-year sea ice cover. These physical properties can be considered typical of sea ice close to the ice-water interface.

The interesting possibility to estimate the brine volume fraction, v_b, optically was explored in the model work. $a_{tot}(\lambda)$ at longer wavelengths is dominated by $a_{sw}(\lambda)$ and $a_{pi}(\lambda)$

(Figure 4.9). Because $a_{sw}(\lambda)$ increases more sharply than $a_{pi}(\lambda)$ from 700 to 750 nm, realistic ν_b could be deduced from the spectra. Model results suggest that about a 2-3 ‰ salinity reduction occurred in the bottommost 0.1 m of the sea ice due to brine drainage after sampling, while drainage was negligible in the 0.1-0.2 m layer.

Additionally, the scattering coefficient, b_{tot}, could be deduced from these calculations. For the two bottommost 0.05 m layers, b_{tot} was around 400 m^{-1}, while at the 0.1-0.2 m layer b_{tot} decreased to 165 m^{-1}. Using $a_p(\lambda)$ combined with a wavelength independent b_{tot} as inputs to DISORT adequately explained the radiative transfer near the bottom layers of first-year sea ice. Scattering processes within the sea ice can be described by Mie scattering theory using spherical inclusions, however, the assumption of sphericality of at least brine inclusions does not characterize the microstructure realistically, especially at the relatively high temperatures and porosities found near the ice-water interface where brine inclusions are highly interconnected. Once sufficiently detailed microstructural observations exists, the volume-area equivalent spheres theory (*Grenfell and Warren*, 1999), used by e.g. *Light et al.* (2004), can be utilized to further explore structural-optical relationships.

As is typical for landfast first-year sea ice, ice core sampling and irradiance measurements revealed very low concentrations of ice algae above the bottom 0.05 m of the sea ice. For the bottom layer, chl *a* concentrations ranged from 16.6 to 242 mg m^{-3} and were more than an order of magnitude less in overlying layers. This algal layer had a marked effect on the spectral distribution and magnitude of transmitted irradiance beneath the ice.

Particulate absorption spectra, $a_{p(f)}(\lambda)$, from melted ice samples showed that the chloroplastic pigments may have been degraded in the period between sampling and measurement. That is, the spectral shape of $K_d(\lambda)$ could not be explained by the measured $a_{p(f)}(\lambda)$ for the bottommost ice algae layer using the filter technique. Interior ice layers did, however, show similar spectral shapes in absorption to measurements made from melted samples providing evidence of pigment degradation within these layers. Iterations of DISORT to match the *in situ* $K_d(\lambda)$ resulted in reasonably shaped estimates of $a_p(\lambda)$. Based on the spectral shape of the modeled $a_p(\lambda)$, it was suggested that the ice algae within the bottommost layer were healthy, while pigment degradation modified the spectral absorption increasingly with distance from the ice-water interface.

CHAPTER 5: Surface albedo and transmittance observations of Hudson Bay landfast sea ice during the spring melt

5.1 Preface

In this chapter I address research questions III and IV. A version focusing on the components of the surface energy balance and spectral albedo has been published as: Ehn, J. K., M. A. Granskog, T. Papakyriakou, R. Galley and D. G. Barber (2006), Surface albedo observations of Hudson Bay landfast sea ice during the spring melt, *Ann. Glaciol.*, 44, 23-29, Reproduced with permission of the International Glaciological Society. I was responsible for the maintenance of the meteorological station and the spectral radiation measurements during the time I was in Button Bay, i.e. April to early May 2005. I conducted physical snow and ice sampling in collaboration with the co-authors. Furthermore, I had a lead role in data analysis and the manuscript writing.

5.2 Introduction

The ice albedo feedback mechanism, as a key factor affecting the energy and mass balance of the Arctic, has frequently been emphasized in climate studies (e.g., *Curry et al.*, 1995; *Perovich et al.*, 2002). During the winter, the sea ice surface albedo is generally high (>0.8) since a layer of dry snow mostly covers the sea ice. With spring, increased shortwave radiation levels result in sufficient absorption within the sea ice/snow volume to trigger melting and a consequent reduction in albedo. Synoptic weather events, such as inflow of warm air masses and/or rain events, significantly alter the surface albedo (*Ohmura*, 1982; *Robinson et al.*, 1986). With the advancing melt season, the snow cover gradually disappears and surface melt puddles form. With these changes, the net shortwave radiation contributes an increasing portion of the net radiation at the surface.

Recent albedo investigations in the high Arctic have demonstrated the importance of systematic time series observations (*Perovich et al.*, 2002). Time series observations are central to the understanding of the seasonal development of sea ice/snow covers, and for physical/biogeochemical studies. The Arctic seas exhibit strong seasonal variations in albedo largely due to the sea ice cover, thus any changes in the snow and ice cover would impact the global albedo and thereby influence climate. The sub-Arctic regions are a particularly good place to study the time-dependence of radiative exchange due to the strong diurnal forcing in radiation and the advection of warm air masses which increases temperature and occurrences of rain. A temporal study of radiative exchange at the surface is thus warranted for these sub-Arctic seas and knowledge gained here may also be useful for near future arctic conditions if climate variability/change progresses as projected (*ACIA*, 2005; *Johannessen et al.*, 2004).

5.3 Site description

5.3.1 Site description

We present data that was collected over a period of 46 days, from 19 March (day of year (YD) 78) to 3 May (YD 123) 2005, on the landfast sea ice in Button Bay (58° 48.5 N, 94° 17.2 W, near Churchill, Manitoba), in western Hudson Bay (Figure 5.1a). The data consists of a

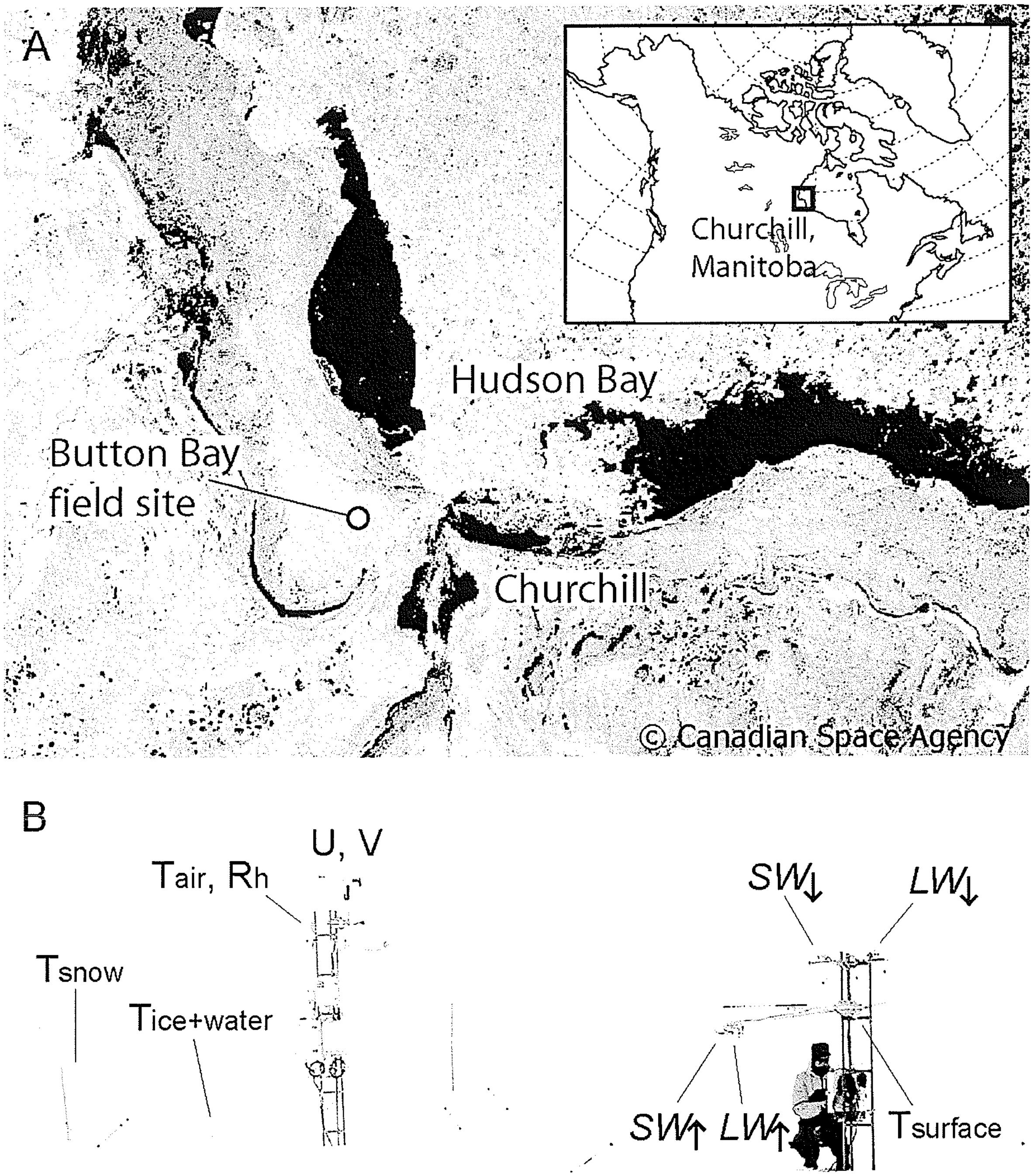

Figure 5.1. (a) The Button Bay study area in Hudson Bay, and (b) the surface energy balance station. The satellite image in (a) is a Radarsat SAR image taken on 17 April. The surface type surrounding the field site shows the extent of the landfast sea ice. A flaw lead polynya has formed between the fast ice edge and the mobile pack. The photograph in (b) was taken on 27 April (YD 117) (photo M.A. Granskog).

continuous record of the sea ice surface energy balance at a fixed site (Figure 5.1b) and a series of spectral albedo measurements at six adjacent locations on the sea ice. At two of the locations, the spectral albedo observations were substantiated by coincident measurements of spectral transmittance (note: transmittance measurements not included in the published version). The observations were a part of a pilot study for theme 3 of ArcticNet (http://www.arcticnet-ulaval.ca). To the best of the author's knowledge, these are the first ever of such time series measurements along the western side of Hudson Bay over a typical spring period. In this chapter, a description of the surface radiation balance and use the surface temperature as a proxy integrator for the overall surface energy balance is provided.

The ice cover in Hudson Bay is seasonal. The bay becomes fully ice covered during winter, and ice-free from mid-August to late October (*Wang et al.*, 1994; *Gough et al.*, 2004). In the Churchill region, the ice grows typically 1.3 to 2.0 m thick and ice breakup occurs on average in early July (*Stirling et al.*, 2004). Under predominantly northwest winds the ice pack moves to the southeast, removing ice from the northwest and encouraging new ice growth. However, changing winds may rapidly move the mobile pack ice onshore. Strong winds and tidal mixing result in reoccurring polynyas and leads in the western Hudson Bay. High tides (up to 4 m between low and high water at Churchill port) further aid in breaking up and piling ice floes against the coast or landfast ice boundary. The sea ice in Button Bay thus consisted of a collection of advected ice floes, which during early winter adhered into a continuous landfast ice sheet. Sharp, uneven surface features, rubble fields and pressure ridges were common in the area in 2005. However, in order to obtain more representative temporal samples, the sampling stations were located on relatively undeformed ice in Button Bay (Figure 5.1b). At the time of the experiment, the level ice reached its maximum thickness of 1.5 m, although large horizontal variability was observed in the area. At the location of the meteorological site, ice thickness increased from roughly 1.2 m to 1.5 m between YD 96 and 123).

Before the field program commenced (i.e. from YD 1 to 78) the air temperature averaged –25 °C (Fig. 5.2a) (National Climate Data and Information Archive, Environment Canada). Two significant low-pressure systems, centered on YD 33 and YD 62, respectively, caused air temperatures to rise above –10 °C, and for 2-3 hours even above 0 °C in the case of the former. At the start of the experiment winter conditions prevailed. Air temperatures averaged –19 °C. The ice was snow covered as snow precipitation was ongoing at the time. On YD 87 the thickness of the snow cover was 0.26 m and could generally be characterized as dry snow. These conditions continued about 10 days into the experiment (i.e., YD 88), after which rapid changes in the surface properties occurred. In this study, the focus is on the period that followed (until YD 123) during which the ice evolved from winter conditions to the early stages of melt pond formation. The oceanic heat flux did not significantly affect the sea ice energy balance during the measurement period, as the water column below the sea ice was completely mixed and near the freezing point (unpublished data). The main environmental conditions with effects on the surface albedo were identified as a) advection of warm air masses, b) cloud cover, c) precipitation in solid phase, and d) precipitation in liquid phase.

5.3.2 Field observations

The surface meteorology station at the Button Bay field site was assembled on YD 78 and recovered on YD 123 (Figure 5.1b). The monitored parameters included air temperature and relative humidity, wind speed and direction, turbulent fluxes of heat, water vapour, momentum and CO_2 in the atmospheric boundary layer, ice and snow temperatures using thermocouple strings extending through the ice/snow cover, surface skin temperature and the components of the radiation balance. In this study the focus is on the latter two.

The components of the radiation balance are summarized as

$$Q^* = SW^* + LW^* = SW_{\downarrow} - SW_{\uparrow} + LW_{\downarrow} - LW_{\uparrow}, \tag{5.1}$$

where Q^* is the net all-wave radiation, SW^* the net of the incident and reflected shortwave solar radiation (i.e., $SW_{\downarrow}$ and $SW_{\uparrow}$), and LW^* the net of the incoming and outgoing longwave radiation (i.e., $LW_{\downarrow}$ and $LW_{\uparrow}$). Positive net values indicate energy input to the surface.

The radiation balance was measured at 2-second intervals and stored as 15-minute averages using two pyranometers (The Eppley Laboratory, Inc., Model PSP, wavelength range from 285 to 2800 nm) and two pyrgeometers (The Eppley Laboratory, Inc., Model PIR, range from 3.5 to 50 μm) for down- and upwelling shortwave and longwave radiation, respectively. The sensors were mounted about 1.5 m above the surface facing south (Figure 5.1b). The surface below the radiometers was of the white ice type (see below). During post processing, the longwave radiation was corrected for dome and case temperatures using methods described in *Marty et al.* (2003). Frost and water droplets were removed from the sensor domes before 8:00 every morning. For most weather conditions the sensor domes remained clear from frost or water droplets during daytime, however, during rain events it was not possible to keep domes clear and these data may be affected by the water droplets. At the start of the experiment (YD 78) sunrise was around 6:30 local time and sunset around 18:30. The solar zenith angle was about 78° and 79° at 8:00 and 17:00, respectively. Thus to reduce measurement errors due to the pyranometers imperfect cosine response at high zenith angles, broadband albedos were calculated from $SW\downarrow$ and $SW\uparrow$ data for periods between 8:00 and 17:00 (*Pirazzini*, 2004; *Warren*, 1982). At the end of the experiment sunrise and sunset were around 4:30 and 19:45, respectively and daytime (8:00-17:00) solar zenith angles were smaller than 68°.

Coincident surface skin temperature was obtained at the meteorology station using an infrared temperature transducer (Everest Interscience, Inc., Model 4000.4ZL). The instrument operates in the 8-14 μm spectral range with an accuracy of ±0.5 °C and a resolution of 0.1 °C for the temperature range between –40 and +100 °C. It was pointed with a ~45° viewing angle towards the surface below the radiation sensors. The surface temperature is important as it can be regarded as an integrator of surface energy fluxes, i.e., radiation and turbulent fluxes from above and conductive fluxes from below.

The spectral albedo, $\alpha(\lambda)$, is the fraction of incident shortwave irradiance that is backscattered from the surface:

$$\alpha(\lambda) = \frac{SW_{\uparrow}(\lambda)}{SW_{\downarrow}(\lambda)}, \tag{5.2}$$

where λ is the wavelength. The albedo is of interest as it is a measure of solar radiation absorbed by the snow, sea ice and ocean. The wavelength-integrated albedo, α , is commonly used in climatological studies:

$$\alpha = \frac{\int \alpha(\lambda) SW_{\downarrow}(\lambda) d\lambda}{\int SW_{\downarrow}(\lambda) d\lambda}. \tag{5.3}$$

In this chapter, the wavelength-integrated albedo is defined to have integration limits between 350 and 1050 nm, which are the spectral limits of the dual-headed spectroradiometer (FieldSpec, Analytical Spectral Devices, Inc., Boulder, Colorado) used, while the broadband albedo to have integration limits encompassing the nearly the entire solar shortwave spectrum, i.e., from 285 to 2800 nm. The spectral albedo was obtained with the spectroradiometer by alternating between up- and downwelling irradiance measurements. The cosine collector was attached to the end of a 1.5-m-long rod extending from a tripod. The setup was kept horizontal about 0.7 m above the surface by using a bubble level. The footprint, from where roughly 90 percent of the measured upwelling radiation originates, is thus within a circle with a radius double the height above the surface (in case of isotropic incident radiation). A second cosine collector (180° field-of-view) was used for coincident monitoring of changes in incoming spectral irradiance. Spectral albedo was repeatedly measured at six sites considered representative of the area from YD 97 onwards. Three of the sites were classified as blue ice sites and three as white ice. All six sites chosen were large and homogeneously composed of only one ice surface type. The blue and white ice sites thus represented a minimum and maximum albedo in the measurement area. The blue ice sites tended to loose their snow cover quickly and were darker in their appearance compared to the white ice sites which appeared white throughout the experiment and formed mounds of snow or drained soft granular ice.

Similarly, the downwelling irradiance measurements above and below the ice were used to calculate the bulk spectral transmittance, $T(\lambda)$. Details on the methods used are provided in subsection 6.3.1.

5.4 Results and Discussion

5.4.1 Seasonal evolution

From YD 78 to 88, air temperatures remained below –10 °C, averaging –19 °C. The period shows large variations in the measured broadband albedo due to variable weather conditions (mainly snowfall, snowdrift, freezing fog and cloud coverage). On YD 89 conditions changed dramatically when a low-pressure system moved in increasing $LW\downarrow$ and causing heavy snowfall and freezing rain (Figure 5.2). This resulted in a crusty top layer of snow with a density of 413 kg m^{-3} on YD 90, an increase from 366 kg m^{-3} on YD 88. The next low-pressure event occurred two days later on YD 92. This time air temperatures rose above 0 °C and with significant rainfall to the surface (28 mm of total precipitation observed at Churchill meteorological station, Environment Canada). Also the surface skin temperature rose for the first time of the year above 0 °C (Figure 5.2d). Subsequently ice lenses formed at various levels in the snow pack. Following these synoptic scale weather events the broadband albedo dropped from a high of 0.74 (YD 89) to 0.71 (YD 92) and to 0.64 (YD 95) in six days (Figure 5.2d). These events mark the beginning of the melt season.

Rainfall occurred on five occasions (Figure 5.2b). The most significant of these took place around YD 100-101 and was accompanied by thunderstorms. All rain events were marked by increased levels of $LW\downarrow$ (Figure 5.2b) associated with the cloud cover, increased humidity and warmer air. Recorded values ranged from 310 to 332 Wm^{-2}. During snowfall events $LW\downarrow$ was generally below 310 Wm^{-2}. As the cloud covered conditions were accompanied by low levels of $SW\downarrow$, little difference was observed in the daily averaged net all-wave radiation, Q^*; the daily

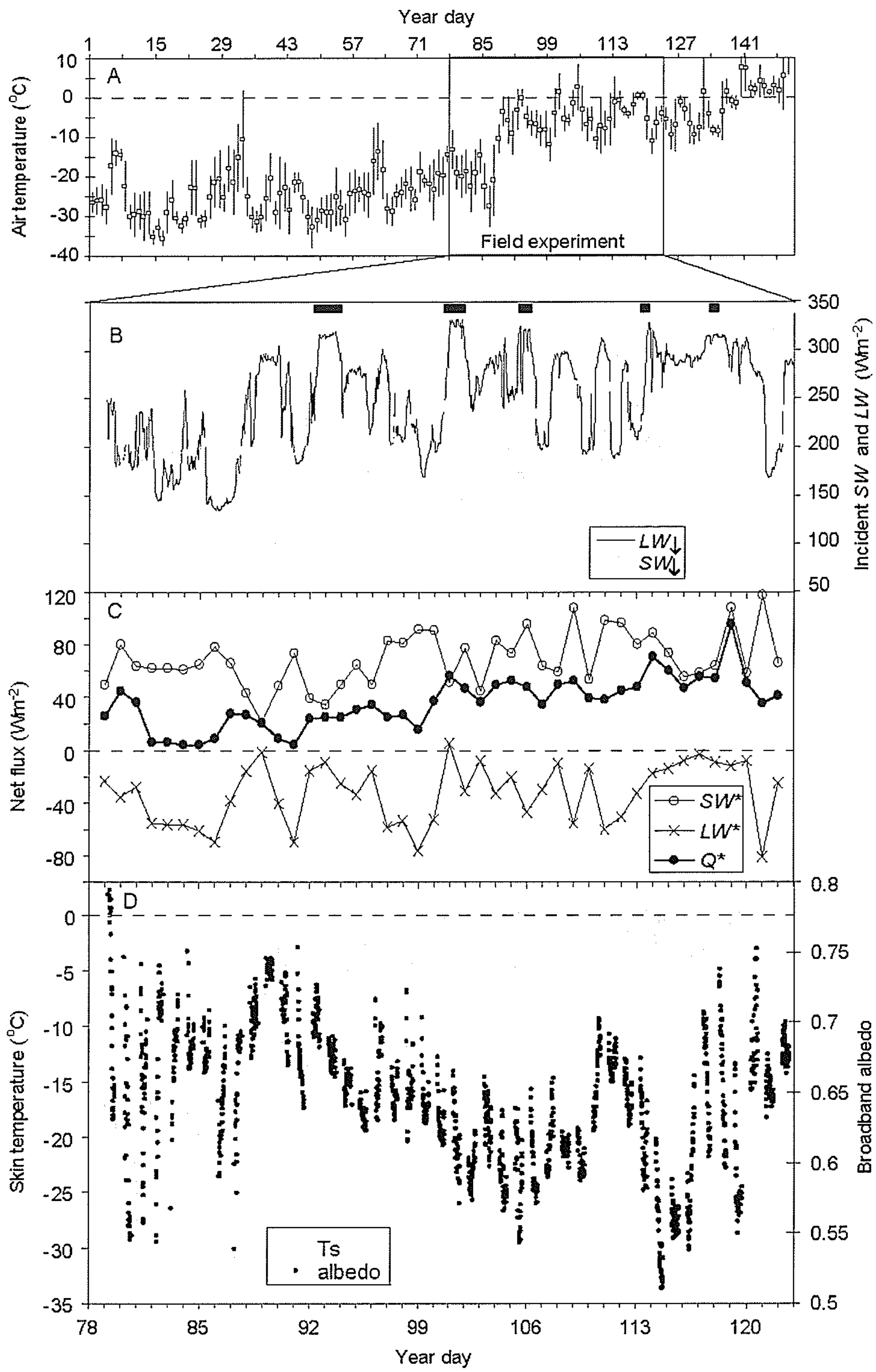

Figure 5.2. (a) The daily maximum, mean and minimum air temperatures (Ta) from Churchill (Environment Canada). (b) Hourly averages of incoming longwave radiation ($LW\downarrow$) and daily averages of incoming shortwave radiation ($SW\downarrow$) from 19 March (YD 78) to 3 May 2005 (YD 123). Also shown in the upper part are the occurrences of snow (grey) and rain (black). (c) Daily averages of the net shortwave (SW^*), longwave (LW^*) and all-wave (Q^*) radiative energy over the surface. (d) 15-min averages of the surface skin temperature (Ts) and the broadband albedo.

averaged components for SW^* and LW^* tend to cancel each other out (Figure 5.2c). Concurrently there was a subtle seasonal rise in the daily averages of Q^* that may be described by 1.09·YD – 74.1 ($R^2 = 0.52$), while over the same period the slopes for SW^* and LW^* are 0.64 and 0.45, respectively, with weak correlation ($R^2 = 0.16$ and 0.06). For the duration of the experiment, the net radiative energy balance was positive, i.e., the surface received more radiative energy than it emitted/reflected. Prior to the thunderstorm on YD 100-101, Q^* averaged 21.5 Wm^{-2}, and afterwards 50.5 Wm^{-2} – an indication of the physical changes that occurred in the snow due to the rain.

After the first rain event and the subsequent formation of ice lenses, measurements of the snow properties were increasingly difficult to conduct. Some sporadic layers between the ice lenses could however be measured in the period after YD 101. On YD 101 the density of these individual layers ranged from 250 to 470 kg m^{-3}. Bulk density measurements for the snow pack resulted in 750 kg m^{-3} for a snow depth of 0.25-0.27 m on YD 103 and 650 kg m^{-3} for a 0.21 m snow depth on YD 105. By YD 105 the ice surface had fractionated into areas of blue ice and white ice, i.e., depressed areas of bare ice and mounds with a snow cover over the ice (Figure 5.3a). On this day an up to 1-cm-deep layer of melt water was observed on the bare ice. On YD 110 the snow pack on the white ice was modified all the way through by freeze-thaw processes and composed mostly of ice lenses. The snow/ice interface was difficult to determine as metamorphosed snow formed superimposed ice (based on stable oxygen isotopic composition (unpublished data); see, e.g., *Eicken et al.*, 1994) which merged with the surface ice causing the interface to become highly uneven (Figure 5.3b-c). From YD 110 snow temperatures, as measured with the thermocouple strings, were adversely affected by transmitting solar radiation, leaving the surface skin temperature as the best indicator for thermodynamic and metamorphic changes in the snow pack (Figure 5.2d).

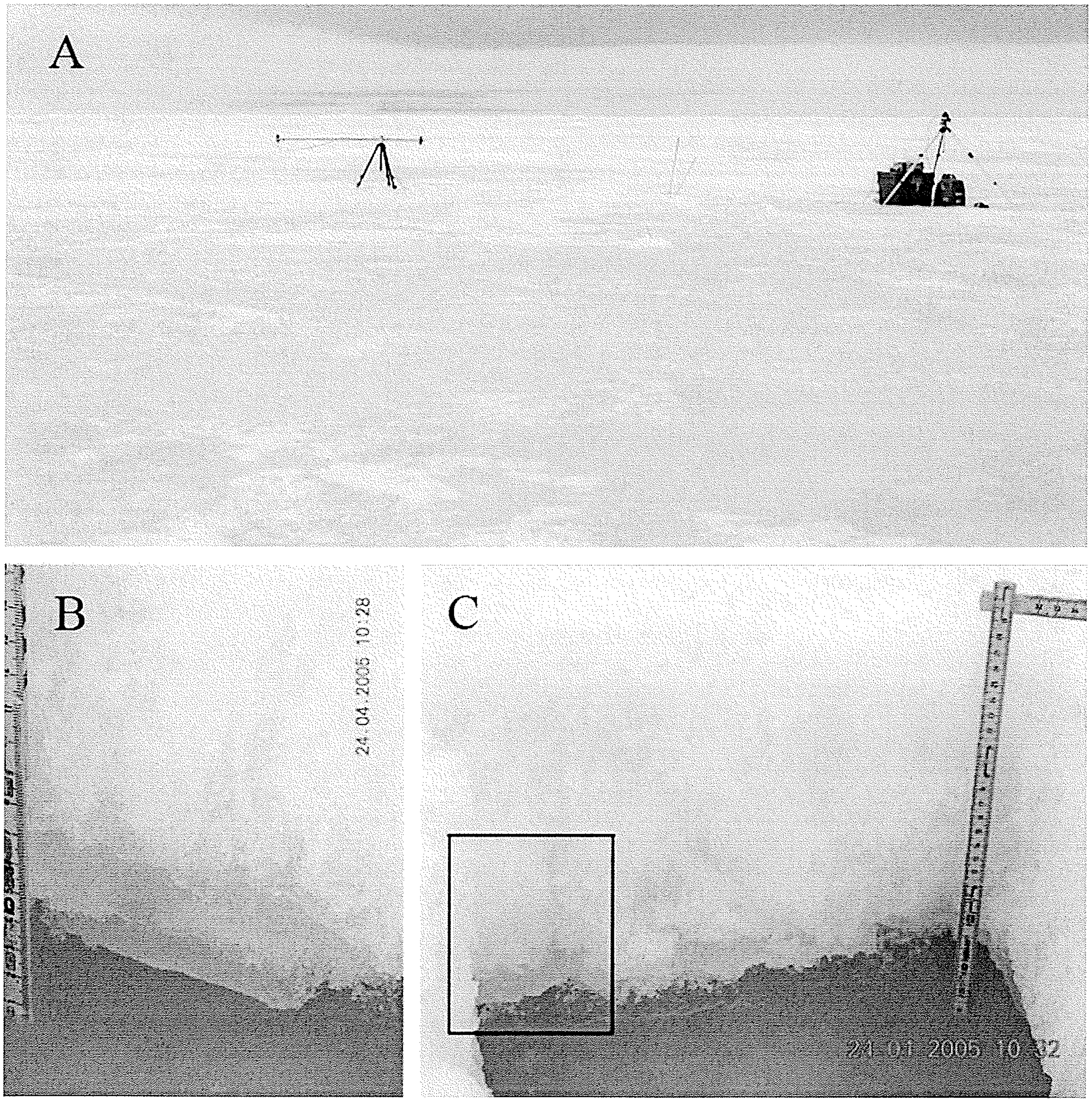

Figure 5.3. Surface conditions on YD 114. (a) Spectral albedo measurement setup at sites b5 and w6 (photo J.K. Ehn). The photo illustrates how the surface had partitioned into two surface types. (b) Close-up of the snow/ice interface, marked by the rectangle in (c) showing a layer of superimposed ice (photo M.A. Granskog). (c) Excavated white ice snow pack showing ice lenses, meltwater drainage pathways and superimposed ice. These features are enhanced by the addition of a red-colored dye to the surface and that was allowed to drain over 24 hours before excavation of the snow pit (photo M. A. Granskog).

5.4.2 Diurnal radiative properties

The daily cycle of broadband albedo showed considerable variations depending on weather conditions. A cloud cover may increase the broadband albedo by up to 10% from clear-sky values by increased absorption in infrared wavelengths (*Barry*, 1996). Furthermore the albedo is sensitive to metamorphic changes in the snow pack, such as grain size and liquid water content (*Warren*, 1982). During the melt season these properties change rapidly. In this section, the daytime evolution of the white ice albedo related to cloud and surface conditions is examined.

The diurnal trends in sea ice/snow surface properties for the melt period were characterized by a daily thaw/night-time refreeze cycle. The surface skin temperature decreased during the night and showed a daytime low in the morning (Figure 5.2d). During the day, surface temperatures increased reaching the melting point. At the same time the broadband albedo decreased during the day in response to the freeze-thaw cycle (Figure 5.2d). During night the surface refroze resulting in an albedo increase.

Superimposed on the daily decreasing trend are effects from the sky conditions on the broadband albedo. Under clear-sky, the albedo decreased during the course of day. Minimum values were reached in the early afternoon after which increasing values were observed (e.g., YD 99, 100 and 111 in Figure 5.4). This increase can be attributed to decreasing solar zenith angles and decreasing $SW\downarrow$ when the direct component of the $SW\downarrow$ dominates (*Pirazzini*, 2004). Under overcast conditions the zenith angle has a smaller effect on albedo, as $SW\downarrow$ mainly is composed of diffuse radiation. When $LW\downarrow$ is increased by the cloud coverage, no substantial decrease in all-wave energy input to the surface was observed. Furthermore, during an overcast sky, air temperatures tend to be higher than during clear-sky conditions. Thus through the course of the day the albedo shows a stronger decrease under overcast conditions compared to clear-sky (Figure 5.4).

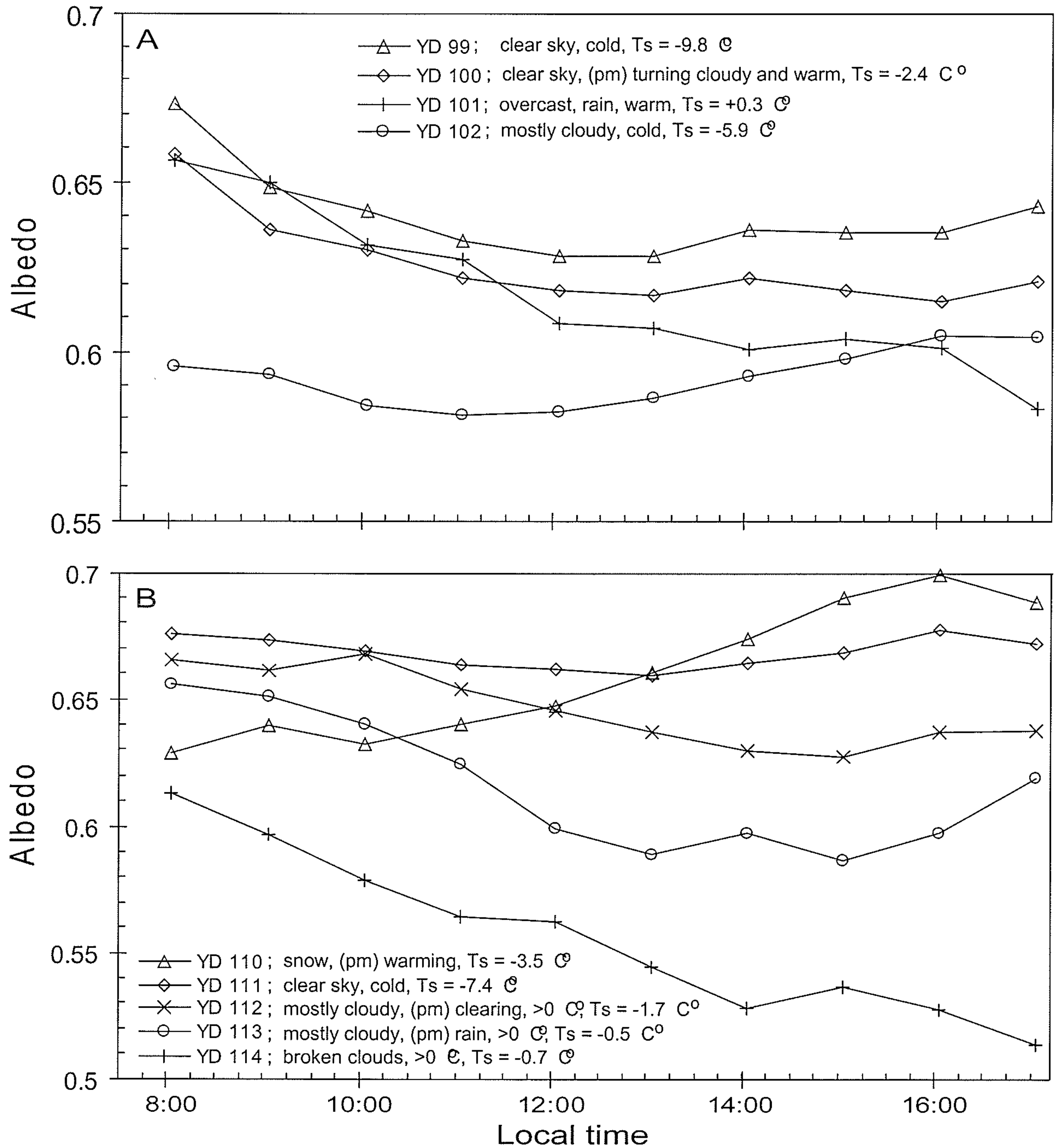

Figure 5.4. Daily broadband albedo variations for a sequence of days. Legends show the day of year and prevailing sky and weather conditions. Ts are daily (08:00 to 17:00) averages of the surface skin temperature.

The snow event on YD 110, with the drop in air temperatures, briefly increased the broadband albedo to ~0.7 (Figures 5.2d and 5.4b). The density of the new snow varied from 165 to 180 kg m^{-3}. However, the new snow was short lived as the warm temperatures that followed quickly caused extensive melt. Consequently the albedo abruptly dropped to 0.51, the lowest observed value during experiment. The abrupt effect of snow and rain events is illustrated in Figure 5.4b. The snowfall on YD 110 caused a daytime (8:00-17:00) increase in albedo by 0.07 or 11%, while the effect of the rain and the warm weather on YD 114 decreased the albedo by 0.1 or 16%. The rate of decrease of albedo during the five-day period was –0.047 per day. Such rapid changes were also observed over multiyear ice during the melt period by *Perovich et al.* (2002). In general, the daytime change in the broadband albedo over white ice ranged from a 0.01 per hour increase to a decrease of 0.014 per hour.

5.4.3 Spectral albedo

The spatial and temporal variability of the broadband and wavelength-integrated albedo is illustrated in Figure 5.5. On YD 97 the surface looked spatially uniform due to recent snowfall. The snow depth at the albedo sites were 0.08-0.28 m. The surface was covered with 2-3 mm thick new snow layer above a hard crust. Consequently the integrated albedos were near 0.9 (Figure 5.5). At this point differences in surface elevation already revealed where melt ponds were likely to form. By YD 101 albedo had decreased to ~0.8 at the sites of the previous measurements (b1 and w2). The albedo was dominated by the wet snow cover; at b1 and w2 snow depth had decreased by about 0.04 m. However the melt had progressed more rapidly at b3 where the albedo was measured over a 0.05 m thick, very wet and patchy snow surface. At b3 the albedo had reduced to 0.62 and most likely represents the minimum in the area. On YD 105 the surface had fractionated into bare blue ice and snow covered white ice. The blue ice areas had a lower elevation than the white ice which appeared as mounds. On the surface of b1 was a 1-cm-thick slushy and dark snow layer, while b3 had a 1-cm-deep melt water layer with small roughness elements protruding above the surface. Minimum albedos were related to warm days when the surface temperature rose to the melting point. The lowest albedo for both the blue and the white ice was observed around YD 113-115 (Figure 5.5).

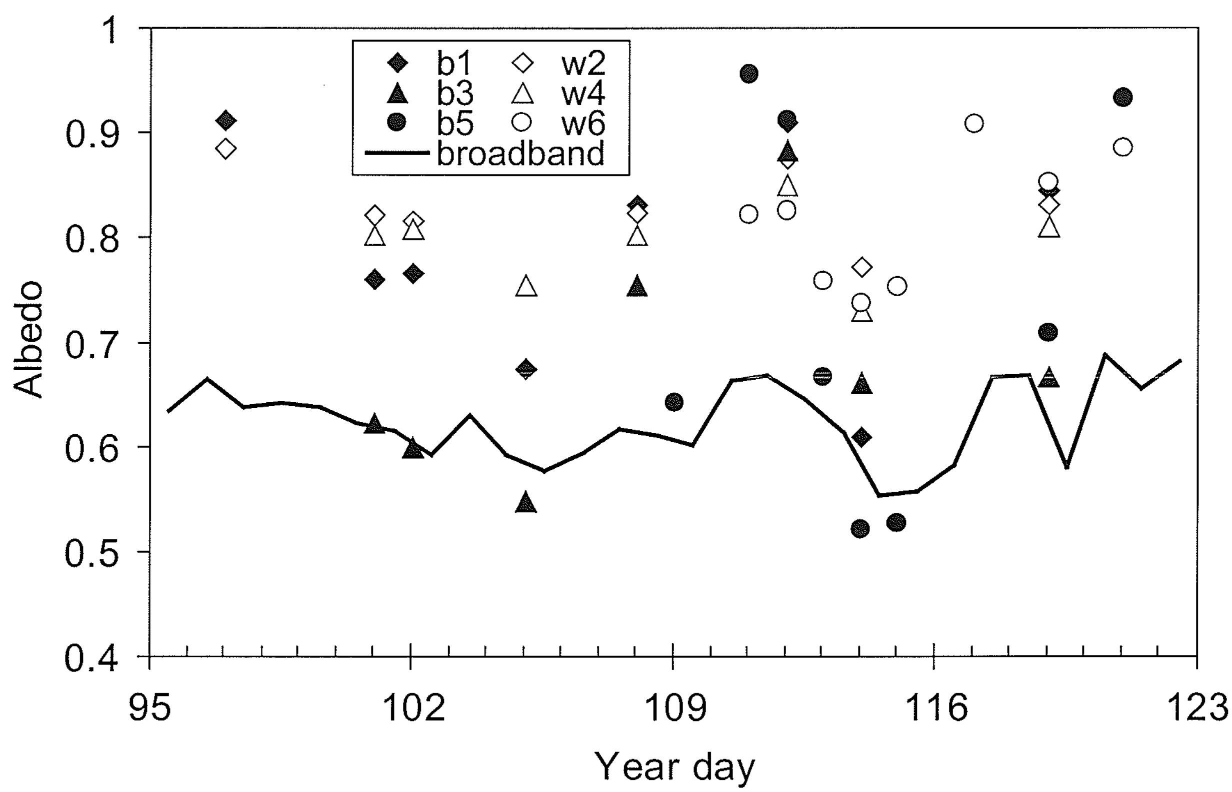

Figure 5.5. Time series of the wavelength-integrated albedo at three blue ice (b1, b3, b5) and three white ice sites (w2, w4, w6), and the daily averaged broadband albedo at the surface meteorology station (white ice).

During the following days snowfall and snowdrift increased the surface albedo. For the blue ice the highest integrated albedo (0.95) was observed on YD 111 when the daily averaged air temperatures were –9 °C and a 0.06 m new snow layer (with a density of 160-180 kg m^{-3}) covered the surface. Similarly the high values for white ice occurred on YD 121 when snowfall from the day before, clear skies and a cold spell that depressed the surface temperature below –10 °C. Interestingly, areas of blue ice (early stages of melt ponds) caught more of the snow due to larger surface roughness compared to white ice mounds where the snow cover was more affected by erosion by wind. The albedo for blue ice areas thus rose to higher values than the white ice after snow events (Figure 5.5, YD 111-112 and 121). However the initially determined locations for depressions and mounds remained the same once the new snow melted.

The magnitude and shape of the spectral albedo was similar to spectra obtained during the melt season in the Arctic (e.g., *Grenfell and Perovich*, 1984). High values observed after snow events show little spectral dependence in the visible and a modest decrease towards near infrared wavelengths (Figure 5.6). Minimum albedos that occurred as a result of warm days and rain events show considerably more wavelength-dependence. A local maximum is observed at 500 nm and a considerable decrease with wavelength by up to 0.6 or 86% (Figure 5.6a).

The effect of liquid water present on the surface on the spectral shape is illustrated by the albedo extremes in Figure 5.6b. The albedo at infrared wavelengths is very sensitive to liquid water content which greatly increases absorption and reduces scattering (*Grenfell and Perovich*, 1984). On YD 117 after the snow event, a 0.06-0.07 m thick, wet new snow layer covered the old snow surface. Surface temperatures were at the melting point (Figure 5.2d). Consequently the albedo decreased substantially in the near infrared. The albedo during the clear and cold conditions on YD 121 (see above), on the other hand, shows significantly less wavelength-dependence. The spectral differences between YD 113 and 114 are more indicative of spatial variability in the snow pack; the broadband albedo on YD 114 is smaller than on YD 113 (Figure 5.4b), while the spectral shape for the albedo for YD 113 would suggest lower broadband values.

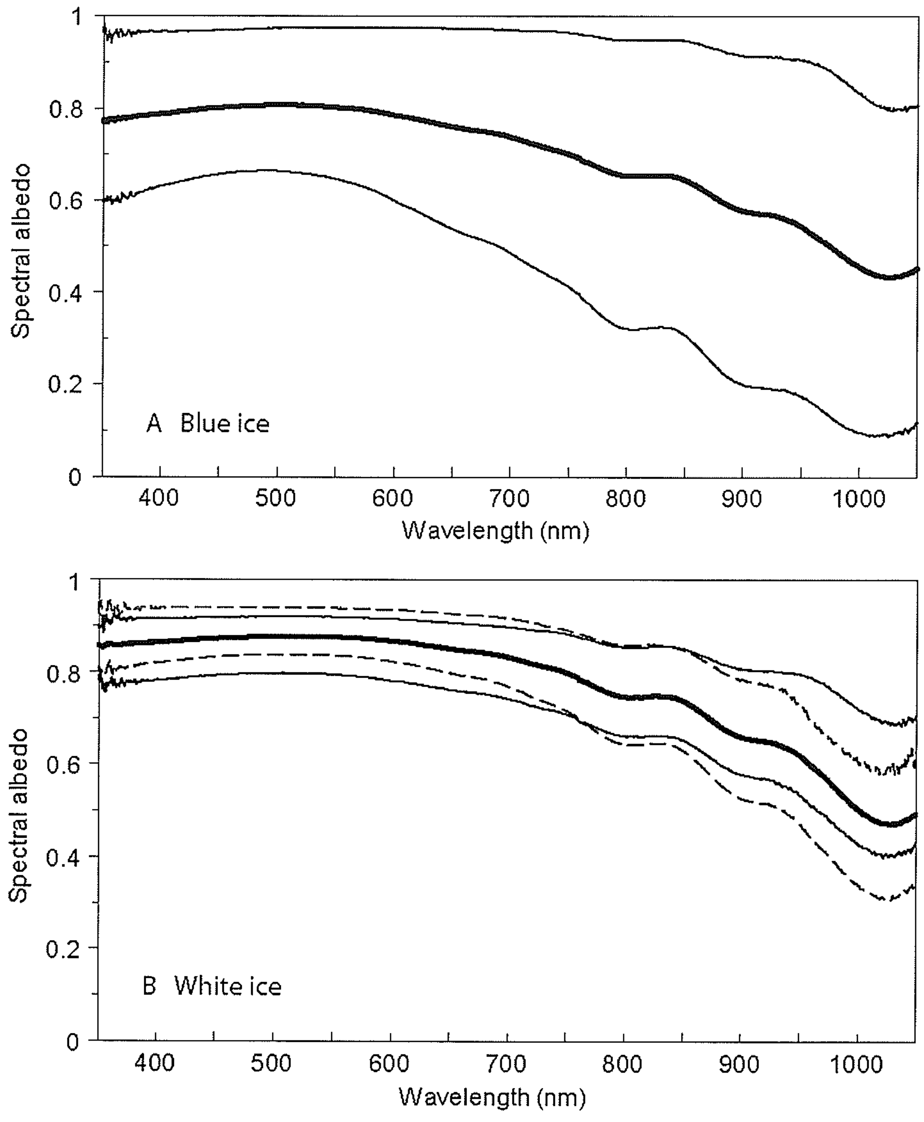

Figure 5.6. Summary for spectral albedos over (a) blue ice and (b) white ice sites from YD 97 to 121. The thick lines are the averages for three sites each during the sampling period, while the thin lines show the extremes. In (a) the maximum albedo was observed on YD 111 and the minimum on YD 115. In (b) the maximum albedo for $\lambda < 845$ nm (dashed line) was observed on YD 117 and for $\lambda > 845$ nm (solid line) on YD 121. The minimum for $\lambda < 767$ nm (solid line) was found on YD 114 and for $\lambda > 767$ nm (dashed line) on YD 113.

5.4.4 Shortwave energy partitioning from albedo and transmittance time series

Further data on spectral albedo and transmittance at sampling location b5 and w6 is provided in Figure 5.7. These data were collected nearly coincidentally in a sequential fashion from A to B to C to D. The spectral albedos have already been discussed in the context of Figure 5.6 and same conclusions apply.

Downwelling shortwave irradiance measurements above and below the ice were used to calculate the bulk spectral transmittance, $T(\lambda)$,

$$T(\lambda) = \frac{SW_{\downarrow}(\lambda, z)}{SW_{\downarrow}(\lambda, 0^{+})}, \tag{5.4}$$

where z denote the thickness of the ice/snow cover. Under ice $T(\lambda)$ was measured directly below where the albedo was measured using an underwater cosine receptor (Analytical Spectral Devices, Inc.) attached to a double-jointed swivel arm (see Figure 6.1 and section 6.3.1).

The spectral transmittance show maximum values at 500-550 nm (Figure 5.7c-d) and little radiation remaining outside the visible range of the spectrum. The pattern that deviates from a smooth curve between 400 and 500 nm in Figure 5.7c illustrates the effect of ice algae absorption. Overall, the magnitude of the transmittance spectra appear to be controlled by surface processes, such as deposition of new snow. This was the case for blue ice on 1 May when new snow was collected in significant quantities on the surface and consequently resulted in very low transmittance values. In contrast, snow was not collected on the white ice mounds and transmittance increased to the highest observed values. It is likely that this increase can be explained by a decrease in scattering in the ice cover based on the measured increases in both temperature and brine volumes within the ice (data not shown). Unfortunately, the time series collection was discontinued due to rapidly changing ice conditions.

Contrary to integrated values shown in Figure 5.5, the values shown in Figure 5.8 are integrated over the total shortwave solar spectra using Eq. 5.3. In case of the albedo, the extension over the spectral range of the spectroradiometer was accomplished by applying the formulations provided in *Allison et al.* (1993). Transmittance values above about 800 nm were, however, so small that their contribution could be neglected. Furthermore, as the spectroradiometer was not calibrated for absolute values, the incident shortwave spectra, $SW{\downarrow}(\lambda)$,

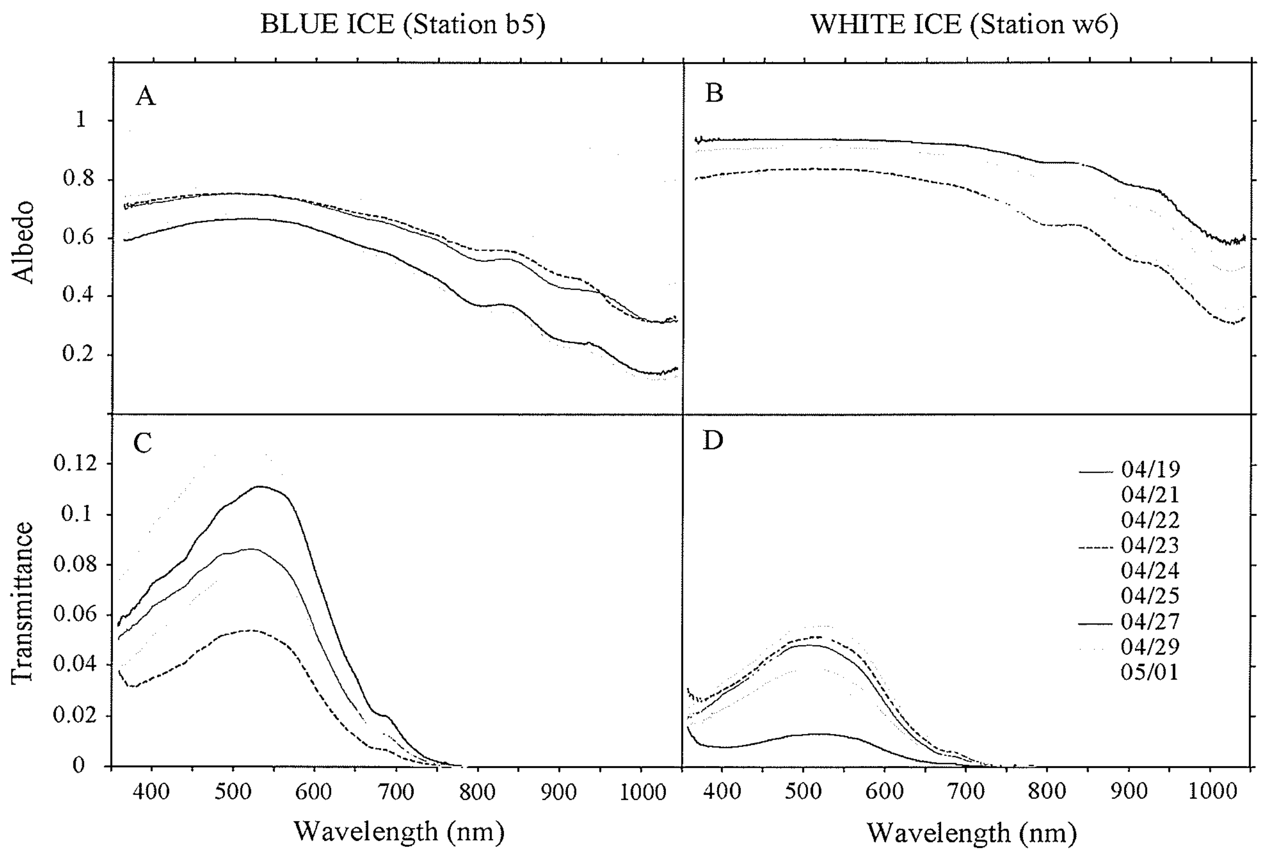

Figure 5.7. Spectral albedos (a-b) and spectral transmittances (c-d) for blue ice station b5 and white ice station w6. Estimates of integrated values are shown in Figure 5.8. The date April 19 compares to YD 109.

needed to be estimated. Representative incident solar spectra from 300 nm to 2500 nm for clear and cloudy skies (stratus cloud with an optical depth of 17) were obtained using the atmospheric radiative transfer model SBDART (e.g., *Ricchiazzi et al.*, 1998) and their magnitude scaled to match the incident irradiance. Based on the observed sky conditions at the time of measurements, either the clear or the cloudy sky incident spectra was used. For days with mixed sky conditions, e.g. 22 April, an average spectrum between clear and cloudy conditions was used.

A discussion on the spatial and temporal variability in wavelength-integrated albedo has already been provided in subsection 5.4.3. It is noted, however, that total shortwave albedo values in Figure 5.8a are consisted with broadband values obtained at the meteorological station (Figure 5.5), although they appear to be somewhat higher. This may be related to site specific differences. The wavelength-integrated transmittance (Figure 5.8b) ranged between 0.5% and 10%-—related inversely to the albedo. Similarly, the absorptance (here defined as 1 – albedo – transmittance) was inversely related to the albedo (Figure 5.8c) illustrating the effect of the surface albedo on the overall shortwave energy partitioning in the ocean–sea ice–atmosphere system. Absorptance values ranged between 15% and 51% for blue ice and 16% and 33% for white ice (Figure 5.8c). How shortwave radiation is distributed within the sea ice/snow cover is returned to with further details in section 6.4.7.

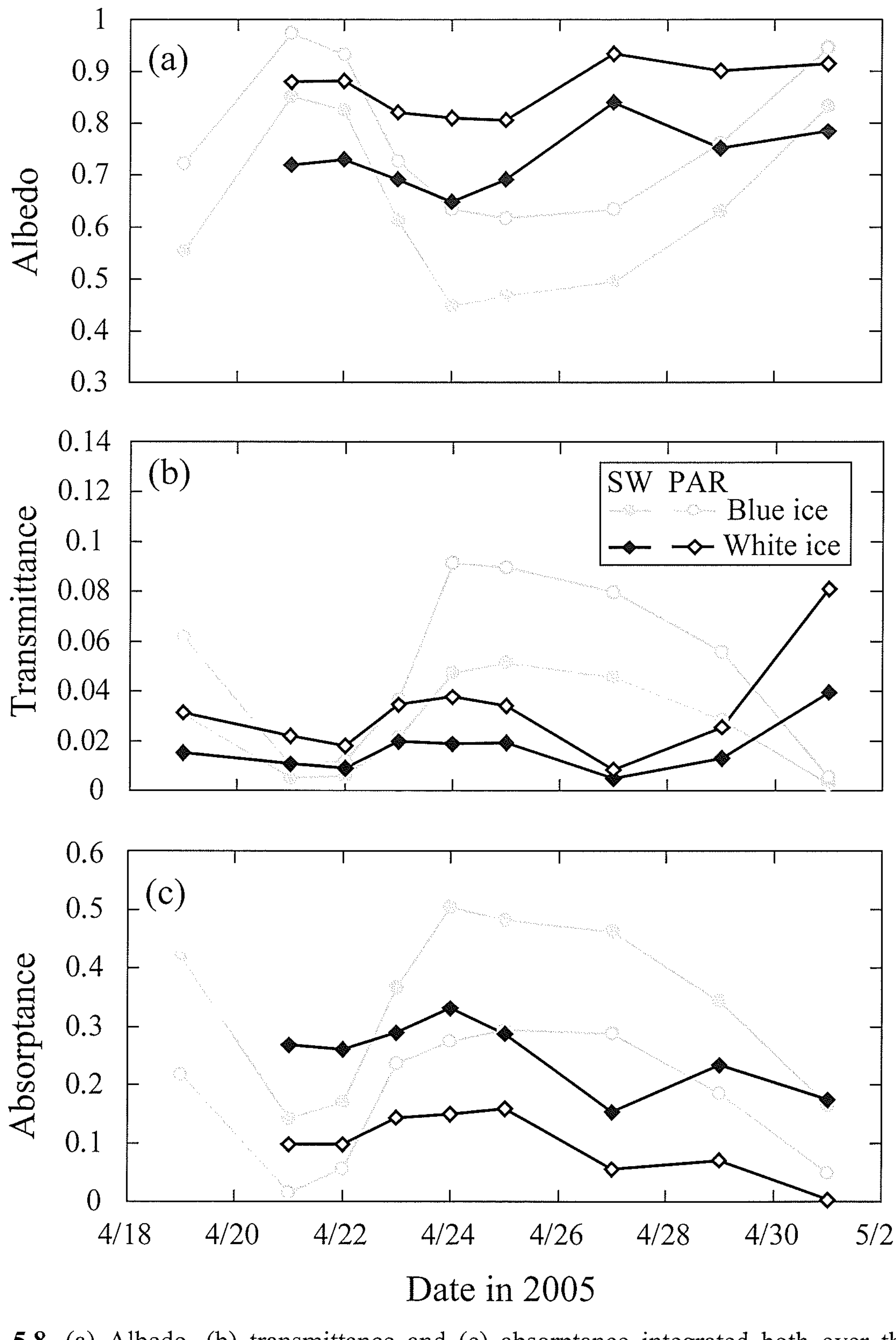

Figure 5.8. (a) Albedo, (b) transmittance and (c) absorptance integrated both over the total shortwave (SW) wavelength range (290-3000 nm) and over PAR (400-700 nm) at sites b5 and w6. SW values were estimated following the method of *Allison et al.* (1993).

5.5 Conclusions

The seasonal evolution of the landfast sea ice surface albedo in Button Bay was found to be affected by synoptic weather events that caused abrupt fluctuations in values (Figure 5.2d). These events can be summarized as a) advection of warm air masses, b) cloud cover, c) precipitation in solid phase, and d) precipitation in liquid phase. In general, the albedo was spatially fairly uniform during winter. As melting progressed the overall albedo decreased and spatial variability increased. The surface partitioned into regions of highly reflective white ice and absorptive blue ice. These changes in surface properties controlled also the portion of solar radiation that was absorbed within and transmitted through the ice cover.

The effect of cloud cover was to decrease $SW\downarrow$ and increase $LW\downarrow$. Their combined effect was thus to even out the radiative energy input to the surface along the day, although the daily average Q^* showed little change. When cloudy conditions were correlated with high air temperatures, extensive surface melting caused the albedo to decrease throughout the day (Figure 5.4). In contrast, clear skies resulted in daytime melting and a consequent reduction in albedo, however in the afternoon the surface begun refreezing and the albedo increased.

Climate forecasts using GCM's, indicate that we should expect a warmer and wetter winter season in the Arctic regions (*ACIA*, 2005; *Johannessen et al.*, 2004). The observations during a sub-Arctic spring presented here provide a glimpse of the surface radiation budget's response to such conditions. Rain events caused a rapid change in the snow cover properties and caused a non-recoverable decrease in the surface albedo due to metamorphoses in the snow pack. Snowfall temporarily increased the albedo by about 0.1, however with the return of warm weather the effect was brief. The precipitation events caused diurnal changes in the albedo of roughly ±10 percent. These results are similar to those observed by *Perovich et al.* (2002) during the SHEBA field experiment in the Arctic basin.

CHAPTER 6: Inference of optical properties from radiation profiles within melting sea ice

6.1 Preface

This chapter has been accepted for publication as Ehn, J. K., T. N. Papakyriakou, D. G. Barber (2007), Inference of optical properties from radiation profiles within melting sea ice, Accepted for publication in Journal of Geophysical Research—Oceans. Copyright 2008 American Geophysical Union. Reproduced by permission of American Geophysical Union. It addresses reseach questions IV and V by examing the connections between IOPs and AOPs within the spring sea ice cover. I was responsible for developing the radiation profiler, data collection and analysis, and the programming of the computer model. I had a lead role in the writing of the manuscript.

6.2 Introduction

The connection between the physical, biological, and optical properties of sea ice has long been recognized by studies in the polar regions (e.g., *Maykut and Grenfell*, 1975; *Grenfell and Maykut*, 1977). During winter and early spring, the snow cover controls the interaction between incoming shortwave radiation and sea ice by scattering back a major fraction (> 0.8) of the incident radiation from the surface. This fraction decreases as the snow and ice begin to melt during late spring, and consequently more radiation reaches further below the surface. A portion of the radiation is absorbed within the ice causing internal melting and warming (e.g., *Perovich* *et al.*, 1998; *Zeebe et al.*, 1996). The absorption is influenced by dissolved and particulate matter incorporated into the sea ice and snow and has been the subject of several recent studies (e.g., *Belzile et al.*, 2000; *Light et al.*, 1998; *Perovich et al.*, 1998; *Grenfell et al.*, 2002; *Flanner et al.*, 2007). Radiation passing through the ice becomes available for primary production and heating of the seawater (*Maykut and Grenfell*, 1975). Furthermore, available radiation causes photooxidation of organic matter which produces CO and CO_2 (*Xie and Gosselin*, 2005).

The melting of the snow cover on landfast sea ice is commonly triggered by incursions of warm southerly air and associated rain events (e.g., *Robinson et al.*, 1986). Melting and metamorphism in the snowpack result in an irreversible darkening of the surface causing more radiation to be absorbed within the snow and sea ice. Sustained melting leaves the surface fractionated into so-called blue ice and white ice areas, i.e. depressed areas of bare ice and mounds composed of highly deteriorated snow or ice with a snow-like appearance. As the melt season progresses, the blue ice generally evolves in to melt ponds, which is followed by the ice cover breaking up into floes and dispersing.

Melting sea ice conditions characterize the Arctic Ocean for up to 4-5 months (April-August) of the year. Melting conditions prevail at a time when primary productivity is at its highest and changes in sea ice thickness and extent are most sensitive to thermal forcing. It is critical that large-scale climate models and more detailed radiative transfer models (e.g., *Jin et al.*, 1994) have the information needed to predict changes occurring during the melt period. Yet, there are limited field observations available. Most observations are limited to measurements that can be conducted above and below the surfaces and optical properties of the snow and ice inferred indirectly (e.g., *Grenfell and Maykut*, 1977; *Buckley and Trodahl*, 1987; *Belzile et al.*, 2000; *Hamre et al.*, 2004). In-ice measurements within landfast sea ice have been carried out prior to the melt season (*Maffione et al.*, 1998; *Pegau and Zaneveld*, 2000). More recently, *Grenfell et al.* (2006) used an in-ice radiation profiler to measure attenuation coefficients for the interior portions of both first- and multiyear ice during melt season.

Here, field observations of vertical radiation profiles within melting landfast sea ice in Button Bay (58° 48.5 N, 94° 17.2 W) located near Churchill, Manitoba, in western Hudson Bay are presented. The attempt is to build upon previous studies by verifying against independent irradiance measurements both above and below the sea ice cover, as well as observations of physical and optical properties from extracted ice samples. The objective of this study is to determine the optical properties of the deteriorated and melting ice cover, and to identify layers with distinct optical character. The DISORT radiative transfer code (*Stamnes et al.*, 1988) was used iteratively to deduce information on the inherent optical properties (IOPs) from in-situ observations of apparent optical properties (AOPs) in a manner similar to Chpater 4 (*Ehn et al.*, 2008). We believe that results obtained here are relevant and generally applicable to seasonal sea ice in the Arctic during the beginning of the melt season (e.g., *Hanesiak et al.*, 2001). This work thus represents a step towards an improved treatment of shortwave radiation in studies dealing with the energy partitioning and biological production in the sea ice environment.

6.3 Data and Methods

6.3.1 Field program

A previous study by *Ehn et al.* (2006) has reported on the evolution of the surface energy balance and the shortwave surface albedo during April-May at the Button Bay site. In short, winter-like conditions remained until the end of March. The sea ice was generally covered by dry snow. A few days into April conditions changed dramatically when a low-pressure system moved in bringing heavy rainfall. This rain event caused the formation of ice lenses in the snowpack, a significant reduction in surface albedo and generally marked the beginning of the melt season. From that point on, weather conditions were highly variable with sporadic rain and snowfall being common.

By 25 April, the ice surface had fractionated into areas of blue ice and white ice. The snowpack on the white ice was modified all the way through by freeze–thaw processes and was composed mostly of coarse grains and ice lenses. The snow/ice interface was difficult to determine as extensive snow melting and drainage had formed superimposed ice (e.g., *Kawamura et al.*, 1997) and an uneven snow/ice interface. It appeared that snowfall from previous days had melted and refrozen overnight to form high-scattering superimposed ice layer, which had become wet and slushy by the time of the optical measurements. The bottommost few centimeters of the ice cover was discolored by a dense sea ice algae community. No evidence of impurities could be visibly detected within other parts of the ice column.

Measurements of AOPs included spectral albedo and transmittance through the entire ice sheet (hereafter referred to simply as transmittance), and vertical profiles using a custom built ice profiler that was placed within auger holes drilled through the ice (Figure 6.1). The measurements were performed at one blue ice and one white ice site in the vicinity of the six sites included in *Ehn et al.* (2006). All optical measurements were conducted using a dual-headed spectroradiometer (FieldSpec, Analytical Spectral Devices, Inc.) which measures radiation between 350 nm and 1050 nm. The total ice and snow cover thicknesses, at the exact

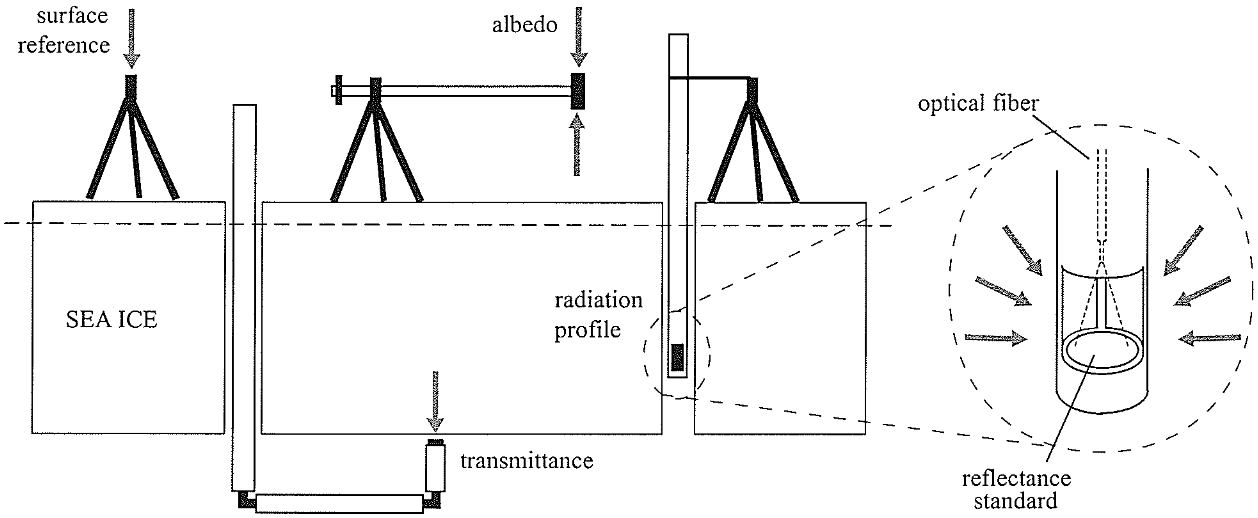

Figure 6.1. Overview sketch of the optical measurements.

location of the radiation profiles, were about 1.50 m for blue ice and 1.70 m for white ice, with freeboards of 13 cm and 32 cm, respectively, implying that thickness differences between the two were mainly due to upper surface roughness features related to melting. The ice thicknesses were somewhat thinner immediately above the location where bulk transmittances were measured. A thickness difference of 7 cm for blue ice and 3 cm for white ice were measured. Thus, radiation levels beneath the sea ice can be expected to be slightly higher were the ice cover is thinner. The optical measurements were accompanied by physical measurements to characterize the snow and the sea ice as described below.

Above surface measurements were used to calculate the spectral albedo, $\alpha(\lambda)$,

$$\alpha(\lambda) = \frac{F_{\uparrow}(\lambda,0^{+})}{F_{\downarrow}(\lambda,0^{+})}, \tag{6.1}$$

where $F\uparrow(\lambda,0^+)$ and $F\downarrow(\lambda,0^+)$ denote upwelling and downwelling spectral irradiance above the surface, respectively. The spectral albedo was obtained with the spectroradiometer by alternating between up- and downwelling irradiance measurements at a height of 70 cm above the surface. The cosine collector was attached to the end of a 1.5-m-long rod extending from a tripod. A second cosine collector (180 degree field-of-view) was used for coincident monitoring of changes in incoming spectral irradiance and remained in use through the rest of the measurement sequence.

Downwelling irradiance measurements above and below the ice were used to calculate the bulk spectral transmittance, $T(\lambda)$,

$$T(\lambda) = \frac{F_{\downarrow}(\lambda, z)}{F_{\downarrow}(\lambda, 0^+)}, \tag{6.2}$$

where z denote the thickness of the ice/snow cover. Under ice $T(\lambda)$ was measured directly below where $\alpha(\lambda)$ was measured using an underwater cosine receptor (Analytical Spectral Devices, Inc.) attached to a double-jointed swivel arm (Figure 6.1). The swivel arm was made out of a white polyvinyl chloride (PVC) pipe that snugly fit through a 5-cm ice auger (Kovacs Enterprises, Inc.) hole and allowed for measurements 1.5 m away from the drilled hole. The set-up was designed to minimize the effect of the hole on the radiation field. The fiber-optical cable, that connected the cosine receptor to the spectroradiometer, ran on the inside of the pipe. An immersion correction factor, $F_i(\lambda)$, was not supplied by the manufacturer of the underwater cosine receptor. A laboratory experiment was thus performed following the procedure outlined in *Mueller et al.* (2003) (their section 3.5). The obtained $F_i(\lambda)$ could be expressed by 0.075 $\ln(\lambda)$ +

0.243, which agrees well with the immersion factor supplied for the LI-1800UW underwater spectroradiometer (LI-COR Biosciences).

Vertically resolved radiation profiles, within the sea ice and water column to a maximum distance of 2.5 m from the surface, were measured using an ice profiler (Figure 6.1) with a 10 cm vertical resolution. The vertical measurement resolution was increased to 2.5 cm near the ice-water interface in order to better characterize the bottom biological community. The same auger holes used for transmittance measurements were reused for the radiation profiles. The ice profiler was also constructed of a white PVC pipe. A disc-shaped diffuse reflectance standard (WS-1, Ocean Optics, Inc.) was mounted at the base of the pipe facing upward (Figure 6.1). Equal square openings were cut in the pipe so that three 1 cm wide support beams remained attaching the reflectance standard to the pipe. The height from the surface of the reflectance standard to the top of the opening was 5 cm. A fiber-optic cable with a 25 degree field-of-view fore-optic was attached at a distance of 4.5 cm immediately above the reflectance standard looking downward. The field-of-view thus remained within the diameter of the reflectance standard. After a measurement above the surface in the air, the first usable measurement within the ice was conducted at a sufficient depth below the waterline so that the profiler sensing head was fully submerged in seawater. This distance from the surface was 20 cm for the blue ice and 40 cm for the white ice as the freeboards for the two sites were 13 cm and 32 cm (including snow), respectively. Except for the location of the upper surface, the relative distance between measurement levels was estimated with a ±1 mm precision causing a basic measurement uncertainty affecting the subsequent calculation of the attenuation coefficient. The location of the surface of melting sea ice is difficult to define to a similar precision due to significant small-scale variability.

Ice cores were obtained using a MARK II coring system (0.09 m diameter, Kovacs Enterprise) at a location situated about 50 m northwest of where optical measurements were conducted. The ice surface was of the white ice type. An ice core starting from the hard superimposed ice surface, generally about 0.2 m below the snow surface, through the full length of the ice cover was used to measure temperatures immediately after extraction using a handheld drill and a temperature probe (Traceable Digital Thermometer, Model 4000). A second ice core for salinity determination was immediately cut into 0.1 m sections, which were placed into plastic jars or airtight plastic bags before transfer back to the camp where they were melted overnight. Measurements of snow properties were exceedingly difficult to conduct after rain events and freeze-thaw processes had transformed the white ice snow pack to be composed mostly of ice lenses (*Ehn et al.*, 2006). However, bulk samples were taken for salinity determination and density estimates, and temperatures were measured at selected depths where possible. Conductivity was measured from the melted ice and snow sections using a handheld conductivity meter (Hoskin Scientific Cond 330i; accuracy ±0.5% of reading), and converted into salinity units using UNESCO algorithms (*Fofonoff and Millard*, 1983).

A 20 cm thick bulk snow sample was collected from the white ice site on 21 April. The sample was melted in dark and filtered onto glass fiber filters (Whatman GF/F, nominal pore size 0.7 μm). The particulate absorption spectra, $a_p(\lambda)$, was calculated as

$$a_p(\lambda) = \frac{2.303 \ln[I_0(\lambda)/I_f(\lambda)]}{\beta V A^{-1}}, \qquad [\mathrm{m}^{-1}] \tag{6.3}$$

where I_0 and I_f are the spectral intensities measured through a filter wetted with milli-Q water and the same filter after the filtration, β is the pathlength amplification factor and approximately equal to 2 for high particulate concentrations, *V* the volume filtered, and *A* ($= \pi r^2$) is the surface area of the filter (e.g., *Roesler*, 1998). Eq. 6.3 was also used to obtain $a_p(\lambda)$ for bottom ice samples with microalgae and detrital particles, however, the spectra were forced to zero at 750 nm by subtracting the background intensities (e.g., *Roesler*, 1998).

6.3.2 Radiative transfer model and spectral decomposition

The discrete-ordinate radiative transfer (DISORT) code (*Stamnes et al.*, 1988) was used to link physical properties and inherent optical properties (IOPs) with observed apparent optical properties (AOPs). As in *Ehn et al.* (2008), the use of DISORT was limited to snow, sea ice and seawater, and changes in the refractive index at layer boundaries were not considered (*Jin et al.*, 1994). The radiation field at layer interfaces were characterized by 32 streams. This provides sufficient polar angle resolution to evaluate the conditions under which the asymptotic state of the radiation field is reached. In the asymptotic state the shape of the radiation field does not significantly change with depth, which entails that the irradiance attenuation coefficient equals the radiance attenuation coefficient obtained from the use of any polar angle. *Pegau and Zaneveld* (2000) found that a near-asymptotic state was reached within 25 cm from the sea ice surface even when the snow cover was removed and sky conditions were cloud free (see also *Maffione et al.*, 1998). On 25 April the sky was completely overcast and the solar disc could not be seen through the clouds. Hence, in the model, incident irradiance to the surface was assumed diffuse. Additionally, near the ice/water interface the radiation field becomes increasingly affected by the presence of the water column with little backscattering (e.g., *Ehn et al.*, 2008).

Radiation that is transmitted through sea ice has been found to be largely downward directed (*Buckley and Trodahl*, 1987).

The sea ice was divided into horizontally homogeneous layers based on temperature, salinity and radiation profile observations. In addition, a 40 m thick homogeneous seawater layer was included below the ice. For each of the layers, DISORT requires information on the IOPs, i.e., spectral absorption coefficient, $a_{tot}(\lambda)$, scattering coefficient, b_{tot}, and phase function, $p(\theta)$, to solve the equation of radiative transfer (e.g., *Thomas and Stamnes*, 1999). Details on this division and the input values are provided in the results section. In general, IOPs were obtained by iterations of DISORT until the model calculated attenuation coefficient matched the diffuse attenuation coefficient measured with the ice profiler, $K_{profiler}(\lambda)$, to within ±0.002 m^{-1} for all selected depth intervals simultaneously with the exception of the surface layer. The effect of immersion was not known for the ice profiler. Therefore, effective diffuse attenuation coefficients were estimated for the uppermost layers so that the model calculated albedos matched the observations to within ±0.001. A similar approach has been taken by *Light et al.* (1998). A 5% specular reflection was assumed for the bare blue ice, however, neglected for white ice following, e.g., *Perovich* (1990).

It was quickly realized that the model calculated downwelling irradiance attenuation coefficient, $K_d(\lambda)$, could not be used to match $K_{profiler}(\lambda)$, as comparisons against measured $T(\lambda)$ revealed that the magnitude of the simulated transmittance was significantly underestimated for both blue and white ice. A reason for this was that downwelling irradiance did not represent the radiation field seen by the profiler. The profiler essentially records radiation (F_p) incident on the diffuse reflectance standard from between zenith angles 45° and 90°. Thus a profiler specific attenuation coefficient, $K_p(\lambda)$, was defined as

$$K_p(\lambda) = \ln\left[\frac{F_p(\lambda, z)}{F_p(\lambda, z + \Delta z)}\right] \Big/ \Delta z, \tag{6.4a}$$

where z denote the depth to the layer and Δz the layer thickness, and

$$F_p(\lambda, z) = \int_0^{2\pi} d\varphi \int_{\pi/4}^{\pi/2} I(\lambda, z, \theta) \cos(\theta)\, d\theta \tag{6.4b}$$

where I is the radiant intensity at wavelength λ and θ is the polar angle. $K_p(\lambda)$ was thus the property calculated during each model iteration and used to match against the measured $K_{profiler}(\lambda)$.

For each layer a dominant scatterer was defined; i.e., snow grains for the snow layers, air bubbles for the drained ice layers located above the waterline, and brine inclusions below the waterline. Scattering was assumed to be well represented by spherical inclusions of an effective radius r_{eff}. The corresponding scattering coefficient was modeled as

$$b_{tot} = \frac{3}{2} \frac{v_j}{[r_{eff}]_j}, \tag{6.5}$$

where v_j is the volume fraction of the dominant scatterer j. b_{tot} is considered independent of wavelength since these scatterers are typically significantly larger than the wavelength of the radiation within the visible light regime (e.g., *Grenfell*, 1983). The angular distribution of the scattered radiation was calculated using the Henyey-Greenstein phase function (see Eq. 2.32)

(*Henyey and Greenstein*, 1941), where g_j is the average cosine or the asymmetry parameter for the dominant scatterer j, and θ the scattering angle. The asymmetry parameter was set to a constant value of 0.855 for snow and drained ice layers, and 0.995 for layers below the waterline (*Light et al.*, 2004). This results in a strongly forward scattering phase function which is typical for the sea ice and seawater environment (e.g., *Mobley et al.*, 1998).

Any wavelength dependence in attenuation is assumed to be caused by absorption (e.g., *Grenfell*, 1983). For each sea ice layer, $a_{tot}(\lambda)$ was calculated as the sum of absorbing components:

$$a_{tot}(\lambda) = v_{pi}a_{pi}(\lambda) + v_b a_{sw}(\lambda) + a_{imp}(\lambda), \tag{6.6}$$

where $a_{pi}(\lambda)$ and $a_{sw}(\lambda)$ are the absorption coefficients for pure ice and brine (assumed identical to pure seawater), which are multiplied by their respective volume fractions, v_{pi} and v_b. Values for pure ice and brine absorption were taken from *Warren et al.* (2006) and *Pope and Fry* (1997), respectively. $a_{imp}(\lambda)$ is the absorption coefficient for impurities including absorption by algal and non-algal particulate matter and colored dissolved organic matter (CDOM) within sea ice layers and soot in the surface layer. Essentially, $a_{imp}(\lambda)$ is the residual absorption required to explain $a_{tot}(\lambda)$ and thus one of the unknowns being iterated for.

6.4 Results and Discussion

6.4.1 Physical properties

Temperature and salinity profiles were measured every other day at a white ice site about 50 m from the radiative transfer measurement location to estimate general ice conditions. At the time of the investigation, temperatures were rising throughout the sea ice column (Figure 6.2a). On 21 April, the lowest ice temperature of -3.5 °C was recorded close to the surface. Temperatures in the snow decreased to values below -4 °C when approaching the surface. By 25 April, the snow and surface ice temperatures had increased significantly. Ice temperatures had increased by as much as 2.5 °C, resulting in a C-shaped profile with minimum temperatures of about -2.6 °C at a depth of 0.75 m. Near the ice bottom, ice temperature was about -1.7 °C, which closely matched the seawater temperature (data not shown). Ice thickness decreased from about 1.6 m on 25 April to 1.5 m on 29 April. This may also be due to local thickness variability, and is thinner than what was observed at the radiative transfer site. The lowest temperature in the ice profile on 29 April was -2.2 °C at about 0.9 m depth. At this time, an ice core taken at a blue ice site revealed large drainage channels and cavities in the bottom part of the ice.

Salinities in the snow near the surface were close to zero. The snowpack was composed of ice lenses and very coarse polymorphic aggregate snow grains. The uppermost 10 cm of the ice below the snow cover had a salinity of about 0.9‰ on 25 April (Figure 6.2b). This layer was likely so-called superimposed ice formed from refreezing melted snow and rain. Densities within the snow pack could not be measured in traditional methods. By forcing a metal pipe with a known inner diameter into the surface layer, a bulk density estimate of about 750-770 kg m^{-3} for the uppermost 28 cm was obtained. It was not possible to collect replicate samples using this technique to provide a precision estimate of this snow/ice density. Maximum bulk sea ice salinities were found in the layer immediately below the waterline (i.e., 30-40 cm from the surface) and near the bottom of the ice. Salinities decreased over time in the layers above a depth of 50 cm from the surface. In the 30-40 cm layer, salinities decreased from 11.9‰ on 21 April, to 9.8‰ on 25 April and to 7.9‰ on 29 April. However, below the 50 cm depth, salinity profiles remained nearly unchanged over time. This suggests that brine drainage or flushing was insignificant even though the sea ice was found to have a high porosity. We speculate that surface flushing was hindered by the capping of the ice surface with a layer of fresh and nearly impermeable superimposed ice. We additionally note that the salinity reduction within the uppermost layers must have been accounted for by lateral drainage towards some larger scale drainage feature (such as a previously drilled core hole or adjacent ice cracks) or fresh water input from precipitation. An additional possibility is increased brine drainage due to increased temperature as the ice core was removed from the ice cover. The processes controlling the geophysical evolution of the ice are very difficult to measure at this time of year and a detailed treatment of these processes is beyond the scope of this thesis.

Brine volumes were calculated using expressions developed by *Cox and Weeks* (1983) and *Leppäranta and Manninen* (1988). Because a constant density of 920 kg m^{-3} was used, incorrect values especially in layers above the waterline may result. These values represent rather the brine mass fraction. Even though salinities decreased or remained unchanged over time, brine volume fractions within the snow/ice increased at all depths (Figure 6.2c). The brine volume increase within the ice cover was in response to the temperature increase. On 25 April, from 50 cm to 130 cm brine volume fractions were nearly constant with depth (0.097 ± 0.008). From April 21 to 29, brine volume increased by about 0.039, while the temperature increased by 1.0 °C. Maximum values near the bottom were 0.198 and 0.237 at the 30-40 cm layer (Figure 6.2c).

The volume fractions are sufficiently large to expect brine drainage (e.g., *Golden et al.*, 1998), which however was not observed, as explained above.

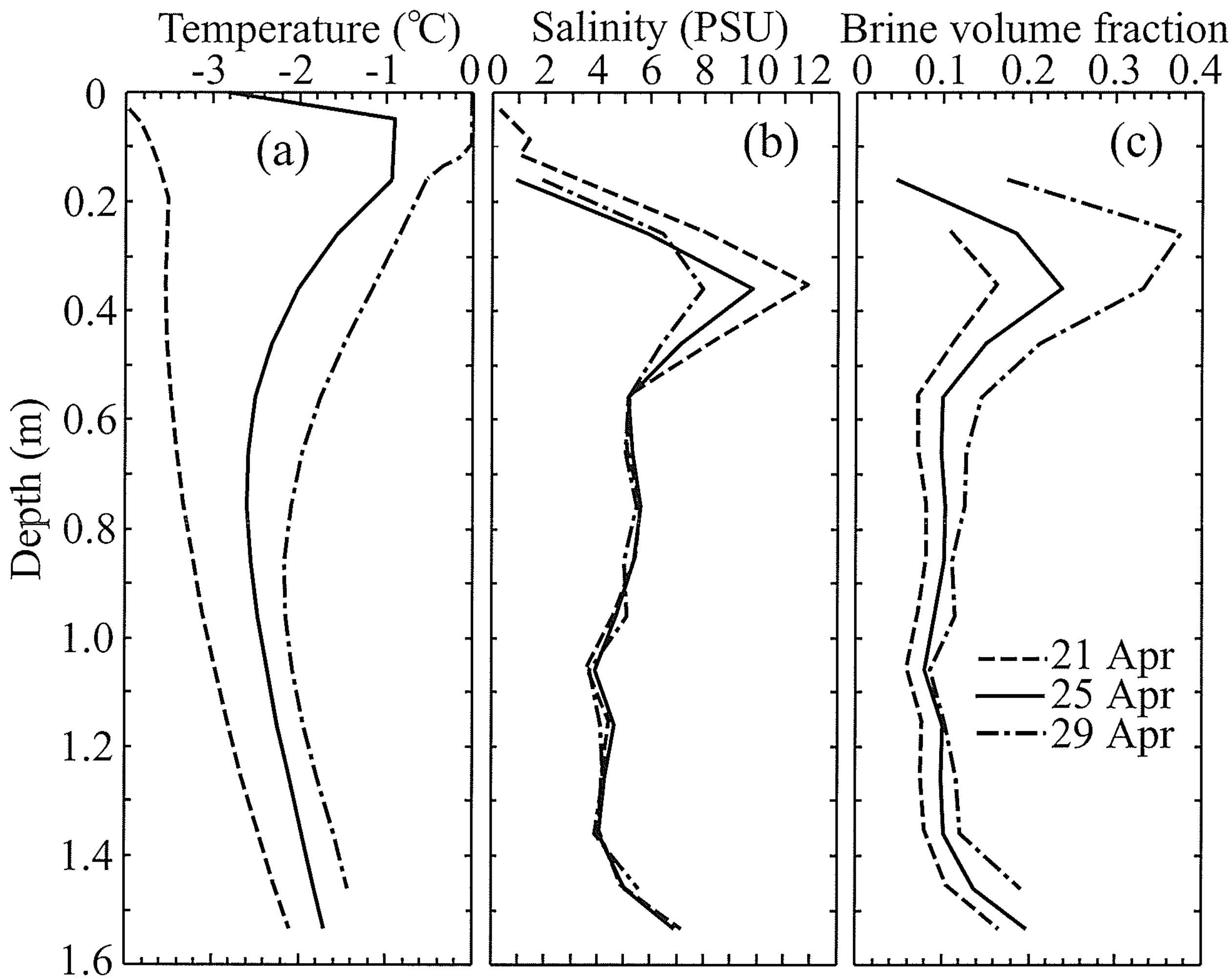

Figure 6.2. Profiles of (a) temperature, (b) salinity, and (c) brine volume fraction from a nearby white ice sampling site. Profiles extend from snow surface to ice bottom.

6.4.2 Observed apparent optical properties on 25 April

In-ice transmittance profiles for selected wavelengths, obtained by normalizing radiation profiles, $F_p(z)$, against surface incident values, are shown in Figure 6.3a. As radiation decreases approximately exponentially with depth, the ice-profiler diffuse attenuation coefficient, $K_{profiler}(\lambda)$, can be obtained as the slope of the $\ln(F_p(\lambda))$ versus depth fit. Examples of fits to selected wavelengths in Figure 6.3a show that the profiles, for both blue and white ice, can be

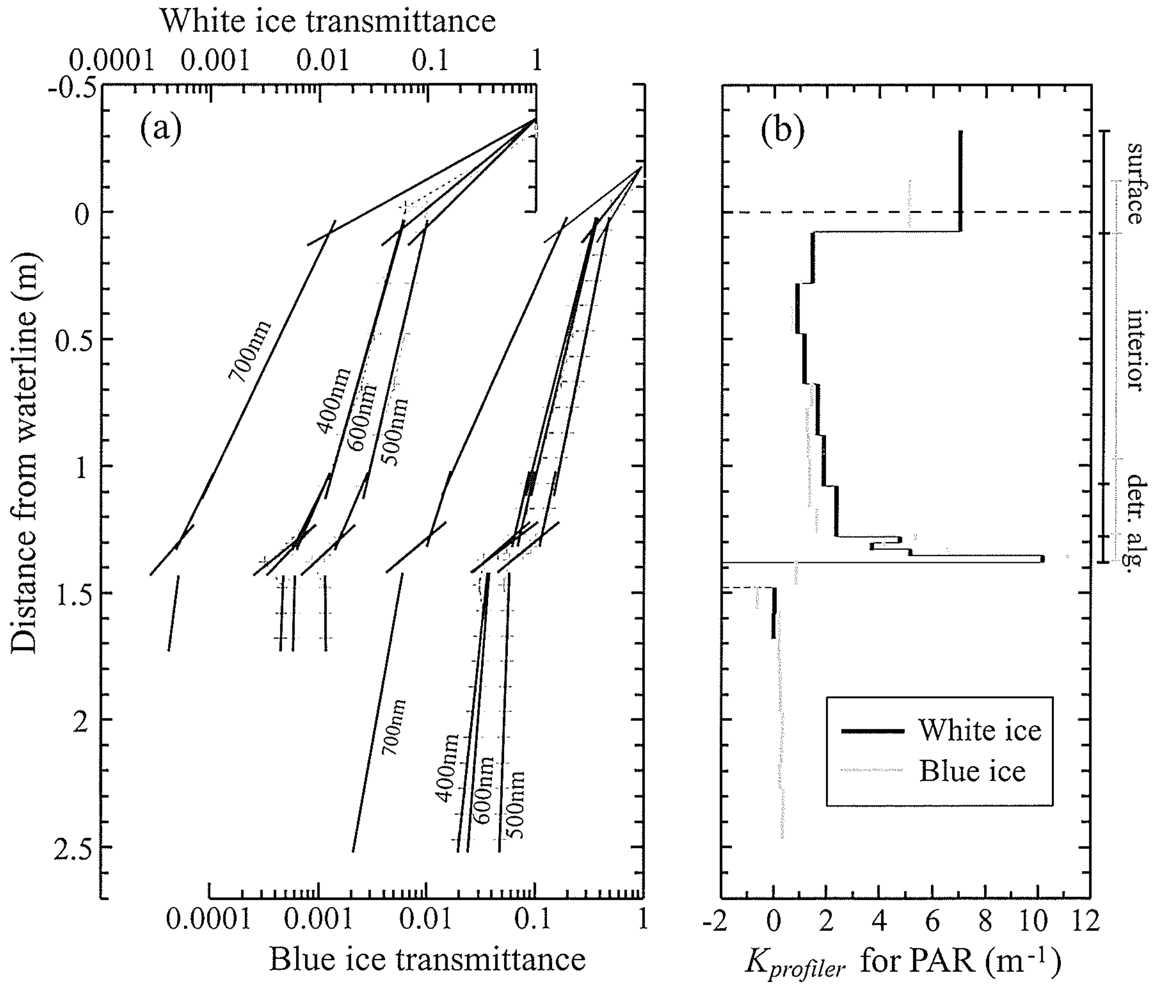

Figure 6.3. (a) Profiles of transmittance for 4 wavelengths measured at selected depths (+ symbols) using the ice profiler within blue and white ice on 25 April. Blue ice profiles have been shifted by an order of magnitude relative to white ice profiles for clarity. In (b) the spectral diffuse attenuation coefficients have been integrated over the PAR and calculated for each layer between measured distances shown in (a). Negative distances refer to ice or snow above the waterline.

represented by four layers in addition to seawater with distinct slopes. These four layers include (1) surface layer mainly of snow, superimposed ice and granular ice, (2) interior ice layer of predominately columnar ice, (3) detrital layer and (4) algae layer. Depth intervals for each layer type are shown at the right of Figure 6.3b. The fit is between two transmittance values for the surface layers and for the white ice detrital layer (i.e. $r^2=1$). The fits explained at least 99% of the variance in the transmittance (p-value < 0.0001) for all wavelengths between 400 nm and 700 nm in both the blue and white ice interior as well as the seawater below the ice. Similarly, at least 96% of the variance in the transmittance within the algae layer was explained (p-value < 0.004).

However, small variability can be seen and is related to measurement errors and small-scale structural changes in the ice (*Pegau and Zaneveld*, 2000). This variability is better visualized in Figure 6.3b where vertical profiles of $K_{profiler}(\lambda)$ are calculated per measurement interval and integrated over the wavelength range of photosynthetically active radiation (PAR), i.e., 400-700 nm. The profiles show that high attenuation values are found at the boundary layers of the ice. After the initial high and site specific values near the surface, attenuation was similar between the white ice and blue ice sites. Other profiles measured in the region confirm this pattern (data not shown). Minimum PAR attenuation values are found at a depth around 40 cm below the waterline (0.8 m^{-1} for blue ice and 0.9 m^{-1} for white ice). For the blue ice interior, the highest value of 1.6 m^{-1} was found immediately below the surface layer. For white ice interior the highest value of 1.9 m^{-1} was observed at about 1 m depth close to the detrital layer. For the blue and white ice sites, high attenuation within the ice algae layers coincided at approximately the same distance from the waterline. The range of $K_{profiler}$(PAR) values observed within the 10 cm thick algae layers were 3.7-10.2 m^{-1} for the white ice and 4.2-11.1 m^{-1} for the blue ice.

An interesting feature in the profiler data is that negative $K_{profiler}$ values were commonly obtained for the seawater layer immediately below the ice. Negative attenuation coefficients were also observed by *Pegau and Zaneveld* (2000) and related to horizontal propagation of radiation from "clean" to sediment-laden ice. However, negative values were pronounced in the blue ice profile (Figure 6.3b) where horizontal propagation may be expected to increase the attenuation coefficient. We are not able to explain this phenomenon, but speculate that a change in the radiation field may be partially responsible; if the laminar crystal structure of the bottom sea ice mushy layer preferentially redirects or transmits radiation in a downward direction, less radiance may reach the diffuse reflectance standard plate at the interface compared to further down in the water column were the radiation field perhaps again becomes more diffuse. It is only possible to speculate here, and note that further research is required to confirm this speculation. With further depth into the water column, $K_{profiler}$(PAR) values stabilize to about 0.29 m^{-1}, which suggests that this is the distance at which the sea ice no longer affects the radiation field (i.e., an asymptotic state). This can also be seen from the excellent fit to data in Figure 6.3a.

Based on the exponential fits, examples of which are seen in Figure 6.3a, $K_{profiler}(\lambda)$ profiles for both ice types were divided into four distinct layers in addition to a seawater layer (Figure 6.4). As mentioned above, the uppermost layer thickness was 20 cm for blue ice and 40 cm for white ice due to the freeboard. The interior portion of the ice was grouped into a 1-m-thick homogeneous layer. Measurements within this layer showed that $K_{profiler}(\lambda)$ spectra had similar shapes and magnitudes. The increase in temperature together with the decrease in salinity with depth resulted in a relatively constant brine volume fraction within the interior ice layer (Figure 6.2c). Thus the optical properties within the interior ice could be considered relatively

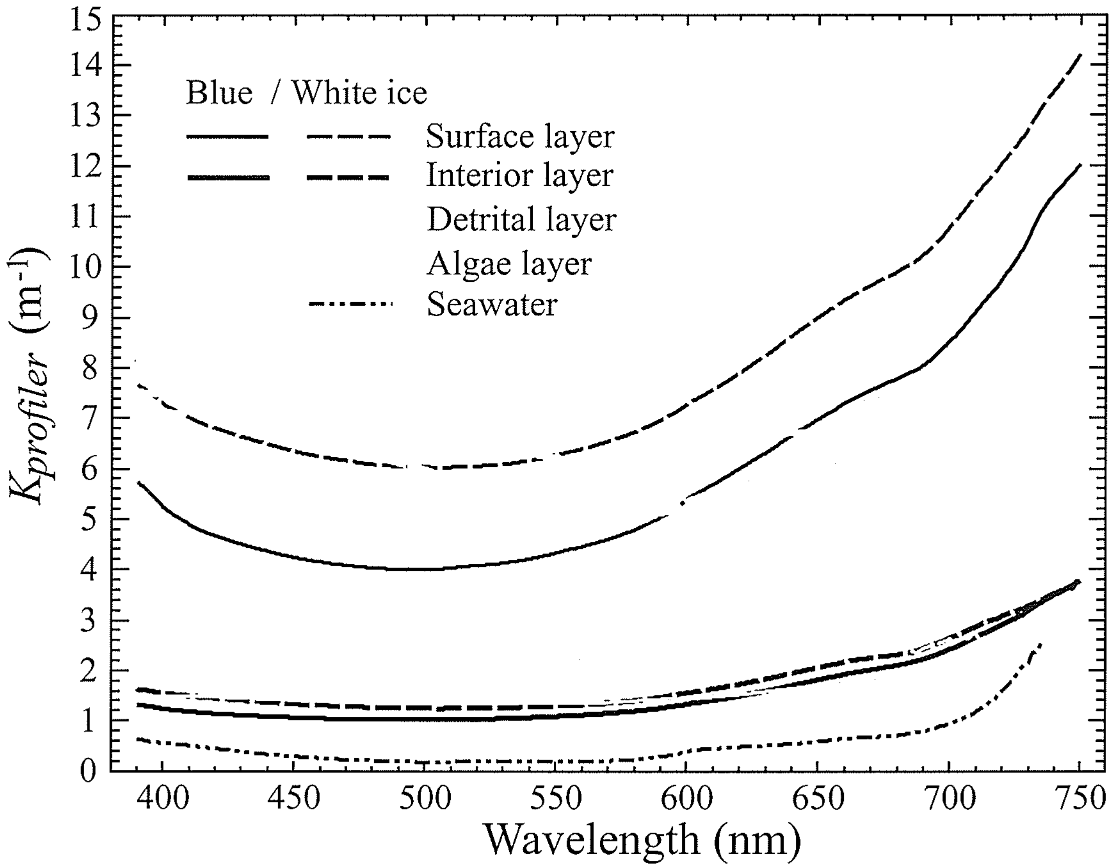

Figure 6.4. Profile of the spectral diffuse attenuation coefficient measured using the ice profiler within blue and white ice on 25 April. Values at each wavelength are obtained from the slope of the exponential fit of transmittance versus depth for intervals denoted in Figure 6.3.

homogeneous. Additionally, the grouping was supported by initial DISORT model runs that included multiple layers within the interior part of the ice and that showed that an asymptotic state of the radiation field had essentially been reached. Similar distances were found by, e.g., *Pegau and Zaneveld* (2000) and *Grenfell et al.* (2006). Significant deviations from the spectral shape of the interior ice $K_{profiler}(\lambda)$ were observed for the ice near the bottom. Not only is this due to an increased concentration of particulates and dissolved material, but also the brine volume increased markedly when approaching the ice/water interface (Figure 6.2).

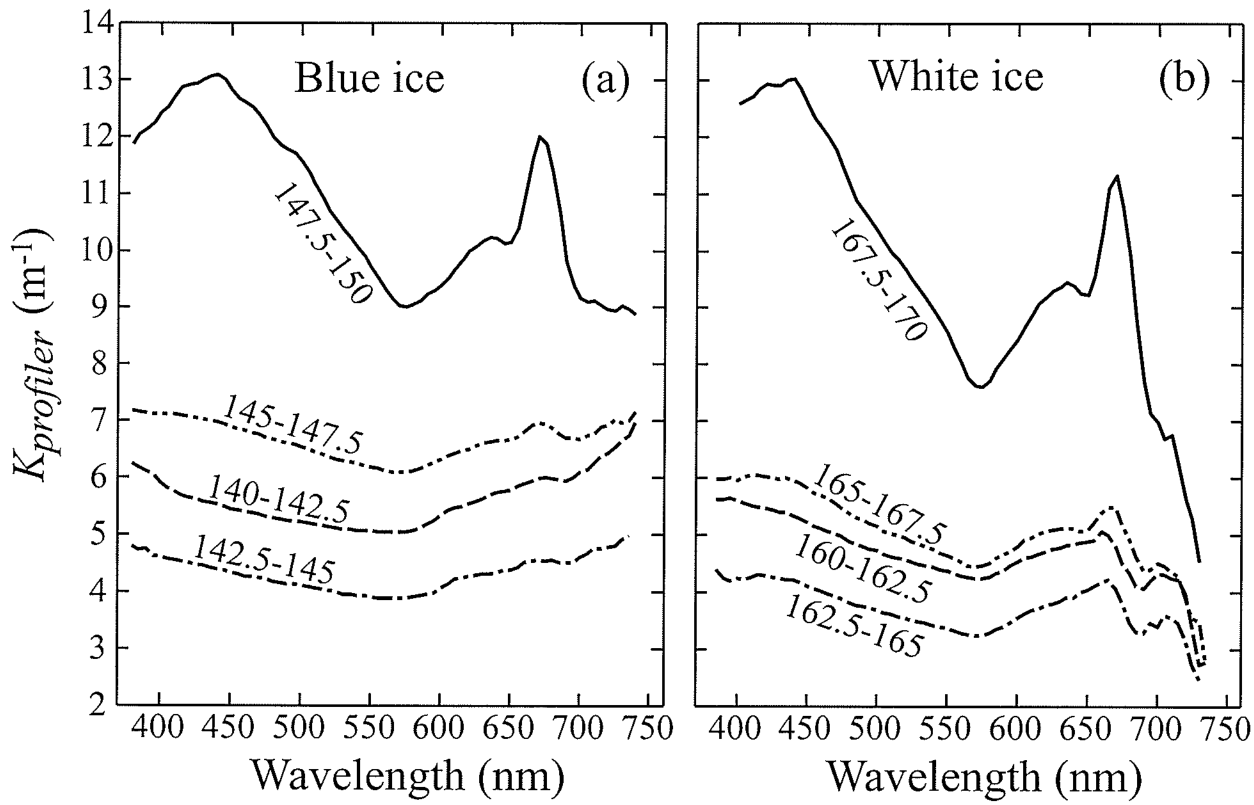

Figure 6.5. Vertical variation in the ice profiler spectral diffuse attenuation coefficient near the ice/seawater interface.

Ice algae are a significant factor in determining the optical properties of near-bottom sea ice. In Button Bay ice algae were most abundant within 2.5 cm of the ice/water interface (Figure 6.5). Maximum $K_{profiler}(\lambda)$ values were located at the chlorophyll *a* (chl *a*)-related peaks at 440 nm and 670 nm, suggesting that the main absorption was from living microalgal cells. Ice algae concentrations decreased rapidly away from the ice/water interface, and $K_{profiler}$ spectra showed indications of the presence of detrital matter or dead algal cells (e.g., *Bricaud and Stramski*, 1990). This material is probably due to partly degraded remnants from a previously active bottom ice algae layer that became trapped as the ice grew. Further up, in the detrital layer (Figure 6.4), the chl *a* peaks are further diminished. The small $K_{profiler}(\lambda)$ values above about 680 nm seem implausible since ice and brine themselves are expected to cause increased absorption at longer wavelengths. It is unclear whether chl *a* fluorescence, stimulated by available PAR, may have contributed to the low values, or if they are solely due to measurements uncertainties at low radiation levels. Note also that similar features were observed by *Ehn et al.* (2008).

The spectral albedo and transmittance through the ice sheet was measured immediately prior to the profile measurements. The white ice albedo had a maximum value of 0.82 at 510-520 nm (Figure 6.6a). At 750 nm it had dropped to about 0.72. The blue ice albedo was lower and showed more wavelength dependence: the maximum value was 0.67 at 480-500 nm and decreased to 0.41 at 750 nm. PAR albedos integrated over 400 to 750 nm were 0.81 and 0.62 for white and blue ice, respectively. Similarly, the total shortwave albedos were calculated following *Allison et al.* (1993) to be about 0.69 and 0.47. The corresponding transmittance spectra are

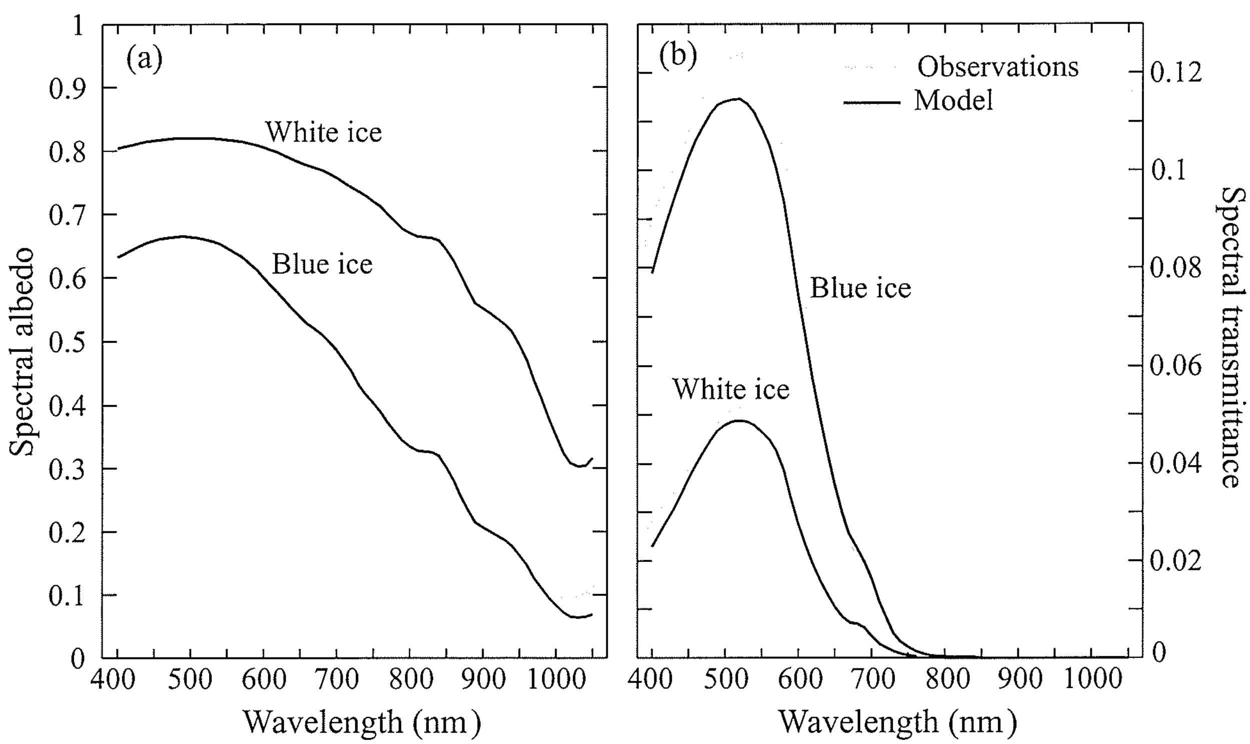

Figure 6.6. Measured and modeled spectral (a) albedo and (b) transmittance for white and blue ice types.

shown in Figure 6.6b. Peak transmittances were found at about 530 nm and were 0.051 and 0.124 for white and blue ice, respectively. At 750 nm values had decreased below 1.9×10^{-3}. Thus essentially only visible radiation remains below the ice cover. The PAR (and total shortwave) transmittances were calculated to be 0.034 (0.019) for white ice and 0.090 (0.051) for blue ice. These values suggest that about 29% (in white ice) and 48% (in blue ice) of the incident shortwave radiation was absorbed within the ice/snow cover.

6.4.3 Model iterations

For model iterations, the temperature of each layer was fixed from measurements (Figure 6.2a) and the density was kept constant at 920 kg m^{-3}. Salinity (to change the brine volume) and the effective radius of the dominant scatterers, r_{eff}, were changed in each layer until the slope and magnitude of the modeled $K_p(\lambda)$ spectra between 700 and 720 nm matched the measured $K_{profiler}(\lambda)$ spectra, thereby allowing for an estimate of the volume fractions of brine and pure ice where absorption by particulates and CDOM was small (see Eq. 6.6) (*Ehn et al.*, 2008).

In the bottom algae layers and in the white ice detrital layer (Figures 6.4 and 6.5), this was not possible due to contamination by particulates that resulted in unrealistic values above 680-700 nm. For these cases, the brine volume was taken from Figure 6.2c. A normalized particulate absorption spectrum, $a_p(\lambda)$, (presented in the spectral decompositioning subsection below) was utilized following the method described in *Ehn et al.* (2008) to estimate the absorption at longer wavelengths. Briefly, the ratio a_{imp}(570 nm)/a_{imp}(670 nm) was assumed equal to a_p(570 nm)/a_p(670 nm). These two wavelengths were chosen to represent the minimum and maximum absorption by ice algae (Figures 6.4 and 6.5). The magnitude of $a_{imp}(\lambda)$ was then adjusted (using chl *a* concentration as a multiplier) together with r_{eff} (for scattering by brine inclusions) during the iterations of the model until the model estimated $K_p(\lambda)$ matched $K_{profiler}(\lambda)$ at 570 nm and 670 nm.

The optical properties of the seawater were not the focus of this study. Thus it was opted to model the seawater following formulations found in, e.g., *Morel and Maritorena* (2001) and *Hamre et al.* (2004) and to include crude estimates of spectral absorption by both CDOM and phytoplankton based on the shape of $K_{profiler}(\lambda)$. In brief, CDOM absorption was expressed as $a_{dom}(\lambda) = a_{dom}(440\text{ nm}) \exp[S_{dom}\,(440-\lambda)]$, where $a_{dom}(440\text{ nm}) = 0.16\text{ m}^{-1}$ and $S_{dom} = 0.018\text{ nm}^{-1}$. Phytoplankton absorption was calculated as a function of chl *a* concentration C_{chl}, i.e., $a_{chl}(\lambda) = 0.06\, A_{chl}(\lambda)\, C_{chl}^{0.65}$, where C_{chl} was set to 0.6 mg m^{-3}, and $A_{chl}(\lambda)$ is a particulate absorption spectra measured for the bottom ice algae layer and normalized to unity at 440nm. Scattering for seawater was modeled as $b_{sw}(\lambda) = (129\ \lambda^{-1})^{4.32}$ and contributions by phytoplankton were considered negligible. This gives a $b_{sw}(550\text{ nm}) = 0.0029\text{ m}^{-1}$, i.e., orders of magnitudes smaller than for sea ice, effectively rendering reasonable changes in seawater IOPs insignificant in influencing sea ice IOPs.

Input values obtained through the iterations are summarized for each layer in Table 6.1. Note that it is the combination of the volume fraction and the effective radius of the dominant scatterer that determines b_{tot} (Eq. 6.5). For example, b_{tot} for the interior ice layer (layer 2) in white ice is higher than for blue ice even though the blue ice has a higher v_b estimate. The actual effect of scattering on the radiation field is also dependent on the asymmetry parameter, g_{tot}, and the absorption of the medium. A similarity parameter, $S_{tot} = [1 + (1-g_{tot})\, b_{tot}\, a_{tot}^{-1}]^{-1/2}$, was defined by *van de Hulst* (1980) so that a high-scattering media with varying IOPs but with the same S_{tot}

Table 6.1. Layer properties used in model: layer thickness, density, brine and air volume, effective radius of scatterers, asymmetry parameter, scattering coefficient, and similarity parameter. The similarity parameter was calculated with a_{tot}(500 nm).

	Layers	Δz (m)	ρ (kg m^{-3})	v_b (%)	v_a (%)	r_{eff} (mm)	g_{tot}	b_{tot} (m^{-1})	S_{tot}
Blue ice	1a	0.001	800	3.84	13.18	2.750	0.855	71.9	0.8432
	1b	0.129	800	3.84	13.18	2.750	0.855	71.9	0.0355
	1c	0.07	920	31.50	3.25	2.750	0.995	172	0.1792
	2	1.00	920	13.69	1.47	0.3215	0.995	639	0.0927
	3	0.20	920	8.02	0.67	0.297	0.995	405	0.2364
	4	0.10	920	27.27	2.94	0.325	0.995	1258	0.3654
White ice	1a	0.17	240	0.00	73.83	1.850	0.855	212	0.0673
	1b	0.15	800	2.74	13.09	2.750	0.855	71.4	0.0548
	1c	0.08	920	14.87	1.52	2.750	0.995	81.1	0.2768
	2	1.00	920	5.64	0.43	0.107	0.995	790	0.0914
	3	0.20	920	20.69	2.19	0.550	0.995	564	0.2995
	4	0.10	920	27.27	2.94	0.475	0.995	861	0.4608
Seawater	5	40.0	1000	100	0				

displayed the same AOPs. A version of S_{tot} was applied successfully to sea ice radiative transfer modeling by, e.g., *Light et al.* (2004). Blue and white ice interior ice layers have nearly identical S_{tot} values (Table 6.1). A comparison between other layers shows larger variations, however, the shapes of S_{tot} profiles are consistent between the two ice types.

The surface layer was treated with an alternative approach because the matching of $K_p(\lambda)$ against the measured $K_{profiler}(\lambda)$ resulted in significant underestimation of the transmittance through the ice (about 40% for blue ice and 80% for white ice) and overestimation of albedo (about 9% and 18%, respectively). Instead, the IOPs within the surface layer were modified in order to match the measured albedo (Figure 6.6a) and maintain a good agreement with the transmittance (Figure 6.6b). The surface layers were highly variable and complex, and it is impossible within this study to represent them fully. Furthermore, when using only one homogeneous layer in the model, it was impossible to model the spectral shape and magnitude of both transmittance and albedo reasonably. Thus, the main goal to obtain a representative radiation field and magnitude at the top of the interior ice layers could not be accomplished. We therefore opted to divide the surface layer based on field observations of snow thickness and freeboard. The blue and white ice surface layers were both modeled by three layers – two above the waterline (1a, 1b) and one below (1c). Layer 1a for blue ice was identical to layer 1b except that it included absorption by soot. For white ice, layer 1a was modeled as snow with optical properties determined by snow grains and soot. The total thickness of layers 1a to c were 20 cm for blue ice and 40 cm for white ice to correspond with $K_{profiler}(\lambda)$ depth intervals (Figure 6.3). In the following, a description of how the arbitrary yet physically plausible input values given to the surface layers were derived is provided.

To obtain reasonable agreement with albedo and transmittance measurements, ice, brine and air volume fractions, scattering and absorption by soot needed to be considered (following *Warren*, 1982; *Grenfell*, 1983; *Grenfell et al.*, 2002). Soot is an effective absorber especially in visible wavelengths (e.g., *Bond and Bergstrom*, 2006). However, at near-infrared wavelengths, the effect on albedo by the absorption of natural concentrations of soot in snow is reduced compared to that of the ice itself. At λ > 1000 nm it is negligibly small (e.g., *Grenfell et al.*, 2002). Thus, r_{eff} and the density (i.e., scattering and absorption) for "pure" sea ice or snow could be inferred.

A density of 800 kg m^{-3} was given to layer 1b, which resulted in a high air volume fraction (~13%) above the waterline. This is feasible as gravity would tend to force liquid towards the waterline. The low salinities that were measured and the large air pockets that were observed also support this and suggest that this ice layer was composed of superimposed ice. The optical effect of the density decrease was to decrease $a_{tot}(\lambda)$ (see Eq. 6.6) and thus reduce the wavelength dependence of the spectral albedo so that values observed between 700 and 750 nm could be matched for the bare blue ice case. A good match at these longer wavelengths was obtained when r_{eff} for the air bubbles (dominant scatterers) was set to 2.75 mm. For convenience the same r_{eff} of 2.75 mm, but for brine inclusions, was given to layer 1c, resulting in a relatively low scattering coefficient (Table 6.1). However, the value is plausible as the ice was found to have a very high brine volume.

Layers 1b and 1c in white ice were assumed to have the same r_{eff} as in blue ice. Density for snow layer 1a was set to 240 kg m^{-3} and r_{eff} to 1.85 mm. It was indeed observed that the deteriorated snow pack was composed of very coarse grains. The use of this density in the model resulted in too small of an albedo at longer wavelengths; however, correcting this would require using an unrealistically low density (about 150 kg m^{-3}). The adopted values, however, resulted in excellent agreement within 400-750 nm – the wavelength region most important for transmission.

Spectral absorption coefficient of soot was modeled as $a_{soot} = C_{soot}\ MAC_{soot}\ 550\ \lambda^{-1}$, where λ is wavelength (nm), C_{soot} is the soot concentration (g m^{-3}) and MAC_{soot} is the mass absorption cross-section with a constant value of 7.5 m^2 g^{-1} at 550 nm (*Bond and Bergstrom*, 2006; *Flanner et al.*, 2007). The λ^{-1} relationship was in good agreement with $a_p(\lambda)$ measured from a melted snow sample on 21 April (see below). However, lacking detailed measurement of soot distribution and concentration within the snow and ice, it was inferred from the optical measurements (Figure 6.6) using the model. The albedo is most strongly controlled by the layer bordering the surface (*Grenfell et al.*, 2002). Thus, it was sufficient to include soot only in layer

1a, and the thickness of this layer and its soot concentration was used to control the magnitude of the transmittance and albedo. The results indicate that soot was concentrated in a very thin surface layer on the blue ice. Thus, the soot on blue ice was modeled by adding a 1 mm thick surface layer with C_{soot} = 2.9 g m^{-3}. This is identical to 3625 ng g^{-1} when dividing by density. The average concentration over layers 1a and 1b (13 cm) is 0.022 g m^{-3} or 27.9 ng g^{-1}. For white ice, a good agreement was found when adding 0.013 g m^{-3} (54.2 ng g^{-1}) of soot evenly throughout the 17 cm thick snow layer. It is plausible that soot would be distributed more homogenously within a snow pack compared to blue ice where the melting of the snow cover would tend to collect soot on the bare ice surface (*Light et al.*, 1998; *Grenfell et al.*, 2002).

Finally, $a_{imp}(\lambda)$ was fine-tuned for each wavelength and each layer to obtain the desired agreement between $K_p(\lambda)$ and $K_{profiler}(\lambda)$ between 400 nm and 720 nm. This was done by including an extra absorption coefficient, $\Delta a_{imp}(\lambda)$, to Eq. 6.6 that was used to adjust $a_{tot}(\lambda)$. In the following, the fine-tuned spectral diffuse attenuation coefficients and absorption coefficients are presented. Then the results are evaluated by comparison to independent observations at the measurement site and to spectra found in the literature.

6.4.4 Inferred optical properties

The modeled $K_d(\lambda)$ are always smaller than $K_p(\lambda)$ due to a non-isotropic and increasingly more downward directed radiation field with depth caused by multiple scattering within the snow/ice and the comparatively small scattering in the air and seawater (Figure 6.7). The difference between the two is, however, small for the interior ice, implying that the radiation field has reached a near-asymptotic state. The difference is 0.035 m^{-1} and 0.05 m^{-1} on average between 400 nm and 750 nm for blue ice and white ice, respectively. The largest difference for

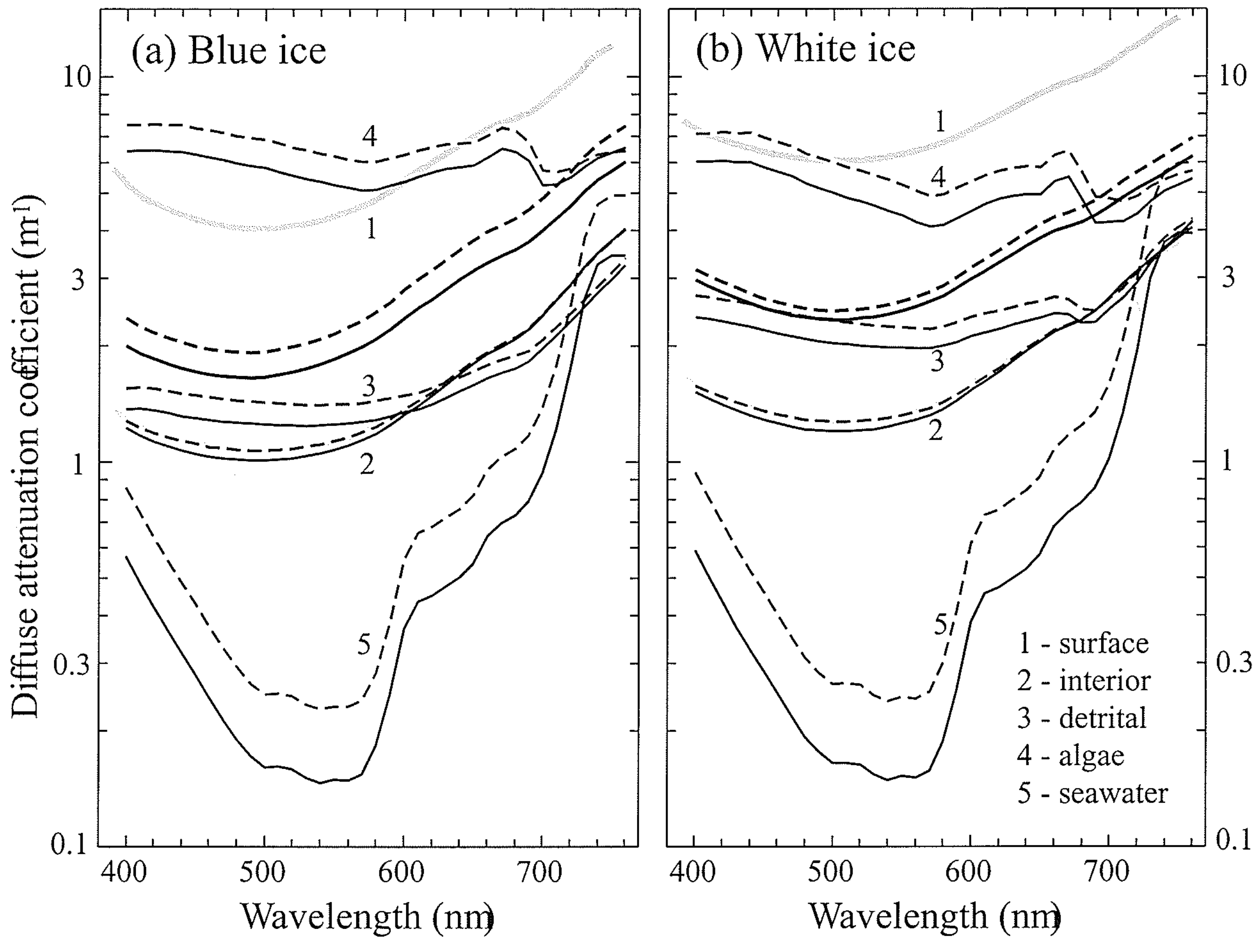

Figure 6.7. Diffuse attenuation coefficient for (a) blue and (b) white ice layer types. The measured (ice profiler-specific) values are shown by the thick grey lines, while the modeled K_d and K_p are shown by the thin solid and dashed lines. Spectra with corresponding shapes belong to the same layer type denoted by the integer.

interior blue ice was 0.056 m^{-1} at 470 nm, and 0.07 m^{-1} for interior white ice at 480 nm. However, values merged to within ±0.01 m^{-1} at 700-750 nm and at longer wavelengths there was essentially no difference as absorption gained in importance. Seawater $K_{profiler}(\lambda)$ are in better agreement with $K_d(\lambda)$ than $K_p(\lambda)$ above 600 nm. This may be indicative of a phase function that did not fully represent the radiation field in the seawater.

The commonly used cold blue ice $K_d(\lambda)$ of *Grenfell and Maykut* (1977) (as reported by *Perovich*, 1990) fall between our $K_d(\lambda)$ estimates for blue and white ice interior below about 660 nm. From about 570 nm, our spectra show less increase with wavelength. *Pegau and Zaneveld* (2000) obtained spectra similar to *Grenfell and Maykut* (1977). $K_d(\lambda)$ for bare ice in the coastal zone by *Grenfell et al.* (2006), measured similarly to ours, compare reasonably with our observations up to about 600 nm, but then show even less increase towards longer wavelengths.

There is a significant difference between $K_{profiler}(\lambda)$ measured for the surface layers and $K_p(\lambda)$ inferred from spectral albedo (Figure 6.7). The minimum difference occurred at 510 nm for both blue and white ice, and was about 2.1 m^{-1} and 3.6 m^{-1}, respectively. At 400 nm the difference was 2.9 m^{-1} for blue ice and 4.1 m^{-1} for white ice, and increased to values above 5 m^{-1} and 7.7 m^{-1}, respectively, above 750 nm. The difference to $K_d(\lambda)$ was correspondingly larger – the minimum difference at 510 nm was about 2.4 m^{-1} and 3.7 m^{-1}, respectively. There are a few possible causes for the difference. Firstly, $K_{profiler}(\lambda)$ data were not corrected for the immersion effect. Secondly, the difference in indices of refraction across the air/ice interface may result in an apparent increase in downwelling irradiance below the surface (*Jin et al.*, 1994; *Jiang et al.*, 2005). However, no observational evidence, apart from theoretical studies assuming completely flat surfaces, exists to my knowledge in order to evaluate this effect for natural sea ice with small-scale surface roughness features. Neglecting these effects would tend to underestimate radiation levels within the ice. In addition, the incident radiation field was modeled as completely diffuse while it may have included a direct component. However, sky conditions were fully overcast, the sun was not visible through the clouds and no shadows could be detected on the ground.

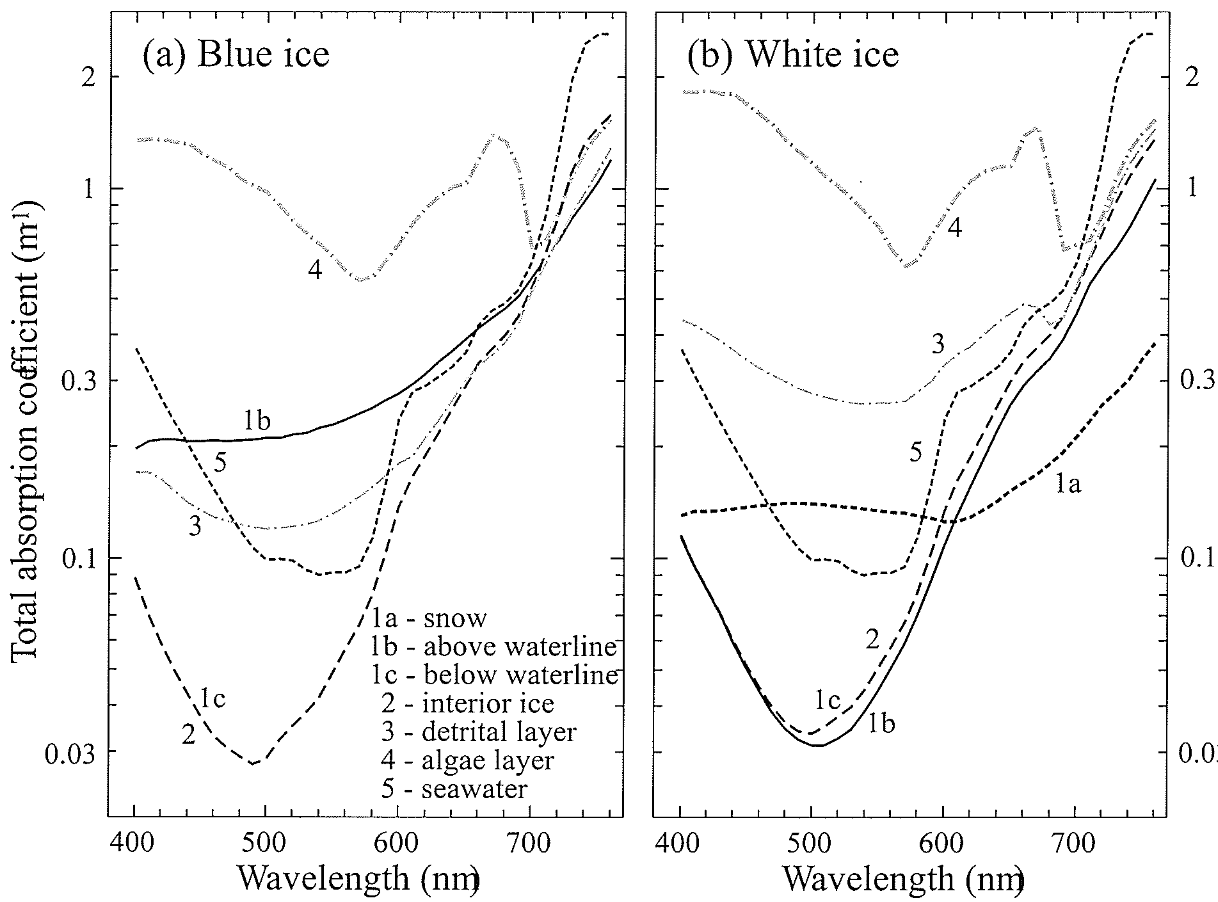

Figure 6.8. Estimate of the total absorption coefficient for layers characterizing blue ice (a), white ice (b) and seawater. Curve 1b for blue ice represents a thickness-weighted average for layers 1a with impurities and 1b.

The total absorption coefficient for each layer of the model is presented in Figure 6.8. A striking feature is the low absorption within interior portions of the ice relative to layers near boundaries and even the seawater. The higher seawater $a_{tot}(\lambda)$ is mostly due to more CDOM. This is expected as sea ice growth is known to reject dissolved salts and other impurities like CDOM, and low biological activity within the interior ice would result in little locally produced CDOM. The low absorption in snow for $\lambda > 600$ nm (Figure 6.8b) follows directly from the use of a low density. In general, $a_{tot}(\lambda)$ is controlled by impurities within visible wavelength, while ice and seawater become more important at longer wavelengths. In the following, $a_{tot}(\lambda)$ and the effects of impurities are examined in more detail.

6.4.5 Spectral decomposition

A particulate absorption spectrum, $a_p(\lambda)$, was measured from a bulk snow sample taken on 21 April. A regression of the form $a_p(\lambda) = 114.9\lambda^{-1} - 0.0845$ explained the impurity spectra from the bulk snow sample collected on 21 April with a $r^2 = 0.99$ between 400 nm and 720 nm (Figure 6.9a). Values increased sharply below 400 nm, and became noisy above 720 nm. The λ^{-1} fit related to soot concentrations of 0.022 g m^{-3} and 0.013 g m^{-3} did not represent $a_{imp}(\lambda)$ for blue and white ice inferred from the spectral albedo to the same degree (Figure 6.9a). In general, the $a_{imp}(\lambda)$ inferred using the model are consistent with the observations, however, they show a more variable spectral signature and less increase towards shorter wavelengths. It thus appears that

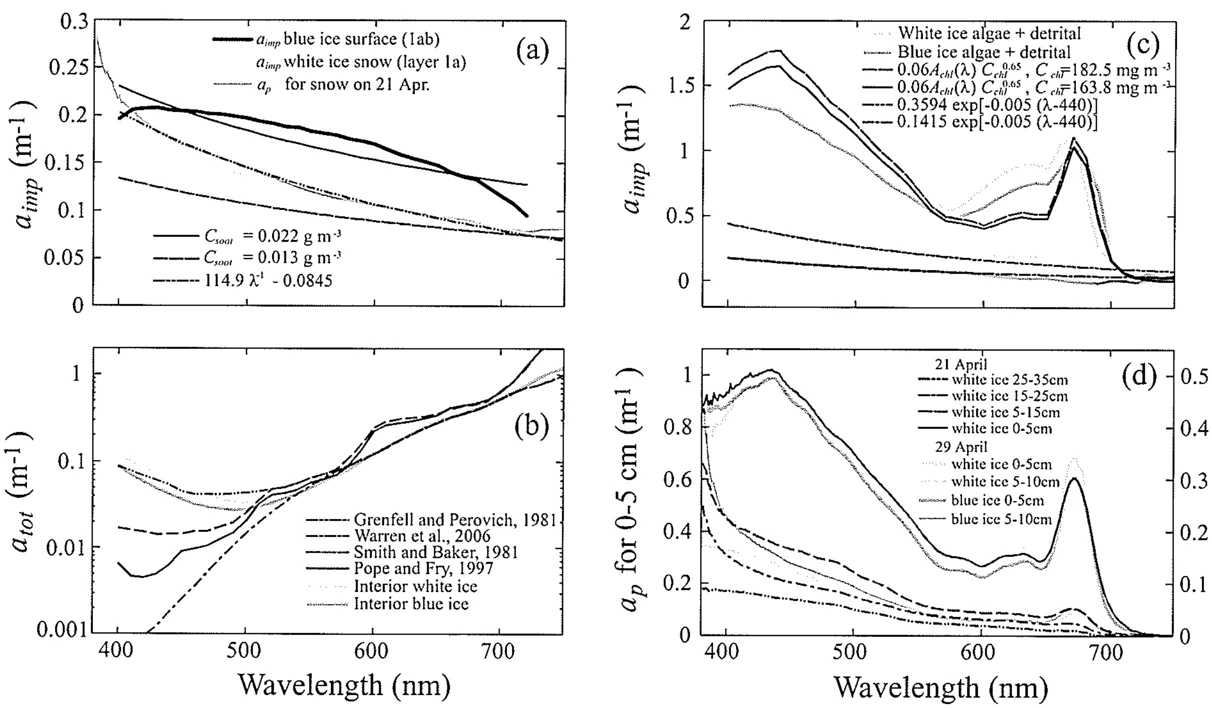

Figure 6.9. Absorption coefficients in three layers: (a) absorption by impurities within snow (white ice layer 1a) and blue ice surface layer (1ab) with measurements from snow samples taken on 21 April, (b) total absorption coefficient for sea ice compared to published pure ice and seawater spectra, (c) absorption by impurities within the bottom layers, and (d) measured particulate absorption spectra. The algorithm by, e.g., *Morel and Maritorena* (2001) shown in the legend of (c) was used for chl a estimation.

some absorbing components were not included in the snow sample or retained on the filter.

Interior ice absorption was in good agreement with pure ice absorption coefficients (*Grenfell and Perovich*, 1981; *Warren et al.*, 2006) (Figure 6.9b). The increase in absorption towards shorter wavelengths could be explained by adding CDOM absorption a_{dom}(440nm) = 0.04 m^{-1} for blue ice and a_{dom}(440nm) = 0.05 m^{-1} and non-algal (or detrital) particulate absorption a_{nap}(440nm) = 0.01 m^{-1} for white ice, with exponential slopes of S_{dom} = 0.018 nm^{-1} and S_{nap} = 0.005 nm^{-1}, respectively, to the absorption coefficients by *Pope and Fry* (1997) and Warren et al. (2006). However, the increase is very similar to pure ice values reported by *Grenfell and Perovich* (1981). This suggests that the interior ice was very clean in Button Bay. Brine absorption following *Smith and Baker* (1981) can also be used with a slight adjustment to $a_{imp}(\lambda)$. Values between 540-600nm were lower by about 0.01 m^{-1} than those found in literature. A part of this is due to air inclusions within the ice, however, an about 9% air volume would have been required to account for the lower values, which can be considered unreasonably high when typical values reported in the literature range 0-1%. The observations presented here confirm that the use of pure ice and seawater absorption for interior parts of sea ice is appropriate in radiative transfer modeling.

Excellent agreement of shapes was found between $a_p(\lambda)$ from GF/F filter and $K_{profiler}(\lambda)$ for bottommost 2.5 cm (Figures 6.5 and 6.9d). However, the large difference in algae layer $K_{profiler}(\lambda)$ between 570-670 nm is explained by the different shape of $a_{imp}(\lambda)$ away from the bottom 2.5 cm. Interestingly, this also coincides with the increased absorption in seawater compared to ice, however, increasing the brine volume for the algae layer to 100% (no ice) was not sufficient to explain the discrepancy. $a_p(\lambda)$'s for the detrital layer further up in the ice are well described by λ^{-1} relationships; however, at $\lambda > 570$ nm the agreement does not hold (Figure 6.9c). Generally, there was a good agreement with $a_p(\lambda)$ filter measurements from melted ice samples and model iterations (Figure 6.9cd). Chl *a* concentration was measured fluorometrically (*Parsons et al.*, 1984) from the same filters on 29 April. Measured chl *a* concentrations of the 0-5 cm and 5-10 cm layers were 133 mg m^{-3} and 5.6 mg m^{-3} for white ice and 104 mg m^{-3} and 7.8 mg m^{-3} for blue ice, respectively. The chl *a* concentrations of 163.8 and 182.5 mg m^{-3} obtained as tuning parameters to the algorithm presented in *Morel and Maritorena* (2001) are somewhat higher (Figure 6.9c).

6.4.6 Verification of the modeled spectral albedo and transmittance

A way to verify the assumptions used in the model is to compare model results against measured albedo and transmittance spectra. The simulated transmittance for both blue and white ice is underestimated (Figure 6.6b) when the attenuation for the surface layer is inferred from spectral albedo (Figure 6.6a). Blue ice transmission is underestimated by up to about 11% (0.08 versus 0.09 at 400 nm), however, it is less than 7% above 450 nm. Similarly, for white ice the difference is up to 20% between 400 and 450 nm. The underestimation within other wavelengths is less than 4%. However, the agreement is very good when considering that albedo and transmittance were not measured at the exact same location (1.5 m apart) as the profile measurements.

As previously mentioned, the thickness differences were about 7 cm at the blue ice site and 3 cm at the white ice site, which implies that it is feasible that radiation levels could have been lower. However, with only the two thickness measurement pairs, a detailed characterization of the spatial variability cannot be attempted, but with the model it is possible to estimate the thickness reduction required to match observations. A reduction in thickness of interior blue ice by 10 cm (to 0.9 m) results in an excellent agreement. A 6 cm interior ice thickness reduction was required to increase transmittance levels sufficiently for white ice, however, values below 450 nm were still underestimated. Other layers with larger optical thicknesses would require smaller thickness adjustments, and a perfect match can be obtained without large changes.

There are a number of other possible ways to account for the difference in the model transmittance. For example, by confining the field-of-view of the profiler to more horizontal directions (Eq. 6.4), $K_d(\lambda)$ can be decreased compared to $K_p(\lambda)$ especially for layers near boundaries. Accounting for the difference in index of refraction at air/ice interface may be expected to increase transmission (*Jin et al.*, 1994). The complexity of the model can be further increased by introducing additional layers. Soot in white ice snow can be concentrated closer to the surface, which would increase transmission in similar ways as for blue ice. Another likely reason to the underestimation is, however, the modeling of the bottom algae layer as one 10 cm layer. There is a large variability in properties within this layer (Figures 6.5 and 6.9d). Concentrating algae at the ice/water interface has a similar effect as concentrating soot near the upper surface. However, this would require the addition of a layer and further increase the complexity of the model. More targeted studies that focus on the air/ice interface or bio-optical properties may need to characterize properties near interfaces in more detail (e.g., *Mundy et al.*, 2007).

6.4.7 Implications for interior ice melt

In the period from 21 to 25 April, the interior ice temperature at the white ice site rose by about 0.5 °C on average in the 1 m layer and the brine volume by about 2 %-units, while the salinity remained unchanged (Figure 6.2). This corresponds to an energy requirement of about 7.1 MJ m^{-3}, or about 20.6 W m^{-3} on average over the four day period (noon to noon). The energy required for phase change was about 7 times that for temperature increase. For the period 21-29 April, the analogous figures were about 1.0 °C, 3.9 %-units and about 20.2 W m^{-3}, respectively.

By applying the results from the radiative transfer modeling, the attempt in this section is to provide an assessment on how important shortwave radiation absorption is in bringing about the change seen in interior ice. This analysis serves to set the AOPs observations in a context of energy partitioning within the sea ice. The analysis is limited to 21-25 April because of the albedo increase and variable conditions that followed on 26 April due to snowfall and drift. Additionally, only interior white ice is considered because its physical properties are known from measurements.

The energy partitioning in the ocean/sea ice/atmosphere system is readily obtained from observations of shortwave albedo and transmittance. $\alpha(\lambda)$ and $T(\lambda)$ were observed daily around noon in the period between 21 and 25 April. The spectra were extended to encompass the total shortwave spectrum using formulations in *Allison et al.* (1993). This requires an incident solar spectrum covering the range 300-2500 nm. It was obtained using the atmospheric radiative transfer model SBDART (e.g., *Ricchiazzi et al.*, 1998) for a cloudy sky with stratus clouds (an optical depth of 17) and its magnitude scaled to match the incident irradiance. The uncertainty in the total albedo is estimated to be < 0.01, while total transmittance values were obtained directly from measurements. The white ice albedo remained fairly constant at 0.70 ± 0.03 over 21-25 April. Over the same time, the blue ice albedo showed a significant decrease from about 0.85 (new snow deposition) to 0.45-0.47 (bare ice surface) (*Ehn et al.*, 2006). Correspondingly, white ice transmittance was 0.016 ± 0.005. From 21 to 25 April (solar noon to noon) the average incident shortwave irradiance was measured to be 230 W m^{-2}. Thus, the above values suggest that the average shortwave absorption in white ice was about 65 W m^{-2} (22.5 MJ m^{-2}). These calculations assume that surface conditions did not significantly change within a day. There were indications that this did occur (see *Ehn et al.*, 2006). This shortwave absorption is large enough to explain the observed increase in temperature and brine volume, if the heating effect would be distributed evenly within the ice cover. However, most radiation is absorbed in the surface layers.

The difference in net irradiance (downwelling - upwelling) above and below a layer gives the shortwave energy absorbed within it. With values shown in Table 6.1 and Figure 6.8, and with a representative surface incident solar spectrum, DISORT outputs both up- and downwelling spectral irradiances at every layer interface. The net irradiances were then integrated over 400-1050 nm. Radiation outside this wavelength range was assumed to have been absorbed within the surface layer as can be expected from the high absorption by water and ice. The absorbed solar energy in the interior white ice was found to be about 8.6 W m^{-3}, which represents only 4% of the incident radiation. However, this implies that about 40% of the energy responsible of the internal melting was provided directly by shortwave solar radiation, while the rest is due to heat conduction. Based on the three temperature and salinity profiles in Figure 6.2, the conductive heat flux from below was estimated to be about 3 W m^{-2} using the thermal conductivity, k_{si}, expression $k_{si} = k_i + 0.13\ S_{si}/T_{si}$ by *Untersteiner* (1961), where $k_i = 2.1$ W m^{-1}

K^{-1} is the thermal conductivity of pure ice, S_{si} and T_{si} the salinity and temperature of the bottom ice layer. The heat conducted from above was more variable: on 21 April it was -0.5 to 0 W m^{-2}, on 25 April about 6.1 W m^{-2} and on 29 April about 4.5 W m^{-2}. The values obtained from these rough calculations (i.e., up to 17.7 W m^{-3} or 86%) do not quite add up to the estimated energy needed for the melting and temperature increase, however, magnitudes are comparable. A higher frequency in temperature profile measurements may furthermore improve conductive heat flux estimates. This basic energy balance calculation suggests that shortwave radiation and heat conduction supplied roughly equal parts of what was needed for the observed interior ice change during this study, and that neither can be neglected if the evolution of the ice melt is to be predicted.

6.5 Conclusions

Spectral radiation profiles measured using a custom built in-ice profiler (Figure 6.1) within melting landfast sea ice in western Hudson Bay are presented. The profiler views a limited portion of the radiation field between about 45° and 90° from the zenith. This complicates the assessment of the optical properties of the medium. For example, the profiler-specific diffuse attenuation coefficient, $K_{profiler}(\lambda)$, overestimate $K_d(\lambda)$ for downwelling irradiance, especially near the upper and lower boundary, because radiation becomes increasingly downward directed with depth within sea ice. Thus, to infer down- and upwelling spectral irradiance profiles, and IOPs, a radiative transfer model (*Stamnes et al.*, 1988) was utilized and the results verified against independent measurements of spectral albedo and bulk transmittance. As in other studies (e.g., *Maffione et al.*, 1998; *Pegau and Zaneveld*, 2000;

Grenfell et al., 2006) the radiation field was found to reach a near-asymptotic state within 20-40 cm from boundaries where $K_d(\lambda)$ approximated $K_{profiler}(\lambda)$. The interior portion of the sea ice could therefore be modeled as single 1-meter-thick homogenous layer.

Our observations confirm that the use of pure ice and seawater absorption for interior parts of sea ice is appropriate in radiative transfer modeling. $a_{imp}(\lambda)$ for the thermodynamically grown interior ice was very small. Representative values for b_{tot} ranged about 600-800 m^{-1} when g_{tot} = 0.995 for the high ice temperatures (*Light et al.*, 2004). Radiative transfer was much complicated near the boundaries. Freeze-thaw processes had modified the surface into areas of bare ice (blue ice) and snow-like mounds (white ice) (*Ehn et al.*, 2006). Layers above the waterline were highly porous due to gravity drainage. Liquid water was present in high volume fractions immediately below the waterline (Figure 6.2). Superimposed ice formation was detected. Absorption within visible wavelengths was significantly affected by impurities (Figure 6.9a). Model simulations suggested that soot was concentrated in a thin layer on the blue ice surface, while more evenly distributed within the white ice snowpack.

Organic matter produced by biological activity was the most significant factor affecting radiative transfer in the bottom sea ice layers, mostly through absorption. Algae typically inhabit a thin layer at the ice/water interface. As sea ice grows, a portion of the ice algae become entrapped within the ice. With time the optical signature of the trapped material resemble increasingly that of detrital matter (Figure 6.9cd). It appears that b_{tot} was smaller in the detrital layer compared to interior ice, and then increased to higher values for the bottom 10 cm algae layer (Table 6.1). It is, however, difficult to asses the effect of organic particulates on scattering, as particulate concentrations increased towards the ice/water interface together with significant structural changes in the sea ice. Additionally, low backscattering from the seawater significantly affects the radiation field within the bottommost part of the sea ice.

A minimum of seven layers were required to simulate both albedo and transmittance measurements: 1) melting snow, 2) ice above the waterline, 3) ice below the waterline, 4) interior ice, 5) bottom detrital layer, 6) bottom algae layer, and 7) seawater. With fewer layers, both the spectral albedo and transmittance could not be represented simultaneously. Including more layers mimic the ice more closely, however, increase the complexity of the modeling.

These findings are consistent with previous studies in the Arctic (*Pegau and Zaneveld*, 2000; *Grenfell et al.*, 2006; *Ehn et al.*, 2008). The variable melting and freezing conditions that are typical for the sub-Arctic seasonal sea ice region are indicative of conditions that may become more common in the Arctic. They, however, represent only a snapshot in time and space. Here, the attempt has been to limit both of these aspects. Nevertheless, some consistent features in the melt progression were identified. Continuous melting appears to regenerate the white ice surface layer and keep the albedo at a roughly constant value (in this case at about 0.70). Similarly, relatively little variations in time were observed in $a_p(\lambda)$ for the bottommost algae layer (Figure 6.9d). Future research may need to increasingly focus on issues related to variability and determine the conditions at which these quasi-stable melt conditions break down.

CHAPTER 7: Summary, Conclusions and Recommendations

7.1 Summary and conclusions

The sea ice cover at high latitudes is a key component in the earth's climate system in large part due its interaction with solar shortwave radiation (e.g., *Curry et al.*, 1995). Furthermore, sea ice is of considerable ecological importance as its porous structure creates a stable habitat for a thriving ice algal and microbial community, while at the same time limiting sub-ice primary production by controlling the availability of photosynthetically active radiation (PAR). Presently, the sea ice in the Arctic Ocean is undergoing an escalating reduction in both ice extent and thickness (*Yu et al.*, 2004; *Nghiem et al.*, 2007; *Comiso et al.*, 2008). Recent satellite-derived estimates (*Maslanik et al.*, 2007) have shown that the Arctic Ocean is transforming rapidly towards a seasonal sea ice regime, i.e., ice-covered winters and ice-free summers, not unlike what is experienced in Hudson Bay at present. As such, the relative expansion of seasonal sea ice warrants thorough investigation to further the understanding of its seasonal evolution and to improve its representation in climate models. An integral component in such investigations is to gain an improved understanding on the complex nature of solar radiation interaction with the sea ice environment. Presently, advances are hampered by the scarcity of observational data.

My thesis focuses on the determination of apparent and inherent optical properties (AOPs and IOPs), and the underlying physical conditions that determine them, for seasonal sea ice during fall freeze-up and the spring melt periods. To accomplish this I use both field observations and radiative transfer modeling. Particular attention is directed towards 'warm sea ice', which is loosely defined here as sea ice with temperatures above -5°C (*Golden et al.*, 1998). Note that the 'warm' state of sea ice is not unusual (either spatially or temporally). It is the prevailing state near the bottom portion of sea ice which is affected by underlying warm seawater. In addition, temperatures are typically 'warm' throughout the sea ice cover during the spring and summer melt season, and when the sea ice is sufficiently thin. Temperature increases above -5°C have been shown to correspond to dramatic porosity increases resulting in the enlargement and merger of individual brine inclusions to eventually form connected brine networks (*Cox and Weeks*, 1983; *Leppäranta and Manninen*, 1988; *Golden et al.*, 1998; *Light et al.*, 2003). Connected brine networks provide the premise for brine dynamic processes to significantly alter the ice properties over time (e.g., *Vancoppenolle et al.*, 2007). In fact, it can be postulated that a large portion of the variability observed in sea ice structural and physical properties (and thus also IOPs and AOPs) can be related to processes that take place at temperatures above -5°C. Optically, the anisotropic nature of warm sea ice, with mainly vertically oriented brine inclusions (tubes and channels), may complicate, or even invalidate, the treatment of scattering in radiative transfer models that are based on the assumption of a homogeneous media with distinct, evenly distributed spherical inclusions.

In Chapter 1, I first provided the scientific rationale for sea ice research in view of the dramatic changes in the ice environment that we are now witnessing in the Arctic. I then provided the context and rationale for my thesis and provide a series of research questions to structure my thesis. In Chapter 2, I reviewed the pertinent literature and theory required to understand sea ice radiative transfer and the thermophysical changes, which affect both the inherent and apparent optical properties of snow covered sea ice in the spring and fall seasons.

In Chapter 3, I presented a study on newly formed ice types during the fall freeze-up period in Amundsen Gulf (Cape Bathurst polynya) which focused on determining physical, structural and apparent optical properties of the sea ice. The sampled sea ice was typically less than 0.3 m thick (Figure 3.4), i.e., the samples were of new and young ice types (*World Meteorological Organization*, 1985). This observational study is a significant contribution to the scientific literature as published accounts on newly formed ice during the fall freeze-up period are sparse (e.g., *Perovich*, 1991; *Maksym et al.*, 2002). Observations into newly forming sea ice in early springtime leads and artificially grown in a laboratory setting are also sparse (e.g., *Perovich*, 1990b; *Perovich and Richter-Menge*, 1994; *Martin et al.*, 1995; 1996; *Perovich and Gow*, 1996). None of these, to my knowledge, provide a detailed and coincident description of physical, structural and optical properties.

The results showed that spectral reflectance for the thin, newly formed sea ice types was most strongly related to surface features such as dry or slushy bare ice, frost flowers or snow cover. Ice thickness was also important, however, mostly because surface features were associated with thickness. For example, ice thinner than 10 cm (i.e., nilas) was typically not covered by snow as snow grains were dissolved or merged with the salty and warm brine skim layer on the surface. Surface conditions on thicker ice types were, on the other hand, cold and dry enough to support a snow cover. Any increase in ice thickness was found to have little effect on the reflectance once a 20-30 mm thick snow layer was present. In general, reflectance from the surface increased exponentially with an ice thickness increase, however, variability within ice thickness types were very large.

It is evident that a more complete treatment of brine movement towards the surface of the ice cover and the formation of surface features is required in order to understand the surface reflectance or albedo of newly formed sea ice. Such a treatment was beyond the scope of the present study, however, a main goal in Chapter 3 was to provide a detailed characterization of the physical and structural properties to facilitate future research into coupling brine dynamics to surface features and through that to electromagnetic (optical and microwave) properties of sea ice.

Large variability was also observed in all physical properties of the new sea ice. This is illustrated by crystallographic analysis on 33 ice cores that revealed highly variable growth conditions and formation mechanisms (Figure 3.4). The mean fraction of granular ice was 33%, while intermediate granular-columnar and columnar ice contributed 37% and 30%, respectively. Salinity profiles in the ice were C-shaped (Figure 3.8) and as the ice grew thicker, bulk salinities decreased according to $4.582 + 13.358/h_i$ (cm) (Figure 3.9b). These conditions resulted in brine volumes ranging from 4% to 46%. Salinities up to 40‰ were observed in brine skim layer present on bare ice surfaces. After suitable conditions frost flowers had formed on the ice surface and their presence was related to characteristic ice microstructure with crystals that appeared disc-like in shape (see 15 mm level in Figure 3.5). This structure may be related to freezing of the brine skim layer on the surface. On the other hand, fine-grained snow-ice was formed when snow merged with surface brine to create a complex hyper-saline surface at the snow/ice interface.

The experiments described in the other three Chapters 4-6 are situated within the spring season. I begin the summary with Chapter 5 as it deals with the surface conditions during the spring. I then turn to Chapters 4 and 6 with a focus on the warm sea ice bottom layers.

Chapter 5 reports on spectral albedo measurements that were conducted at six adjacent sites in Button Bay, 2005, encompassing two major surface types (i.e., blue and white ice) throughout the month of April. Furthermore, the total shortwave albedo and the other components of the surface energy balance were continuously recorded at a nearby micrometeorological site. Subsequent to the melt onset in Button Bay (~30 March), melt processes quickly transformed the ice surface topography from a relatively homogenous snow cover into elevated areas (white ice) and depressed areas (blue ice). The spectral albedo integrated over 350-1050 nm varied between 0.52-0.95 at the blue ice sites, while it varied between 0.73-0.91 at white ice sites. Similarly, total shortwave albedo estimates following *Allison et al.* (1993) ranged 0.45-0.85 and 0.65-0.84 for blue and white ice, respectively (Figure 5.8a). Interestingly, blue ice showed a larger range in albedo than white ice. Although generally lower, the blue ice albedo was temporarily enhanced after snow events because new snow tended to collect within blue ice depressions even while no new snow accumulation was seen on the white ice mounds. At the meteorological station, variability on the order of ±10 percent in the white ice total shortwave albedo resulted from the diurnal freeze-thaw cycle, but also from synoptic weather events. In general, rapid temporal changes in the albedo were found to relate to typical sub-Arctic climate conditions, i.e., frequent incursions of southerly air, resulting snow and rain events and the generally high maximum solar insolation levels. The transmittance through the sea ice was found to be largely controlled by surface properties as well (Figure 5.7).

Transmittances during April ranged 0.5-2% for white ice and 0.5-5% for blue ice of the incident total shortwave irradiance (Figure 5.8b).

Within the bottom sea ice layers, 'warm sea ice' conditions with temperature above -3°C (Figures 4.5 and 6.2) prevailed both in Franklin Bay and Button Bay. This is typical, and the physical and structural properties that are presented in Chapters 4 and 6 can be considered representative of seasonal sea ice close to the ice/water interface in general. In both experiments, *in situ* measurements with a high vertical resolution were conducted within the bottom layers—however using different methods (see Figures 4.2 and 6.1)—in an effort to obtain sea ice AOPs and IOPs for bio-optical modeling purposes.

The measured radiation profiles were found to be strongly affected both by changes in the radiation field near the ice/water interface and by the presence of ice algae at this interface. The use of a radiative transfer model, i.e., DISORT (*Stamnes et al.*, 1988), was required in order to account for the non-asymptotic radiation field near the sea ice boundaries. Then an iterative approach was used to infer IOPs for layers between measurement intervals. Note that ice algae were visible within the bottommost centimeters of the sea ice, as is typical for sea ice in early spring prior to the start of extensive ice melt and flushing (e.g., *Zeebe et al.*, 1996; *Lavoie et al.*, 2005).

Particulate absorption spectra, inferred from measured AOPs within the bottom few centimeters, showed characteristics of a living (and healthy) diatom-dominated ice algae layer (Figures 4.10 and 6.9). The spectra are consistent with what have been inferred from AOPs in other studies (e.g., *Perovich et al.*, 1993; *Hamre et al.*, 2004; *Mundy et al.*, 2007). Biomass concentrations up to about 240 and 130 mg chl *a* m^{-3} were recorded in bottom ice samples taken in Franklin Bay and Button Bay, respectively. This algae layer had a marked effect on the spectral distribution of transmitted irradiance beneath the ice (Figures 4.6 and 6.3). However, particulate absorption decreased quickly within the ice above the living algae layer. Additionally, as the distance from the ice/water interface increased, spectral characteristics of partly deteriorated algae cells (i.e., NAP or detrital matter) became increasingly prevalent. The optical characteristics of the bottom layers above the immediate bottom algae layer has not been published before in the literature.

In general, Chapter 6 showed that AOPs and inferred IOPs for the bottom layers of the sea ice significantly differed from the interior ice. This is expected as the bottom ice is typically very porous and has a lamellar platelet structure resulting in a highly anisotropic structure. In addition, high concentrations of biological matter are commonly contained within the brine-filled interstices. On the other hand, the interior portion of the sea ice that had mainly formed during the dark winter period, at a time of low biological production and river discharge, was found to be essentially free of impurities. Absorption within interior ice layers was found to be well represented by pure ice and seawater spectra (Figure 6.9). Furthermore, scattering inclusions were more distinct, which makes a Mie scattering approximation assuming spherical inclusions applicable in interior ice (e.g., *Grenfell et al.*, 1983).

Scattering within porous and warm sea ice bottom layers has eluded thorough *in situ* investigations. Therefore, the scattering coefficient has generally been used as a tuning parameter in sea ice radiative transfer model studies (e.g., *Grenfell et al.*, 1983; *Jin et al.*, 1994; *Hamre et al.*, 2004). Scattering within the skeletal layer has either been assumed negligible compared to ice algae absorption (e.g., *Perovich et al.*, 1993; *Mundy et al.*, 2007), or it has been assumed to be identical to interior ice scattering (e.g., *Perovich*, 1990). In Chapters 4 and 6, an iterative approach was used to estimate wavelength-independent total scattering coefficients b_{tot} (see values in Table 4.1 and 6.1). In general, it was noted that b_{tot} was highly sensitive to the choice or approximation of g_{tot} (the Henyey-Greenstein asymmetry parameter). The choice of g_{tot} varied between layers in Franklin Bay (see Table 7.1), while it was kept at a constant 0.995 for layers below the waterline in Button Bay. Therefore, b_{tot} values are not directly comparable, however, the similarity parameter with the form $(1-g_{tot})b_{tot}$ (*van de Hulst*, 1980; *Light et al.*, 2004) can be used to transform these values to be representative of g_{tot} = 0.995. Firstly, the transformation results in values that are more consistent with values obtained for Button Bay sea ice (Table 7.1). Secondly, b_{tot} values are vertically highly variable near the bottom boundary. It is unclear whether the variations stem directly from structural properties that determine b_{tot} or to what degree an incomplete characterization of the radiation field in the typically anisotropic bottom ice affect these values. The *in situ* radiation profile measurements presented in Chapters 4 and 6 do not resolve the shape of the radiation field and can therefore not be used to verify the applicability of Mie theory to the warm sea ice bottom layers, but only to tune b_{tot} to match observations.

Table 7.1. Total scattering coefficient, b_{tot}, for Franklin Bay (FB) bottom sea ice transformed to g_{tot} = 0.995 and compared against Button Bay (BB) blue ice and white ice bottom layer values. g_{tot} values are shown in brackets.

Depth (m)	FB (original) b_{tot} (m^{-1})	FB (transformed) b_{tot} (m^{-1})	Depth (m)	BB (blue ice) b_{tot} (m^{-1})	BB (white ice) b_{tot} (m^{-1})
0.10-0.20	165 [0.980]	661 [0.995]	0.10-0.30	405 [0.995]	564 [0.995]
0.05-0.10	431 [0.980]	1724 [0.995]	0-0.10	1258 [0.995]	861 [0.995]
0-0.05	370 [0.997]	222 [0.995]			

7.2 Seasonal sea ice stages

The experiments described in Chapters 3-6 were conducted during various stages of the annual cycle with a particular emphasis on the fall and spring periods. When comparing these experiments it is useful to consider them in context of a conceptual seasonal progression in graphical form (Figure 7.1). This schematic provides a conceptual summary of the seasonal evolution of seasonal sea ice and the typical features that control solar radiation interaction with the sea ice system. Transitions from one sea ice stage to another are indicated by the vertical dashed lines denoted by letters 'A' to 'E' (Figure 7.1).

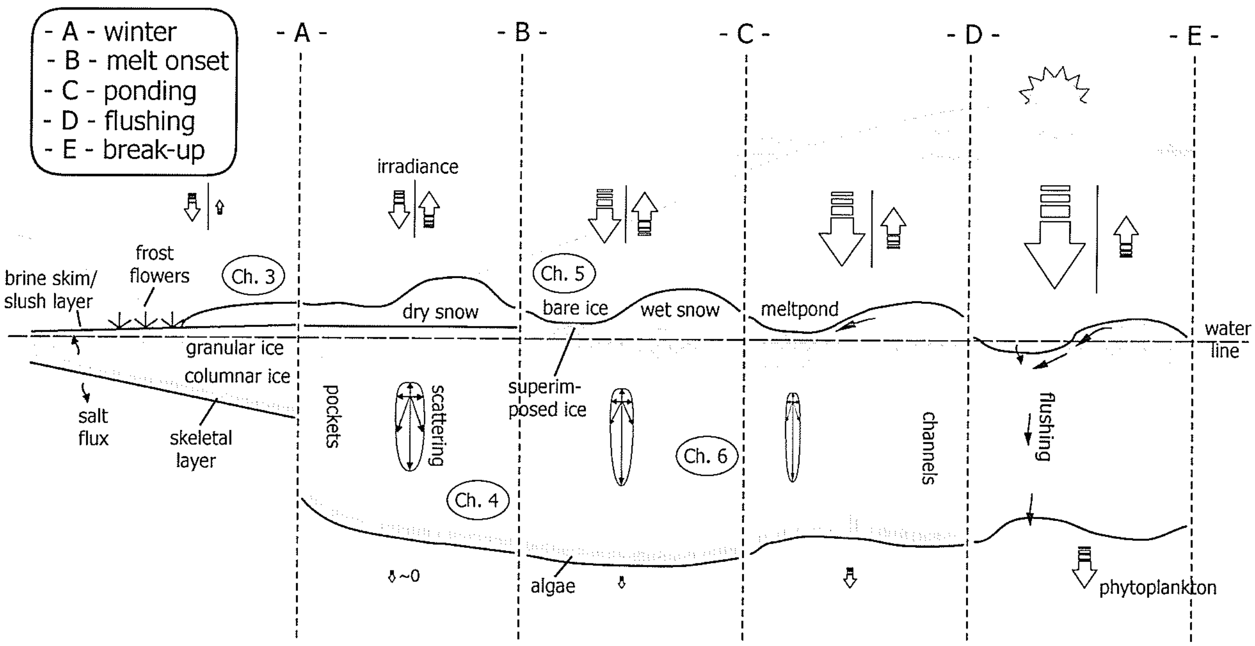

Figure 7.1. Schematic overview of the fall freeze-up (up to 'A') and the spring melt periods ('A' to 'E'). Large arrows indicate irradiances which are readily measured and used to calculate AOPs. The absorption coefficient (IOP) in the sea ice cover is related to liquid water content and impurities, and thus typically increases as the melt season progresses. Hence, absorption is represented by the gray tone in the figure. Scattering is more complicated as it depends on the surface area of the scatteres (e.g., snow grains, air bubbles, brine pockets.). As brine volumes increase within sea ice, the scattering coefficient (IOP) will tend to increase; however, the merger of brine inclusions has the opposite effect and will tend to decrease scattering.

I presented a study on newly formed ice types during the fall freeze-up period (Chapter 3). The fall period in the Arctic is characterized by diminishing radiation levels and low solar angles. It is also characterized by high spatial and temporal variability in all sea ice physical properties and morphology; e.g., ridged, rafted and thermodynamically grown sea ice at various stages could be observed within relatively small areas (Figure 3.2). By the end of the fall experiment, it was dark and cold, and the sea ice was covered with an optically thick snow layer. As such, sea ice conditions were typical for the winter season. The winter season—although lasting from about November to April—is simply marked by 'A' in Figure 7.1 as it is optically relatively unimportant due to low solar insolation levels and the cold and dry snow cover that will backscatter most radiation back to the atmosphere.

The experiments described in the other three chapters are situated within the spring season (Figure 7.1). The early spring ('A' to 'B') is marked by the return of solar insolation. Surface conditions remain essentially unchanged until the high pressure dominated sky conditions give way to intruding low pressure systems (represented by clouds in Figure 7.1). Thus at this stage, surface energy balance becomes positive (increases in both incident shortwave and longwave radiation), which gradually lead towards increased snow and ice temperatures. Chapter 4 presented *in situ* irradiance measurements within the bottom layers of landfast sea ice in Franklin Bay (see Figure 4.1) during early spring. More specifically, the Franklin Bay study occurred between 22 April and 9 May 2004 during the last phase of the over-wintering portion of the CASES 2004 experiment. The sea ice thickness had reached its maximum of about 1.8 m and primary production had been initiated within the bottommost 2-3 cm skeletal layer (as evidenced by its coloring). During the experiment, ice surface temperatures increased from about -12°C to -6.4°C. This increase, however, was not enough to cause surface melting and consequently the snow cover, and the upper portion of the sea ice, remained cold and dry (Figure 4.5) and the surface albedo remained high.

However, at some point an intrusion of sufficiently warm southerly air can bring liquid precipitation. Such a rain event was observed both during the CASES 2004 (around 24 May; see *Hwang et al.*, 2007b) and the Button Bay 2005 experiment (Chapters 5 and 6) and caused surface melting and a consequent non-reversible decrease in surface albedo. Thus, it coincides with the melt onset 'B' in Figure 7.1. The first rain event in Button Bay occurred on 30 March (YD 89)—almost two months prior to the melt onset in Franklin Bay the year before. This illustrates the difference in climate between the two regions (Arctic vs. sub-Arctic). Consequently, by April, when the program for spectral radiation measurements was initiated, the ice surface was in an advanced stage of melt and had partitioned into multiple surface types ranging from highly reflective white ice to absorptive blue ice. The white ice snow cover was transformed throughout into melt/freeze metamorphosed snow and superimposed ice (Figure 5.3). Note, however, that the maximum ice thickness in April of 1.5-1.7 m was comparable to the thickness in Franklin Bay suggesting that wintertime growth conditions were similar in Button Bay to its Arctic counterpart up until stage 'A' in Figure 7.1. Therefore, the Button Bay 2005 experiment was situated within the period from 'B' to 'C' in Figure 7.1. This period was characterized by diurnally varying insolation levels that together with reduced reflection from the surface caused daytime melting and nighttime refreezing of the snow pack and upper surface layers.

7.3 Future directions and recommendations

As mentioned above, predicted trends in the climate (*ACIA*, 2005; *IPCC*, 2007) suggest the diminishing of perennial ice, and that seasonal sea ice will in the near future become the dominant ice type in the Arctic. Consequently, surface features, such as frost flowers, which are related to brine expulsion in new forming ice, will become more important for the overall energy balance during fall and in winter/early-spring leads. In summertime sea ice, improvements in the understanding of melt water percolation and pathways are needed to correctly predict melt rates and the sea ice mass balance, as well as the evolution of sea ice AOPs. For example, we need to consider the presence of the highly scattering surface layer, even in the absence of a snow cover, and the drainage of melt ponds ('D' to 'E'; Figure 7.1) that together contribute to an albedo increase of such magnitude that it is the difference between existence and non-existence of the Arctic sea ice cover (*Curry et al.*, 1995; *Eicken*, 2003). While the surface white ice may regenerate and reflect significant portions of shortwave radiation back to the atmosphere, the general decrease in ice thickness and the presence of open water areas will contribute to increased absorption within the bottom ice and the surface layers of the ocean. Consequently, lateral and bottom melting are likely to become even more important processes in understanding the sea ice mass balance. Additionally, the transition towards seasonal sea ice has impacts on the marine food web, starting from ice algae, which may receive higher light levels but may not be able to remain in the ice and thereby loose their stable growth platform (*Zeebe et al.*, 1996; *Lavoie et al.*, 2005). Polynya environments (with their thinner ice cover) or the sub-Arctic Seas (already seasonal ice cover) may serve as good proxies for the future Arctic sea ice environment. This is a main reason why my thesis has focused on these two types of environments.

Thus, an improved representation of melting/freezing and related brine/meltwater dynamics of sea ice is underlined. Primarily, a better understanding of the timing for transitions between the stages 'B' to 'E' depicted in Figure 7.1 is needed and of the preconditioning required (weather patterns, forcing, snow distribution on the surface, snow melting and superimposed ice formation, internal melting of sea ice and permeability, etc.) for melt pond formation, evolution and their eventual drainage. These processes essentially control the regional-scale albedo of the sea ice environment and thus the energy balance. An improved understanding requires long-term, intensive field investigations, similar to, e.g., CASES 2004, that focus on obtaining time series at preferably one location. Unfortunately, neither during the CASES 2004 fast ice experiment nor in Button Bay 2005 was it possible—for various reasons—to extend the duration of the ice camp over to melt pond formation and beyond (i.e., the summer melt season, 'C' onwards in Figure 7.1). During the mobile (ship-based) portion of CASES 2004 we, however, obtained an extensive data set on deteriorating summertime sea ice including melt ponds, but it has not been published to date. A number of studies have, furthermore, observed AOPs for ponded summertime sea ice in the Arctic (e.g., *Grenfell and Maykut*, 1977; *Morassutti and LeDrew*, 1995; *Perovich et al.*, 1998; *Hanesiak et al.*, 2001). Only recently have a few studies focused on melt water path ways through sea ice (e.g., *Eicken et al.*, 2004; *Vancoppenolle et al.*, 2007, and references therein), however, these studies are only the first steps towards an improved representation and need support from field observations.

Improvements in the methods used to obtain information on the physical, structural and biological properties of sea ice and the snow cover are needed. Existing standard methodology are problematic especially when attempting to characterize warm sea ice. For example, while extracting ice cores, core holes are first flooded with seawater, which may infiltrate the ice cores, and then brine is drained from the ice cores when lifted above the water line. This makes it difficult to asses what the salinity or density in the undisturbed ice cover was. The stress associated with melting ice samples may, furthermore, cause algae cells to undergo lysis and light absorbing pigments to degrade (e.g., *Garrison and Buck*, 1986; *Stramski et al.*, 1990). Standard crystallographic techniques of preparing thin sections for structure analysis necessitate the ice sample to be cooled from an *in situ* temperature of above -5°C to a temperature below at least -15°C (*Perovich and Gow*, 1996; *Eicken et al.*, 2000; *Light et al.*, 2003) thereby significantly affecting brine inclusion size, shape and numbers in non-reversible and unpredictable ways. Freeze-thaw processes result in a snow cover structure that is too complex for direct application of Mie scattering theory to explain observed AOPs.

The work presented in my thesis, although relying on these standard methods, consistently point out these methodological deficiencies and uncertainties in estimates of sea ice and snow physical properties. It appears necessary to develop non- or less invasive techniques to determine optically important physical state parameters of sea ice. For warm sea ice, arguably the most critical parameters to characterize are the brine volume and inclusion structure and bottom ice algae. Techniques using nuclear magnetic resonance imaging (*Eicken et al.*, 2000) or ground penetrating radars (GPR) are promising for characterization of snow and sea ice structure but still require continued development to be applicable for more than thickness measurements. The spectral dependence of irradiance transmitted through the snow and sea ice cover can be used to deduce information on bottom algal biomass and spectral absorption (e.g., *Perovich et al.*, 1993; Mundy et al., 2007). Promisingly, *Mundy et al.* (2007) showed, in an extensive time series examination of transmitted irradiance, that a carefully chosen single irradiance ratio accounted for up to 89% of the total variation in algal biomass within a landfast sea ice cover.

Furthermore, I showed that absorption spectra at wavelengths over about 700 nm can potentially be used to indirectly and non-invasively determine the brine volume within sea ice (Chapters 4 and 6). However, a more thorough understanding of these structural-optical relationships is ultimately hampered by the lack of understanding of the radiation field in the sea ice. Thus, innovative ways of measuring the angular distribution of radiation, especially near the upper and lower boundaries, in sea ice are called for. The currently ongoing Circumpolar Flaw Lead (CFL) system study, as a part of the International Polar Year (IPY), will provide an excellent opportunity to address the above mentioned issues.

To fully understand field observations, they need to be corroborated with radiative transfer modeling. Due to the anisotropic nature of warm sea ice (vertically oriented crystals and brine inclusions), a geometrical optics approach, utilized using a Monte Carlo-type model, may be necessary in order to address process such as internal reflection and refraction in addition to scattering. Such a model is presently being developed by the author. A similar approach may furthermore be desirable for the treatment of a complex deteriorated snow cover (see, e.g., *Zhou et al.*, 2003b; *Kaempfer et al.*, 2007).

However, the ultimate goal should not be to obtain a perfect understanding of radiative transfer in a limited one-dimensional environment, but to gain a thorough insight into climatologically and biologically meaningful processes in the sea ice environment. Detailed modeling should preferably be used to develop and test structural-optical relationships that relate to the seasonal progression (such as depicted in Figure 7.1) and to general processes such as sea ice formation and growth and brine dynamics (desalination, porosity-permeability). These may then be applied in integrated multi-field sea ice model studies that combine optical, physical, structural and biological processes. Broad multi-field studies are essential in the sea ice environment because all the above processes are highly interrelated and coupled; a fact that optical studies quickly reveal. Such models do not yet exist, and the challenge ahead lies in their development. The key to success in such an endeavor is an improved treatment of brine and melt water related processes in sea ice and snow. Brine appears to be the constituent in sea ice that combines nearly all fields of study and makes sea ice special from other materials. Recent advances in halo-thermodynamic sea ice modeling (*Vancoppenolle et al.*, 2007) show promise in predicting sea ice desalination during the melt season. The study by *Vancoppenolle et al.* (2007) pointed out the importance of an impermeable layer of superimposed ice in hindering melt water from penetrating interior parts of the ice cover thus maintaining surface melt ponds ('C' to 'D'; Figure 7.1) and the role of shortwave radiation absorption in eventually triggering flushing and the drainage of melt ponds ('D' to 'E'). Carrying out investigations with a focus on improving upon our understanding of these transitions, as illustrated in Figure 7.1, is my main objective in upcoming research activities as a part of the IPY-funded CFL project.

CHAPTER 8: References

Aagaard, K. and E. C. Carmack (1989), The role of sea ice and other fresh water in the arctic circulation, *J. Geophys. Res.*, 94, 14485-14498.

ACIA (2005), Arctic Climate Impact Assessment, Cambridge University Press, NY, 1042 p.

Allison, I., R. E. Brandt, and S. G. Warren (1993), East Antarctic sea ice: Albedo, thickness distribution and snow cover, *J. Geophys. Res.*, 98, 12417-12429.

Anderson, L. G., E. Falck, E. P. Jones, S. Jutterström, and J. H. Swift (2004), Enhanced uptake of atmospheric CO_2 during freezing of seawater: A field study in Storfjorden, Svalbard, *J. Geophys. Res.*, 109, C06004, doi:10.1029/2003JC002120.

Apel, J. R. (1987), *Principles of Ocean Physics*, International Geophysics Series, Vol. 38, Academic Press, London, U.K., pp. 634.

Arrigo, K. R. (2003), Primary production in sea ice, in *Sea ice: An Introduction to its Physics, Chemistry, Biology and Geology, D.N. Thomas and G.S. Dieckmann* (Eds), Blackwell Science Ltd., Oxford, UK., 143-183.

Arrigo, K. R., and G. L. van Dijken (2004), Annual cycles of sea ice and phytoplankton in Cape Bathurst Polynya, southeastern Beaufort Sea, Canadian Arctic, *Geophys. Res. Lett.*, 31, L08304, doi:10.1029/2003GL018978.

Assur, A. (1958), Composition of sea ice and its tensile strength, Arctic Sea Ice, U.S. National Academy of Sciences-National Research Counsil, Pub. 598, 106-138.

Barber, D. G. and A. Thomas (1999), The Influence of Cloud on the Radiation Balance, Physical Properties and Microwave Scattering of First Year and Multi-Year Sea Ice, *IEEE Trans. on Geosci. Remote Sensing*, 36(1), 38-50.

Barber, D. G., and J. J. Yackel (1999), The physical, radiative and microwave scattering characteristics or melt ponds or Arctic landfast sea ice, *Int. J. Remote. Sens.*, 20, 2069-2090.

Barber, D.G., J. Yackel, and J. Hanesiak (2000), Sea ice, RadarSat-1, and Arctic climate processes: A review and update, *Canadian Journal of Remote Sensing*, 27(1), 51-61.

Barber, D.G., and J. Hanesiak (2004), Meteorological forcing of sea ice concentrations in the Southern Beaufort Sea over the period 1978 to 2001, *J. Geophys. Res.*, 109, C06014, doi:10.1029/2003JC002027.

Barber, D.G., and R.A. Massom (2006), The role of sea ice in bipolar polynya processes. In. W.O. Smith and D. G. Barber (Eds.) Polynyas: Windows into Polar Oceans, Elsevier Series in Oceanography, in press.

Barry, R.G. (1996), The parameterization of surface albedo for sea ice and its snow cover, *Prog. in Phys. Geogr.*, 20(1), 63-79.

Belchansky, G. I., D. C. Douglas and N. G. Platonov (2004), Duration of the Arctic sea ice melt season: Regional and interannual variability, 1979-2001, *J. Climate.*, 17, 67-80.

Belzile, C., S. C. Johannessen, M. Gosselin, S. Demers, and W. L. Miller (2000), Ultraviolet attenuation by dissolved and particulate constituent of first-year ice during late spring in an Arctic polynya, *Limnol. Oceanogr.*, 45, 1265– 1273.

Bitz, C. M., and W. H. Lipscomb (1999), An energy-conserving thermodynamic model of sea ice, *J. Geophys. Res.*, 104, 15669-16677.

Bond, T. C., and R. W. Bergstrom (2006), Light absorption by carbonaceous particles: An investigative review, *Aerosol Sci. Technol.*, 40, 27-67, doi:10.1080/02786820500421521.

Brandt, R. E., S. G. Warren, A. P. Worby, and T. C. Grenfell (2005), Surface albedo ot the Antarctic sea ice zone, *J. Clim.*, 18, 3606-3622.

Bricaud, A., and D. Stramski (1990), Spectral absorption coefficients of living phytoplankton and nonalgal biogenous matter: A comparison between the Peru upwelling are and the Sargasso Sea, *Limnol. Oceanogr.*, 35, 562-582.

Bricaud, A., M. Babin, A. Morel and H. Claustre (1995), Variability in the chlorophyll-specific absorption coefficients of natural phytoplankton: Analysis and parameterization, *J. Geophys. Res.*, 100 (C7), 13321–13332.

Buckley, R. G., and H. J. Trodahl (1987), Scattering and absorption of visible light by sea ice, *Nature*, 326, 867-869.

Carmack, E., R. W. Macdonald, J. E. Papadakis (1989), Water mass structure and boundaries in the Mackenzie shelf estuary, *J. Geophys. Res.*, 94 (C12), 18043-18055.

Colbeck, S. C. (1982), An overview of seasonal snow metamorphism, *Rev. Geophys. Space Phys.*, 20, 45-61.

Cole, D. M., and L. H. Shapiro (1998), Observations of brine drainage networks and microstructure of first-year sea ice, *J. Geophys. Res.* 103(C10), 21739-21750.

Comiso, J. C., D. J. Cavalieri, and T. Markus (2003), Sea ice concentration, ice temperature, and snow depth using AMSR-E data, *IEEE Trans. Geosci. Remote Sens.*, 41(2), 243-252.

Comiso, J. C. (2003), Large-scale characteristics and variability of the global sea ice cover, in *Sea Ice: An Introduction to its Physics, Chemistry, Biology and Geology, D.N. Thomas and G.S. Dieckmann* (Eds), Blackwell Science Ltd., Oxford, UK., 112-142.

Comiso, J. C., C. L. Parkinson, R. Gersten, and L. V. Stock (2008), Accelerated decline in the Arctic sea ice cover, *Geophys. Res. Lett.*, 35, L01703, doi:10.1029/2007GL031972.

Cox, G. F. N., and W. F. Weeks (1974), Salinity variations in sea ice, *J. Glaciol.*, 13(67), 109-120.

Cox, G. F. N., and W. F. Weeks (1983), Equations for determining the gas and brine volumes in sea ice samples, *J. Glaciol.*, 29, 306-316.

Cox, G. F. N., and W. F. Weeks (1988), Numerical simulations of the profile properties of undeformed first-year ice during the growth season, *J. Geophys. Res.*, 93 (C10), 12449-12460.

Crocker, G. B. (1984), A physical model for predicting the thermal conductivity of brine-wetted snow, *Cold Reg. Sci. Technol.*, 10, 69-74.

Curry, J. A., J. L. Schramm, and E. E. Ebert (1995), Sea ice-albedo climate feedback mechanism, *J. Clim.*, 8, 240-247.

Curry, J. A., J. L. Schramm, A. Alam, R. Reeder, T. E. Arbetter, and P. Guest (2002), Evaluation of data sets used to force sea ice models in the Arctic Ocean, J. Geophys. Res., 107(C10), 8027, doi:10.1029/2000JC000466.

De Abreu, R. A., J. Key, J. A. Maslanik, M. C. Serreze, and E. F. LeDrew (1994), Comparison of *in situ* and AVHRR-Derived broadband albedo over Arctic sea ice, *Arctic*, 47(3), 288-297.

Dera, J. (1992), *Marine Physics*, Elsevier Science Publishers, Amsterdam, The Nederlands.

Drobot, S. D., and J. A. Maslanik (2003), Interannual variability in summer Beaufort sea ice conditions: Relationship to spring and summer surface and atmospheric variability, *J. Geophys. Res.*, 108(C7), 3233, doi:10.1029/2002JC001537.

Ebert, E. E., and J. A. Curry (1993), An intermediate one-dimensional thermodynamic sea ice model for investigating ice-atmosphere interactions, *J. Geophys. Res.*, 98 (C6), 10085-10109.

Ehn, J. K., M. A. Granskog, T. Papakyriakou, R. Galley and D. G. Barber (2006), Surface albedo observations of Hudson Bay landfast sea ice during the spring melt, *Ann. Glaciol.*, 44, 23-29.

Ehn, J. K., B. J. Hwang, R. Galley, D. G. Barber (2007), Investigations of newly formed sea ice in the Cape Bathurst polynya: 1. Structural, physical, and optical properties, *J. Geophys. Res.*, 112, C05002, doi:10.1029/2006JC003702.

Ehn, J. K., C. J. Mundy, and D. G. Barber (2008), Bio-optical and structural properties inferred from irradiance measurements within the bottommost layers in an Arctic landfast sea ice cover, *J. Geophys. Res.*, 113, C03S03, doi:10.1029/2007JC004194.

Eide, L. I., and S. Martin (1975), The formation of brine drainage features in young sea ice, *J. Glaciol.,* 14 (70), 137-154.

Eicken, H., and M. A. Lange (1989), Development and properties of sea ice in the coastal regime of the southeastern Weddell Sea, *J. Geophys. Res.*, 94(C6), 8193-8206.

Eicken H., M. A. Lange, H.-W. Hubberten and P. Wadhams (1994), Characteristics and distribution patterns of snow and meteoric in the Weddell Sea and their contribution to the mass balance of sea ice, *Ann. Geophys.*, 12, 80-93.

Eiken, H., C. Bock, R. Wittig, H. Miller and H.-O. Poertner (2000), Nuclear magnetic resonance imaging of sea ice pore fluids: methods and thermal evolution of pore microstructure, *C. Reg. Sci. Tech.*, 31, 207-225.

Eiken, H. (2003), From the microscopic, to the macroscopic, to the regional scale: growth, microstructure and properties of sea ice, in *Sea Ice: An Introduction to its Physics, Chemistry, Biology and Geology, D.N. Thomas and G.S. Dieckmann* (Eds), Blackwell Science Ltd., Oxford, UK., 22-81.

Eicken, H., T. C. Grenfell, D. K. Perovich, J. A. Richter-Menge, and K. Frey (2004), Hydraulic controls of summer Arctic pack ice albedo, *J. Geophys. Res.*, 109, C08007, doi:10.1029/2003JC001989.

Fett, R. W., S. D. Burk, W. T. Thompson, and T. L. Kozo (1994), Environmental phenomena of the Beaufort Sea observed during the LEADS experiment, *Bull. Am. Meteorol. Soc.*, 75, 2131-2145.

Flanner, M. G., C. S. Zender, J. T. Randerson, and P. J. Rasch (2007), Present day climate forcing and response from black carbon in snow, *J. Geophys. Res.*, 112, D11202, doi:10.1029/2006JD008003.

Flato, G. and R. D. Brown (1996), Sensitivity of landfast Arctic sea ice to changes in snow cover and climate as determined by a one-dimensional thermodynamic model, *J Geophys. Res.*, 101, 25767-25777.

Fofonoff, P., and R. C. Millard Jr. (1983), Algorithms for computation of fundamental properties of seawater, *UNESCO Tech. Pap. Mar. Sci.*, 44, 53 p.

Fröhlich, C. and J. Lean (1998), Total solar irradiance variations: The construction of a composite and its comparison with models, in F. L. Deubner (ed.), IAU Symposium 185: New Eyes to See Inside the Sun and Stars, Kluwer Academic Publ., Dortrecht, The Netherlands, 89-102.

Garison, D. L. and K. R. Buck (1986), Organism losses during ice melting: A serious bias in sea ice community studies, *Polar Biol.*, 6, 237-239.

Golden, K. M., S. F. Ackley, and V. I. Lytle (1998), The percolation phase transition of sea ice, *Science*, 282, 2238-2241.

Gough, W. A., A. R. Cornwell and L. J. S. Tsuji (2004), Trends in seasonal sea ice duration in southwestern Hudson Bay, *Arctic*, 57(3), 299-305.

Grenfell, T. C. (1983), A theoretical model of the optical properties of sea ice in the visible and near infrared, *J. Geophys. Res.*, 88 (C14), 9723-9735

Grenfell, T. C., and G. A. Maykut (1977), The optical properties of ice and snow in the Arctic basin, *J. Glaciol.*, 18, 445-463.

Grenfell, T. C., and D. K. Perovich (1981), Radiation absorption coefficients of polycrystalline ice from 400 – 1400 nm, *J. Geophys. Res.*, 86, 7447-7450.

Grenfell, T. C. and D. K. Perovich (1984), Spectral albedos of sea ice and incident solar irradiance in the southern Beaufort Sea, *J. Geophys. Res.*, 89(C3), 3573-3580.

Grenfell, T. C., D. G. Barber, A. K. Fung, A. J. Gow, K. C. Jezek, E. J. Knapp, S. V. Nghiem, R. G. Onstott, D. K. Perovich, C. S. Roesler, C. T. Swift, and F. Tanis (1998), Evolution of electromagnetic-signatures of sea ice from initial formation through the establishment of thick first-year ice, *IEEE Trans. Geosci. Remote Sens.*, 36 (5), 1642–1654.

Grenfell, T. C., and S. G. Warren (1999), Representation of a nonspherical ice particle by a collection of independent spheres for scattering and absorption or radiation, *J. Geophys. Res.*, 104(D24), 31697-31709.

Grenfell, T. C., B. Light, and M. Sturm (2002), Spatial distribution and radiative effects of soot in the snow and sea ice during the SHEBA experiment, J. Geophys. Res., 107, 8032, doi:10.1029/2000JC000414.

Grenfell, T. C., B. Light, and D. K. Perovich (2006), Spectral transmission and implications for the partitioning of shortwave radiation in arctic sea ice, *Ann. Glaciol.*, 44, 1-6.

Guéguen, C., L. Guo, N. Tanaka (2005), Distributions and characteristics of colored dissolved organic matter in the western Arctic Ocean, *Cont. Shelf. Res.*, 25, 1195-1207.

Hall, A. (2004), The role of surface albedo feedback in climate, *J. Climate*, 17 (7), 1550-1568.

Hamre, B., J.-G. Winther, S. Gerland, J. J. Stamnes, and K. Stamnes (2004), Modeled and measured optical transmittance of snow-covered first-year sea ice in Kongsfjorden, Svalbard, *J. Geophys. Res.*, 109, C10006, doi:10.1029/2003JC001926.

Hanesiak, J. M, D. G., Barber, R. De Abreu, and J. J. Yackel (2001), Local and regional albedo: Observations of Arctic first-year sea ice during melt ponding, *J. Geophys. Res.*, 106, 1005-1016.

Haines, E. M., R. G. Buckley, and H. J. Trodahl (1997), Determination of the depth dependent scattering coefficient in sea ice, *J. Geophys. Res.*, 102(C1), 1141-1151.

Henyey, L. G., and J. L. Greenstein (1941), Diffuse radiation in the galaxy, *Astrophys. J.*, 23, 70-83.

Holland, M. M., C. M. Bitz, and Bruno Tremblay (2006), Future abrupt reductions in the summer Arctic sea ice, *Geophys. Res. Lett.*, 33, L23503, doi:10.1029/2006GL028024.

Horner, R., S. F. Ackley, G. S. Dieckmann, B. Gulliksen, T. Hoshiai, L. Legendre, I. A. Melnikov, W. S. Reesburgh, M. Spindler, and C. W. Sullivan (1992), Ecology of sea ice biota 1. Habitat, terminology, and methodology, *Polar Biol.*, 12, 417-427.

Hwang, B. J., J. K. Ehn, D. G. Barber, Relationships between albedo and microwave emissions over thin newly formed sea ice during fall freeze-up, *Geophys. Res. Lett.*, 33, L17503, doi:10.1029/2006GL027300, 2006.

Hwang, B. J., J. K. Ehn, D. G. Barber, R. Galley and T. C. Grenfell (2007), Investigations of newly formed sea ice in the Cape Bathurst polynya: 2. Microwave emission, *J. Geophys. Res.*, 112, C05003, doi:10.1029/2006JC003703.

Hwang, B. J., A. Langlois, D. G. Barber and T. N. Papakyriakou (2007b), On detection of the thermophysical state of landfast first-year sea ice using *in-situ* microwave emission during spring melt, *Rem. Sens. Environ.*, 111, 148-159, doi:10.1016/j.rse.2007.02.033.

Hwang, B. J., J. K. Ehn, and D. G. Barber (2008), Impact of ice temperature on microwave emissivity of thin newly formed sea ice, *J. Geophys. Res.*, 113, C02021, doi:10.1029/2006JC003930.

IPCC (2007), Climate Change 2007: The Physical Science Basis. Contribution of Working Group I to the Fourth Assessment Report of the Intergovernmental Panel on Climate Change [Solomon, S., D. Qin, M. Manning, Z. Chen, M. Marquis, K.B. Averyt, M. Tignor and H.L. Miller (eds.)], Cambridge University Press, Cambridge, United Kingdom and New York, NY, USA, 996 pp.

Jiang, S., K. Stamnes, W. Li, and B. Hamre (2005), Enhanced solar irradiance across the atmosphere-sea ice interface: a quantitative numerical study, *Appl. Opt.*, 44, 2613-2625.

Jin, Z., K. Stamnes, W. F. Weeks, and S.-C. Tsay (1994), The effect of sea ice on the solar energy budget in the atmosphere-sea ice ocean system: A model study, *J. Geophys. Res.*, 99, 25281-25294.

Johannessen, O. M., L. Bengtsson, M. W. Miles, S. I. Kuzima, V. A. Semenov, G. V. Alekseev, A. P. Nagurnyi, V. F. Zakharov, L. P. Bobylev, L. H. Pettersson, K. Hasselmann and H. P. Cattle (2004), Arctic climate change: observed and modelled temperature and sea-ice variability, *Tellus*, 56A, 328-341.

Junge, K., H. Eicken, J.W. Deming (2004), Bacterial activity at -2 to -20°C in Arctic wintertime sea ice, *Appl. Environ. Microbiol.*, 70, 550-557, doi:10.1128/AEM.70.1.550–557.2004.

Kawamura, T., K. I. Ohshima, T. Takizawa, and S. Ushio (1997), Physical, structural, and isotopic characteristics and growth processes of fast sea icein Lützow-Holm Bay, Antarctica, *J. Geophys. Res.*, 102, 3345-3355.

Kawamura, T., K. Shirasawa, N. Ishikawa, A. Lindfors, K. Rasmus, M. A. Granskog, J. Ehn, M. Leppäranta, T. Martma, and R. Vaikmäe (2001), Time series observations of the structure and properties of brackish ice in the Gulf of Finland, the Baltic Sea, *Ann. Glaciol.*, 33, 1–4.

Kawamura, T., K. Shirasawa, K. Kobinata (2001), Physical properties and isotopic characteristics of landfast sea ice around the North Water (NOW) polynya region, Atmosphere-Ocean, 39(3), 173-182.

Kaempfer, T. U., M. A. Hopkins, and D. K. Perovich (2007), A three-dimensional microstructure-based photon-tracking model of radiative transfer in snow, *J. Geophys. Res.*, 112, D24113, doi:10.1029/2006JD008239.

Kirk, J. T. O. (1994), Light and Photosynthesis in Aquatic Ecosystems, Cambridge University Press, Cambridge, UK., 525 p.

Kovacs, A. (1996) Sea Ice Part I. Bulk Salinity Versus Ice Floe Thickness, *CRREL Report 96-7*, Cold Regions Research and Engineering Lab., Hanover, NH..

Krembs, C., H. Eicken, K. Junge, J. W. Deming (2002), High concentrations of exopolymeric substances in Arctic winter sea ice: Implications for the polar ocean carbon cycle and cryoprotection of diatoms, *Deep Sea Res.*, 49, 2163-2181.

Lake, R. A., and E. L. Lewis (1970), Salt rejection by sea ice during growth, *J. Geophys. Res.*, 75(3), 583-597.

Langlois, A., C. J. Mundy and D. G. Barber (2006), On the winter evolution of snow thermophysical properties over land-fast first-year sea ice, *Hydrol. Process.*, doi:10.1002/hyp.6407.

Lavoie, D., K. Denman and C. Michel (2005), Modeling ice algal growth and decline in a seasonally ice-covered region of the Arctic (Resolute Passage, Canadian Archipelago), *J. Geophys.Res.*, 110, C11009, doi:10.1029/2005JC002922.

Leppäranta, M. and T. Manninen (1988), The brine and gas content of sea ice with attention to low salinities and high temperatures, *Finnish Inst. Marine Res.*, Internal Rep. 88-2, Helsinki.

Leppäranta, M. (1993), A review of analytical models of sea-ice growth, *Atmosphere-Ocean*, 31, 123-138.

Light, B., H. Eicken, G. A. Maykut, and T. C. Grenfell (1998), The effect of included particles on the spectral albedo of sea ice, *J. Geophys. Res.*, 103, 27739-27752.

Light, B., G. A. Maykut, and T. C. Grenfell (2003), Effects of temperature on the microstructure of first-year Arctic sea ice, *J. Geophys. Res.*, 108(C2), 3051, doi:10.1029/2001JC000887.

Light, B., G. A. Maykut, and T. C. Grenfell (2004), A temperature-dependent, structural-optical model of first-year sea ice, *J. Geophys. Res.*, 109, C06013, doi:10.1029/2003JC002164.

Light B., T. C. Grenfell, D. K. Perovich (2008), Transmission and absorption of solar radiation by Arctic sea ice during the melt season, *J. Geophys. Res.*, 113, C03023, doi:10.1029/2006JC003977.

Lizotte, M. P. (2003), The microbiology of sea ice, in *Sea Ice: An Introduction to its Physics Chemistry, Biology and Geology,* D.N. Thomas and G.S. Dieckmann (Eds), Blackwell Science Ltd., Oxford, UK., 22-81.

Lofgren, G. and W. F. Weeks (1969), Effect of growth parameters on substructure spacing in NaCl ice crystals, *J. Glaciol.*, 8, 153-164.

Macdonald, R. W., S. M. Solomon, R. E. Cranston, H. E. Welsh, M. B. Yunker, and C. Gobeil (1998), A sediment and organic carbon budget for the Canadian Beaufort Shelf, *Marine Geology*, *144*, 255-273.

Maffione, R. A., J. M. Voss, and C. D. Mobley (1998), Theory and measurements of the complete beam spread function in sea ice, *Limnol. Oceanogr.*, 43(1), 34-43.

Maksym, T., M. Van Woert, W. Dierking, S. V. Nghiem (2002), Sea ice microstructural characteristics in the Barents Sea in autumn: Relevance to microwave remote sensing, International Geoscience and Remote Sensing Symposium / Institut of Electrical and Electronics, IEEE, 4, 2176-2178.

Martin, S., R. Drucker, and M. Fort (1995), A laboratory study of frost flower growth on the surface of young sea ice, *J. Geophys. Res.*, 100(C4), 7027-7036.

Martin, S., Y. Yu, and R. Drucker (1996), The temperature dependence of frost flower growth on laboratory sea ice and the effect of the flowers on infrared observations of the surface, *J. Geophys. Res.*, 101(C5), 12111-12125.

Marty, C., R. Philipona, J. Delamere, E. G. Dutton, J. Michalsky, K. Stamnes, R. Storvold, T. Stoffel, S. A. Clough and E. J. Mlawer (2003), Downward longwave irradiance uncertainty under arctic atmospheres: Measurements and modeling, *J. Geophys. Res.*, 108(D12), 4358, doi:10.1029/2002JD002937.

Maslanik, J., C. Fowler, J. C. Stroeve, S. D. Drobot, H. J. Zwally, D. Yi, and W. J. Emery (2007), A younger, thinner Arctic ice cover: Increased potential for rapid, extensive sea-ice loss, *Geophys. Res. Lett.*, 34, L24501, doi:10.1029/2007GL032043.

Maus, S. (2007), On brine entrapment in sea ice: Morphological stability, microstructure and convection, Logos Verlag Berlin, Berlin, Germany, pp. 538.

Maykut, G. A. (1978), Energy exchange over young sea ice in the central Arctic, *J. Geophys. Res.*, 83, 3646-3658.

Maykut, G. A. (1986), The surface heat and mass balance, *The Geophysics of Sea Ice*, N. Untersteiner (Ed), NATO ASI Series B: Physics vol. 146, Plenum Press, New York, 395-464.

Maykut, G. A., and T. C. Grenfell (1975), The spectral distribution of light beneath first-year sea ice in the Arctic Ocean, *Limnol. Oceanogr.*, 20 (4), 554-563.

Maykut, G. A. and M. G. McPhee (1995), Solar heating of the Arctic mixed layer, *J. Geophys. Res.*, 100, 24691-24703.

Melling, H., D. A. Riedel, and Z. Gedalof (2005), Trends in the draft and extent of seasonal pack ice, Canadian Beaufort Sea, *Geophys. Res. Lett.*, 32, L24501, doi:10.1029/2005GL024483.

Michel, C., L. Legendre, J. C. Therriault, S. Demers, T. Vandevelde (1993), Springtime coupling between ice algal and phytoplankton assemblages in southeastern Hudson Bay, Canadian Arctic, *Polar Biol.*, 13, 441-449.

Miller, L. A., O. Owens, A. Mucci, T. N. Papakyriakou, N. E. Sutherland, J. Ehn, and C. J. Mundy (2005), Sea-ice carbon biogeochemistry: Relationship to atmospheric CO2 fluxes, *37th International Liège Colloquium on Ocean Dynamics, Gas Transfer at Water Surfaces*, 2-6 May.

Mobley, C. D., G. F. Cota, T. C. Grenfell, R. A. Maffione, W. S. Pegau, and D. K. Perovich (1998), Modeling light propagation in sea ice, *IEEE Trans. Geosci. Remote Sens.*, 36, 1743– 1749.

Morales Maqueda, M. A., A. J. Willmott, N. R. T. Biggs (2004), Polynyas and climate: a review of observations and modelling, *Reviews of Geophysics*, 42 (RG1004), doi:10.1029/2002RG000116.

Morassutti, M. P., and E. F. LeDrew (1995), Melt pond dataset for use in sea-ice and climate-related studies, Earth Observations Laboratory Technical Report, ISTS-EOL-TR95-001, University of Waterloo, Waterloo, ON, Canada, pp. 53.

Morel, A., and S. Maritorena (2001), Bio-optical properties of oceanic waters: A reappraisal, *J. Geophys. Res.*, 106, 7163-7180.

Mueller, J. L., C. Pietras, S. B. Hooker, R.W. Austin, M. Miller, K.D. Knobelspiesse, R. Frouin, B. Holben and K. Voss (2003), Ocean Optics Protocols For Satellite Ocean Color Sensor Validation, Revision 4, Volume II: Instrument Specifications, Characterization and Calibration, J. L. Mueller, G. S. Fargion and C. R. McClain (eds.), NASA/TM-2003-21621/Rev-Vol II, National Aeronautical and Space Administration, Goddard Space Flight Space Center, Greenbelt, Maryland 20771, pp. 57.

Mundy, C. J., D. G. Barber, and C. Michel (2005), Variability of snow and ice thermal, physical and optical properties pertinent to sea ice algae biomass during spring, *J. Mar. Sys.*, 58, 107-120, doi:10.1016/j.jmarsys.2005.07.003.

Mundy, C. J., J. K. Ehn, D. G. Barber and C. Michel (2007), Influence of snow cover and algae on the spectral dependence of transmitted irradiance through Arctic landfast first-year sea ice, *J. Geophys. Res.*, 112, C03007, doi:10.1029/2006JC003683.

Mundy, C. J., D. G. Barber, C. Michel, and R. F. Marsden (2007b), Linking ice structure and microscale variability of algal biomass in Arctic first-year sea ice using an in situ photographic technique, *Polar Biol.*, 30, 1099-1114, doi:10.1007/s00300-007-0267-1.

Nakawo, M. and N. K. Sinha (1981), Growth rate and salinity profile of first-year sea ice in the high Arctic, *J. Glaciol.*, 27, 315-330.

Nakawo, M. and N. K. Sinha (1984), A note on brine layer spacing of first-year sea ice, Atmosphere-Ocean, 22, 193-206.

Nghiem, S. V., I. G. Rigor, D. K. Perovich, P. Clemente-Colón, J. W. Weatherly, and G. Neumann (2007), Rapid reduction of Arctic perennial sea ice, *Geophys. Res. Lett.*, 34, L19504, doi:10.1029/2007GL031138.

Nicolaus, M., C. Haas, and J. Bareiss (2003), Observations of superimposed ice formation at melt-onset on fast ice on Kongsfjorden, Svalbard, *Physics and Chemistry of the Earth*, 28, 1241–1248.

Papakyriakou, T. N. (1999), An Examination of Relationships among the Energy Balance, Surface Properties and Climate over Snow Covered Sea Ice during the Spring Season, PhD. Thesis, University of Waterloo, 364 p.

Parkinson, C. L., D. J. Cavalieri, P. Gloersen, H. J. Zwally, J. C. Comiso (1999), Artic sea ice extents, areas, and trends: 1978-1996, *J. Geophys. Res.*, 104(C9), 20837-20856.

Parsons, T. R., Y. Maita, and C. M. Lalli (1984), *A manual of chemical and biological methods for seawater analysis*, Pergamon Press, Toronto.

Pegau, W. S., and J. R. V. Zaneveld (2000), Field measurements of in-ice radiance, *Cold Reg. Sci. Techn.*, 31, 33-46.

Perovich, D. K. (1990), Theoretical estimates of light reflection and transmission by spatially complex and temporally varying sea ice covers, *J. Geophys. Res.*, 95, 9557-9568, 1990.

Perovich, D. K. (1990b), The evolution of sea ice optical properties during fall freeze-up, in Ocean Optics 10, *Proc. SPIE Int. Soc. Opt. Eng.*, 1302, 520-531.

Perovich, D. K. (1991), Seasonal changes in sea ice optical properties during fall freeze-up, *Cold Reg. Sci. Techn.*, 19, 261-273.

Perovich, D. K. (1996), The optical properties of sea ice, *CRREL Report* 96-1, Cold. Reg. Res. and Eng. Lab., Hanover, N.H..

Perovich, D. K. and G. A. Maykut (1990), Solar heating of a stratified ocean in the presence of a static ice cover, *J. Geophys. Res.*, 95, 18233-18245.

Perovich, D. K., G. F. Cota, G. A. Maykut, and T. C. Grenfell (1993), Bio-optical observations of first-year Arctic sea ice, *Geophys. Res. Lett.*, 20, 1059– 1062.

Perovich, D. K., and J. A. Richter-Menge (1994), Surface characteristics of lead ice, *J. Geophys. Res.,* 99(C8), 16341-16350.

Perovich, D. K. and A. J. Gow (1996), A quantitative description of sea ice inclusions, *J. Geophys. Res.*, 101(C8), 18327-18343.

Perovich, D. K., J. Longacre, D. G. Barber, R. A. Maffione, G. F. Cota, C. D. Mobley, A. J. Gow, R. G. Onstott, T. C. Grenfell, W. S. Pegau, M. Landry and C. S. Roesler (1998), Field observations of the electromagnetic properties of first-year sea ice, *IEEE Trans. Geosci. Remote Sens.*, 36, 1705-1715.

Perovich, D. K., C. S. Roesler, and W. S. Pegau (1998), Variability in Arctic sea ice optical properties, *J. Geophys. Res.*, 103, 1193-1208.

Perovich, D. K., T. C. Grenfell, B. Light and P. V. Hobbs (2002), Seasonal evolution of the albedo of multiyear Arctic sea ice, *J. Geophys. Res.*, 107(C10), 8044, doi:10.1029/2000JC000438.

Pirazzini, R. (2004), Surface albedo measurements over Antarctic sites in summer, *J. Geophys. Res.*, 109, D20118, doi:10.1029/2004JD004617.

Pope, R. M., and E. S. Fry (1997), Absorption spectrum (380-700 nm) of pure water. II. Integrating cavity measurements, *Appl. Opt.*, 36, 8710-8723.

Oertling, A. B. and R. G. Watts (2004), Growth of and brine drainage from NaCl-H_2O freezing: A simulation of young sea ice, *J. Geophys. Res.*, 109, C04013, doi:10.1029/2001JC001109.

Ohmura, A. (1982), Climate and energy balance on the Arctic tundra, *J. Climatol.*, 2, 65-84.

Oke, T. R. (1987), Boundary Layer Climates, Second edition, Routledge, London and New York, 435 p.

Ricchiazzi, P., S. Yang, C. Gauthier, and D. Sowle (1998), SBDART: A research and teaching software tool for plane-parallel radiative transfer in the Earth's atmosphere, *Bull. Amer. Meteor. Soc.*, 79 (10), 2101-2214.

Richardson, C. (1976), Phase relationships in sea ice as a function of temperature, *J. Glaciol.*, 17, 507-519.

Richter-Menge, J., J. Overland, A. Proshutinsky, V. Romanovsky, L. Bengtsson, L. Brigham, M. Dyurgerov, J. C. Gascard, S. Gerland, R. Graversen, C. Haas, M. Karcher, P. Kuhry, J. Maslanik, H. Melling, W. Maslowski, J. Morison, D. Perovich, R. Przybylak, V. Rachold, I. Rigor, A. Shiklomanov, J. Stroeve, D. Walker, and J. Walsh (2006), State of the Arctic Report, NOAA OAR Special Report, NOAA/OAR/PMEL, Seattle, WA, 36 p.

Robinson, D. A., G. Scharfen, M. C. Serreze, G. Kukla and R. G. Barry (1986), Snow melt and surface albedo in the arctic basin, *Geophys. Res. Let.*, 13, 945-948.

Roesler, C. S. and R. Iturriaga (1994), Absorption properties of marine-derived material in Arctic sea ice, in *Ocean Optics* 12, *Proc. SPIE Int. Soc. Opt. Eng.*, 2258, 933-943.

Roesler, C. S., and M. J. Perry (1995), In situ phytoplankton absorption, fluorescence emission, and particulate backscattering spectra determined from reflectance, *J. Geophys. Res.*, 100(C7), 13279-13294.

Roesler, C. S. (1998), Theoretical and experimental approaches to improve the accuracy of particulate absorption coefficients derived from the quantitative filter technique, *Limnol, Oceanogr.*, 43(7), 1649-1660.

Rothrock, D. A., Y. Yu, and G. A. Maykut (1999), Thinning of the Arctic sea-ice cover, Geophys. Res. Lett., 26, 3469– 3472.

Rysgaard, S., R. N. Glud, M. K. Sejr, J. Bengtsen, and P. B. Christensen (2007), Inorganic carbon transport during sea ice growth and decay: A carbon pump in polar seas, *J. Geophys. Res.*, 112, C03016, doi:10.1029/2006JC003572.

Saloranta, T. M. (1998), Snow and ice in sea ice thermodynamic modeling, Master's thesis, Department of Geophysics, University of Helsinki, Finland.

Semiletov, I., A. Makshtas, S.-I. Akasofu (2004), Atmospheric CO_2 balance: The role of Arctic sea ice, *Geophys. Res. Lett.*, 31, L05121, doi:10.1029/2003GL017996.

Serreze M. C., J. A. Maslanik, T. A. Scambos, F. Fetterer, J. Stroeve, K. Knowles, C. Fowler, S. Drobot, R. G. Barry, and T. M. Haran (2003), A record minimum arctic sea ice extent and area in 2002, *Geophys. Res. Lett.*, 30 (3), 1110, doi:10.1029/2002GL016406.

Shih, S. -E., K. –H. Ding, S. V. Nghiem, C. –C. Hsu, J. A. Kong, and A. K. Jordan (1998), Thin saline ice thickness retrieval using time-series C-band polarimetric radar measurements, *IEEE Trans. Geosci. Remote Sens.*, 36 (5), 1589–1598.

Smedsrud, L. H. and R. Skogseth (2006), Field measurements of Arctic grease ice properties and processes, *Cold Reg. Sci. Technol.*, 44, 171-183.

Smith, R. C., and K. S. Baker (1981), Optical properties of the clearest natural waters (200-800 nm), *Appl. Opt.*, 20, 177-184.

Smith, R. E. H., W. G. Harrison, L. R. Harris and A. W. Herman (1990), Vertical fine structure of particulate matter and nutrients in sea ice of the high arctic, *Can. J. Fish. Aquat. Sci.*, 47, 1348-1355.

Stamnes, K., S.-C. Tsay, W. Wiscombe, and K. Jayaweera (1988), Numerically stable algorithm for discrete-ordinate-method radiative transfer in multiple scattering and emitting layered media, *Appl. Opt.*, 27, 2502–2509.

Steffen, K. and T. DeMaria (1996), Surface energy fluxes over Arctic winter sea ice in Barrow Strait, *J. Appl. Meteor.*, 35, 2067-2079.

Stirling, I., N. J. Lunn, J. Iacozza, C. Elliott and M. Obbard (2004), Polar bear distribution and abundance on the southwestern Hudson Bay coast during open water season, in relation to population trends and annual ice patterns, Arctic, 57(1), 15-26.

Sturm, M., D. K. Perovich and J. Holmgren (2002), Thermal conductivity and heat transfer through the snow on the ice of the Beaufort Sea, *J. Geophys. Res.*, 107, doi:10.1029/2000JC000409.

Stramski, D. (1990), Artifacts in measuring absorption spectra of phytoplankton collected on a filter, *Limnol. Oceanogr.*, 35(8), 1804-1809.

Stramski, D., and C. D. Mobley (1997), Effects of microbial particles on oceanic optics: A database of single-particle optical properties, *Limnol. Oceanogr.*, 42(3), 538-549.

Stroeve, J. C., M. C. Serreze, F. Fetterer, T. Arbetter, W. Meier, J. Maslanik, and K. Knowles (2005), Tracking the Arctic's shrinking ice cover: Another extreme September minimum in 2004, *Geophys. Res. Lett.*, 32(4), L04501, doi:10.1029/2004GL021810.

Thomas, G. E. and K. Stamnes (1999), Radiative Transfer in the Atmosphere and Ocean, Cambridge University Press, Cambridge, UK., 517 p.

Untersteiner, N. (1961), On the mass and heat budget of Arctic sea ice, *Arch. Meteorol. Geophys. Bioklim.*, Ser. A, 12, 151– 182.

Untersteiner, N. (1968), Natural desalination and equilibrium salinity profile of perennial sea ice, *J. Geophys. Res.*, 73, 1251–1257.

Vancoppenolle M., C. M. Bitz and T. Fichefet (2007), Summer landfast sea ice desalination at Point Barrow, Alaska: Modeling and observations, *J. Geophys. Res.*, 112, C04022, doi:10.1029/2006JC003493.

van de Hulst, H. C. (1980), *Multiple light scattering tables, formulas, and applications*, vols. 1-2, pp. 739, Academic, San Diego, Calif.

Vermote, E. F., N. El Saleous, C. O. Justice, Y. J. Kaufman, J. L. Privette, L. Remer, J. C. Roger, and D. Tanré (1997), Atmospheric correction of visible to middle-infrared EOS-MODIS data over land surfaces: Background, operational algorithm and validation, *J. Geophys. Res.*, 102(D14), 17131-17141.

Vinje, T. (2001), Fram strait ice fluxes and atmospheric circulation: 1950-2000, *J. Climate*, 14, 3508-3517.

Wadhams, P. (1981), The ice cover in the Greenland and Norwegian seas, *Rev. Geophys. Space Phys.*, 19, 345–393.

Wadhams P., M. A. Lange, and S. F. Ackley (1987), The ice thickness distribution across the Atlantic sector of the Antarctic ocean in midwinter, *J. Geophys. Res.*, 92, 14535-14552.

Wadhams, P., and N. R. Davis (2000), Further evidence of ice thinning in the Arctic Ocean, *Geophys. Res. Lett.*, 27 (24), 3973-3975.

Wang, J., L. A. Mysak and R. G. Ingram (1994), Interannual variability of sea-ice cover in Hudson Bay, Baffin Bay and the Labrador Sea, Atmosphere-Ocean, 32, 421-447.

Warren, S. G. (1982), Optical properties of snow, *Rev. Geophys. Space Phys.*, 20, 67–89.

Warren, S. G. (1984), Optical constants of ice from the ultraviolet to the microwave, *Appl. Opt.*, 23, 1026-1225.

Warren, S. G., R. E. Brandt, and T. C. Grenfell (2006), Visible and near-ultraviolet absorption spectrum of ice from transmission of solar radiation into snow, *Appl. Opt.*, 45, 5320-5334.

Winsor, P. and G. Björk (2000), Polynya activity in the Arctic Ocean from 1958 to 1997, *J. Geophys. Res.*, 105(C4), 8789-8803.

Weeks, W. F. (1998), Growth conditions and the structure and properties of sea ice, in M. Leppäranta (ed.), *Physics of Ice-Covered Seas*, vol. 1, 25-104, Helsinki University Press, Helsinki.

Weeks W. F. and S. F. Ackley (1982), *The growth, structure, and properties of sea ice, Cold. Reg. Res. Eng. Lab*, Monograph 82-1, Hanover, New Hampshire.

Weeks, W. F., and W. L. Hamilton (1962), Petrographic characteristics of young sea ice, Point Barrow, Alaska, *American Mineralogist*, 47(7-8), 945-961.

Welch, H. E. and M. A. Bergmann (1989), Seasonal development of ice algae and its prediction from environmental factors near Resolute, N.W.T., Canada, *Can. J. Fish. Aquat. Sci.*, 46, 1793-1804.

World Meteorological Organization (1985), WMO sea-ice nomenclature, terminology, codes and illustrated glossary, *WMO/DMM/BMO 259-TP-145*, Secretariat of the WMO, Geneva.

Xie, H., and M. Gosselin (2005), Photoproduction of carbon monoxide in first-year sea ice in Franklin Bay, southeastern Beaufort Sea, *Geophys. Res. Lett.*, 32, L12606, doi:10.1029/2005GL022803.

Yen, Y. C. (1981), Review of thermal properties of snow, ice and sea ice, *CRREL Report* 81-10, Cold. Reg. Res. and Eng. Lab., Hanover, N.H..

Yu, Y., G. A. Maykut, and D. A. Rothrock (2004), Changes in the thickness distribution of Arctic sea ice between 1958–1970 and 1993–1997, *J. Geophys. Res.*, 109, C08004, doi:10.1029/2003JC001982.

Yu, Y. and Stern, H. L., Decline of arctic landfast ice between 1975 and 2003, *Geophys. Res. Lett.*, submitted (see http://arcticchamp.sr.unh.edu/featuredproject/archive/yu_stern.shtml).

Zeebe, R. E., H. Eicken, D. H. Robinson, and D. Wolf-Gladrow (1996), Modeling the heating and melting of sea ice through light absorption by micoralgae, *J. Geophys. Res.*, 101, 1163– 1181.

Zhou, X, and S. Li (2002), Sub-pixel correction in comparison between in situ and satellite derived spectral reflectance, IEEE 2002 International Geoscience and Remote Sensing Symposium, Toronto, Ontario Canada, 24-28 June 2002, 976-978.

Zhou, X., and S. Li (2003), Comparison between *in situ* and MODIS-derived spectral reflectances of snow and sea ice in the Amundsen Sea, Antarctica, *Int. J. Remote Sensing*, 20, 5011-5032.

Zhou, X., S. Li, and K. Stamnes (2003b), Geometrical-optics code for computing the optical properties of large dielectric spheres, *Appl. Opt.*, 42, 4295-4306.